

The Nanoscale Organisation of Human Macrophage Surfaces Studied by Super-resolution Microscopy

A thesis submitted to the University of Manchester for the degree of
Doctor of Philosophy in the Faculty of Biology, Medicine and Health

2021

Susanne Dechantsreiter

School of Biological Sciences

Contents

List of Figures	5
List of Tables	7
Abbreviations	8
Abstract.....	11
Declaration.....	12
Copyright Statement.....	13
Publications.....	14
Acknowledgements.....	15
Chapter 1 – Introduction	17
1.1 Macrophages.....	17
1.1.1 Macrophage Origins	18
1.1.2 The Contribution of Monocyte-derived Macrophages.....	19
1.1.3 Macrophage Ontogeny vs. Tissue Niche Influences	21
1.1.4 Macrophage Phenotypes.....	25
1.1.5 Generation of Different Macrophages <i>in vitro</i>	27
1.2 Lung Macrophages	30
1.2.1 Alveolar Macrophages	32
1.2.2 Interstitial Macrophages.....	33
1.3 Autofluorescence	34
1.3.1 Autofluorescent Lung Macrophages in STORM.....	36
1.3.2 Accounting for Autofluorescence	39
1.4 Nanoscale Organisation of Receptor Molecules	40
1.5 Studying the Phagocytic Synapse.....	42
1.6 Extracellular Vesicles (EV)	45
1.6.1 Studying EV with Super-Resolution Microscopy	50
1.7 Microscopy	53
1.7.1 Fluorescence Microscopy and the Diffraction Limit.....	53
1.7.2 Breaking the diffraction limit.....	58
1.8 Aims.....	59
Chapter 2 Experimental Procedures	61
2.1 Cells	61
2.1.1 Generation of Macrophages from Blood Monocytes.....	61
2.1.2 HEK293T/17 Cell Line.....	62
2.1.3 Human Lung Macrophages	62
2.2 Antibodies	63
2.2.1 Antibody Labelling	64
2.3 Preparation of Coated Slides, Bilayers and Beads	65
2.4 Flow Cytometry	66
2.5 Enzyme-linked immunosorbent assay (ELISA)	66
2.6 Microscopy	67
2.6.1 Sample preparation	67
2.6.2 Widefield Microscopy.....	68

2.6.3	Confocal Microscopy	68
2.6.4	STED Microscopy	69
2.6.5	TIRF and STORM Microscopy.....	69
2.7	Microscopy data analysis	70
2.7.1	STORM Data Analysis and Filtering Strings.....	70
2.7.2	Co-localisation analysis.....	71
2.8	Simulated Data.....	71
2.9	Background Correction Technique.....	73
2.9.1	Evaluation of Corrected Images.....	73
2.10	Assessment of Lung Macrophage Protrusions.....	74
2.11	Quantitative Analysis of Vesicles	74
2.12	Isolation of Extracellular Vesicles (EV)	76
2.13	Proteomics analysis.....	77
2.13.1	Heatmaps.....	79
2.14	Statistics	79
Chapter 3 – Establishing an Imaging System to Investigate the Nano-scale Organisation of the Membrane of Human Macrophages.....		81
3.1	Introduction	81
3.2	Summary of Chapter Aims	83
3.3	Results	84
3.3.1	Generation and Characterisation of Human Macrophages	84
3.3.2	Activating Macrophages on IgG Coated Surfaces.....	91
3.3.3	Imaging Autofluorescent Human Lung Macrophages	97
3.4	Discussion.....	106
3.4.1	Summary of Results	106
3.4.2	Morphology and Phenotype of Macrophages.....	106
3.4.3	Model of the Phagocytic Synapse.....	110
3.4.4	The Natural Autofluorescence of Human Lung Macrophages	112
3.4.5	Conclusions.....	116
Chapter 4 – Establishment of a novel background correction technique to study the nanoscale organisation of the membrane of human lung macrophages		117
4.1	Introduction	117
4.2	Summary of Chapter Aims	119
4.3	Results	120
4.3.1	Background Correction Technique	120
4.3.2	Validation of Background Correction Technique.....	121
4.3.3	Applying Correction Technique to Stained Lung Macrophages	148
4.3.4	Observation of Protrusion-Like Structures on the Surface of Human Lung Macrophages	150
4.3.5	Background correction reveals nanometre-scale ring structures at the membrane of human lung macrophages	154
4.4	Discussion.....	156
4.4.1	Summary of Results	156
4.4.2	Background Correction Technique	156

4.4.3	Protrusion-like Structures Tipped with MHC class I	161
4.4.4	CD81 at the Membrane of Human Lung Macrophages.....	162
4.4.5	Conclusions.....	163
Chapter 5 – Macrophages Secrete Distinct Populations of Extracellular Vesicles upon Stimulation through their Fcγ receptor I.....		165
5.1	Introduction	165
5.2	Summary of Chapter Aims	168
5.3	Results.....	169
5.3.1	CD81 forms into nanometer-scale ring structures at the membrane of activated, human macrophages	169
5.3.2	Formation of CD81-Rings at the Membrane of Human Macrophages Incubated on Activating Lipid Bilayers.....	179
5.3.3	Macrophages Secrete Extracellular Vesicles across the Immune Synapse	184
5.3.4	Isolation of Extracellular Vesicles via Ultracentrifugation.....	193
5.3.5	Macrophage Vesicles are being secreted through Holes in the Actin Mesh at the Immune Synapse	195
5.3.6	Proteomics Analysis of Macrophage Vesicles Reveal Distinct Contents for Different Macrophages.....	197
5.3.7	Preliminary Data Confirms LILRB1 in M0-like and M2-like Macrophage Vesicles	208
5.4	Discussion.....	213
5.4.1	Summary of Results.....	213
5.4.2	CD81 Nanometer-scale Ring Structures at the Synapse of IgG-activated Macrophages are Extracellular Vesicles	213
5.4.3	Characteristics of Extracellular Vesicles Change with Culture	218
5.4.4	Analysis of Macrophage Secretions.....	219
5.4.5	Extracellular Vesicles are being secreted through Holes in the Actin Mesh	220
5.4.6	Proteomics Data Confirms Discrete Contents for Macrophage Vesicles	221
5.4.7	MHC class I co-localises with LILRB1 on M0-like Macrophage Vesicles .	224
5.4.8	Conclusions.....	225
Chapter 6 – Final Remarks.....		227
References.....		230

Word count:

66,119 words in total

56,754 words excluding bibliography

List of Figures

Figure 1-1: Schematic illustration of the niche model.	23
Figure 1-2: Anatomy of the respiratory tract.	31
Figure 1-3: Sources of autofluorescence within the cell.	35
Figure 1-4: The process of phagocytosis.	43
Figure 1-5: Extracellular vesicle (EV) biogenesis and composition.	46
Figure 1-6: Tetraspanins in extracellular vesicle (EV) biology.	49
Figure 1-7: The principle of fluorescence radiation.	54
Figure 1-8: Composition of fluorescence widefield and confocal microscopes.	55
Figure 1-9: The principle of total internal reflection fluorescence (TIRF) microscopy.	57
Figure 1-10: Principles of super-resolution microscopy.	59
Figure 2-1: N-Hydroxysuccinimide (NHS) esters attached to fluorophores and primary amines on antibodies form stable amino bonds.	64
Figure 2-2: Simulating STORM data sets.	72
Figure 3-1: Generation and isolation of human macrophages.	85
Figure 3-2: M0-like, M1-like and M2-like macrophages display distinct morphologies.	86
Figure 3-3: Human lung macrophages were selected from lung immune cell suspension by adhesion.	87
Figure 3-4: Characterisation of monocyte-derived macrophages by flow cytometry.	89
Figure 3-5: Optimising the amount of GM-CSF to generate M1-like macrophages.	90
Figure 3-6: Incubation of macrophages on IgG-coated glass slides induces cytokine secretion.	92
Figure 3-7: Activation of macrophages via IgG coated glass slides induces cell spreading.	93
Figure 3-8: Planar lipid bilayer are immobile.	95
Figure 3-9: Incubation of macrophages on IgG-containing lipid bilayers introduces cytokine secretion of macrophages.	96
Figure 3-10: Spectral range of unstained lung macrophages.	99
Figure 3-11: Imaging sparse antibodies on glass.	101
Figure 3-12: The effect of autofluorescence in STORM.	103
Figure 3-13: Autofluorescence of lung macrophages varies from cell to cell.	104
Figure 3-14: Autofluorescence is not bleachable.	105
Figure 4-1: Principle of background correction technique.	121
Figure 4-2: Overview of simulated data used to validate the background correction technique.	122
Figure 4-3: Intensity profiles of simulated ground truth and acquired data.	124
Figure 4-4: Intensity profiles of simulated backgrounds.	125
Figure 4-5: Comparing intensities of simulated ground truths and backgrounds.	126
Figure 4-6: Principle of the validation of the correction technique.	127
Figure 4-7: Correction method does not aggravate data sets without background.	131
Figure 4-8: Moving median correction prior to image processing successfully corrects simulated, constant backgrounds.	133
Figure 4-9: Moving median correction successfully corrects simulated, linearly decaying backgrounds.	135
Figure 4-10: Moving median correction successfully removes simulated, non-linearly decaying backgrounds.	137
Figure 4-11: 50 frames is the ideal group size for the moving median correction.	139
Figure 4-12: Intensity profiles of unstained, autofluorescent lung macrophages.	142
Figure 4-13: Application of moving median filter successfully corrects recorded autofluorescence.	143
Figure 4-14: Displaying calculated autofluorescence background.	145

Figure 4-15: Correcting recorded STORM data sets from separately acquired, severe autofluorescence.	147
Figure 4-16: Successfully correcting autofluorescent lung macrophages using moving median filter.	149
Figure 4-17: Lung macrophages form protrusions upon activation through Fc receptors.	151
Figure 4-18: Nanoscale investigation of macrophage protrusions.	153
Figure 4-19: CD81 forms into nanometer-scale ring structures at the membrane of IgG-activated lung macrophages.	155
Figure 5-1: CD81 forms into nanometer-scale ring structures at the synapse of activated macrophages.	170
Figure 5-2: Line profiles of CD81-ring structures confirm circular nature of observations.	171
Figure 5-3: Activation through FcγRI induces the formation of rings.	172
Figure 5-4: Different macrophage populations show distinct characteristics for nanometer-scale ring structures.	173
Figure 5-5: Ring structures appear in different areas across the synapse.	175
Figure 5-6: Formation of CD81 nanometer-scale ring structures over time.	176
Figure 5-7: Culturing lung macrophages influences their CD81 ring characteristics.	178
Figure 5-8: CD81 forms into nanometer-scale ring structures at the membrane of macrophages incubated on planar lipid bilayers containing IgG.	180
Figure 5-9: Line profiles of CD81-ring structures at the membrane of macrophages activated on planar lipid bilayers.	181
Figure 5-10: Incubation of macrophages on activating planar lipid bilayers induced CD81-ring formation.	182
Figure 5-11: Characteristics of CD81-rings at the membrane of macrophages activated on lipid bilayers.	183
Figure 5-12: Shadow imaging reveals the secretion of extracellular vesicles by IgG-activated macrophages.	185
Figure 5-13: Line profiles of extracellular vesicles secreted by macrophages onto activating lipid bilayers.	186
Figure 5-14: Automated analysis of vesicle characteristics using a custom-made macro.	188
Figure 5-15: Macrophages secrete vesicles when activated on lipid bilayers containing IgG.	190
Figure 5-16: Characteristics of vesicles left behind on lipid bilayers.	191
Figure 5-17: Vesicles isolated via ultracentrifugation appear as nanometer-scale ring structures when imaged with STORM.	194
Figure 5-18: Line profiles of extracellular vesicles (EV) isolated with differential ultracentrifugation.	195
Figure 5-19: Macrophage vesicles are secreted through holes in the actin mesh.	196
Figure 5-20: Schematic of macrophage preparation for proteomics analysis.	198
Figure 5-21: Extracellular vesicles (EV) from different macrophages show distinct protein contents.	200
Figure 5-22: Gene Ontology (GO) annotation of all proteins identified in proteomics analysis.	201
Figure 5-23: Hierarchical clustering reveals distinct populations of small extracellular vesicles (EV) for M0-, M1- and M2-like macrophages.	203
Figure 5-24: Hierarchical clustering reveals distinct populations of large extracellular vesicles (EV) for M0-, M1- and M2-like macrophages.	205
Figure 5-25: M0- and M2-like macrophage vesicles contain inhibitory receptor LILRB1.	209
Figure 5-26: Positive control for two colour STORM.	210
Figure 5-27: Inhibitory receptor LILRB1 and MHC class I co-localise at the membrane of M0-like macrophages.	212

List of Tables

Table 1-1: Overview of physical properties of macrophages relevant for microscopy.	18
Table 1-2: Differentiation of blood monocytes into macrophages.....	29
Table 2-1: Monoclonal antibodies (Abs) used for flow cytometry.	63
Table 2-2: Monoclonal antibodies (Ab) used for microscopy.	63
Table 2-3: Filtering parameters for STORM.	71
Table 3-1: Patient data of all lung tissues used in this chapter.	98
Table 4-1: Removing simulated backgrounds from simulated SMLM data.	129
Table 5-1: Small extracellular vesicles (EV) of M1-like macrophages contain high levels of HLA-DR.	204
Table 5-2: Small extracellular vesicles (EV) of M1-like macrophages contain low levels of Leukocyte immunoglobulin-like receptors (LILRs).	204
Table 5-3: Large extracellular vesicles (EV) of M1-like macrophages contain high levels of HLA class II.	206
Table 5-4: Large extracellular vesicles (EV) of M2-like macrophages contain high levels of HLA class I.	207
Table 5-5: Inhibitory leukocyte immunoglobulin-like receptors (LILRs) LILRB1 and LILRB2 increased detected in M2-like macrophages.	207

Abbreviations

Ab	antibody
AF	AlexaFluor
Ag	antigen
ALI	acute lung injury
AM	alveolar macrophages
APC	antigen presenting cell
AREG	amphiregulin
ASM	airway smooth muscle
BAL	bronchoalveolar lavage
BALF	bronchoalveolar lavage fluid
BM	bone marrow
CaOx	Calcium oxalate
CCR2	chemokine receptor type 2
CI	confidence interval
CLEM	correlative light and electron microscopy
CM-DiI	1,1'-dioctadecyl-3,3',3'-tetramethylindocarbocyanine perchlorate
COPD	chronic obstructive pulmonary disease
DAMP	damage-associated molecular pattern
DC	dendritic cell
DMEM	Dulbecco's Modified Eagle Medium;
DNA	deoxyribonucleic acid
DOPC	dioleoylphosphatidylcholine
EGFR	epidermal growth factor receptor
ELISA	enzyme-linked immunosorbent assay
EM	electron microscopy
EMCCD	electron-multiplying, charge-coupled device
EMP	erythro-myeloid progenitors
ERM	ezrin–radixin–moesin
ESCRT	endosomal sorting complexes required for transport
EV	extracellular vesicles
FcγRI	Fc gamma receptor I
FDA	Food and Drug Administration
FMO	fluorescence minus one
FRAP	fluorescence recovery after photobleaching
GILZ	glucocorticoid-induced leucine zipper
GM-CSF	granulocyte-macrophage colony-stimulating factor
GO	Gene Ontology

GYEVM	Gly-Tyr-Glu-Val-Met
h	hour
HDAC2	histone deacetylase 2
HS	human serum
HSCs	hematopoietic stem cells
IFNγ	interferon gamma
Ig	immunoglobulin
IgE	immunoglobulin E
IL	interleukin
ILVs	intraluminal vesicles
IM	interstitial macrophages
iNOS	inducible nitric oxide synthase
IRM	interference reflection microscopy
IS	immunological synapse
IκBα	inhibitor of kappa B - α
LED	light emitting diode
LFA-1	lymphocyte function-associated antigen 1
LILRB1	leukocyte immunoglobulin-like receptor B1
LPS	lipopolysaccharide
mAb	monoclonal antibody
ManARTS	Manchester Allergy, Respiratory and Thoracic Surgery
MDCK	Madin-Darby Canine Kidney
MDM	monocyte-derived macrophages
MFI	mean fluorescence intensity
MHC	major histocompatibility complex
min	minutes
miRNA	microRNA
MKP1	MAP kinase phosphatase 1
MPs	microparticles
MV	microvesicles
MVB	multivesicular bodies
NA	numerical aperture
NAD	nicotinamide-adenine dinucleotide
NHS	National Health Service
NK	Natural killer
NKG2D	natural killer group 2D
NO	nitric oxide
NTA	nanoparticle tracking analysis
PAMP	pathogen-associated molecular patterns

PAP	pulmonary alveolar proteinosis
PBMCs	peripheral blood mononuclear cells
PLL	poly-L-lysine
PRRs	pattern recognition receptors
PSF	point spread function
RNA	ribonucleic acid
ROI	regions of interest
ROS	reactive oxygen species
RPMI	Roswell Park Memorial Institute
RT	room temperature
s	seconds
SHP-1	src homology 2 domain-containing tyrosine phosphatase-1
SIRPα	signal-regulatory protein α
SLPI	secretory leukocyte protease inhibitor
SMLM	single-molecule localization microscopy
STED	stimulated emission depletion
STORM	stochastic optical reconstruction microscope
Syk	spleen tyrosine kinase
TCR	T cell receptor
TEMS	tetraspanin enriched microdomains
TIRF	total internal reflection fluorescence
TLR	toll-like receptor
TM	transmembrane domain
TNF-α	tumour necrosis factor α
TRPS	tuneable resistive pulse sensing
WGA	wheat germ agglutinin
YXX\emptyset	Tyr-Xaa-Xaa- \emptyset

Abstract

Recent advances in super-resolution microscopy revealed that the function of receptor molecules is influenced by their nanoscale organisation within the membrane. This especially applies to macrophages who are one of the most plastic cell types known with a large repertoire of surface receptors tightly regulating their many different functions. In addition, macrophage phenotype is highly influenced by the tissue of residence. However, very little studies have imaged tissue-derived macrophages due to their high autofluorescence. To address this, a novel background correction technique was developed to correct for autofluorescence in stochastic optical reconstruction microscopy (STORM) data sets. Here, a moving median filter was applied prior to image reconstruction to subtract unwanted backgrounds. Importantly, this enabled the investigation of the membrane of human lung macrophages on a nanometer-scale for the first time. Macrophages were activated through their Fc receptors by IgG-coated surfaces, representing a 2D model of the phagocytic synapse. Interestingly, upon activation, lung macrophages formed MHC class I–tipped protrusions. This is consistent with a role of macrophage protrusions in antigen presentation. In addition, macrophages secreted extracellular vesicles (EV) upon activation with IgG. Here, lung- and monocyte-derived macrophages (MDM) were stained for the tetraspanin and EV marker CD81. Crucially, EV were captured directly upon secretion, on a nanometer-scale, enabling the accurate detection of EV diameters and the analysis on a cell-by-cell basis which is not possible, when studying EV as often done in bulk after isolation. The comparison of M0-like, M1-like, M2-like and lung macrophages revealed distinct vesicle characteristics, suggesting distinct functions and mechanisms of biogenesis. Crucially, the number of vesicles secreted differed greatly between single cells, highlighting the heterogeneity of cellular secretions. Proteomics analysis of MDM-derived EV confirmed discrete contents of EV with MHC class I and leukocyte immunoglobulin-like receptor B1 (LILRB1) being enriched in vesicles derived from M2-like and M0-like macrophages, while MHC class I was enriched in M1-like macrophage vesicles. Interestingly, two colour STORM of the LILRB1 and MHC class I showed their co-localisation on M0-like macrophage vesicles.

Declaration

No portion of the work referred to in this thesis has been submitted in support of an application for another degree or qualification of this or any other university or other institute of learning. The findings presented in this report are my own work unless stated otherwise and with the following exceptions:

- Primary cells were isolated from healthy donors by Dr. Kevin Stacey (Daniel Davis Lab, University of Manchester)
- Ming Lim (Daniel Davis Lab, University of Manchester), was an undergrad student supervised by myself during her final year project. Under my supervision, she contributed to three figures in this thesis. Ming Lim counted the cells for Figure 3-5 and imaged and analysed two out of four donors of M1-like macrophages which contributed to Figure 5-3 and Figure 5-4
- As part of two joint publications, Dr. Ashley Ambrose (Daniel Davis Lab, University of Manchester) contributed to the work as follows:
 - In Figure 4-2, panel i – iv, he created the background images. The expansion of these background images to 10000 frame strong data sets with varying intensities was done by myself, which were then used to validate the background correction technique in Chapter 4
 - In Figure 4-15, panel B bottom, he imaged the actin-stained HEK cells
 - He has written the ImageJ macros for batch processing of images with the background correction technique and vesicle quantitative analysis
- Dr. Jonathan Worboys (Daniel Davis Lab, University of Manchester) created the heat maps shown in Figure 5-23 and Figure 5-24.

Copyright Statement

i. The author of this thesis (including any appendices and/or schedules to this thesis) owns certain copyright or related rights in it (the “Copyright”) and s/he has given The University of Manchester certain rights to use such Copyright, including for administrative purposes.

ii. Copies of this thesis, either in full or in extracts and whether in hard or electronic copy, may be made only in accordance with the Copyright, Designs and Patents Act 1988 (as amended) and regulations issued under it or, where appropriate, in accordance with licensing agreements which the University has from time to time. This page must form part of any such copies made.

iii. The ownership of certain Copyright, patents, designs, trademarks and other intellectual property (the “Intellectual Property”) and any reproductions of copyright works in the thesis, for example graphs and tables (“Reproductions”), which may be described in this thesis, may not be owned by the author and may be owned by third parties. Such Intellectual Property and Reproductions cannot and must not be made available for use without the prior written permission of the owner(s) of the relevant Intellectual Property and/or Reproductions.

iv. Further information on the conditions under which disclosure, publication and commercialisation of this thesis, the Copyright and any Intellectual Property and/or Reproductions described in it may take place is available in the University IP Policy (see <http://documents.manchester.ac.uk/DocuInfo.aspx?DocID=24420>), in any relevant Thesis restriction declarations deposited in the University Library, The University Library’s regulations (see <http://www.library.manchester.ac.uk/about/regulations/>) and in The University’s policy on Presentation of Theses.

Publications

Dechantsreiter, S.*, Ambrose, A. R.* , Lim, M, Shah, R., Montero, M. A., Quinn, A. M., Tannahill, G. M., Davis, D. M. (2021). STORM Reveals MHC class II-Enriched Extracellular Vesicles for M1 but not M2 Macrophages. In preparation.

Ambrose, A. R. *, **Dechantsreiter, S. ***, Shah, R., Montero, M. A., Quinn, A. M., Hessel, E. M., Beinke, S., Tannahill, G. M., & Davis, D. M. (2020). Corrected Super-Resolution Microscopy Enables Nanoscale Imaging of Autofluorescent Lung Macrophages. *Biophysical Journal*, 119(12), 2403–2417.

*These authors contributed equally.

Acknowledgements

First of all, I want to thank my supervisor, Prof Daniel M. Davis for giving me the opportunity to work in the field of immunology while coming from another field of study. Your passion for science is inspiring and your guidance and advice during my PhD taught me critical thinking on the highest level.

Secondly, I would like to thank my supervisors at GSK: Dr Edith Hessel, Dr Soren Beinke and Dr Gillian Tannahill. Your advice was always useful and went beyond feedback regarding my project. Thank you very much.

I would also like to acknowledge all members of the Davis lab for creating a great working environment. I especially want to thank Dr Ashley Ambrose whom I worked very closely with. Thanks for your help and patients throughout our collaborations. And to Rajia, for keeping my French skills going, and a wonderful friendship. I would also like to extend my gratitude to the Hussell lab and in particular to Karishma Mohamed who helped me with lung tissue perfusions. In addition I would like to thank the team of the ManARTS biobank and in particular Jenny Hankinson, who coordinated these interactions.

An especially heartfelt thanks to my friends here in Manchester. Jess, Chandan, Bee, Liz, Melissa and Hannah, what a wonderful friendship we've developed during the last few years. Living abroad, far away from my family and friends, you were my home. I am incredibly grateful for the time spent together and am looking forward to future adventures! Reka, I will always think back to our canal boat trip with a smile. And to Poppy, thanks for being my outdoor guru and travel agency, for your generosity, for making me try new things and countless walks together. Thanks to the SHE choir community, which was a constant source of joy, help and empowerment.

An equally warm thank you to my friends back home in Germany and in particular to Julz, Jessi, Kathi, Kathi and Vicky. Despite the distance, we kept in touch with countless hours on the phone and video chats. Your visits here in Manchester meant the world to me. Thank you so much.

And finally, I want to thank my family. Especially my brother Christoph and his daughter Emilia who kept me going with loving letters and messages from afar. Thanks to my father, Martin, who was as always a massive help during my whole PhD! And my mother, Inge, who stands to me no matter what.

To all the strong and independent women out there;
we surely need more of them in science.

Chapter 1 – Introduction

Macrophages are a type of innate immune cell that can be found all through the body. They form the very first line of defence of the immune system and play a key role in initiating and coordinating an immune response as well as homeostasis. Interestingly, macrophages are well known to act pro- as well as anti-inflammatory and their function and phenotype is highly influenced by their environment^{1,2}. In fact, macrophages comprise a large repertoire of cell-surface receptors, allowing them to navigate many different tasks. In recent years, it has become clear that receptor-ligand interactions depend not only on ligand specificity and binding affinities but also on the nanometer-scale organisation of the molecules involved³⁻⁶. Advances in super-resolution imaging present a great tool to learn more about these processes. However, despite their importance, very little studies imaged tissue-derived macrophages applying super-resolution microscopy. This is likely to be due to sample availability as well as intrinsic autofluorescence, which interferes with light microscopy. To advance this knowledge, the focus of this study was the nanometer-scale organisation of the membrane of lung- and monocyte-derived macrophages. In addition, super-resolution microscopy was applied to study extracellular vesicles, directly upon secretion on a cell-by-cell basis.

This first chapter will give an overview of macrophage origin and function, with a focus on monocyte- and lung-derived macrophages. It will then discuss the importance of the nanometer-scale organisation of surface receptor molecules and how super-resolution microscopy presents a unique tool to study extracellular vesicle secretion. Finally, this chapter will highlight the function and use of different microscopy techniques to study immune cells.

1.1 Macrophages

Macrophages are mononuclear phagocytes that arise from myeloid precursor cells. They can be found in tissues throughout the body and their main function is to engulf and digest foreign material, infected or dead cells, and cell debris. They play a

key role in initiating and coordinating an immune response. As macrophages phagocytose foreign particles and infected cells as well as cell debris or dead cells it is not surprising that they play an important role in host protection as well as in tissue development and wound healing⁷. With diameters ranging from approximately 20 to 30 μm macrophages are relatively large cells. Due to their adherent properties, they are ideal candidates for microscopy studies and can be activated, for example by coated surfaces. Table 1-1 summarises typical physical properties of macrophages relevant for microscopy.

Table 1-1: Overview of physical properties of macrophages relevant for microscopy.

Physical property	Values
Approximate diameter in non-activated conditions	20 μm
Approximate diameter in activated conditions	30 μm
Granularity	high
Adhesion	strong
Intrinsic fluorescent properties	high

Depending on the tissue of residence, macrophages show great diversity regarding phenotype and function, demonstrating their ability to adapt to their microenvironment^{8,9}. This makes it very difficult to introduce a classification scheme for macrophages. Over 20 years ago, Mills and co-workers classified macrophages into two distinct subsets, namely M1 and M2 macrophages, also referred to as classically activated macrophages with mainly pro-inflammatory features and alternatively activated macrophages with mainly immuno-modulating features¹⁰. Since then, other classifications have been proposed including a classification based on homeostatic functions⁷ but the reassessment of current models is still ongoing¹¹.

1.1.1 Macrophage Origins

As well as their diversity, the origins of macrophages display an ongoing challenge for scientists. Classically, macrophages were thought to originate from circulating monocytes that migrate into tissues where they mature and become macrophages¹². However, there is increasing evidence that the majority of tissue-resident macrophages

have prenatal origin and maintain their populations via self-renewal and longevity¹³. For example, monocytopenic mice displayed relatively normal levels of tissue macrophages^{14,15}. In addition, many fate mapping studies in mice have determined that macrophages colonise developing organs in three distinct but overlapping waves during embryogenesis^{16,17}. Here, the first wave occurs at embryonic day 7 (E7) in the extraembryonic yolk sac where primitive erythroid, megakaryocyte and macrophage progenitors arise^{18–20}. This process is called primitive haematopoiesis. Then, also occurring in the yolk sac, around E8.25 a second wave gives rise to multipotent erythromyeloid progenitors (EMP), which will differentiate into tissue-resident macrophages^{21,22}. The functions of these tissue-resident macrophages then strongly depend on the specific tissue niche that they populate. The final wave of macrophages originates from hematopoietic stem cells (HSCs) that emerge at E10.5 in the aorta-gonad-mesonephros and populate the fetal liver^{23,24}. Rapid expansion of the stem cells makes the liver the predominant embryonic site of haematopoiesis at this moment. Finally, fetal-liver derived HSCs travel through the circulatory system to colonise the bone marrow (BM) and spleen, which then becomes the primary site of haematopoiesis^{23,24}. Many of these tissue-specific macrophages that arise during embryogenesis remain into adulthood due to their ability to self-renew *in situ*^{16,25,26}.

Even though these studies enabled the re-definition of macrophage development, which is necessary to fully understand macrophage biology, they were all conducted in mice. Information on human tissue macrophages is sparse, yet urgently needed. Thus, an effort should be made to study human macrophages from different tissues.

1.1.2 The Contribution of Monocyte-derived Macrophages

Despite the fact that most tissue-specific macrophages in the steady state are derived prenatally, monocyte-derived macrophages also play a vital role for the immune system. They can complement tissue populations and some tissue populations even rely on monocytes to maintain their numbers²⁷. In fact, it has been shown that macrophages from the heart, liver, pancreas, dermis and intestine are all maintained

by blood monocytes^{28–32}. In the heart and the liver, embryonic macrophages are replaced by circulating monocytes that differentiate into tissue macrophages after birth and are then constantly replenished by monocytes^{28,33}. The same happens in the intestine and dermis, where Ly6C^{hi} monocyte recruitment depends on the chemokine receptor type 2 (CCR2)³⁴. Thus, it is not surprising that there were substantially less macrophages in the intestine and skin of CCR2^{-/-} compared to WT mice^{28,30}. This shows the importance of monocytes in the generation of tissue-specific macrophages before as well as after birth.

Other macrophage populations including alveolar macrophages (AM), microglia and Langerhans cells on the other hand are thought to mainly self-maintain with only very little input of blood monocytes at the steady state^{21,25,35,36}. However, during inflammation, circulating monocytes are recruited into the tissue where they differentiate into inflammatory macrophages³⁷. For example, influenza A- or lipopolysaccharides (LPS)-challenged mice displayed high numbers of inflammatory airway macrophages a few days after challenge while macrophage numbers returned to pre-injury levels as the inflammation resolved³⁸. Crucially, the increase of macrophages during inflammation was solely caused by monocyte-derived macrophages. As the inflammation resolved, monocyte-derived macrophages underwent apoptosis while numbers of tissue-resident macrophages were stable throughout the whole inflammation. In contrast here to, arterial macrophages, initially derived from embryonic precursors are replaced immediately after birth by circulating monocytes that are then sustained by proliferation rather than further monocyte recruitment³⁹. Together, this highlights not only the important role of monocytes within tissues during inflammation but also that some tissue-specific macrophage populations are not replenished or replaced by monocytes while others are.

Taken together, tissue macrophages have distinct origins, with most tissues homing macrophages of two or more origins. In addition, maintaining of macrophage

populations in different tissues underlies distinct mechanisms. Some populations have the ability to self-renew their numbers while others rely on circulating monocytes.

1.1.3 Macrophage Ontogeny vs. Tissue Niche Influences

With tissues homing macrophages from different origins underlying distinct mechanisms to maintain their populations the questions arises what dictates macrophage phenotype and function – ontogeny or the tissue niche? Many studies exist that highlight distinct transcriptional and epigenetic features for different tissue-specific macrophages^{40–45}. However it is unclear, to what degree these features are imprinted during development compared to how strong the influence of the tissue environment is.

Lavin et al. performed several genome-wide assays including RNA- and chromatin immunoprecipitation sequencing for seven different tissue macrophage populations to determine their transcriptional and epigenomic landscapes⁴⁰. Interestingly, macrophages with similar environmental stimuli, for example macrophages from the small and large intestine, showed very similar transcriptional and epigenomic landscapes. Along these lines, the transfer of bone marrow into bone marrow-depleted mice showed that monocyte-derived macrophages in the lung and peritoneal cavity gained about 90% of the transcriptional profile of embryonic macrophages⁴⁰. However, macrophages in the liver were only able to gain 47% of their embryonic counterpart. Similarly, analysis of monocyte-derived vs. embryonic microglia revealed 2000 differentially expressed genes⁴⁶. Interestingly, this indicates that the phenotype of some tissue macrophages, for example lung and peritoneal macrophages, is mostly dictated by the tissue environment while the embryonic origin is crucial for microglia and Kupffer cells. However, it is also possible that the irradiation of the animals significantly altered the tissue which led to only partial differentiation of monocytes into macrophages. This is supported by work from Scott et al. who showed that circulating monocytes are able to fully differentiate into Kupffer cells³². In fact, only 12 genes were ≥ 1.5 -fold differentially expressed between monocyte- and embryonically

derived macrophages. Crucially, these monocyte-derived Kupffer cells also gained the ability to self-renew, a property long believed to be an exclusive trait of embryonic macrophages. Taken together, this data highlights the enormous influence the tissue environment has on macrophage differentiation and challenges the concept that ontogeny dictates macrophage phenotype and function.

This led to the development of the niche model, where embryonic progenitors colonise tissues before birth, however when a macrophage niche becomes available BM-derived monocytes compete with resident macrophages to fill the spot^{32,47}. More precisely, the model can be broken down into three questions. The first question is, if the tissue is accessible. Due to the blood-brain barrier for example monocytes cannot enter the adult brain. It is thus not surprising that microglia are exclusively derived from yolk-sac macrophages^{17,48}. Similarly, during embryonic development several tissue niches are not yet formed when the yolk sac is the primary site of haematopoiesis and are thus not available. This is the case for the alveolar space and therefore most alveolar macrophages arise from foetal liver monocytes^{17,21}.

If the tissue is accessible, the second question is if macrophage niches within the tissue are available. Niches might get available due to growth of the tissue, for example during the neonatal window, or death of resident macrophages, for example due to inflammation. This fits with the fact that during embryogenesis macrophage population occurs in distinct waves. Once the tissue niches are fully formed and available, they are populated by macrophage precursors that differentiate into tissue macrophages. It also explains why BM-derived monocytes give rise to fully differentiated Kupffer cells. That is because the liver of a mouse does grow until four weeks after birth, thereby creating new tissue niches that are then filled by circulating monocytes^{32,48,49}. In tissues that are constantly replenished by circulating monocytes, for example the intestine, heart and dermis, niches might be constantly available due to the lack of self-renewal of macrophages. The mechanisms by which macrophages fail to self-maintain their population is thought to be connected to environmental clues within these tissues, for

example the microbiota in the intestine, however detailed processes are not understood^{28,30,47}.

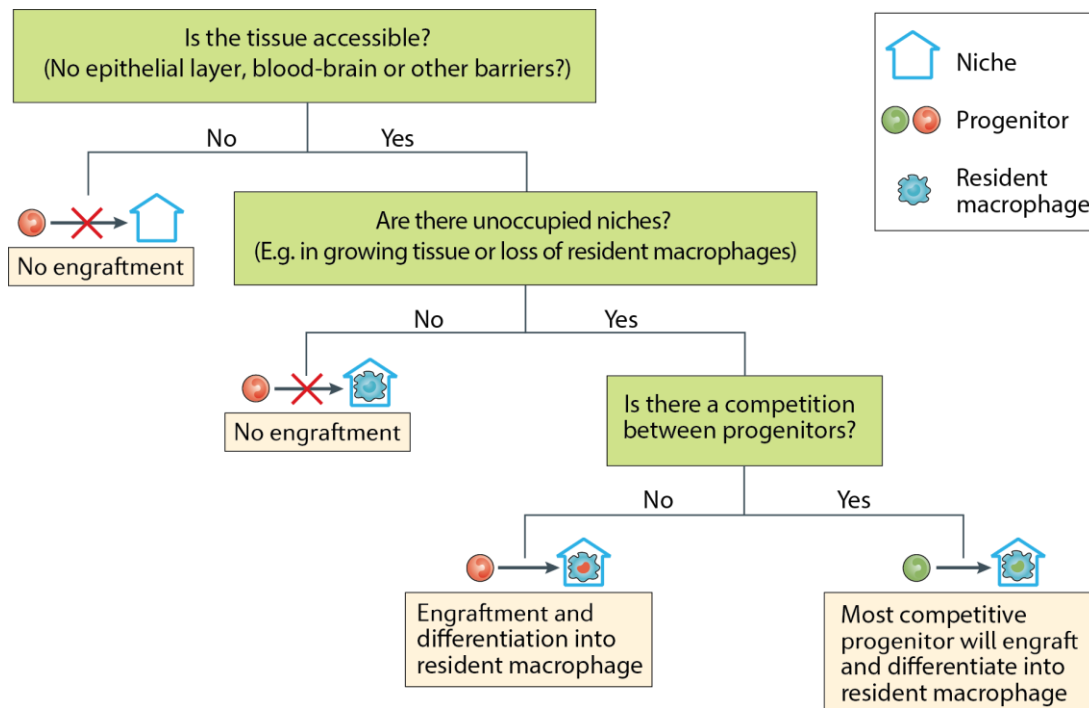


Figure 1-1: Schematic illustration of the niche model. If a precursor will differentiate into a resident macrophage depends on the accessibility and availability of tissue-specific niches. The first question is if the precursor is able to reach the tissue niches. In adulthood, circulating monocyte are for example not able to pass through the blood-brain barrier and are thus not able to populate the brain, even if niches would be available. This leads to the second question, that if they can reach the tissue, are there unoccupied niches available? This question relies on the hypothesis that there is a finite number of tissue niches available per tissue. Once all niches are occupied, progenitors will pass through the tissue, sensing the present population and exit the tissue without engraftment. If there are unoccupied niches available, for example due to the loss of resident macrophages during inflammation, progenitors will populate the tissue and differentiate into resident macrophages. However, there might be more than one progenitor available, which leads to the last line of questioning. Which progenitor is the most potent one? Niches could be filled for example with circulating monocytes or by enhanced proliferation of the resident tissue population. In this case, the most competitive progenitor will populate the niche and differentiate into a tissue-resident macrophage. This Figure is adapted from Guilliams and Scott, 2017⁵⁰.

If the tissue is accessible and niches are available, macrophage precursors inhabit these niches and differentiate into tissue-specific macrophages. This leads to the final question of the model: is there a competition for the niche? As already discussed, macrophages can arise from different precursors. Even though it is possible that specific precursors are more suitable for different tissues, it has been shown for some tissues that different precursors are able to give rise to fully functional tissue-resident macrophages. Van de Laar and co-workers transferred three macrophage precursors, namely yolk sac macrophages, fetal liver and BM monocytes individually into the lung of neonatal *Csf2rb*^{-/-} mice where they differentiated into almost identical macrophage populations⁵¹. However, when transferring all three precursors at a 1:1:1 ratio, fetal liver monocytes outgrew the other precursors. This was likely due to the increased potential of fetal liver monocytes to respond to granulocyte-macrophage colony-stimulating factor (GM-CSF), one of the main driving forces behind alveolar macrophage development. Importantly, this competition was only observed within the first two weeks after transfer. Once inhabiting a niche and differentiated into alveolar macrophages, all three precursors displayed similar rates of self-renewal. This shows that intrinsic differences could indeed prefer a certain precursor to populate a specific tissue. However, it also highlights the fact that all macrophage precursors are highly plastic and capable to differentiate into tissue macrophages with nearly no differences detectable in the resulting tissue populations. A schematic illustration of the niche model can be found in Figure 1-1.

Even though the niche model fits experimental data very well and explains otherwise inexplicable findings it has to be kept in mind that this model assumes that there is a limited amount of niches available per tissue, which can be sensed by the cells. Once the tissue is 'full', precursors will migrate through and exit the tissue without differentiating into macrophages. The mechanisms underlying this quorum sensing are not well studied. It is clear though, that not only passing precursors but also resident tissue macrophages do sense it. For example, partial depletion of Kupffer cells led to increased proliferation of the tissue resident population that then went on to populate empty niches³². The same was shown for microglia in the absence of irradiation⁴⁶. In

addition, partial depletion of macrophage populations in the lung, spleen and peritoneum also resulted in increased proliferation and re-population of the tissues⁵². These studies highlight that tissue macrophages are able to sense the availability of niches around them, which leads to the proliferation and population of empty spaces.

Taken together, macrophages display an outstanding plasticity depending on the tissue of residence. In addition, different macrophage precursors are able to differentiate into the same tissue-resident macrophages, with almost no transcriptional or functional differences. Here, tissue niche accessibility and availability dictate the phenotype of macrophages.

1.1.4 Macrophage Phenotypes

Macrophage plasticity is also evident in their different phenotypes. In fact, macrophages display a whole spectrum of different phenotypes. Here, classically (M1) and alternatively (M2) activated macrophages are the opposite ends of the spectrum, with M1 macrophages having pro-inflammatory properties while M2 macrophages play a major role in wound healing and homeostasis. This classification was first introduced by Mills et al. in 2000 and based on the observation that macrophages from a typical Th1 mouse strain (C57BL/6J) more easily produced nitric oxide (NO) compared to macrophages from a typical Th2 strain (Balb/c), when activated with interferon (IFN)- γ or LPS¹⁰. On the contrary, LPS increased arginine metabolism to ornithine in M2 but not M1 macrophages, followed by a Th2 response. This was taken further by establishing that M2 macrophages can be derived from exposure to interleukin (IL)-4 or IL-13, cytokines typically produced during a Th2 response⁵³. These alternatively activated macrophages were different to IL-10-driven macrophages. Since then, further macrophage stimuli apart from LPS/IFN- γ and IL-4/IL-13 have been identified. Amongst other things, GM-CSF was found to generate M1-like macrophages which produced increased amounts of tumour necrosis factor (TNF)- α , while M-CSF generated IL-10 and CCL2 secreting M2-like macrophages⁵⁴. Importantly, these early studies laid the fundament for understanding macrophage activation and phenotype. However, most

studies on macrophage phenotype were conducted in mice, especially evaluating phenotypes *in vivo*. Studying human macrophages of different tissues and phenotypes is thus urgently needed.

Functionally, M1 macrophages fight pathogens and parasites, present antigens and secrete an array of pro-inflammatory cytokines including IL-6, IL-12, IL-1 β , IL-23 and TNF- α ^{55,56}. These cytokines are responsible for recruiting other immune cells and polarising them towards Th1 type responses. In rodent models, M1 polarisation is accompanied by the expression of inducible nitric oxide synthase (iNOS) which leads to the synthesis of NO⁵⁷. However, this does not occur in human macrophages.

Alternatively activated M2 macrophages on the other hand are involved in wound healing and tissue remodelling; they promote angiogenesis and parasite clearance and secrete high levels of IL-10. Depending on the exposed stimuli, four different M2 macrophages were characterised *in vitro*: macrophages stimulated with IL-4 and/or IL-13 are termed M2a macrophages, M2b macrophages are exposed to immune complexes, M2c macrophages to TGF- β or glucocorticoid and finally, M2d macrophages are generated by exposure to IL-6 and adenosine⁵⁸. However, it has become clear, that macrophage phenotype and function is displayed as a continuum rather than discrete macrophage subset. This continuum is closely linked to environmental (or exposed) stimuli. In fact, cell polarisation depends on the maturation status of the cell (which is greatly influenced by the tissue of residence) and stimulus provided (for example cytokines, PAMPs and DAMPs)^{55,59}. Thus, a new nomenclature was suggested in which the exact stimulus is named – M(stimulus)⁶⁰. For example, M(IFN- γ) and M(LPS/IFN- γ) are two different M1 macrophages and M(IL-4) and M(M-CSF) M2 macrophages.

It is important to note that most studies use the terms ‘differentiate’, ‘activate’ and ‘polarise’ interchangeable when it comes to macrophages. However, this led to much confusion and these terms should be used accurately. The differentiation describes the maturation of the macrophage precursor, introduced by the presence of

cytokines, growth factors or other stimuli. For example, when a blood monocyte treated with M-CSF acquires a more macrophage-like phenotype. The activation takes this step further and relates to the phenotype change that occurs when a mature macrophage encounters for example a pathogen or pathogen-related cytokines, for example LPS or IFN γ . The term polarisation can be used interchangeably to activation.

Taken together, macrophages are highly plastic in their phenotype which strongly depends on environmental stimuli. It is thus important to always evaluate phenotype and functions of macrophages with respect to their generation or origin. Many different *in vitro* models have been proposed to generate specific macrophages.

1.1.5 Generation of Different Macrophages *in vitro*

Due to their easy accessibility, most macrophage *in vitro* models in humans rely on differentiating blood monocytes. Here M1-like and M2-like macrophages are generated by culturing monocytes with GM-CSF or M-CSF respectively⁶¹. Both molecules are cytokines that can be found in the body. In fact, M-CSF is readily detected in the steady state while GM-CSF is linked to inflammation⁶². Both cytokines are produced by multiple cell types and promote cell survival and proliferation as well as the differentiation into macrophages. As M-CSF is produced in homeostatic conditions, its sources are for example endothelial cells, fibroblasts and macrophages while GM-CSF is mainly produced by activated leukocytes in response to injury or inflammation⁶³. Thus, it is not surprising that their levels depend on the state of inflammation. In the steady state, M-CSF levels are higher compared to GM-CSF while the opposite is the case during inflammation^{61,64}. For example, in patients suffering from multiple sclerosis (MS) levels of GM-CSF are increased with its main source thought to be CD4⁺ T cells^{65,66}. This generates pro-inflammatory macrophages that secrete IL-6, IL-1 β , and TNF α , leading to damage of the central nervous system^{67,68}.

Other molecules have been suggested to induce M1-like or M2-like phenotypes. IL-34 binds to the same receptor as M-CSF, CSF-1R, and therefore introduces the same

pathway of differentiation leading to a similar phenotype. In fact, there was no detectable difference in the phenotype of these macrophages, however, IL-34-differentiated macrophages secreted higher levels of IL-10 when activated with LPS and IFN γ and higher levels of CCL-17 when activated with IL-4⁶⁹. This might indicate a similar potential to differentiate monocytes but not to polarise the macrophages. M(M-CSF/IL-4) on the other hand showed a greater phagocytic capacity compared to M(IL-34/IL-4). Platelet factor 4, also called CXCL4, introduces a more pro-inflammatory macrophage type, secreting IL-6 and TNF, with reduced phagocytic capacity⁷⁰⁻⁷². On the other hand, the presence of CCL2, the cytokine that is responsible for monocyte recruitment into the tissue, generates a less inflammatory phenotype with reduced levels of IL-6⁷³. Similarly, IL-6 was reported to induce higher levels of CD206, CD163 in macrophages accompanied with the secretion of IL-10 and TGF β , indicating an anti-inflammatory phenotype⁷⁴. Both, IL-6- and CCL2-induces phenotypes could be used for tumour models.

Other than cytokines and growth factors, metabolites are also able to influence macrophage phenotype. Calcium oxalate (CaOx) for example generates pro-inflammatory macrophages, similar to that induced by GM-CSF. It upregulates the expression of CD68 and CD86 but not CD163 and CD206 and leads to increased secretion of TNF- α , IL-1 β and IL-12 while IL-10 secretion was lower compared to M-CSF macrophages⁷⁵. Finally, as already discussed, activation of macrophages has an impact on their phenotype with LPS/IFN γ inducing pro-inflammatory properties while IL-4/IL-13 generate anti-inflammatory macrophages. However, more differentiation protocols are reported continuously, mimicking specific diseases and phenotypes. Table 1-2 gives an overview over the discussed and most commonly used molecules to differentiate blood monocytes into macrophages.

Table 1-2: Differentiation of blood monocytes into macrophages. Summary of molecules used to differentiate blood monocytes into macrophages with their reported phenotype and reference. This list was adapted from Luque-Marin et al.⁶¹.

Molecule	Phenotype relative to M-CSF macrophages	Reference
GM-CSF	<ul style="list-style-type: none"> - More pro-inflammatory phenotype - Higher levels of IL-6, IL-12, IL-1β, IL-23, TNF-α after activation with LPS/IFNγ - Lower levels of IL-10, CD163, CD14 	55,56,76–81
M-CSF + IL-4 and/or IL-13	<ul style="list-style-type: none"> - More anti-inflammatory phenotype - Increased levels of IL-10, CD206, CCL22 - Expression of CD200R 	53,77
IL-34	<ul style="list-style-type: none"> - Anti-inflammatory; very similar to M-CSF - Lower phagocytic capacity and higher levels of CCL-17 when activated with IL-4 - Higher levels of IL-10 after activation with LPS/IFNγ 	69
CXCL4	<ul style="list-style-type: none"> - More pro-inflammatory - Higher levels of IL-6 and TNF - Lower phagocytic capacity 	70–72
IL-6 or CCL2	<ul style="list-style-type: none"> - Less inflammatory - Reduced levels of IL-6 in the case of CCL2 - Higher levels of IL-10, TGFβ, CD206, CD163 for IL-6 	73,74
CaOx	<ul style="list-style-type: none"> - Pro-inflammatory; similar to GM-CSF macrophages - Expression of CD68, CD86 but not CD163, CD206 - Higher levels of TNF-α, IL-1β, IL-12 and lower IL-10 	75

Taken together, many different *in vitro* models for macrophages set out to match the great phenotypic plasticity of these cells. Each model is a compromise and simplification of some sort, yet these models are valid and necessary to shed new light on macrophage biology. The cytokines GM-CSF and M-CSF are still the most common way to differentiate monocytes into M1-like and M2-like macrophages respectively. Differentiated macrophages are then classically activated with LPS/IFN γ for M1 or IL-4/IL-13 for M2 macrophages. However, studies with differently activated macrophages are lacking.

1.2 Lung Macrophages

The lung is one of few organs that are in constant contact with the ambient environment. Billions of foreign particles and organisms enter the lungs every day, carrying a potential challenge for our immune system. The lungs consist of a network of thousands of airways starting from one big airway which branches into smaller bronchiole and terminates finally in millions of small air sacs called alveoli (Figure 1-2).

For the wellbeing of an individual it is essential that the lung tolerates innocuous stimuli while responding immediately to microorganisms that are potentially pathogenic. Here, AM play a key role. They are strategically positioned in the alveolar space of healthy airways and are first to encounter pathogens and other foreign particles. But the lung is populated by other types of macrophages as well. Beside AM, interstitial macrophages (IM) and intravascular macrophages populate lungs; all three subpopulations differ in location and function. AM are believed to remove particles and microorganisms from the alveolar space while IM coordinate inflammation, fibrosis and antigen presentation⁸². Intravascular macrophages seem to have similar functions for the circulation as AM for the alveolar space^{82,83}. Nevertheless, a deeper understanding of lung macrophage populations is needed, especially in the human context. Cai et. al. characterized AM and IM in Indian rhesus macaques, claiming that the monkey model is more accurate to describe human biology than rodent models⁸⁴. According to this study, 70% of all immune response cells in a healthy lung are comprised of AM and IM while approximately 80% of these macrophages are AM. This clearly underlines the importance of macrophages in lung immunity and why further investigation is important.

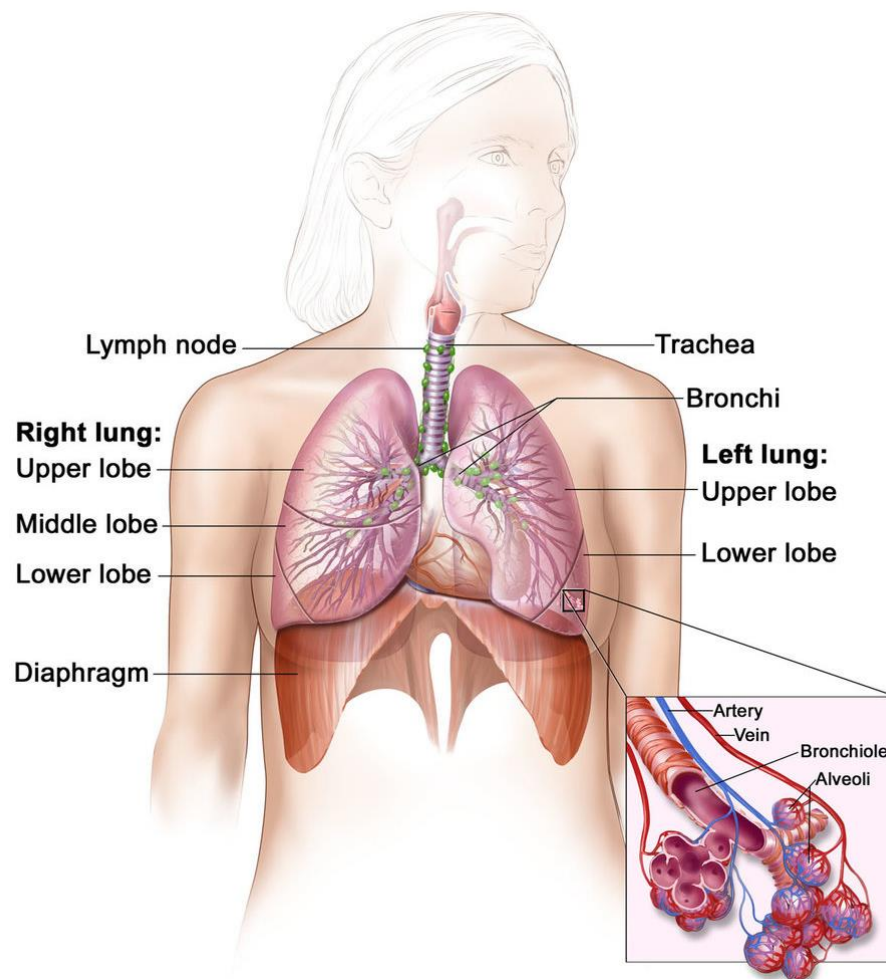


Figure 1-2: Anatomy of the respiratory tract. The main airway termed trachea branches into two big bronchi which further divide into smaller bronchiole and finally terminate in small air sacs called alveoli where gas exchange takes place. This figure was adapted from National Cancer Institute © (2006) Terese Winslow LLC, U.S. Govt. has certain rights and a copyright agreement is in place.

It is important to note that macrophages also populate the larger airways though most publications do not distinguish between alveolar and airway macrophages. Due to the isolation process applied in this project (see 2.1.3) macrophages are likely to be alveolar/airway macrophages. However, a minor contamination with interstitial macrophages is possible. In this project, no distinction was made for alveolar, interstitial and larger airway macrophages; isolated macrophages were termed lung macrophages.

1.2.1 Alveolar Macrophages

AM arise relatively late during embryonic development when fetal liver monocytes populate the forming alveolar tissue niches²¹. Here, GM-CSF is driving the colonisation as knockout mice failed to establish an AM population. However, culturing fetal liver monocytes in the presence of GM-CSF *in vitro* was insufficient to induce AM phenotype^{21,85}. This highlights the important role of the tissue niche in macrophage development and differentiation. Once established, AM maintain their numbers with low-level proliferation and longevity⁵². Importantly, in the steady state circulating monocytes do not contribute to the AM pool^{21,52}. This is thought to be due to the epithelium presenting a barrier for monocytes to access the airways.

In an healthy individual, the alveolar space is mainly populated by macrophages in addition to a small number of lymphocytes including effector and memory T cells^{86,87}. Here, macrophages are sessile and constitute over 95% of all cells with a single AM per three alveoli^{88,89}. Mouse AM have been well characterised with a CD11c^{hi} Siglec-F⁺ CD11b⁻ expression pattern^{21,90,91}. In addition, MerTK and FcγRI expression is characteristic for all lung macrophages²⁹. However, robust markers for human AM are lacking.

Due to the fact that immune cells in the lung are continuously stimulated by inhaled irritants, many suppressing mechanisms, including soluble mediators as well as cell-cell interactions, are in place to avoid unwanted inflammatory responses. Thus, it is not surprising that the clearance of surfactant is thought to be one of AM's major functions⁹². Impaired clearance due to dysfunctional AM, for example caused by the disruption of GM-CSF signalling, leads to pulmonary alveolar proteinosis (PAP) syndrome⁹³. Further, the cell type that plays a major role in restricting AM is alveolar epithelial cells⁹⁰. For example, the human BEAS-2B bronchial epithelial cell line was shown to restrict the pro-inflammatory response of AM *in vitro*⁹⁴. In addition, AM are able to coordinate their responses by signalling through connexin 43-containing gap junctions formed with the epithelium⁸⁸. This has been shown to prevent neutrophil

recruitment and the secretion of pro-inflammatory cytokines in LPS-challenged mice. When a more dangerous invader is present on the other hand, AM are required to quickly initiate an effective immune response. Therefore, macrophages have to balance perfectly between inhibitory and pro-inflammatory responses making functional communication with their environment essential. Any dysregulation of macrophages or the signals they receive could cause disease⁹⁵. Thus, new knowledge about their site-specific regulation in health and disease will help to develop strategies for fighting infections and autoimmune diseases.

1.2.2 Interstitial Macrophages

Interstitial, compared to alveolar macrophages are much less studied and therefore, many aspects of IM biology are poorly understood, especially in humans. This is likely due to the accessibility of tissue samples. Alveolar macrophages can be obtained by bronchoalveolar lavage (BAL), where the lower airways are washed with a saline solution to collect the cells. To isolate IM on the other hand, lung tissue is cut up and digested⁹⁶. In addition, IM were long thought to present an intermediate state during the differentiation of circulating monocytes into alveolar macrophages⁹⁷. Nowadays it is widely accepted that IM are a distinct and heterogeneous macrophage population residing within the lung tissue, but not the airways. Even though IM development has not been studied extensively, IM are thought to arise from multiple origins, namely from yolk sac macrophages and BM monocytes⁹⁸. In mice, they are characterised as CD11c^{int} Siglec-F⁻ CD11b⁺ ^{97,99–101}. However, recent studies have shown that IM are heterogeneous with at least two distinct monocyte-derived IM subpopulations^{102,103}.

Functionally, IM (like AM) phagocyte apoptotic cells, pathogens and other particles and microorganisms and can thus be seen as defence mechanism^{100,104}. However, studies have shown a more regulatory function for IM. For example, increased MHC class II expression may suggest a prominent role in antigen presentation^{97,101,105,106}. In addition, mice as well as human IM secrete IL-10 in the steady state and increased levels during challenge with bacterial products^{97,107,108}.

Further, IM inhibited the migration and maturation of dendritic cells (DC) during LPS challenge, thereby preventing the initiation of a Th2-type response¹⁰⁰. Thus, overall IM are thought to have immunosuppressive and regulatory rather than inflammatory properties.

Taken together, different macrophage populations inhabit the lung with AM being responsible for clearing the alveolar space and a heterogeneous population of IM performing homeostatic functions. All macrophage populations were shown to derive from multiple progenitors during embryonic development until adulthood. Even though a big amount of work went into understanding the biology of these macrophages, there is a great paucity of human studies. This is certainly linked to the availability of human lung samples. However, in addition human lung macrophages are known to be highly autofluorescent, which makes their investigation with fluorescent based methods challenging¹⁰⁹.

1.3 Autofluorescence

When a molecule is subjected to light of the right energy or wavelength, it absorbs a photon and transitions from the ground state into an excited state. In reverse, a molecule emits a photon (light) when it transitions from the excited state to the ground state. This emission is termed fluorescence. Fluorescence is typically of lower energy than the absorbed light because of energy losses within the process. Molecules that emit fluorescence are termed fluorophores. Many chemical compounds with optimised fluorescent properties are commercially available and widely used as fluorescent labels. For a more detailed description of fluorescence and fluorescence microscopy see page 53.

Autofluorescence is naturally occurring fluorescence without the addition of exogenous markers. The German physiologist Hans Stübel was one of the first to report intrinsic fluorescence of various biological materials and acknowledged already in 1911

the potential of autofluorescence analysis¹¹⁰. Indeed, in the following years, autofluorescence has been used for example to study plant morphology and physiology or discriminate bacterial pathogens^{111–114}. Until now, specific molecules have been identified as source of cellular autofluorescence including aromatic amino acids, nicotinamide-adenine dinucleotide (NAD), flavins and lipopigments^{114,115}. An overview of the most important sources of autofluorescence within mammalian cells can be found in Figure 1-3. NAD and flavins are thought to be responsible for most of the cytoplasmic autofluorescence. Interestingly, the autofluorescence of these molecules changes with their oxidative state, presenting a unique tool to study changes in cell or tissue metabolism^{116,117}. This can be exploited for diagnostic purposes as metabolic and structural changes in cells and tissues are likely to occur in early stages of diseases. Autofluorescence is for example used to detect tumours *in vivo*^{114,118,119}. It has also been used to monitor the infection of human HeLa cells with enterohemorrhagic *Escherichia coli* as well as to detect and identify bacteria in food^{120–124}.

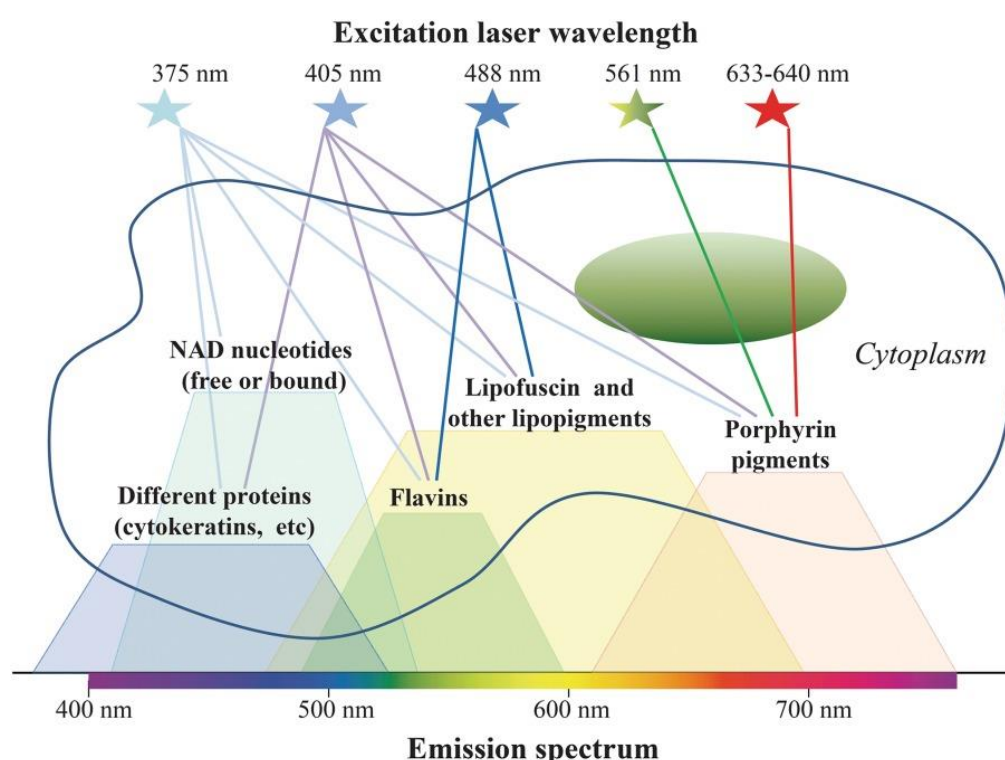


Figure 1-3: Sources of autofluorescence within the cell. The most important autofluorescent components with their according excitation laser (top) and approximate emission spectrums (bottom) are shown. This Figure was adapted from Shilova et al. and a copyright agreement with John Wiley and Sons is in place¹²⁵.

Despite the advantages of utilising autofluorescence analysis, including its non-invasive, non-toxic nature, it still comes with challenges. In the case of tissue autofluorescence, the signal arises from intra- and extracellular structures which make it difficult to reveal and process the signal arising from a specific compound. In addition, the overlap of the spectra of individual compounds within tissues or cells result in a broad autofluorescence spectrum which usually displays low quantum yields. This leads to partly overlapping spectra for different fluorophores within one sample, making it difficult to interpret the recorded signal¹²⁶. Moreover, autofluorescence may overlap with the spectrum of exogenous markers, making their usage difficult. It interferes with evoked signal, potentially leading to false conclusions. In fact, Foxp3 was falsely attributed to mouse macrophages due to autofluorescence and later retracted¹²⁷. In addition, autofluorescence impeded accurate detection of bacterial biofilms in clinical tissue samples¹²⁸.

1.3.1 Autofluorescent Lung Macrophages in STORM

Lung macrophages are one focus of this project and this cell type is well-known to be especially autofluorescent. Already in 1985 Edelson and co-workers reported of the difficulties of investigating lung macrophages with immunofluorescence technologies¹⁰⁹. Since then, several studies have characterised their autofluorescence and its sources. In general, the spectrum of autofluorescence was found to cover the whole spectral range with being highest in the green and yellow channel^{109,129}. More precisely, Edelson et al. detected the maximum emission at a wavelength of 541 nm with a shoulder at 580 nm¹⁰⁹. The most common observation is a strong relation between smoking history and the level of autofluorescence^{129–131}. Therefore, tobacco tar has been discussed as a possible source of autofluorescence^{129,132,133}. Another common observation is the presence of cytoplasmic inclusion bodies in highly autofluorescent cells^{129,132,134,135}. These inclusion bodies and their levels of autofluorescence were retained in long term culture (>6 weeks)¹³². Together with the great phagocytic nature of macrophages this might suggest that airway macrophages take up autofluorescent particles, for example tar from cigarette smoke, and store them long term in inclusion bodies inside the cell, thereby inheriting the particles' fluorescent

properties. This would also explain why airway macrophages are much more autofluorescent than macrophages from other tissues; that is due to billions of particles enter the lung every day.

Several super-resolution microscopy techniques are available nowadays, including electron microscopy (EM), photo-activated localization microscopy (PALM), stochastic optical reconstruction microscopy (STORM), and stimulated emission depletion (STED). For details on functional principals of these techniques please see 1.7.2. Due to the aim of studying the nanoscale organisation of the membrane STED microscopy was disregarded as this technique does not yield the necessary resolution. Electron microscopy does yield a very high resolution, but sample preparation is laborious, and it is difficult to stain for multiple proteins. PALM and STORM both take advantage of the blinking characteristics of fluorophores and are operated in TIRF mode. Thus, these techniques proved to be especially useful for studying the nanometer-scale organisation of immune synapses^{3,136–140}. However, in PALM, the proteins of interest are tagged genetically with fluorescent proteins which is very challenging for macrophages. In STORM on the other hand, proteins are labelled by antibodies conjugated to fluorophores. Therefore, STORM was chosen as best method to study the nanoscale organisation of macrophage membranes.

One has to keep in mind though that STORM utilises high laser powers to stochastically switch fluorescent labels from a dark to a fluorescent state (more detail on STORM see 1.7.2). These high laser powers potentially exacerbate the obstructive effects of autofluorescence, thereby making the application of STORM challenging for autofluorescent samples. Thus, it is not surprising that there is a great paucity in studying human tissue macrophages with STORM. In fact, to my knowledge human lung macrophages have never been investigated with this technique. Bierwagen et al. utilised the high autofluorescence of chlorophyll in spinach chloroplasts to obtain super-resolution images of thylakoid membranes¹⁴¹. High-intensity irradiation at 488 nm switched off the fluorescence of approximately 70% of all autofluorescent

molecules which could be recovered after an average of 1.2s. This was exploited to record super-resolution images based on the principles of STORM. However, this was only possible in a simplified system, precisely 75 – 100 nm thick cryosections of purified chloroplasts where background autofluorescence is minimal. This work was supervised by Stefan W. Hell, who won the 2014 Nobel Prize in Chemistry “for the development of super-resolved fluorescence microscopy” alongside Eric Betzig and William E. Moerner¹⁴².

More recently, Dong and co-workers exploited the intrinsic fluorescent properties of DNA to investigate the spatial organisation of nucleosomes from HeLa cells¹⁴³. Interestingly, they report stochastic blinking of unlabelled nucleic acids. However, similar to Bierwagen et al., DNA strands, cell nuclei and X chromosomes were extracted from the cells which drastically simplified the imaging system. Within a cell or human tissue, many more sources of autofluorescence are present, preventing resolving specific cellular features. In fact, Dong et al. report that even for isolated nuclei the illumination at shorter wavelength (precisely with 488 nm, 445 nm, or 405 nm laser), where autofluorescence is thought to be highest, led to higher backgrounds and poor image quality compared to a 532-nm illumination. This highlights the hampering effect of autofluorescence in light microscopy and the need for labelling with exogenous markers to bring forth selective cell features or molecules. Thus, a correction of autofluorescence is urgently needed to enable the investigation of autofluorescent samples by STORM.

Taken together, human airway macrophages are well known to be highly autofluorescent which presents an obstacle for immunofluorescent techniques including flow cytometry and light microscopy. There is only very little known about the effects of autofluorescence in STORM. Few highly autofluorescent cellular features were isolated and imaged unlabelled. However, in more complex systems like cells and tissues, autofluorescence is undesirable and has to be corrected for.

1.3.2 Accounting for Autofluorescence

Several solutions have been proposed to correct for unwanted autofluorescence and achieve a better signal to noise ratio. The simplest is to avoid the spectral range of autofluorescence¹⁰⁹. However, taken into account the broad emission spectrum of autofluorescence and the fact that most immunofluorescent techniques relying on commercially available fluorophores operating in a certain range, this might not be feasible. There has been success in photobleaching human tissue samples prior to fluorescent staining on the other hand. The autofluorescence of formalin fixed paraffin embedded human lung tissues could be reduced by almost 80% when irradiated with a mercury arc lamp at 20 cm distance in combination with fluotar objective 40X (NA 0.70) for 15 min¹⁴⁴. Irradiation of slide-mounted human brain tissue sections with white light emitting diode (LED) array for up to 48h yielded similar results¹⁴⁵. However, both studies investigated tissue samples, taking large-scale pictures with simple fluorescence or confocal microscopes. In addition, photobleaching of single cells was less successful¹²⁹.

Another common solution to the problem of autofluorescence is chemical quenching. This was successfully applied to human lung macrophages which enabled their analysis by flow cytometry^{146–149}. Here, fixed and permeabilised cells were treated with dyes (for example crystal violet or trypan blue) prior to staining to quench intracellular autofluorescence. However, this was mainly applied for flow cytometry. Arsić et al. recently utilised a commercial mounting media for microscopy (Vectashield) to quench the signal of AF647 in STORM¹⁵⁰. Thus, quenching in STORM is possible, however precise targeting of autofluorescence without affecting the specific staining is challenging.

The correction of autofluorescence post acquisition has been proposed for microscopy. Simple methods like the subtraction of the autofluorescent signal, recorded at an alternative wavelength to the extrinsic marker(s) were suggested nearly three decades ago¹⁵¹. Since then, complicated algorithms and filters were developed to correct for background fluorescence. Due to STORM's computational heavy nature this

is especially true for the processing of STOM datasets. In ThunderSTORM, a commonly used ImageJ plugin for re-constructing and analysing STORM data sets, different algorithm including rolling ball algorithms, wavelet filters and difference of Gaussians algorithms can be applied to remove backgrounds¹⁵². Additional processing steps like a running median filter implemented in Python was shown to correct for complex backgrounds in single-molecule localization microscopy (SMLM) data sets¹⁵³. However, advanced computational capacity and programming skills are necessary to correctly implement many of these techniques, highlighting the need for robust yet simple background correction techniques.

1.4 Nanoscale Organisation of Receptor Molecules

Immune cell function is regulated by cell surface receptors which recognise specific target molecules. Simplified, binding of the receptor to its specific ligand introduces signalling events that result in a change of cell function. Therefore, binding affinities and ligand specificity are two very important factors when it comes to immune cell regulation via surface receptors. However, many receptors recognise molecules on the surface of other cells. Therefore, direct contact between immune cell and target cell has to occur in order to enable interaction. This contact site between an immune cell and its target cell, termed an immunological synapse (IS), is a highly organised area which functions as a dynamic platform for intercellular communication¹⁵⁴. This was first described in T cells^{155,156} and soon afterwards in natural killer (NK) cells¹⁵⁷ where receptor and adhesion molecules are rapidly re-arranged upon contact with the target cell. Importantly, these discoveries revealed that not only binding affinity and ligand specificity define receptor interactions but that surface organisation is also important.

Together with advancing imaging techniques our understanding of the relationship between receptor organisation and regulation of cell function has progressed. For example, receptors at the IS have been reported to form micro-clusters in T cells, B cells, and NK cells^{158–163}. Here, cluster formation was found to play a role in signal transduction. This is best described in T cells. For instance, T cells interacting with

activating lipid bilayers recruit downstream signalling molecules including Lck and ZAP-70 kinases and LAT adaptor in the process of T cell receptor (TCR) cluster formation¹⁵⁹. With duration of the contact, signalling molecules disappear from the centre of the cluster but co-localise with adventitious TCRs in the periphery of the cluster. These peripheral TCRs then move in an actin-dependent manner towards the centre where signalling molecules disappear again. The authors suggested that TCR micro-cluster formation serves as actin-dependent scaffold to amplify signalling events¹⁵⁹.

Development of super-resolution microscopy techniques further advanced our understanding of how receptor organisation impacts cell regulation. In T cells and B cells crucial signalling proteins and receptors were found to form nanoclusters at the cell surface of resting cells and change upon activation^{3,136–140}. This pre-clustering was interpreted as a potential regulatory mechanism for immune cells^{164,165}. In contrast, Rossboth and co-workers reported very recently that such pre-clustering of the TCR does not exist and wrong assumptions emerged from incorrect analysis of super-resolution data¹⁶⁶.

Nevertheless, the nanoscale organisation of various cell surface receptors was shown to change upon activation of the immune cell. For instance, Bálint et al. showed that the NK cell activating receptor natural killer group 2D (NKG2D) is organised in nanoclusters on the surface of NK cells which co-localise with the receptor for IL-15 upon ligation with ULBP2 but not MICA⁶. IL-15, ULBP2 as well as MICA can be found on cancer cells. So far, very little is known about the nanoscale dynamics of cell surface receptors on macrophages. By investigating inhibitory receptor SIRP α and activating Fc γ RI on MDM with the tool of super-resolution microscopy Lopes et al. linked the spatial organization of these receptors to the activation status of the macrophages. First, they showed that Fc γ RI, Fc γ RII and SIRP α are organised in discrete nanoclusters on the surface of macrophages. Fc γ RI but not Fc γ RII nanoclusters were found to be constitutively associated with nanoclusters of SIRP α . Interestingly, proximity of inhibitory and activatory receptor brought tyrosine phosphatase SHP-1 (which binds to

SIRP α 's ITIMs and is known to play an important role in Fc γ RI inhibition) close to activatory receptor Fc γ RI. Upon ligation of Fc γ RI, SIRP α and Fc γ RI nanoclusters segregated which also separated SHP-1 and Fc γ RI. The authors suggest that the relative position of inhibitory and activating receptor is important for the inhibitory mechanism of SIRP α but a clear proof is missing. The detailed mechanisms that control the rearrangements of these receptor-nanoclusters are also unknown. By disrupting the filamentous actin organisation, Lopes et al. showed that nanocluster association was at least to some extent regulated via the actin cytoskeleton.

Taken together, synapses formed at the contact sites between immune and target cells function as dynamic platforms for intercellular communication. Rearrangements of receptor, adhesion and signalling molecules on a nanometer-scale take place within the synapse and influence signal transduction and functional outcome. Thus, studying the molecular dynamics of synapses on a nanometer-scale is crucial for our understanding of cellular activation and function. Here, the IS, formed between lymphocytes and APCs is the best-studied of all synapses, yet other cell types including macrophages have been shown to form them.

1.5 Studying the Phagocytic Synapse

In the tissue, macrophages fulfil an array of different tasks including phagocytosis. The process of phagocytosis is initiated when a damaged or foreign particle is recognized by one of the many macrophage surface receptors including pattern recognition receptors (PRRs), scavenger receptors and high-affinity receptors for specific opsins like antibodies or complement proteins¹⁶⁷. Receptor engagement induces signalling cascades which led to actin rearrangement that drives the engulfment of the particle. The membrane-wrapped particle is then released into the cytoplasm as an independent organelle called a phagosome which fuses with lysosomes forming a phagolysosome. Lysosomes are acidic vesicles that contain proteolytic enzymes that will break down the foreign particle. In addition, macrophages can produce reactive nitrogen and oxygen species that are highly toxic and thus help to kill

engulfed microorganisms (Figure 1-4). Finally, the leftover fragments of biological inactive material are transported out of the cell and peptides originating from engulfed and digested proteins are loaded onto a family of surface proteins called major histocompatibility complex (MHC)¹⁶⁸. MHC molecules play an important role in antigen presentation between different cells. By displaying peptides on its surface macrophages can activate other cell types like T cells which are part of the adaptive immune system.

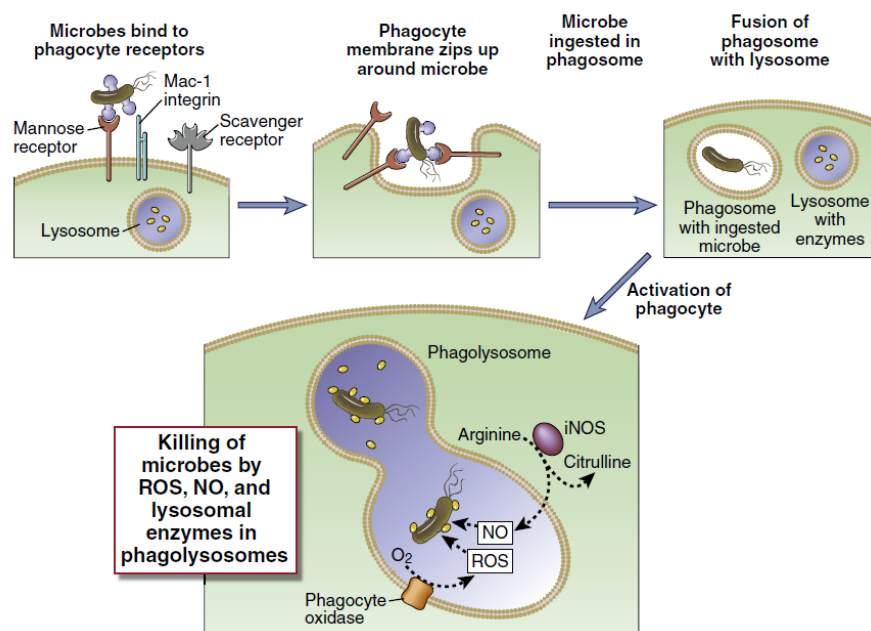


Figure 1-4: The process of phagocytosis. Microbes, dead cells or other particles are recognised by different surface receptors which led to the particle's internalization into a phagosome. The phagosome then fuses with a lysosome to form a phagolysosome where the particles are killed and digested by the interplay of reactive nitrogen and oxygen species as well as proteolytic enzymes. Therefore, the cytosolic enzyme called inducible nitric oxide synthase (iNOS) produces nitric oxide (NO) while another enzyme called phagocytic oxidase produces reactive oxygen species (ROS). NO may combine with ROS to form highly reactive peroxynitrite radicals that can kill microbes. Please note that the final step of disposal of biological inactive material is not shown in this figure. This figure was adapted from Abbas et al. ¹⁶⁹.

Importantly, at the initial contact site between the macrophage and the particle or microorganism, a phagocytic synapse is formed¹⁷⁰. This was proposed by Underhill and colleagues who showed that the stimulation of macrophages with particulate but not soluble β -glucan polymers was able to induce signalling of the pattern-recognition receptor Dectin-1 and phagocytosis¹⁷¹. Crucially, the formation of a synapse between

the macrophage and the β -glucan particle was observed. Within 1 minute, Dectin-1 clustered at the synapse which was accompanied by the recruitment of active Src and Syk kinases. CD45 on the other hand was excluded from the contact site. This shows similarities with the well-studied and already mentioned immunological synapse formed between T cells and an antigen presenting cell (APC) where TCR clusters are forming at the contact site and CD45 being separated to enable TCR signalling¹⁷². These similarities inspired the term phagocytic synapse.

Since then, more studies investigated the dynamics of the phagocytic synapse. Murine bone marrow derived macrophages incubated on IgG-containing lipid bilayers were shown to form Fc γ R-IgG microclusters at the contact site which led to the recruitment of signalling protein Syk and the remodelling of the cytoskeleton driving phagocytosis¹⁷³. In addition, the exclusion of CD45 from the phagocytic synapse was also confirmed for IgG-stimulated macrophages¹⁷⁴. As already mentioned, Lopes et al. conducted one of the only nanometer-scale investigation of the phagocytic synapse⁵. Human macrophages were incubated on IgG-coated glass surfaces, which led to the segregation of nanocluster of activating receptor Fc γ RI and inhibitory receptor SIRP α , possibly hinting a relation between the proximity of activating and inhibitory receptors and cellular activation. This highlights that synapses are highly dynamic communication platforms and that their investigation is crucial for understanding cell signalling and activation. However, compared to the immunological synapse, very little is known about the dynamics and the impact of the phagocytic synapse, especially on a nanometer-scale. Interestingly, in addition to their function as communication platforms, synapses are also sites of molecular exchange. Soluble as well as vesicular particles have been reported to be secreted at the IS, yet very little is known about this in the phagocytic synapse^{175,176}.

1.6 Extracellular Vesicles (EV)

EV are spherical membranous structures that are secreted by all cell types as well as bacteria¹⁷⁷. For a long time they were thought to be a mechanism to depose cellular waste¹⁷⁸. Nowadays it is widely appreciated that EV have a variety of functions including cell-to-cell communication¹⁷⁹. Classically, EV are divided into three subgroups depending on their biogenesis and size (Figure 1-5)^{180–183}. The smallest of all EV are termed exosomes are thought to be under 150 nm of size. Exosomes are generated through inward budding of endosomal membrane which results in the formation of intraluminal vesicles (ILVs) in so called multivesicular bodies (MVB). Fusion of MVB with the plasma membrane releases exosomes into the extracellular space. Microvesicles and apoptotic bodies are thought to be bigger (nm to μm range) and bud off directly from the membrane from living and dying cells respectively. All EV consist of a phospholipid bilayer with a spheroidal shape and contain a range of biological active material including nucleic acids, receptors and other proteins from their cell of origin¹⁷⁹. Thus, due to their overlapping sizes and contents a robust and simple method to identify different EV subsets is still lacking. Consequently, the isolation of pure EV subsets remains a challenge.

Several EV isolation techniques are available, however, they are usually based on physical properties like size or density, which overlap between different EV subsets. The most common used technique is differential ultracentrifugation. According to a research market analysis by the journal GenReports over 56% of all users in the field isolate EV via differential ultracentrifugation¹⁸⁵. However, it has been shown that this leads to co-purification of non EV-associated proteins, including protein aggregates and lipoproteins^{186,187}. In fact, currently available isolation procedures all result in a heterogeneous EV population, making it challenging to address specific scientific questions^{188,189}.

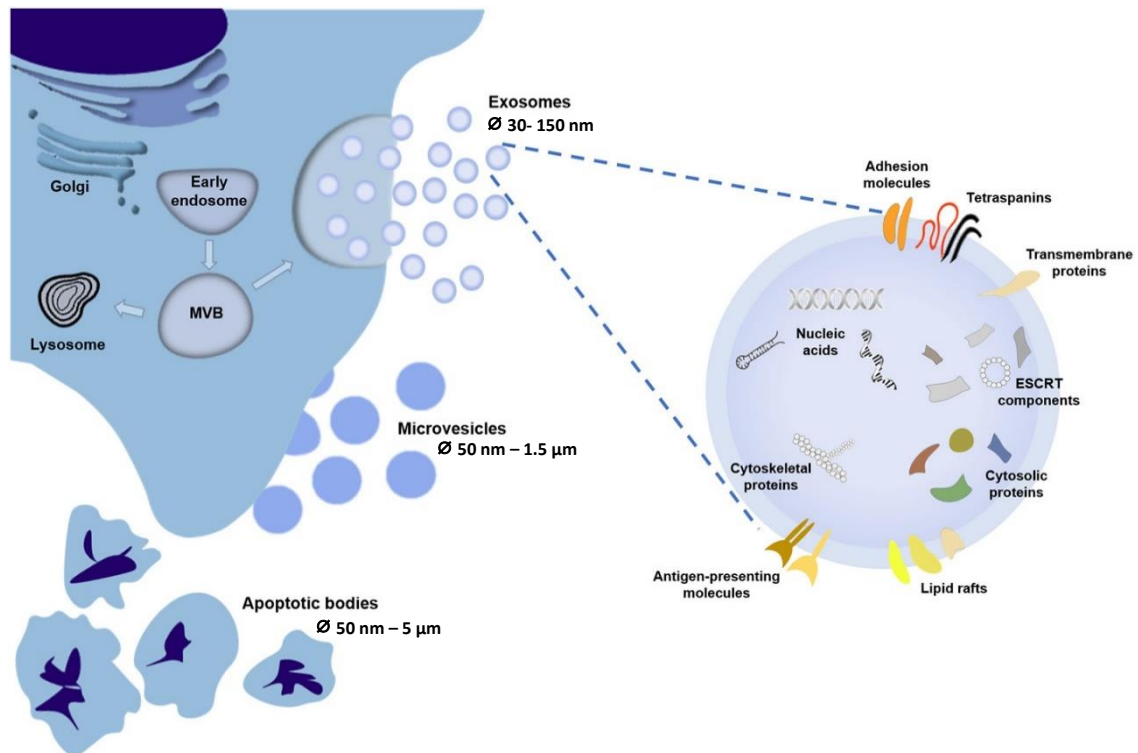


Figure 1-5: Extracellular vesicle (EV) biogenesis and composition. EV are classically divided into three subgroups that differ, yet overlap in size, composition and function. Exosomes, the smallest of all EV have diameters between 30 – 150 nm and are generated by inward budding of endosomal membrane resulting in multivesicular bodies (MVB). Fusion of MVB with the cell membrane releases exosomes into the extracellular space. Alternatively, the fusion with lysosomes leads to the degradation of the MVB. Larger vesicles that bud directly off the plasma membrane are termed microvesicles (MV). Their diameters range from 50 nm – 1.5 μm. When a cell dies, apoptotic bodies are produced by blebbing. These are thought to be the largest of all EV ranging from 50 nm – 5 μm. EV carry biological active cargo including DNAs, RNAs, proteins, metabolites and lipids. Some molecules can be linked to the biogenesis of the EV, for example components of the endosomal sorting complexes required for transport (ESCRT) in the case of exosomes. This figure was adapted from Rufino-Ramos et al.¹⁸⁴.

Nevertheless, many EV characteristics and components were identified over the last two decades shedding new light on EV function and biology. As already mentioned, EV contain a variety of different biomolecules. While some are probably linked to inducing specific biological functions in the recipient cell (for example RNAs), others are responsible for accurate packing and delivery of EV. Tetraspanins, a protein superfamily associated with the organisation of membrane proteins is thought to do the latter. In the plasma membrane, they function as a molecular scaffold to facilitate the formation

of so-called tetraspanin enriched microdomains (TEM), which contain adhesion, signalling and receptor proteins¹⁹⁰. The fact that tetraspanins are abundant in different types of endocytic membranes led to the belief of their involvement in cellular trafficking and EV secretion¹⁹¹. Indeed, tetraspanins, including CD9, CD63 and CD81 have been found to be enriched in EV and are commonly used as EV marker^{192–194}.

All tetraspanins share a similar structure; they contain four transmembrane domains which create a small (EC1) and large (EC2) extracellular loop (Figure 1-6). The latter contains a conserved sequence of Cys-Cys-Gly (CCG) and Cys-Cys which form disulphide bridges. Tetraspanins often contain post-translational modifications including palmitoylation sites and most tetraspanins are also glycosylated¹⁹⁰. This characteristic tetraspanin structure is the fundament for their involvement in a vast number of processes including EV-related mechanisms. For example, their C-terminal domain, which is highly preserved between species, dictates their intracellular location. In the case of CD63, the Gly-Tyr-Glu-Val-Met (GYEVM) sequence was found to target the late endosomal and lysosomal compartment while the Tyr-Xaa-Xaa-Ø (YXXØ) motive was associated with clathrin-coated vesicles^{195,196}. The latter was also found in 12 other tetraspanins¹⁹¹. CD63 was further shown to directly bind to syntenin-1, which plays a major role in exosome biogenesis^{197,198}. Tetraspanins also interact with the cytoskeleton and signalling molecules. For example, CD9 and CD81 both interact with G proteins and the interaction of CD81 with the small GTPase Rac has been shown to regulate tumour and DC migration^{199,200}. CD9 and CD81 have also been shown to interact with the ezrin–radixin–moesin (ERM) protein family which links tetraspanins to the actin cytoskeleton^{201,202}. The latter plays a crucial role in the secretion of EV. For example, actin filaments guide vesicles to the site of exocytosis^{203–205}. Further, the actin cortex controls the fusion of vesicles with the plasma membrane by acting as a barrier that needs to be remodelled before the fusion can take place^{206,207}. Taken together, this highlights the broad involvement of tetraspanins in several aspects of EV biology. They present a robust EV marker, yet they cannot be used to distinguish EV subsets.

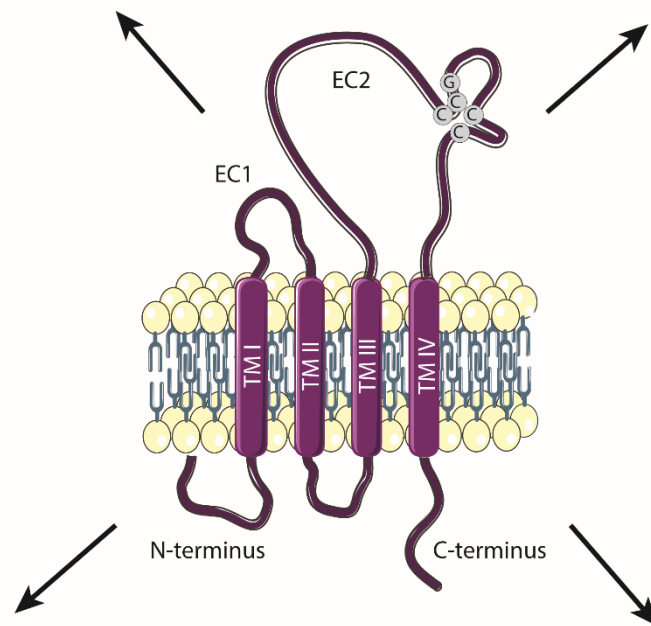
The biogenesis of EV can be summarised in three steps. First, the anticipated cargo has to relocate to either to endosomes (for exosomes) or the plasma membrane (for MV). Second, complex sorting and clustering mechanisms led to the enrichment of cargo molecules, including the binding of soluble factors. Finally, budding and vesicle scission has to take place in order to release the vesicles. Biogenesis of exosomes has been studied in much greater detail compared to MV. Here, the endosomal sorting complex required for transport (ESCRT) machinery, consisting of 4 complexes (ESCRT-0, -I, -II, and -III) and associated proteins (for example ALIX) is involved in sorting proteins into exosomes, thereby playing a major part in exosome biogenesis²⁰⁸. Interestingly, cells with all four ESCRT domains depleted were still able to form CD63⁺ EV²⁰⁹. In addition, CD63 and CD9 have been shown to regulate the incorporation of MHC class II into exosomes^{210,211}. This highlights again a fundamental role of tetraspanins EV biology and in ESCRT-independent EV biogenesis. The generation of MV on the other hand has been much less studied and the mechanistic details are still being revealed. It is clear though, that mechanisms that were first thought to be unique to the biogenesis of endosomal EV also apply to plasma membrane EV. For example, the ESCRT machinery is also involved in the biogenesis of MV¹⁸⁸. Regional calcium fluxes induces changes in the plasma membrane asymmetry which results in the exposure of phosphatidylserine^{188,212,213}. This triggers cytoskeleton remodelling leading to the protuberance of the plasma membrane and vesicle scission.

EV biogenesis

- Directing cargo molecules to sites of EV production
- Binding to signalling and cytoskeletal molecules necessary for EV biogenesis
- Involvement in ESCRT dependent and independent EV biogenesis

Loading of EV

- Sorting and clustering of cargo molecules in TEMs including miRNAs
- Controlling molecule trafficking within the cell



Antigen presentation

- Regulation of the incorporation of MHC class II into EV
- Influencing of lymphocyte activation by delivering inhibitory and stimulatory signals

EV uptake

- Directing adhesion molecules to EV
- Facilitating of binding to the target cell

Figure 1-6: Tetraspanins in extracellular vesicle (EV) biology. Members of the tetraspanin super family display a characteristic structure of four transmembrane domains (TM I-IV) which create a small (EC1) and large (EC2) extracellular loop. A conserved sequence of Cys-Cys-Gly (CCG) and Cys-Cys (CC) on EC2 form disulphide bridges, giving the loop its characteristic fold. Tetraspanins are involved in many aspects of EV biology including EV biogenesis, loading and uptake as well as antigen presentation. ESCRT, endosomal sorting complex required for transport; TEM, tetraspanin enriched microdomains.

Functionally, EV have been shown to induce different effects in their recipient cell which is surprising given the miniscule amounts of material they transport. In fact, quantitative analysis of exosomes showed that only one copy of a given abundant microRNA (miRNA) was found approximately per 100 exosomes²¹⁴. Nevertheless, the treatment of human mast cells with mRNA-containing mouse-derived exosomes induced the expression of mouse proteins in the human cells, highlighting the functional potential of exosomes²¹⁵. Thus, for a relatively small number of EV to accurately deliver their cargo to a specific cell type *in vivo*, a highly selective and efficient mechanism must be in place²¹⁶. In addition, EV do not only influence other cells by cargo delivery but they

can also simply interact with cell surfaces. Here, the most prominent example is the activation of T cells by EV harbouring MHC molecules loaded with cognate peptides^{217,218}. EV have also been shown to interact with molecules within the recipient cell, before being secreted again. This allowed the modification of fibroblast-derived EV with Wnt11 within breast cancer cells and rerelease of altered EV increased the motility of the cancer cells via Wnt-associated signalling²¹⁹. EV were also found to play a vital role in tumour progression²²⁰. For example, EV derived from breast cancer cells delivered miRNA to endothelial cells which resulted in enhanced angiogenesis and metastasis²²¹. In addition, metastatic melanomas were found to secrete PD-L1 harbouring EV to suppress CD8 T cells resulting in increased tumour progression²²².

Taken together, this highlights the involvement of EV in a large variety of biological processes including the modulation of the immune system. Their role in cancer and other diseases makes them prime candidates for therapeutic targets and disease biomarkers as well as targeted drug delivery systems^{223,224}. However, even though the field of EV advanced greatly in the last two decades, its biggest handicap is the ongoing inability to selectively isolate pure subpopulations of EV and the lack of single cell and single vesicle analysis. Development of new isolation and analysis methods is thus necessary and bears great potential to further advance the field. Here, studying EV with super-resolution microscopy presents an attractive option.

1.6.1 Studying EV with Super-Resolution Microscopy

The investigation of biological processes has gone hand in hand with the invention of microscopy techniques since van Leeuwenhoek studied living microorganisms and cells in the 17th century²²⁵. Nowadays, one of the most common techniques used to study living systems is fluorescence microscopy (for details on the principles of fluorescence and super-resolution microscopy see 1.7). However, conventional fluorescence microscopy is limited by the diffraction of light, resulting in a resolution of approximately 250 nm²²⁶. Because EV may be as small as 20 or 30 nm, a higher resolution is needed in order to completely resolve EV.

Nevertheless, due to its ease of use and wide availability, diffraction limited fluorescence microscopy techniques, for example laser scanning confocal microscopy, has been readily applied to study EV biology. In general EV are isolated, stained and either imaged by themselves or added to recipient cells. This allows a clean staining of EV with very low background. For example, confocal microscopy was used to show the localisation of CD63-GFP EV isolated from B and T cells at the membrane of recipient cells but not inside, suggesting that EV were not internalised²²⁷. Similarly, microglial-derived MV have been shown to bind to the surface of neurons without being internalised²²⁸. Exosomes derived from MDCK cells on the other hand were enriched in amphiregulin (AREG), an epidermal growth factor receptor (EGFR) ligand, and taken up by breast cancer cells resulting in increased invasiveness²²⁹. Not only EV uptake but also the secretion was studied by confocal microscopy. However, due to the diffraction-limited resolution, small vesicles could not be resolved but budlike structures identified on GFP-expressing cells²³⁰. The visualisation of MV was more successful, yet quantitative analysis still relied on western blots and flow cytometry of isolated MV pellets²³¹.

The need for a better resolution moved the field towards super-resolution techniques. Indeed, EV are classically characterised by electron microscopy (EM) with most papers containing EM images of isolated EV to confirm their sizes and spherical structure. This can be taken further by utilising correlative light and electron microscopy (CLEM) which combines the nanometer-scale resolution of EM with the advantages of fluorescence microscopy²³². More precisely, the same sample is imaged sequentially by confocal- followed by EM and images are overlaid. Arasu et al. utilised CLEM to study the uptake of GFP-hyaluronan synthase 3 (HAS3) EV derived from melanoma cells, by breast cancer cells²³³. Similar to confocal studies they found that EV accumulate at the cell membrane of recipient cells with only very few vesicles being internalised. Crucially, due to the high resolution they were able to analyse their images on a single cell and single vesicle basis. For example, they were able to determine the number of vesicles bound per recipient cell, which increased over time, indicating a targeted mechanism rather than a random process.

A similar resolution can be achieved with SMLM techniques. Thus, it is not surprising that these techniques gained more and more interest in the field of EV in the last decade. In 2016, Chen and co-workers conducted one of the first studies utilising SMLM to investigate EV²³⁴. Here, isolated EV were imaged by themselves as well as the interaction with recipient cells. A membrane dye, namely 1,1'-dioctadecyl-3,3,3',3'-tetramethylindocarbocyanine perchlorate (CM-DiI) was used to locate exosomes in diffraction limited images followed by STORM imaging of CD63-AF647-labelled EV. Interestingly, when tracking EV uptake in recipient cells, they accumulated in lysosomes, confirming endocytosis of EV and their consequent degradation for the used cell system. Similarly, two years later Nizamudeen et al. applied STORM to characterise stem cell-derived EV²³⁵. Importantly, nanoparticle tracking analysis (NTA) and tuneable resistive pulse sensing (TRPS), two techniques classically used to measure vesicles size, revealed a mean diameter of 120 – 150 nm of the EV while STORM measured a mean diameter of 50 nm for the same samples. This highlights the high precision of SMLM compared to conventional techniques.

In general, imaging single EV by SMLM presents an extremely powerful tool to study EV as it combines a 20 nm resolution with the possibility to determine molecular contents of EV. This was as well exploited by Chen et al. who successfully applied two colour STORM to detect single EV positive for CD63 as well as epidermal growth factor receptor-2 (HER2), an important biomarker in breast cancer diagnostics^{234,236,237}. In a later study from the same group they applied three colour STORM to visualise the exosomal membrane as well as two miRNAs contained within the exosomes, namely mir-21 and mir-31²³⁸. Lennon et al. took the characterisation of isolated EV by SMLM one step further and detected the size as well as the number of EGFR molecules for single EV²³⁹. In addition, by analysing patient-derived EV they revealed a pancreatic cancer-enriched EV population expressing EGFR and CA19–9, two receptors typically found on pancreatic cancer cells.

Further, SMLM is also applicable to live cell imaging. This was exploited in an already mentioned study from Chen and co-workers who utilised two colour live cell SMLM imaging to capture the transfer of miRNAs from EV to the cytoplasm of recipient cells²³⁸. Here, purified EV were visualised by the membrane stain CM-Dil and the miRNA mir-21 was labelled with a fluorescent molecular beacon. With a temporal resolution of approximately 6.4 s they were able to monitor the transfer in real time. Crucially, the SMLM technique enabled the capture of this process with an extremely high resolution. Endocytosis of EV was observed which was followed by the direction into lysosomes and subsequent degradation. However, shortly after internalisation, leaking of the EV cargo into the cytosol was observed, suggesting the delivery of EV soluble cargo by endosomal escape.

Taken together, studies utilising microscopy to study EV showed that EV are either interacting with the cell surface of cells without being internalised, or EV are internalised which is followed by the direction into lysosomes and degradation. The delivery of EV cargo into the cytosol of the recipient cell likely occurs via endosomal escape mechanisms. In any case, the application of super-resolution microscopy to study EV is an extremely powerful approach, especially SMLM techniques that enable the accurate detection of vesicle size and their molecular contents.

1.7 Microscopy

1.7.1 Fluorescence Microscopy and the Diffraction Limit

Our understanding of biological processes that occur in cells is widely built up on direct visualization of these processes using different microscopy techniques. Fluorescence microscopy is one of these techniques and comes with several advantages. By labelling specific molecules in cells, it is possible to observe specific cellular compartments and processes can be observed for example in live cells in real time²⁴⁰. It is therefore not surprising that fluorescence microscopy is one of the most widely used techniques to study processes at the cellular and subcellular level.

The principle of fluorescence microscopy exploits a property called Stokes shift. When a fluorescent molecule absorbs light energy (a photon) it transitions from the ground to an excited state. Transitioning back into the ground state, the molecule emits light, however of lower energy than the absorbed light. This difference is termed Stokes shift (Figure 1-7A). These processes are classically visualised in a Jablonski diagram (Figure 1-7B). Nowadays, many chemical compounds with optimised fluorescent properties are commercially available and widely used as fluorescent labels. These are visualised in fluorescence microscopy where the sample, stained with fluorescent markers, is illuminated and the emission light is separated and captured using dichroic mirrors and filters (Figure 1-8A). Thus, the resulting image only contains the emission light. However, this requires good separation (or a large enough Stokes shift) of excitation and emission spectrum of the fluorophore as the overlap of both spectra would cause problems (Figure 1-7A, Spectral overlap).

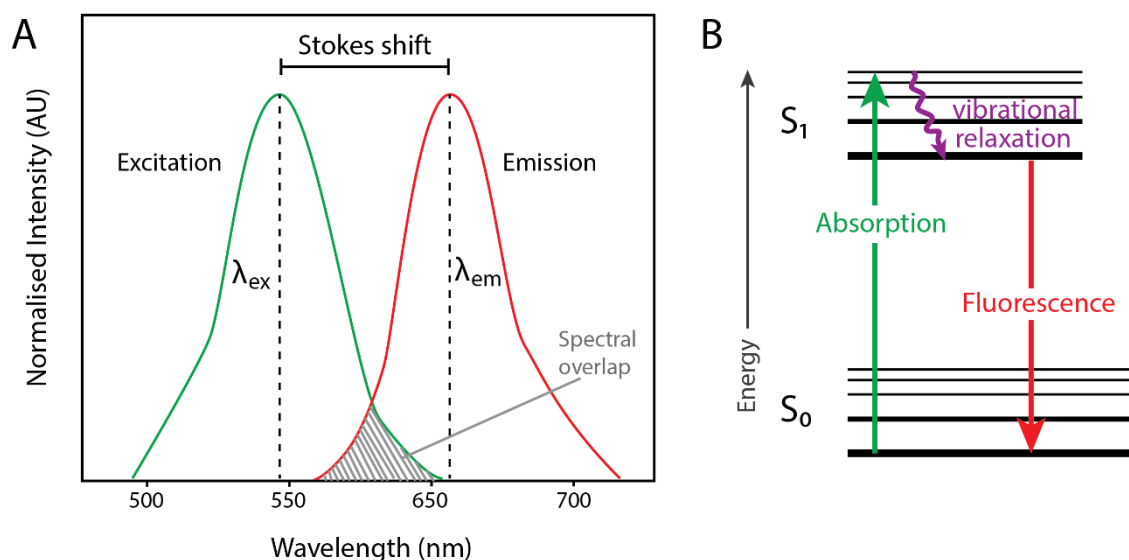


Figure 1-7: The principle of fluorescence radiation. A) Excitation and emission spectrum of a fluorescent molecule. At λ_{ex} , the molecule absorbs the maximum amount of energy, which will be released at lower energy or higher wavelengths in form of fluorescence according to the emission spectrum. Thus, at λ_{em} , fluorescence will be highest. The energy difference is termed Stokes shift. The smaller the Stokes shift, the bigger the spectral overlap and the more difficult it is to separate the emitted light, which is used in fluorescence microscopy. **B)** Jablonski diagram visualising the transition of an electron from the ground state (S_0) to an excited state (S_1). Some of the absorbed energy is lost in non-radiative vibrational transitions. Therefore, the emitted fluorescence will be of lower energy (or higher wavelength) than the absorbed light.

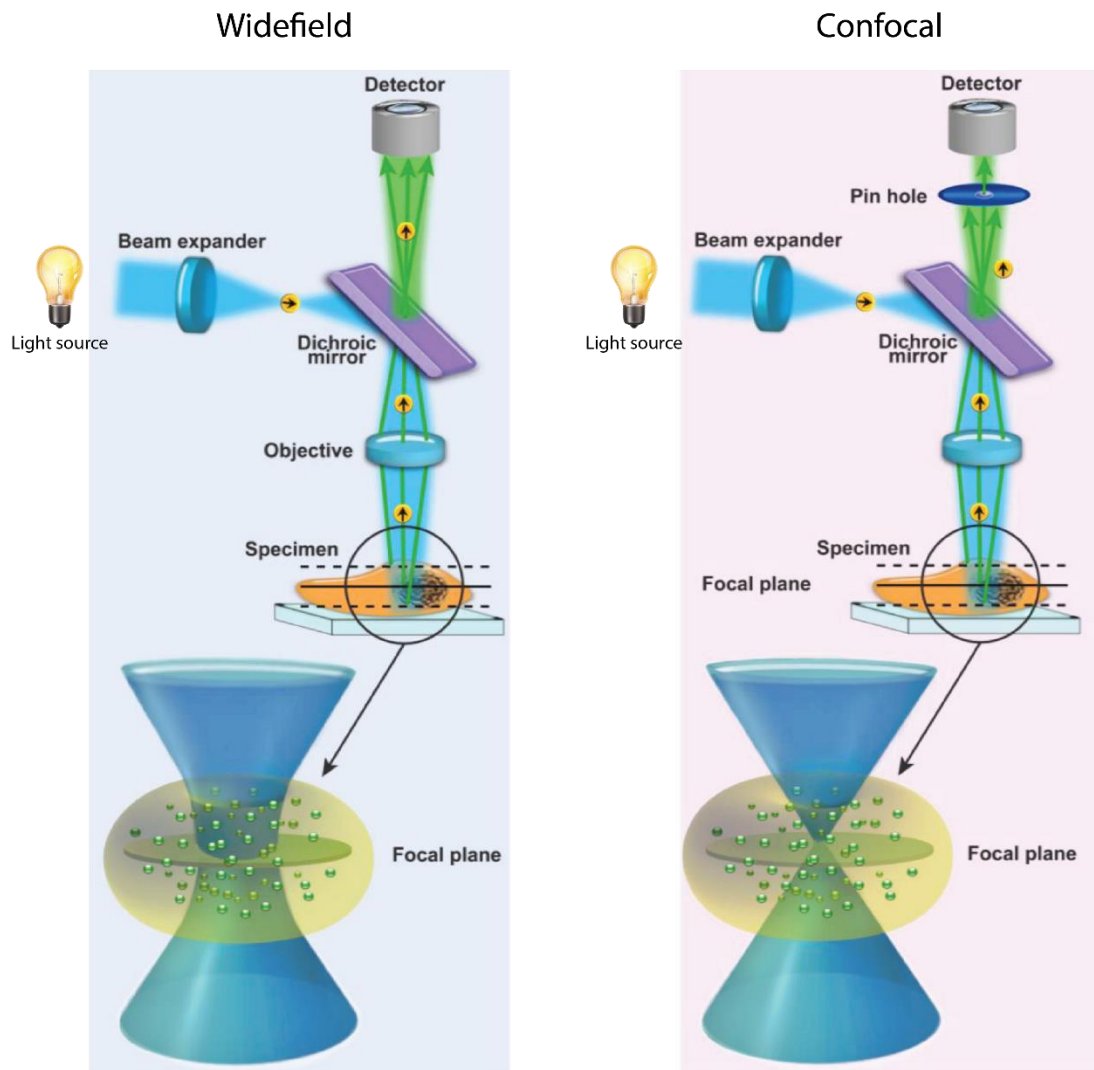


Figure 1-8: Composition of fluorescence widefield and confocal microscopes. In widefield microscopy (left), the sample is illuminated with a simple light source, for example a UV-lamp. This leads to the illumination of a relatively wide field, hence the name. Thus, collected fluorescence originates from a relatively large area. A dichroic mirror ensures the collection of the emission light only, filtering out the excitation light. A confocal microscope (right) on the other hand uses a laser to illuminate the sample, thereby reducing the illumination field to a focal point. The emission from these focal points is collected, however, a pin hole in front of the detector filters out light from out of focus plane (dashed lines). Together this minimises the collection of unwanted fluorescence and results in a higher resolved image. This figure was adapted from Ishikawa-Ankerhold et al.²⁴¹.

Simple fluorescent microscopes illuminate a relatively large area of the sample, exciting not only fluorophores within the desired focal plane but also above and beyond (Figure 1-8, Widefield). This leads to the collection of unwanted emission light, blurring the resulting image. Laser scanning confocal microscopy addresses this by scanning the

sample point-by-point with a focused laser beam instead of illuminating the whole sample at once (Figure 1-8, Confocal). In addition, a pin hole, positioned in front of the detector filters out light from outside the focal plane. Taken together, this will yield a much crisper image.

Another approach to improve the resolution is total internal reflection fluorescence (TIRF) microscopy. Similar to confocal microscopy, TIRF aims to minimise the excitation of fluorophores outside the focal plane. It does that, by shining the laser at the sample (mounted on a glass slide) from below at an angle smaller than the critical angle. This leads to the light being reflected at the interphase between glass and sample, creating an evanescent field on the other side. A wave of light will pass through the sample, decaying exponentially from the glass slide towards the inside of the sample (Figure 1-9). This leads to a typical penetration depth d of approximately 100 - 200 nm that can be expressed as an equation of the wavelength λ , the angle of the laser θ and the refractive indices of the media at the interface n_1 and n_2 :

$$d = \frac{\lambda}{4\pi \cdot (n_1^2 \sin^2 \theta - n_2^2)^{-1/2}} \quad (1)$$

This leads to the illumination of only the fluorophores close to the glass which results in the elimination of background fluorescence coming from out of focus planes²⁴². This form of microscopy presents an excellent model to study the immunological synapse. It has for example been used to show that clustering of MHC class I on B cell surfaces enhances T cell responses²⁴³. TIRF imaging was also applied to study the spreading behaviour and actin dynamics of NK cells after ligation of activating receptor NKG2D in contrast to the integrin LFA-1²⁴⁴. However, due to the small penetration depth of TIRF microscopy it cannot be applied to thicker samples, limiting its application greatly. Therefore, TIRF microscopy is typically applied to study cells interacting with coated glass slides which presents an artificial system and its biological relevance is difficult to assess. This was improved by the introduction of glass-supported

planar lipid bilayers²⁴⁵. Here, proteins are able to move freely, mimicking more closely the surface of a cell.

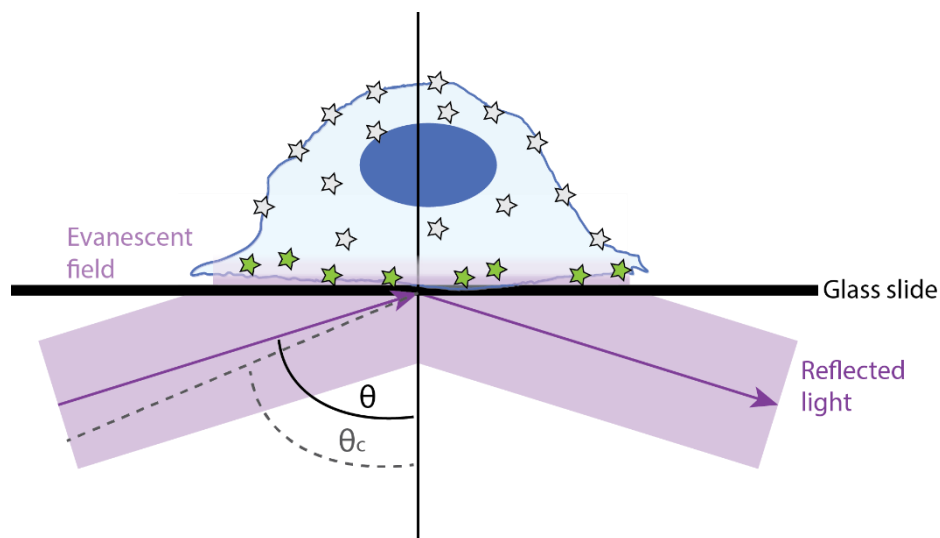


Figure 1-9: The principle of total internal reflection fluorescence (TIRF) microscopy. A stained sample on a glass slide is illuminated from below at an angle θ , which is greater than the critical angle θ_c and results in the reflection of the excitation beam. At point of reflection, an evanescent field that decays in an exponential manner away from the glass slide is created. Consequently, only fluorophores at close proximity to the glass are excited (indicated by the green colour).

Despite the many improvements, fluorescence microscopy is limited by the diffraction of light. Ernst Abbe defined the diffraction limit in 1873 using the following equation:

$$d = \frac{\lambda}{2 \cdot n \cdot \sin(\theta)} = \frac{1}{2} \cdot \frac{\lambda}{NA} \quad (2)$$

Here, d is the lateral diffraction or resolution limit, λ is the wavelength and θ is the aperture angle which gives rise to the numerical apertures NA when multiplied by n , the refractive index of the medium between objective lens and sample. According to this equation, the resolution limit of visible light ($\lambda \approx 500$ nm) is about 250 nm, when we assume a numerical aperture of 1.0. But many subcellular structures are smaller than this and therefore cannot be resolved using commercial fluorescence microscopy.

1.7.2 Breaking the diffraction limit

In recent years, several new fluorescence-based microscopy techniques have been developed to overcome Abbe's diffraction limit. These include stimulated emission depletion (STED) and stochastic optical reconstruction microscopy (STORM). In STED microscopy a special STED-laser is applied for imaging. It consists of a 'normal' excitation laser that is combined with a doughnut-shaped depletion laser (Figure 1-10B). The latter reduces the volume of the focussed excitation beam resulting in a very small excitation area. Like this, unwanted emission from the surrounding is avoided resulting in increased resolution.

STORM on the other hand takes advantage of specific blinking properties of fluorophores in combination with computational post-processing. During acquisition, all fluorophores are forced into a 'dark' state by applying a depletion wavelength and then stochastic blinks of the fluorophores are recorded. Because it is a stochastic process, the probability that fluorophores that are far apart from each other (further than the diffraction limit) blink at the same time is high and thus blinks of individual fluorophores can be recorded. During post-processing, a Gaussian is fitted to the observed fluorophore blinking events to identify their centres which give rise to the super-resolution picture (Figure 1-10C). Thus, the resulting image is built up from calculated coordinates that arise from a series of thousands of blinking events. By operating STORM in TIRF mode, it is especially applicable to study plasma membrane components, as described earlier.

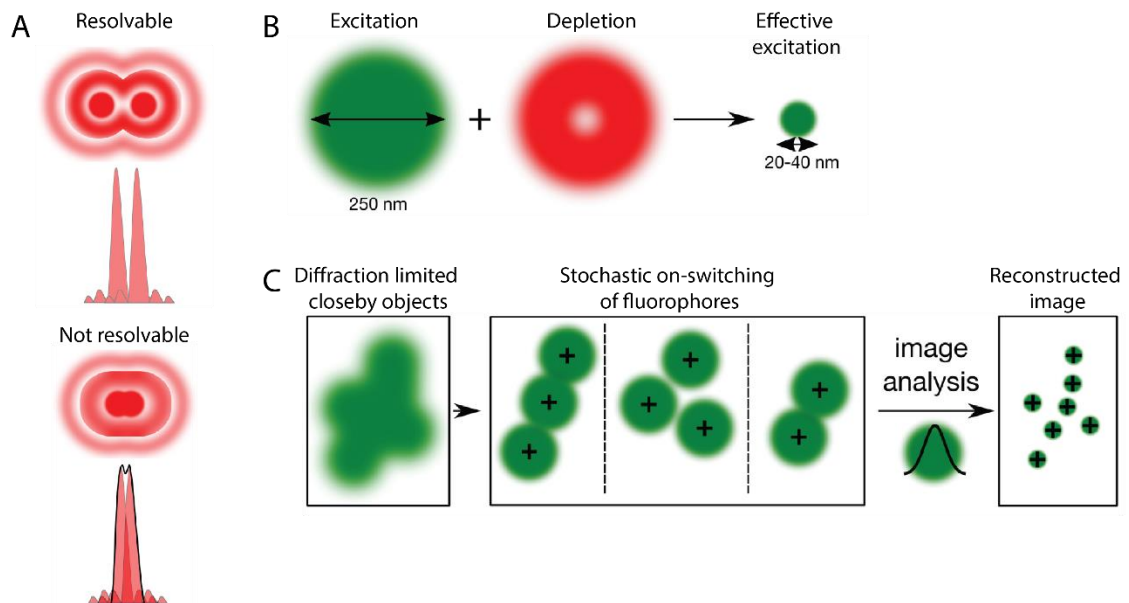


Figure 1-10: Principles of super-resolution microscopy. **A)** Two objects are optically resolvable when they are further apart from each other than the resolution limit (top). When they are closer together they are seen as a single object (bottom). In the latter case, the diffraction patterns of the two objects overlap. **B)** In STED microscopy, the excitation laser is narrowed by a doughnut-shaped depletion laser resulting in a very small area of emission. This allows the excitation of a very small region, reducing unwanted emission in the close surrounding. **C)** In STORM, blinks of individual fluorophores are recorded due to stochastic activation. Post-processing analysis then reconstructs a super-resolution image by fitting Gaussians for the acquired localisations. This figure was adapted from Sezgin et al.²⁴⁶.

1.8 Aims

Advances in microscopy revealed a new paradigm in cell biology – that the nanometer-scale dynamics of biological processes play an important role in the regulation of these processes. For example, not only the binding of a ligand to its receptor determines downstream signalling events and functional outcomes but the immediate environment of the receptor does so as well. Here, activating and inhibitory signals are delicately balanced on the cell surfaces. This is especially true for macrophages, who exhibit a broad spectrum of phenotypes ranging from pro- to anti-inflammatory. They display a large repertoire of receptor molecules on their surface to tightly regulate their immune functions. Thus, the main aim of this study was to investigate the nanometer-scale organisation of the membrane of human macrophages. Importantly, due to sparse availability of human tissue samples, there is

a great paucity in human tissue-derived macrophage studies, including lung macrophages. Thus, the aim was to overcome the well-known problem of autofluorescence and enable STORM for the investigation of human lung macrophages. This could then also be applied to study EV secretion with STORM. The field of EV biology is a rapidly advancing field, however, EV are classically studied in bulk, after isolation which comes with many caveats. Here the aim was to visualise the secretion of EV by human macrophages with a nanometer-scale resolution and characterise this process on a single-cell basis. Overall, the hypothesis of this project was that there are differences in the nanoscale organisation of the membrane of different macrophages. More precisely, macrophages with different phenotypes and from different origins (lung vs. blood-derived macrophages) could potentially display a different membrane organisation reflecting different thresholds of activation. In summary, the three main aims of my thesis are as follows:

1. Establish an experimental approach for studying the nanometer-scale organisation of the membrane of human macrophages (Chapter 3)
2. Enable STORM for autofluorescent lung macrophages (Chapter 4)
3. Utilise STORM to directly visualise and characterise the secretion of EV by different macrophages on a single-cell level. (Chapter 5)

Chapter 2 Experimental Procedures

If not stated otherwise, all incubations were carried out at 37°C and 5% CO₂ and all chemicals were purchased from Sigma Aldrich.

2.1 Cells

2.1.1 Generation of Macrophages from Blood Monocytes

All macrophages were cultured from primary human monocytes isolated from healthy donors (National Blood Service) acquired under ethics license 2017-2551-3945 (University of Manchester). First, peripheral blood mononuclear cells (PBMCs) were isolated by density gradient centrifugation (Ficoll-Paque; GE Healthcare) for 40 min with soft acceleration and no brake. Collected PBMCs were washed once with RPMI and re-suspended in 10 mL of Red Blood Cell Lysing Buffer (Sigma). After 5 min incubation, cells were washed again. CD14⁺ cells were isolated by positive selection using magnetic beads (Miltenyi Biotec) and seeded onto 6-well culture plates at a ratio of 5x10⁵ cells/mL. To generate M0-like macrophages, cells were cultured for 3 days in X-Vivo 10 media (Lonza) supplemented with 1% human serum (Sigma-Aldrich) followed by 5-8 days in DMEM media (Sigma-Aldrich) supplemented with 10 % FCS (Invitrogen), 1% L-glutamine (Gibco), 1% Penicillin/Streptomycin (Gibco) and 10 mM HEPES buffered saline (Sigma-Aldrich). M1-like and M2-like macrophages are generated in RPMI-1640 media (Sigma-Aldrich) supplemented with 10 % FCS (Invitrogen), 1% L-glutamine (Gibco), 1% Penicillin/Streptomycin (Gibco) and 10 mM HEPES buffered saline (Sigma-Aldrich). Here, cells are cultured for 8 days in the presence of 5 ng/mL GM-CSF (Biolegend) or 50 ng/mL M-CSF (Preprotech) for M1-like or M2-like macrophages respectively. Cells were washed with phosphate buffered saline (PBS; Sigma-Aldrich) to remove non-adherent cells and media was renewed every two to three days. Monocyte derived macrophages (MDM) were used between day 8 and day 11. For experiments cells were detached using non-enzymatic cell dissociation solution in PBS without calcium and magnesium (Sigma Aldrich). Therefore, cell media was aspirated from 6-well culture plates, 700 µL of cell dissociation solution was added for 5 min and cells

collected with a cell scraper (Sarstedt Inc). If not stated otherwise at least 3 different donors were used per experiment.

2.1.2 HEK293T/17 Cell Line

The HEK293T/17 cell line was obtained from the American Tissue Culture Collection (Manassas, VA) and cultured in T75 cell culture flask phenol-red free, high-glucose Dulbecco's Modified Eagles Medium (Sigma-Aldrich) supplemented with 10% FBS (Invitrogen) and 1% Penicillin/Streptomycin (Gibco). For detachment, 5 mL trypsin-EDTA solution were added for 2 min and cells were washed off with media.

2.1.3 Human Lung Macrophages

Human lung tissue used in this project was obtained from the ManARTS (Manchester Allergy, Respiratory and Thoracic Surgery) biobank and was collected under National Health Service (NHS) Research Ethics Committee approval (15/NW/0409). The tissue biobank was established in 2009 and recruits cancer patients undergoing lung resection surgery. Non-cancerous tissue from the proximal area of the tumour (at least 10 cm from lung tumour) was selected for research by a pathologist and perfused (see below) within 24h.

To isolate human lung macrophages, lung tissue samples were perfused with PBS. Depending on tissue size (ranging from 5 – 20 g) airways were washed with 100 mL – 150 mL PBS using a 10 mL syringe with a needle of 0.8 mm external diameter (BD Microlance 3). Collected cells were layered over Ficoll-Paque (GE Healthcare) and spun at $400 \times g$ for 30 min with soft acceleration and no brake. Cells were then collected from the layer directly above the Ficoll, washed twice and counted. The mixture of isolated cells, termed perfusate, contained all lung airway immune cells, including alveolar and airway macrophages. For experiments, macrophages were selected via adhesion. At least 3 different donors were used per experiment if not stated otherwise.

2.2 Antibodies

Throughout this work, different antibodies (Abs) were used in flow cytometry and microscopy experiments. These are shown in the tables below.

Table 2-1: Monoclonal antibodies (Abs) used for flow cytometry. Mouse monoclonal and matched isotype control antibodies were used to examine the expression of several cell surface markers on human macrophages. Ab specificity, clone, isotype, conjugated fluorophore, the final concentration used for staining and the supplier are listed.

Antibody specificity	Clone	Isotype	Label	Concentration (µg/mL)	Supplier
CD16	3G8	IgG1 κ	BV421	2	BioLegend
CD86	IT2.2	IgG2b κ	PE	2	BioLegend
CD163	GHI/61	IgG1 κ	ApC-Cy7	2	BioLegend
CD206	19.2	IgG1 κ	FITC	2	BD Pharmagen
HLA-DR	L243	IgG2a κ	AF647	5	BioLegend
Isotype ctrl.	MOPC-21	IgG1 κ	BV421	2	BioLegend
Isotype ctrl.	MPC-11	IgG2b	PE	2	BioLegend
Isotype ctrl.	G18-145	IgG1 κ	FITC	2	BD Pharmagen
Isotype ctrl.	MOPC-21	IgG1 κ	ApC-Cy7	2	BioLegend
Isotype ctrl.	MOPC-173	IgG2a κ	AF647	2	BioLegend

Table 2-2: Monoclonal antibodies (Ab) used for microscopy. Mouse monoclonal antibodies were used to stain cells for microscopy. The Ab specificity, clone, isotype, conjugated fluorophore, final concentration used for staining and the supplier are shown.

Antibody specificity	Clone	Isotype	Label	Concentration	Supplier
CD81	5A6	IgG1 κ	-	10 µg/mL	BioLegend
LIRLB1	HP-F1	IgG1 κ	-	10 µg/mL	eBioscience™
HLA-A,B,C	W6/32	IgG2a κ	AF647	10 µg/mL	BioLegend
Phalloidin	-	-	AF647	3 U/mL	Invitrogen
WGA	-	-	AF488	2 µg/mL	Thermo Fisher Scientific
Streptavidin	-	-	AF488	2 µg/mL	BioLegend

2.2.1 Antibody Labelling

Monoclonal Abs were labelled with Alexa Fluor 647 (AF647) or AF488 by forming stable amino bonds between primary amine residues on Abs and succinimidyl esters attached to the fluorophore (Figure 2-1). Therefore, 50 μ L of purified, unlabelled Ab at a concentration of 1 mg/mL, 6 μ L of 1 M NaHCO₃ and 3 μ L of AF647 or AF488 (Molecular Probes, Life Technologies) were incubated for at least 1h at room temperature. Here, the Ab-dye combination was protected from light and rotated to ensure thorough mixing. After conjugation, excess dye was removed by desalting columns (Zeba™ Spin Desalting Columns, Thermo Fisher Scientific). Therefore, Ab-dye mix was added to empty Zeba columns and spun at 350 \times g for 2 min.

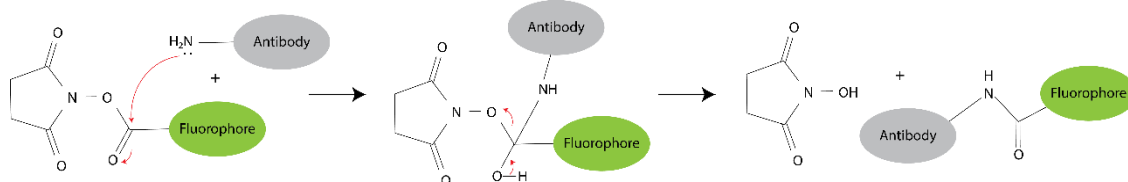


Figure 2-1: N-Hydroxysuccinimide (NHS) esters attached to fluorophores and primary amines on antibodies form stable amino bonds. The free electrons on primary amines react with NHS esters to form an intermediate molecule followed by the elimination of NHS and the formation of a stable amino bond linking the antibody to the fluorophore.

The degree of labelling (DOL) was determined using a NanoDrop 200 spectrophotometer (ThermoFisher Scientific). The absorbance was read out at 280 nm and either 650 nm (for AF647) or 500 nm (for AF488) and the DOL was calculated using the following equation:

$$\text{Moles of dye per mole of protein} = \frac{A_{\text{max}} \cdot \epsilon_{\text{protein}}}{\epsilon_{\text{max}}(A_{280} - (A_{\text{max}} \cdot C_{280}))} \quad (3)$$

Here, A_{max} is the absorption of the fluorophore at its maximum absorption wavelength. It depends on the dye that was conjugated (for example 500 nm for AF488). Further, $\epsilon_{\text{protein}}$ is the molar extinction coefficient at 280 nm of the protein that

the dye got conjugated to (mouse IgG antibody). ϵ_{max} is the molar extinction coefficient of the dye at its maximum wavelength and A_{280} is the absorbance at 280 nm which is used to determine the concentration of the protein. However, the dye might also absorb at 280 nm. This is accounted for with the correction factor C_{280} .

2.3 Preparation of Coated Slides, Bilayers and Beads

Lab-Tek II chambered coverglass slides (Nunc) were coated with 0.01% PLL (Sigma-Aldrich) in dH₂O for 15 min at room temperature, dried at 60°C for at least 30 min and washed with PBS. In activated conditions, cells were stimulated with immobilised ligands. Therefore, the slides were additionally coated with 10 – 100 µg/mL human IgG (Sigma-Aldrich) in PBS overnight at 4°C. Glass slides were then ready for use.

For the preparation of planar lipid bilayers lipids (Avanti Polar Lipids Inc.) were incorporated into liposomes by extrusion as previously described²⁴⁵. These liposomes contained either dioleoylphosphatidylcholine (DOPC) or biotinylCAP-PE. They were added to cleaned Lab-Tek II chambered coverglass slides (Nunc) at a ratio of 95% DOPC and 5% biotinylated liposomes. To clean glass slides, they were incubate with 1 M HCl in 70% ethanol for 20 min, washed 5 times with milliQ water (pH 8, 0.22 µm filter sterilised) followed by 10 M filtered NaOH for 15 min and additional 5 washes. Glass slides were then dried under a stream of argon and 200 µL of liposome mix was added thereby creating a single planar lipid bilayer. From the formation of the bilayer it is important to never aspirate all liquid from the wells. Between each of the following steps, 5 washes with PBS were performed first adding 500 µL, then aspirating the same amount. This ensures that the bilayer is covered with liquid at all times. After blocking with 1% BSA (bovine serum albumin), 10 µg/mL unlabelled streptavidin (Life Technologies) was added for 20 min. Then, biotinylated IgG (Jackson Immuno Research Europe Ltd) in different concentrations (1 – 100 µg/mL) was incubated for 20 min. After final washing steps, slides were ready for use.

In this project, macrophages were also stimulated in solution with IgG-coated polystyrene beads. Therefore, 200 μL of 0.5% (w/v) streptavidin coated polystyrene beads (Spherotech) with a diameter of 6.7 μm were incubated with 2 mL of 10 $\mu\text{g}/\text{mL}$ biotinylated IgG (Jackson Immuno Research Europe Ltd) in PBS for 1h at RT and constant mixing. Beads are washed 3 times with 5 mL PBS at 3000 $\times g$ for 10 min and blocked with 5 mL PBS/3%BSA for 30 min at RT with constant mixing. Finally, beads are pelleted at 3000 $\times g$ for 10 min and re-suspended in 1 mL of PBS. Beads were used at 20% of total volume to stimulate cells.

2.4 Flow Cytometry

200x10³ cells/well were plated into 96 well U-bottom plates (Greiner CELLSTAR® 96 well plates, Sigma-Aldrich) and spun once (all spins were carried out at 500 $\times g$ for 3 min). Cell pellets were re-suspended in 50 μL PBS containing 2 μL live/dead dye Zombie Aqua (Biolegend). After 30 min at 4°C, cells were washed three times and blocked with 50 μL PBS containing 2 μL human serum for 15 min. Then, cells were stained with mAbs (Table 2-1) in FACS buffer (0.5% FCS in PBS) for 30 min at 4°C. Finally, cells were washed three times and fixed with 4% PFA for 20 min. Cells were transferred into FACS tubes and analysed by flow cytometry (BD FACS CANTO). Analysis was performed using FlowJo V10 (LLC).

2.5 Enzyme-linked immunosorbent assay (ELISA)

Human TNF α and IL-10 DuoSet ELISA kit (R&D) was used according to the manufacturer's instructions to measure TNF α and IL-10 in cell supernatants. In brief, ELISA plates (Maxisorb, NUNC) were coated overnight and at room temperature (RT) with capture antibodies in PBS (100 $\mu\text{L}/\text{well}$ at 1 $\mu\text{g}/\text{mL}$). After washing three times with PBS/0.05% Tween 20 plates were blocked for at least 1 h with blocking solution (PBS/1% BSA). After additional three washing steps samples diluted in blocking solution were incubated for 2 h at RT. For reference, recombinant protein was diluted sequentially and added like samples. After incubation, plates were washed three times with PBS/0.05% Tween 20 and incubated with detection antibody (100 $\mu\text{L}/\text{well}$ at 1 $\mu\text{g}/\text{mL}$)

followed by additional three washing steps. Next, 100 μ L of Streptavidin-HRP B in blocking solution was added for 20 min at RT and in the dark. Plates are again washed three times and 100 μ L of TMB ELISA substrate solution (Sigma-Aldrich) was added for 20 min at RT and in the dark. Finally, 50 μ L of 1 M H_2SO_4 (Sigma-Aldrich) were added to stop the reaction and absorbance was measured at 450 nm with a reference line of 570 nm using an ELISA plate reader.

For the collection of the supernatant, cells were plated onto Lab-Tek II chambered coverglass slides (Nunc) coated with 0.01% PLL (Sigma-Aldrich) and varying amounts of human IgG (Sigma-Aldrich) for approximately 20 h. Then, cell suspensions were aspirated, centrifuged at $350 \times g$ for 10 min and the supernatant collected for ELISA. In the case of monocyte-derived macrophages 5×10^5 cells were seeded. For lung macrophages 10×10^5 cells were plated for 30 min, washed once with PBS and then incubated for approximately 20 h in fresh media.

2.6 Microscopy

If not stated otherwise, all images were taken at room temperature.

2.6.1 Sample preparation

MDM were seeded onto coated glass slides or supported lipid bilayer (see 2.3) at 5×10^4 cells/well and allowed to settle for 15 or 20 min respectively at 37°C and 5% CO_2 . To image lung macrophages, perfusate was incubated on glass slides for 15 min at approximately 5×10^4 cells/well at 37°C and 5% CO_2 . Within this time, lung macrophages adhered while other cells remained in solution. By washing the slide once with PBS, lung macrophages were separated from other cell types. MDM and lung macrophages were then fixed with 4% PFA in PBS for 20 min at RT, washed three times with PBS and blocked with 3% BSA in PBS for 1 h at RT. For intracellular staining, cells were permeabilised for 5 min with 0.1% Triton X-100 (Sigma-Aldrich) in PBS before blocking. For actin cytoskeleton staining, 0.01% saponin (Sigma-Aldrich) was added to blocking

and staining solution. Cells were stained with fluorescently conjugated mAbs as indicated in 3% BSA/PBS at 10 µg/mL for 1 h at room temperature, away from light, and washed three times with PBS. Samples were imaged using widefield (Leica DM IL LED), confocal microscopy (Leica TCS SP8) or STORM (Leica SR GSD). A list of all antibodies used for staining can be found in Table 2-2.

To image macrophage cell secretions, cells were plated for 30 min onto supported lipid bilayers as described above and incubated for 20 min at RT with 10 mM lidocaine hydrochloride (Sigma-Aldrich) and 0.5 mM EDTA (Sigma-Aldrich). Cells were detached by forceful pipetting with a total of 3 washes with PBS. Then, cell secretions were fixed with 4% PFA in PBS for 20 min at RT, washed five times with PBS and blocked with 3% BSA in PBS for 1 h at RT followed by the staining as described above. For shadow imaging, slides were in addition stained with 2 µg/mL streptavidin-AF488 (Invitrogen) for 1 min at RT prior to cell detachment.

2.6.2 Widefield Microscopy

The DM IL LED widefield microscope (Leica Microsystems) with a 20X/0.35 dry objective and the Leica DFC3000 G camera was used to capture the morphology of human macrophages. MDM were imaged on day 8 of culturing still in the tissue culture plates. Alternatively, lung immune cell suspensions were allowed to settle for 15 min onto PLL-coated Lab-Tek II 8-well chambered coverglass slides (Nunc; see 2.3) and once washed with PBS. Images were taken before and after the wash.

2.6.3 Confocal Microscopy

The TCS SP8 STED CW (Leica Microsystems) inverted microscope with a 100X/1.40 oil-immersion objective and HyD hybrid photon detectors was used to obtain fluorescence and bright field confocal images. Interference reflection microscopy (IRM) was used to determine the area of cell spreading on the glass slide.

Immobile lipid bilayers were utilised to capture vesicles secreted by macrophages. To test the immobility of the created bilayers on glass slides, fluorescence recovery after photobleaching (FRAP) experiments were carried out. Using the LAS AF FRAP wizard (Leica Microsystems), small regions of interest (ROI) were photobleached with three high-powered laser pulses and fluorescence images taken before and after bleaching. The mean fluorescence intensity of bleached vs. non-bleached regions provided information about the degree of fluorescence recovery.

2.6.4 STED Microscopy

Stimulated emission depletion (STED) microscopy is a second super-resolution imaging technique used in this project. Images were recorded using the TCS SP8 STED CW inverted microscope with a 100X/1.40 oil-immersion objective and HyD hybrid photon detector (Leica Microsystems). A 592 nm continuous-wave depletion laser was applied to samples stained with AF488 with 0.5 ms time-gating.

2.6.5 TIRF and STORM Microscopy

TIRF and STORM images were obtained using the SR GSD (Leica Microsystems) with a 160x 1.43NA oil objective and an Andor iXon Ultra 897 EMCCD camera. For TIRF microscopy, TIRF illumination with a penetration depth of approximately 150 nm was applied. Images were illuminated for 150 ms; the electron multiplying (EM) gain was 120. For STORM imaging, a buffer containing 400 µg/mL glucose oxidase, 40 µg/mL catalase, 50 mM Tris-HCl, 10 mM NaCl, 10% glucose and 1% β-mercaptoethanol in milliQ water (pH 8, 0.22 µm filter sterilised) was added to each well shortly before acquisition. For each super-resolution image, 7000 – 10000 frames were acquired, using TIRF illumination and an EM gain of 120. Single colour experiment were carried out with the 642 nm continuous wave laser (2.1-kW/cm²) set to 35% and a frame exposure of 11 ms. To reactivate AF647 fluorescence, a 405-nm (30-mW) laser was used at 1 – 15% (all lasers from MPB Communications).

2.7 Microscopy data analysis

2.7.1 STORM Data Analysis and Filtering Strings

The acquired fluorescence images (7000 – 15000 images per STORM image) were processed using the ImageJ plugin ThunderSTORM¹⁵². A list of x-y coordinates of events was obtained and used to reconstruct the final STORM image. Within ThunderSTORM, raw images were first filtered to remove noise and improve the quality of event identification. Therefore, a frequency wavelet transformation, using a convolution kernel with a third order B-spline basis function with a scaling factor of 2 was applied²⁴⁷. Then, approximate locations of detected events were obtained using the local maximum localisation method. Here, each pixel of the image is tested for an intensity threshold and relative values of its 8-connected neighbourhood. A maximum was detected when the intensity was greater than 2 times the standard deviation of the intensity values from the first wavelet level F1 and the intensity of its 8 neighbouring pixels. For sub-pixel localisation of individual events, the software fitted a PSF Integrated Gaussian with a 5 pixel-fitting radius through each approximate location. The real PSF recorded with a microscope is known to be well described by the Gaussian function^{248,249}. Its integrated form presents an optimised version by taking into account the block shape of data recorded by a camera^{250,251}. Finally, the precise (x,y) coordinates are obtained from the maximum of the fitted Gaussian curve, using a maximum-likelihood estimation with initial sigma (σ ; standard deviation of the Gaussian curve) set to 1.6 pixel resulting in the ‘unfiltered’ reconstructed STORM image.

Further filtering based upon intensity, sigma and uncertainty values of individual detections removed noise from the reconstructed images. Here, sigma is the standard deviation of the fitted Gaussian distribution and uncertainty the uncertainty of localisation arising from photon counting and background noise. The latter depends on photon count and background noise. The lower the photon count and the higher the background noise is the less accurate is the localisation which results in a higher uncertainty value. Finally, images were drift corrected using cross-correlation and events were merged within a maximum distance and a certain amount of off frames to

combine all events originating from one fluorophore. These filtering strings were determined by imaging empty wells or sparse antibodies on glass and are summarised in Table 2-3.

Table 2-3: Filtering parameters for STORM. Filtering boundaries that were applied to individual detections of re-constructed images using the SR GSD and an excitation laser of 647 nm. They were determined by imaging empty wells or sparse antibodies on glass.

SR GSD	
Intensity (#photons)	> 500
Sigma	50 < sigma < 200
Uncertainty	< 30
Merging radius (nm) /off frames	40/20
Drift Correction #bins / magnification	3/5

2.7.2 Co-localisation analysis

By calculating Manders and Pearsons correlation coefficients (Coloc2, an open-source ImageJ/Fiji plugin) the degree of co-localisation between two images was determined. Another way of comparing two images was the calculation of coordinate-based co-localisation using the ThunderSTORM software which compares single molecule localisations in two channels.

2.8 Simulated Data

Test data stacks, referred to as ground truth, were simulated using an open-source plugin for MatLab (TestSTORM²⁵²). Simulated STORM data sets were generated using scalar point spread functions (PSF) with a sample depth of 5 nm and a focal plane diameter of 300 nm. Three different patterns were chosen (termed Star, Lines or Array; example in Figure 2-2 displays Star; see all patterns in Figure 4-2). By selecting AlexaFluor-647, the software automatically applies the known blinking characteristics of the fluorophore. Acquisition parameters are added to match the camera settings and image/pixel sizes generated of the Leica SR GSD microscope. Thus, like real GSD data,

all simulations measured 180 x 180 pixels with a pixel size of 100 x 100 nm. Finally, background noise of approximately 200 AU was added to images to mimic camera noise. All parameters are displayed in Figure 2-2A which shows the user interface of TestSTORM.

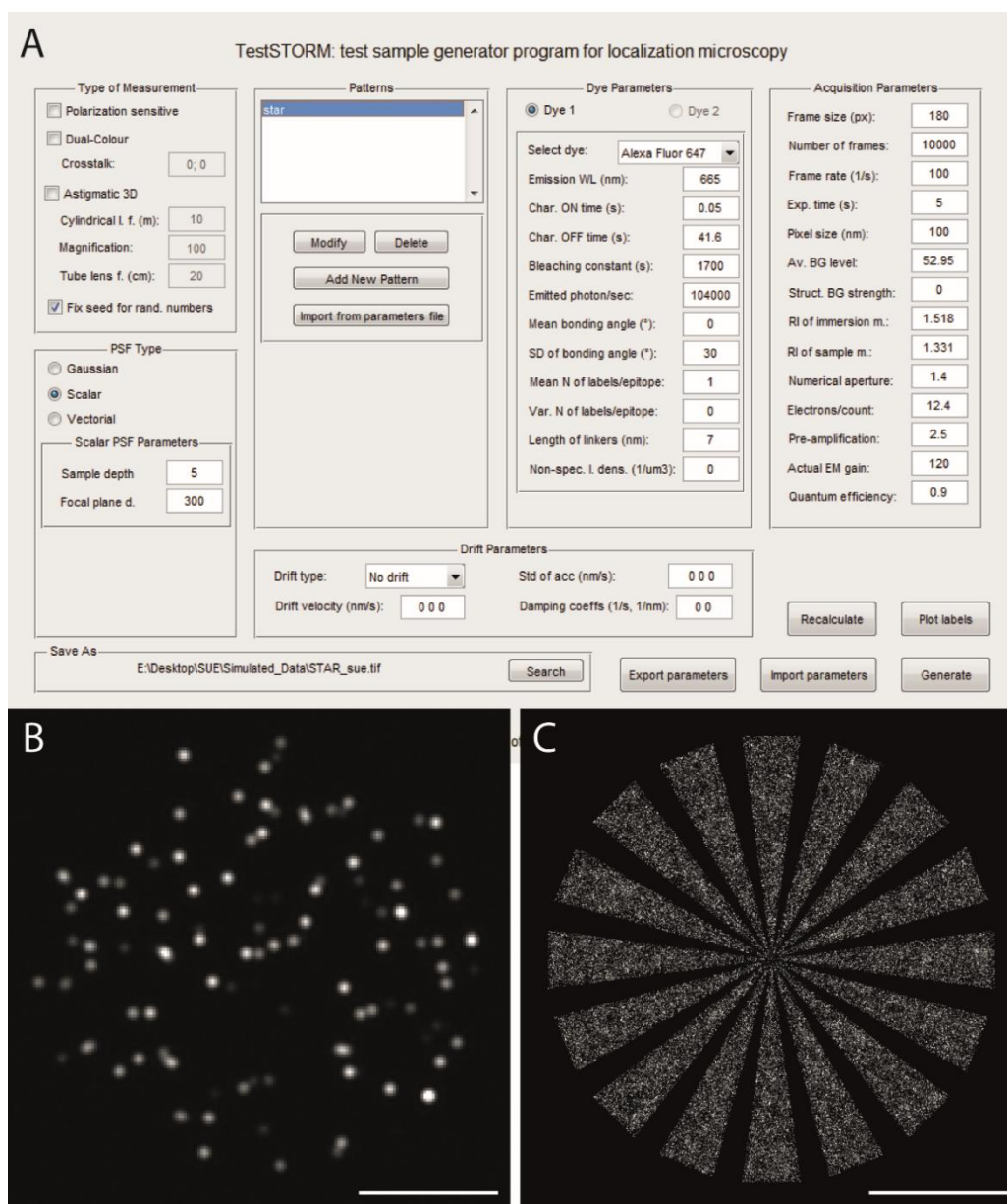


Figure 2-2: Simulating STORM data sets. A) User interface of TestSTORM, an open-source MatLab plug-in used to generate test data sets. Here, all parameters used to generate the STORM image Star, which is displayed in C, are shown. **B)** Example frame of the generated data set, which contains 10000 frames in total. Scale bar 5 μm. **C)** Final, reconstructed STORM image, obtained by processing the simulated data set with ThunderSTORM. Scale bar 5 μm.

To simulate backgrounds, a desired shape was created and saved as a picture. Then, intensity values and pixel size were adjusted in ImageJ to be similar to observed autofluorescence in lung macrophages. Finally, the number of frames was adapted to 10000 frames, using bicubic interpolation. Simulated STORM and background data sets were combined using the image calculator in Fiji. Combined stacks were used to test the described background correction techniques.

All simulated STORM data sets were processed with ThunderSTORM as described above (2.7.1; page 70). However, simulated data was not filtered, merged or drift corrected after reconstruction.

2.9 Background Correction Technique

Where stated, background was removed from STORM datasets using a custom script in FIJI²⁵³, as described in detail in Chapter 4 and a resulting publication²⁵⁴. Briefly, a grouped z-projection using mean or median intensities is performed on STORM data sets (consisting of 7000 – 15000 individual frames), either across the whole data set or a specified number of frames. Then, the z-projection is expanded to the same number of frames as the original stack applying a bicubic interpolation. This presents the calculated background of the data set. Finally, the background is subtracted from the original stack, yielding a corrected set of stacks that can be processed as usual using the ThunderSTORM software.

2.9.1 Evaluation of Corrected Images

In order to evaluate the performance of the background correction technique, corrected vs. not corrected images were assessed using different parameter, all relative to the specific ground truth image. Parameter measured consisted of the percentage of events detected, coordinate based co-localisation (CBC), nearest neighbour distance (NND), Manders' overlap and Pearson's correlation coefficient. Here, the percentage of events, compares the total number of events in the corrected (or not corrected) image

to the number of events detected in the respective ground truth. CBC was calculated using ThunderSTORM. Therefore, every localisation of the reconstructed ground truth image is compared to localisations within a 500-nm radius in the comparative image. This yields a correlation value between -1 (completely separated) and +1 (perfectly co-localised). A random distribution would yield the value 0. NND is also included in the ThunderSTORM package and calculates the distance for every localisation of the reconstructed STORM images to its closest localisation in the comparative data set. Manders' overlap and Pearson's correlation coefficient were calculated using the open source plugin Coloc2 in FIJI. Values range from 0 (completely separated) to +1 (perfectly co-localised).

2.10 Assessment of Lung Macrophage Protrusions

Human lung macrophages were plated as described earlier (2.6.1 on page 67) on microscopy glass slides, coated either with PLL or PLL and 10 µg/mL IgG. Fixed cells were stained with wheat germ agglutinin (WGA)-AF488 to visualise the membrane topology, and anti-human MHC class I mAb conjugated to AF647, to study the distribution of MHC class I in the membrane. TIRF images were taken. Total cell area was measured manually, using ImageJ, according to the presence of fluorescence. The area covered by MHC class I was determined by thresholding TIRF images at 75% of max grey value. The percentage of coverage was calculated relative to the total cell area.

2.11 Quantitative Analysis of Vesicles

Background corrected STORM images of macrophages stained with anti-human CD81 labelled with AF647 were used to quantitatively assess vesicle secretion. Therefore, ring structures were manually counted and their diameter measured using ImageJ. The ring density defined as number of rings per µm² was calculated by dividing the total number of rings of one cell by its cell area. The latter was determined by fluorescent staining of the cell.

The analysis of cell secretions was done in an automated way. Here, STORM images of secretions (stained with anti-CD81-AF647) were thresholded by Otsu's method, inverted and made binary by the command *convert to mask*. Next, the outlines of vesicles were selected and dilated 3 times. After filling holes of joint up pieces of single vesicles, selections were eroded 3 times to reset them to their original size. To separate vesicles that overlapped during dilating steps due to close proximity, watershed segmentation algorithm was applied. Finally, outliers within a radius of 4 pixels and a threshold of 1 were removed and particles were analysed. No particle size was excluded but circularity was set to 0.60 – 1.00 to ensure correct selection of vesicles. The area of outlines was measured and results saved as csv-files. In addition, the tiff image created by the analyser containing all identified and measured vesicles was saved. All of this was carried out with a batch processor in ImageJ:

```
macro "batch-vesicle_Measure"{
    setBatchMode(true);
    file1 = getDirectory("TIFs");
    list1 = getFileList(file1);
    n1 = lengthOf(list1);
    file2 = getDirectory("VesicleAnalysis");
    list2 = getFileList(file2);
    n2 = lengthOf(list2);

    for(i = n2; i < small; i++) {
        name = list1[i];
        open(file1 + list1[i]);
        setAutoThreshold("Otsu dark");
        setOption("BlackBackground", false);
        run("Convert to Mask");
        run("Outline");
        run("Dilate");
        run("Dilate");
        run("Dilate");
        run("Fill Holes");
        run("Erode");
        run("Erode");
        run("Erode");
        run("Watershed");
        run("Remove Outliers...", "radius=4 threshold=1 which=Dark");
        run("Analyze Particles...", "size=0.00-Infinity circularity=0.60-1.00
show=Outlines display clear");
        saveAs("Results.csv", file2 + name + "-analysis.csv");
    }
}
```

```

        run("Close");
        saveAs("tiff", file2 + name + "-vesicles");
        close("*");
    }
}

```

To determine position of vesicle secretion across the synapse TIRF images of macrophages were manually scored for three possible positions: the centre, periphery or whole synapse.

To determine the fluorescence intensity of LILRB1 relative to CD81, the mean fluorescence intensity of TIRF images of M0-like and M2-like macrophage secretions was measured using ImageJ and values of LILRB1 divided by values of CD81.

2.12 Isolation of Extracellular Vesicles (EV)

EV were isolated by differential ultracentrifugation as previously described²⁵⁵. In brief, monocyte-derived macrophages were incubated at $1 - 5 \times 10^6$ cells/mL with 20% (v/v) polystyrene beads coated with 10 μ g/mL (for preparation of beads see 2.3 page 65) in serum free media (DMEM for M0-like and RPMI for M1-like and M2-like macrophages) supplemented with 2 mM CaCl_2 for 90 min at 37°C and constant shaking to secrete EV. Then, all spins were carried out at 4°C. Cells (1st pellet) were separated at $350 \times g$ for 15 min and supernatant was centrifuged at $2000 \times g$ (2nd pellet; was discharged). Cleared supernatant was transferred to new Eppendorf tubes and centrifuged at $10,000 \times g$ for 40 min (3rd pellet; large EV). Finally, supernatant was transferred to OptiSeal Polypropylene Tubes (3.3 mL, Beckman Coulter) and spun at $100,000 \times g$ (4th pellet; small EV) in a TLN100 (Beckman) rotor utilising a Optima Max-XP (Beckman) centrifuge. All apart from the 2nd pellet were washed once in PBS and re-pelleted at the same speed and time. For microscopy, cell pellets were re-suspended in serum free media, counted and plated onto PLL-coated microscopy slides (see 2.3, page 65) at a concentration of 5×10^4 cells/well in 200 μ L for 15 min. Pellets of large and small EV were not counted but re-suspended in 200 μ L of serum free media before adding to

the slides for 15 min. After incubation, cells and EV were fixed for 20 min with 4% PFA, blocked for 1h with PBS/3%BSA and stained with CD81 (see Table 2-2) in PBS/3%BSA. These steps were all carried out at RT. Alternatively, pellets were shock frozen in liquid nitrogen and stored at -80°C for proteomics analysis.

2.13 Proteomics analysis

Samples were prepared according the standard S-Trap sample processing technology protocol (S-Trap™ Micro High Recovery Protocol). In brief, large and small EV pellets (see 2.12) were re-suspended in 25 µL of lysis buffer (5% SDS, 8 M urea, 100 mM glycine, pH 7.55) and clarified by centrifuging for 8 min at 13000 × *g*. To reduce and alkylate proteins, samples were reduced with 100 mM dithiothreitol (DTT) at 37°C for 10 min and 300 mM iodoacetamide (IAM) is added for 30 min in the dark to modify the free cysteines. Then, samples were centrifuged for 10 min at 14000 × *g*. Next, the samples were concentrated and purified in S-Trap micro columns (Protifi). Thus, the supernatant was transferred to a fresh tube and aqueous phosphoric acid was added to have a final concentration of 1.2%. Then, 300 µL S-Trap binding buffer (90% aqueous methanol containing a final concentration of 100 mM triethylammonium bicarbonate (TEAB, pH 7.1) per 50 µL acidified protein lysate are combined and loaded into S-Trap columns by centrifuging filled S-Trap columns placed on a fresh Eppendorf tube for 2 min at 4000 × *g* until the whole sample is loaded. After washing captured protein 4 times with 150 µL of S-Trap binding buffer at 4000 × *g* for 2 min samples were digested by adding 20 µL of digestion buffer (50 mM TEAB) and 1 µg trypsin for 1 h at 47°C without shaking and S-Trap sealed with the lid. Peptides were eluted by adding 65 µL of digestion buffer to the S-Trap column and centrifuging for 2 min at 4000 × *g* followed by one wash with 65 µL 0.1% aqueous formic acid (FA) and one wash with 30 µL of 30% aqueous acetonitrile containing 0.1% FA. Collected samples will thus have a total volume of approximately 200 µL.

To desalt peptides, an R3 desalt protocol was used. Briefly, 10 µL of POROS R3 beads (Oligo™) were added to wells of Corning FiltrEX desalt filter plates (Sigma Aldrich)

and washed once with 200 μ L of 50% acetonitrile and twice with 0.1% FA in water with 1 min spins at $200 \times g$ at each step. Next, the sample (200 μ L) is added and mixed for 5 min on an Eppendorf Thermomixer at 800 revolutions per minute (RPM) at RT, followed by a centrifugation at $200 \times g$ for 1 min. Then, the sample is washed twice with 200 μ L of 0.1 FA by mixing for 2 min at 800 RPM and centrifuging for 1 min at $200 \times g$. Finally, samples are eluted by twice adding 50 μ L of 0.1% FA in 30% acetonitrile, then mixing for 2 min at 800 RPM and centrifuging at $200 \times g$ for 1 min. Here, flow through is collected with a fresh collection plate. The approximately 100 μ L of sample volume was transferred to mass spec sample vials and dried with a Heto vacuum centrifuge (Thermo Fisher).

LC-MS/MS was performed using an UltiMate[®] 3000 Rapid Separation LC (Dionex Corporation) coupled to a QE HF (Thermo Fisher Scientific) mass spectrometer. Here, the buffer A consisted of 0.1% FA in water, buffer B was 0.1% FA in acetonitrile and a 75 mm x 250 μ m i.d. 1.7 μ m CSH C18 analytical column (Waters) was used. A 5 μ L loop was used to load 3 μ L of the sample onto the column at a flow rate of 300 nL/min for 13 min at 5% B. The loop was removed and over 0.5 min the flow was reduced to 200 nL/min. The column gradient was set to change linearly from 5% to 18% B in 34.5 min followed by 18% to 27% B in 8 min and 27% to 60% B in 1 min. Washes occurred at 60% B for 3 min before re-equilibration to 5% B in 1 min. For the last 5 min of the run (at 55 – 60 min) the speed was increased to 300 nL/min.

Separated peptides were analysed following electrospray ionisation into the mass spectrometer. Here, data was acquired in a data directed manner for 60 min and in positive mode. For fragmentation, peptides were selected automatically by data dependant analysis based on the top 12 most intense peptides with m/z between 300 to 1750 Th and a charge state of 2, 3 or 4 with a dynamic exclusion set at 15 sec. MS Resolution was selected at 120,000 with an AGC target of 3×10^6 and a maximum fill time set at 20 ms while MS2 Resolution was set to 30,000, with an AGC target of 2×10^5 , a maximum fill time of 45 ms, isolation window of 1.3 Th and a collision energy of 28.

Raw data was analysed using Proteome Discoverer software (version 2.4; Thermo Scientific) where peptides were identified and quantified from mass spectra. First, raw data files were produced using Xcalibur software (Thermo Scientific), imported into Proteome Discoverer and searched using SEQUEST HT® database search engine (Thermo Fisher Scientific). Here, protein identification was based on the UniProtKB/Swiss-Prot human database (SwissProt TaxID=9606; v2017-10-25 containing 556,006 sequences). Searches were carried out with a precursor mass tolerance of 20 p.p.m., fragment mass tolerance of 0.5 Da and a maximum number of missed cleavage sites of 2. Modifications were restricted to carbamidomethylation of cysteine for static modifications and to the oxidation of methionine, deamidation of asparagine and glutamine residues and the N-terminal acetylation for dynamic modifications. Identified and quantified proteins were then filtered in Proteome Discoverer for high protein False Discovery Rate (FDR) confidence containing at least 1 unique peptide. This pool of filtered proteins was then used to perform Gene Ontology (GO) annotation and principal component analysis (PCA).

2.13.1 Heatmaps

Heatmaps were drawn in two different ways. Firstly, a heatmap of all samples was created in Proteome discoverer using normalised and grouped abundances. Hierarchical clustering was performed on columns and rows using the distance function Pearson and complete linkage method. Columns were scaled before clustering. Secondly, data of regulated proteins from small or large extracellular vesicles was exported from Protein Discoverer. Gene symbols and grouped abundances were imported into R for cluster analysis. Hierarchical clustering was performed on rows using standard settings of the *heatmap* function with no scaling applied.

2.14 Statistics

Statistical significance of results was tested using Graphpad Prism (version 8, Graphpad Prism Software). First, the Shapiro-Wilk normality test was used to determine normality of the results. Data sets with a normal Gaussian distribution were then

analysed using parametrical statistical tests. More precisely, a two-tailed t-test was used to compare two data sets while multiple data sets were analysed using one-way ANOVA. If at least one of the data sets did not have a normal distribution, non-parametric tests were applied. Here, two data sets were compared with a Mann-Whitney test, and a Kruskal-Wallis ANOVA test with Tukey's multiple comparisons was applied to assess multiple data sets. Significances are displayed as follows: non-significant (ns) $p \geq 0.05$., $p < 0.05$ (*), $p < 0.01$ (**) and $p < 0.001$ (***). Thus, differences were only considered statistically significant when the p values were below 0.5. Unless stated otherwise, values cited in the text refer to means \pm standard deviation (SD). A Gaussian fit was used to determine the mode diameter of extracellular vesicles in histograms.

Chapter 3 – Establishing an Imaging System to Investigate the Nano-scale Organisation of the Membrane of Human Macrophages

3.1 Introduction

Macrophages are phagocytic cells that are strategically positioned throughout the entire body. They function as immune sentinels with profound roles in initiating and coordinating an immune response as well as homeostasis and wound healing⁷. First, macrophages were thought to only be derived from blood monocytes, which are recruited into the tissue, where they differentiate into macrophages¹². However, in the last two decades it has been shown that most tissue macrophages are established prenatally and are able to self-maintain within the tissue¹³. Crucially, the function and phenotype of these tissue macrophages is highly dependent on the tissue itself. It is thus vital to study macrophages originating from different tissues to fully understand macrophage biology. Nevertheless, monocyte-derived macrophages also play a vital role during an immune response as well as the steady state. Monocytes are recruited into the tissue for example during acute inflammation where they differentiate, fulfilling the functions of tissue-specific macrophages²⁵⁶. In fact, monocytes have been shown to fully differentiate into tissue-specific macrophages, also gaining the ability of self-renewal^{32,256}.

The great phenotypic plasticity of monocyte-derived and tissue-resident macrophages presents a challenge for the clear definition of different macrophage populations. Classically, macrophages are divided into two subgroups, namely M1 and M2 macrophages. Here, M1 macrophages display a pro-inflammatory phenotype while M2 macrophages are thought to act immuno-suppressive¹⁰. Even though macrophage phenotypes are more complex and the division in two subgroups is a simplification, studying these cells has and will shed new light on macrophage function and plasticity. Monocytes can be differentiated into M1 or M2 macrophages *in vitro* by culturing monocytes in the presence of GM-CSF or M-CSF respectively⁶¹. Full polarisation and

activation is often achieved by further culturing the cells with LPS or IFN γ for M1 macrophages or IL-4 for M2 macrophages. However, this leads to the activation of the generated macrophages and studies investigating differentiated but resting macrophages activated by different stimuli are lacking.

A shared feature across all macrophage types is phagocytosis. Macrophages recognise for example bacteria and viruses that are opsonised by IgG, leading to their activation through Fc γ RI. Crucially, macrophages form a synapse at the contact site with the opsonised target¹⁷⁰. Similar to the immunological synapse formed between lymphocytes and target cells, adhesion and signalling receptors are re-organised. Lin and co-workers showed that murine bone marrow derived macrophages incubated on IgG-containing lipid bilayers formed Fc γ R-IgG microclusters leading to the recruitment of signalling protein Syk and the remodelling of the cytoskeleton driving phagocytosis¹⁷³. Further, Lopes et al. conducted one of the only studies applying super-resolution imaging to the phagocytic synapse⁵. They showed that upon activation with IgG, nanocluster of activating receptor Fc γ RI and inhibitory receptor SIRP α segregate from another, highlighting the interplay of receptor molecules on a nanometer-scale. Thus, the investigation of the phagocytic synapse on a nanometer scale is vital for the understanding of the detailed molecular mechanisms of cellular activation mediated by cell surface receptors. Yet these studies are lacking, especially the investigation of tissue-specific macrophages.

Nanometer-scale investigations are made possible by recent advances in microscopy. Several super-resolution imaging techniques, including Stochastic Optical Reconstruction Microscopy (STORM) were developed, enabling to resolve and study subcellular structures and processes. However, despite their importance, very little studies imaged tissue-derived human macrophages. This is likely due to their high natural autofluorescence which severely interferes with light microscopy techniques. It is long known that human airway macrophages are autofluorescent, especially those of smokers^{129,257}. Edelson et al. described already in 1985 the interference of the

autofluorescence from alveolar macrophages with fluorescence-based techniques including microscopy and flow cytometry¹⁰⁹. Possible solutions have been proposed in the past, like photobleaching and simply avoiding the region of the spectrum where autofluorescence occurs, but the problem persists until today and has rarely been investigated in the context of STORM^{109,143,258,259}. It is thus vital, to improve super-resolution imaging techniques for autofluorescent samples, like human lung macrophages.

The hypothesis was, that activated macrophages with different phenotypes and different origins would display a different nanoscale organisation within the membrane, reflecting different thresholds of activation. To test this, the nanoscale organisation of the membrane of different macrophages was recorded. Thus, this chapter aimed to establish an imaging system to study the nano-scale organisation of human monocyte- and lung-derived macrophages at the phagocytic synapse. Therefore, monocytes were differentiated into M0-like, M1-like and M2-like macrophages while lung macrophages were used fresh, directly after isolation from the lung tissue. Cells were activated on IgG-coated surfaces, presenting a 2D-model of a phagocytic synapse. However, the intrinsic autofluorescence of human lung macrophages interfered with light microscopy. It was further characterised and examined in the context of STORM.

3.2 Summary of Chapter Aims

- a) The generation of M0-, M1- and M2-like macrophages from blood monocytes
- b) Purifying human lung macrophages from lung immune cell suspensions isolated from human lung resections
- c) Establishing an imaging system to study the nano-scale organisation of the phagocytic synapse of human macrophages
- d) Characterising the intrinsic fluorescence of human lung macrophages and its effect in STORM

3.3 Results

3.3.1 Generation and Characterisation of Human Macrophages

Due to the great phenotypic diversity of macrophages, it is crucial to study macrophages from different origins and phenotypes. Thus, in this project four different macrophage types were investigated. M0-like, M1-like, M2-like and lung macrophages (Figure 3-1). The latter was isolated from lung resections and used fresh. M0-like, M1-like and M2-like macrophages were generated from blood-derived monocytes. Notably, monocytes are classically differentiated by the co-culture with the cytokines GM-CSF or M-CSF which is followed by the activation and full polarisation of the macrophages with LPS and IFN γ or IL-4 respectively. Here, monocytes were differentiated but not activated and therefore are termed “-like”. This allowed the investigation of differently differentiated macrophages in a resting state and activated by IgG rather than LPS and IFN γ or IL-4.

For M0-like macrophages, monocytes were cultured for 3 days in X-Vivo media supplemented with 1% human serum (HS) followed by 5 days in DMEM media supplemented with 10% FBS. They were polarised neither towards M1 nor M2 phenotype. For M1-like and M2-like macrophages, monocytes were cultured for 8 days in RPMI media supplemented with 10% FBS. Polarisation towards M1-like or M2-like macrophages was achieved by supplementing GM-CSF or M-CSF respectively.

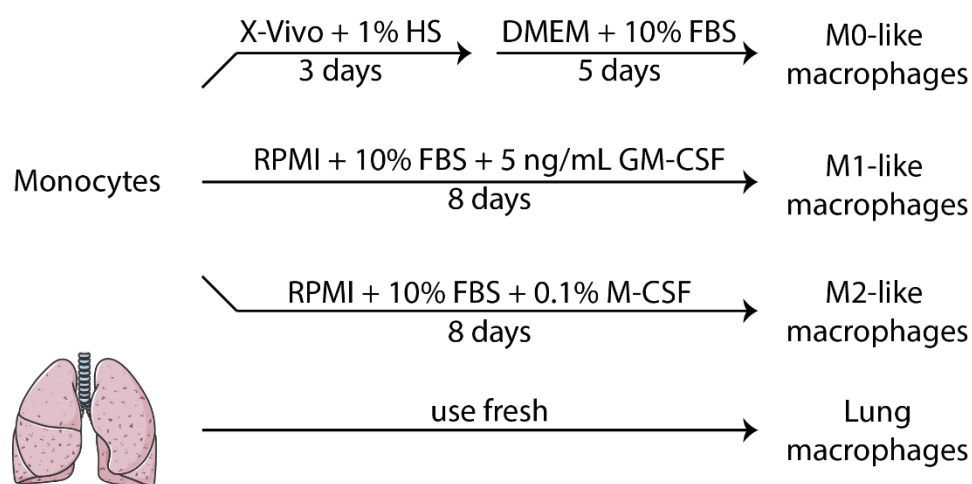


Figure 3-1: Generation and isolation of human macrophages. Human blood-derived monocytes were cultured for 8 days to generate macrophages as indicated. All media was also supplemented with 1% L-glutamine, 1% Penicillin/Streptomycin and 10 mM HEPES buffered saline (not indicated). Lung macrophages were used fresh, directly after isolation from the lung tissue.

Many different morphologies have been reported for macrophages and macrophages cultured with GM-CSF are thought to be roundish while M-CSF treated macrophages are elongated^{260–262}. In fact, Rostam et al. were able to distinguish M1, M2 and naïve macrophages as well as monocytes with an accuracy of 90% in an imaging assay that solely analysed their morphology²⁶³. Thus, to confirm their phenotype, the morphology of monocyte-derived macrophages was investigated using widefield microscopy (Figure 3-2). Therefore, macrophages were examined on day 8 of culture, still in the tissue culture plate. Indeed, M1-like macrophages displayed a roundish morphology while M2-like macrophages were mainly elongated. M0-like macrophages were morphologically similar to M1-like macrophages though they seemed to spread wider. Thus, all three monocyte-derived macrophages displayed distinct morphologies, even though they originated from the same pool of blood-monocytes. This indicates that the differentiation process was successful.

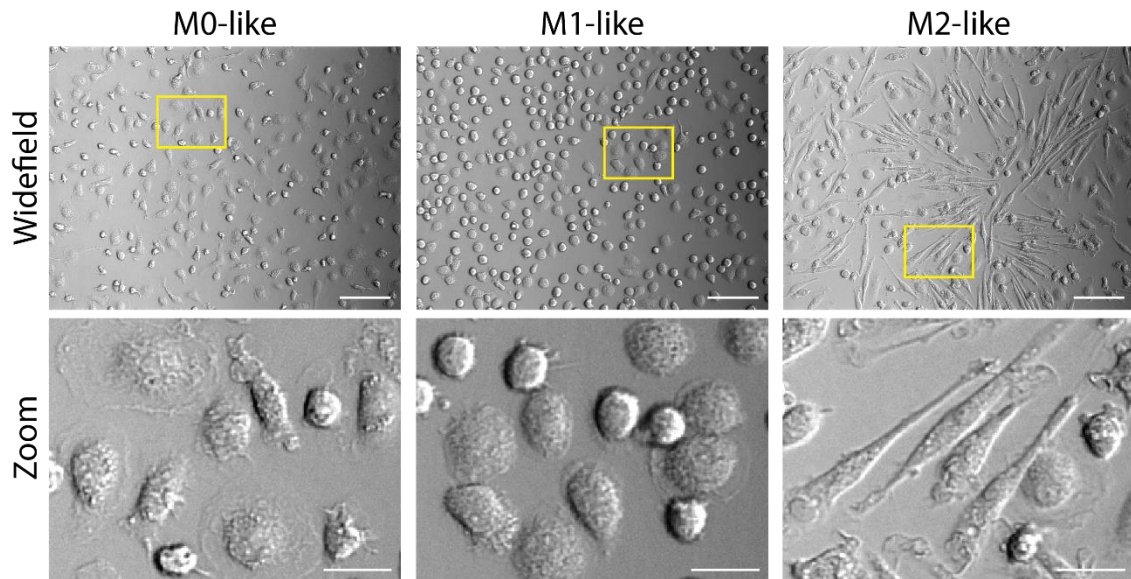


Figure 3-2: M0-like, M1-like and M2-like macrophages display distinct morphologies. Human blood monocytes were differentiated as indicated in Figure 3-1. Representative Widefield and Zoom images of M0-like (left), M1-like (middle) and M2-like (right) macrophages are shown. Scale bar 100 μm , Zoom 30 μm . $n = 36 - 45$ images per condition from 4 individual donors and experiments.

Human lung macrophages were used fresh directly after isolation. Therefore, lung immune cells were extracted from the airways of human lung resections. Even though macrophages are the most abundant immune cell type of the lung, yielding a purity of $\geq 95\%$ in bronchoalveolar lavage (BAL)²⁶⁴, immune cell suspensions might be contaminated with small levels of other cells like for example lymphocytes. However, lung macrophages can be purified by adhesion²⁶⁵. Therefore, to verify the accurate selection of macrophages, their adhesion to tissue culture plates and PLL-coated microscopy glass slides was investigated (Figure 3-3). Indeed, seeding of immune cell suspensions onto tissue culture or PLL-coated glass slides showed many macrophages, distinguished by their big size, but also a clear contamination with other, smaller cells (Figure 3-3, Before Wash). After 15 – 20 min incubation plates and glass slides were washed once with PBS. Crucially, this resulted in a clear purification of macrophages. Only big cells are left behind, while others were washed away (Figure 3-3, After Wash). Thus, lung macrophages in this project were selected by adhesion.

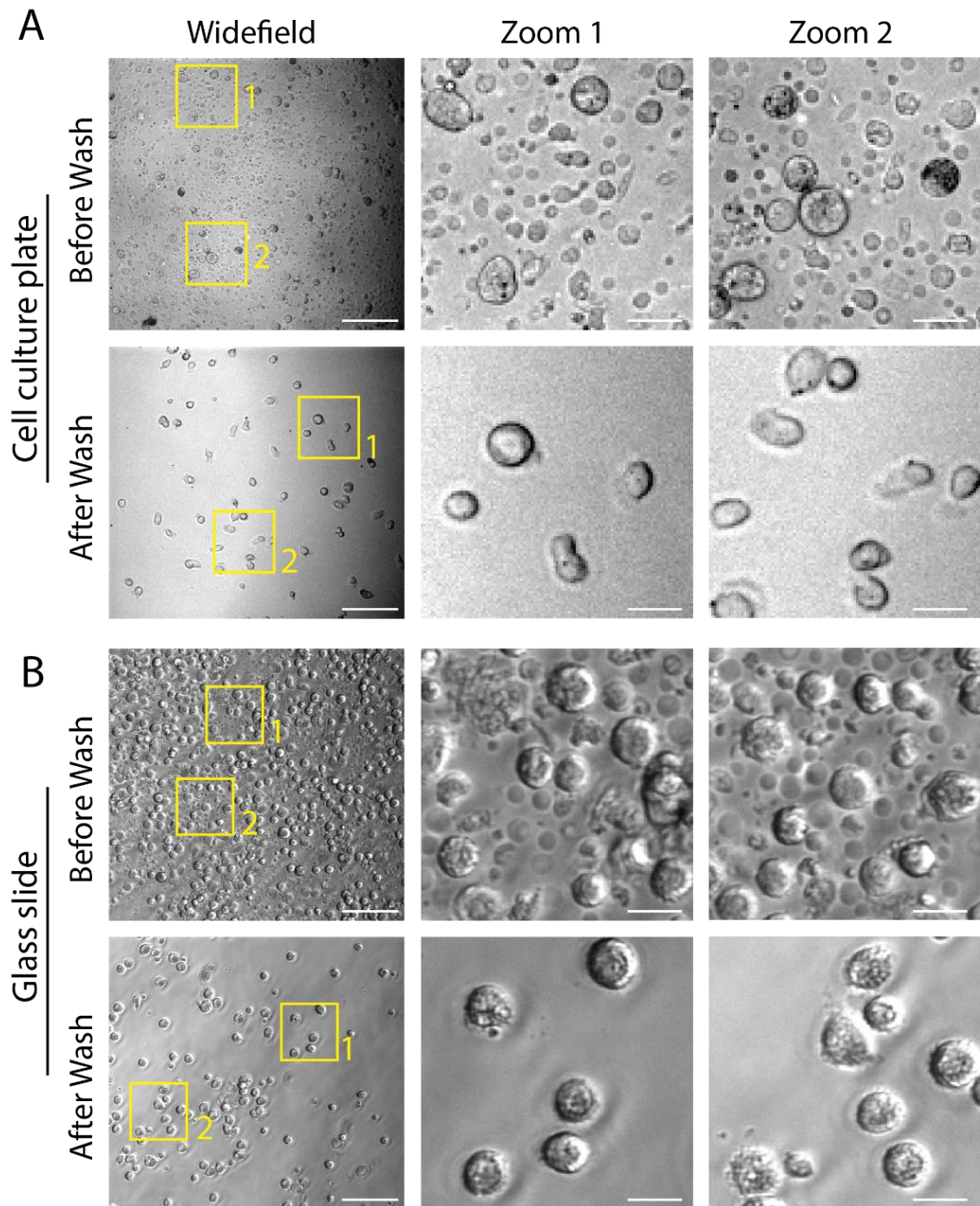


Figure 3-3: Human lung macrophages were selected from lung immune cell suspension by adhesion. To isolate lung macrophages, the airways of lung resections were washed with PBS and immune cells separated by centrifugation over Ficoll-Plaque. The re-suspended immune cell suspension was added to **A)** 6-well cell culture plates or **B)** PLL-coated glass slides and cells were allowed to settle for 15 – 30 min and wells were washed once with PBS. Lung macrophages adhered to the surfaces while other immune cells were washed away. Representative Widefield and Zoom images of a culture plate or PLL-coated glass slide before and after wash shown. Scale bar 100 μ m; Zoom 20 μ m. n = 20 – 28 images per condition from 3 individual donors and experiments.

To further characterise the phenotype of monocyte-derived macrophages, the expression of several surface markers was determined via flow cytometry. According to the literature, M1 macrophages are high in CD86, CD16 and MHC class II while M2 macrophages are high in CD206 and CD163^{59,61,261,266}. However, most studies rely on differentiated as well as activated macrophages while macrophages in this project were differentiated but not activated. Thus, discrepancies are expected. In agreement with the literature, M1-like macrophages displayed high levels of CD86 and MHC class II while being low for CD163 (Figure 3-4). However, they were highest in CD206 and low in CD16. M2-like macrophages expressed as expected high levels of CD206 and CD163, but were also found to be high in MHC class II and CD86. M0-like macrophages were high in CD86, MHC class II and low levels of CD206 and CD163, therefore being phenotypically more similar to M1-like than M2-like macrophages. Nevertheless, all three macrophage types showed distinct expression levels of surface markers, highlighting the successful differentiation of monocytes in three different macrophage subsets. Here, it is important to note that even though histograms follow the same pattern across all three donors, the variability in the mean fluorescence intensity (MFI) was big for some parameters. This was expected for different human donors that were also analysed on different days.

To differentiate blood monocytes into M1-like macrophages, monocytes were cultured for 8 days in the presence of GM-CSF. In the literature, the amount of GM-CSF administered varies between studies. In addition, some toxicity was reported in trials using GM-CSF^{267,268}. Thus, to ensure optimal growth and good health of M1-like macrophages, monocytes were cultured with different amounts of GM-CSF (5, 10 or 20 ng/mL) and cell counts were assessed after 8 days. For all three donors, cell counts decreased with higher levels of GM-CSF, possibly indicating toxicity or diminished growths (Figure 3-5). Because 5 ng/mL shows best health of M1-like macrophages yet it proved to be efficient to induce a M1-like phenotype (Figure 3-2 and Figure 3-4) this concentration was used for differentiating monocytes into M1-like macrophages.

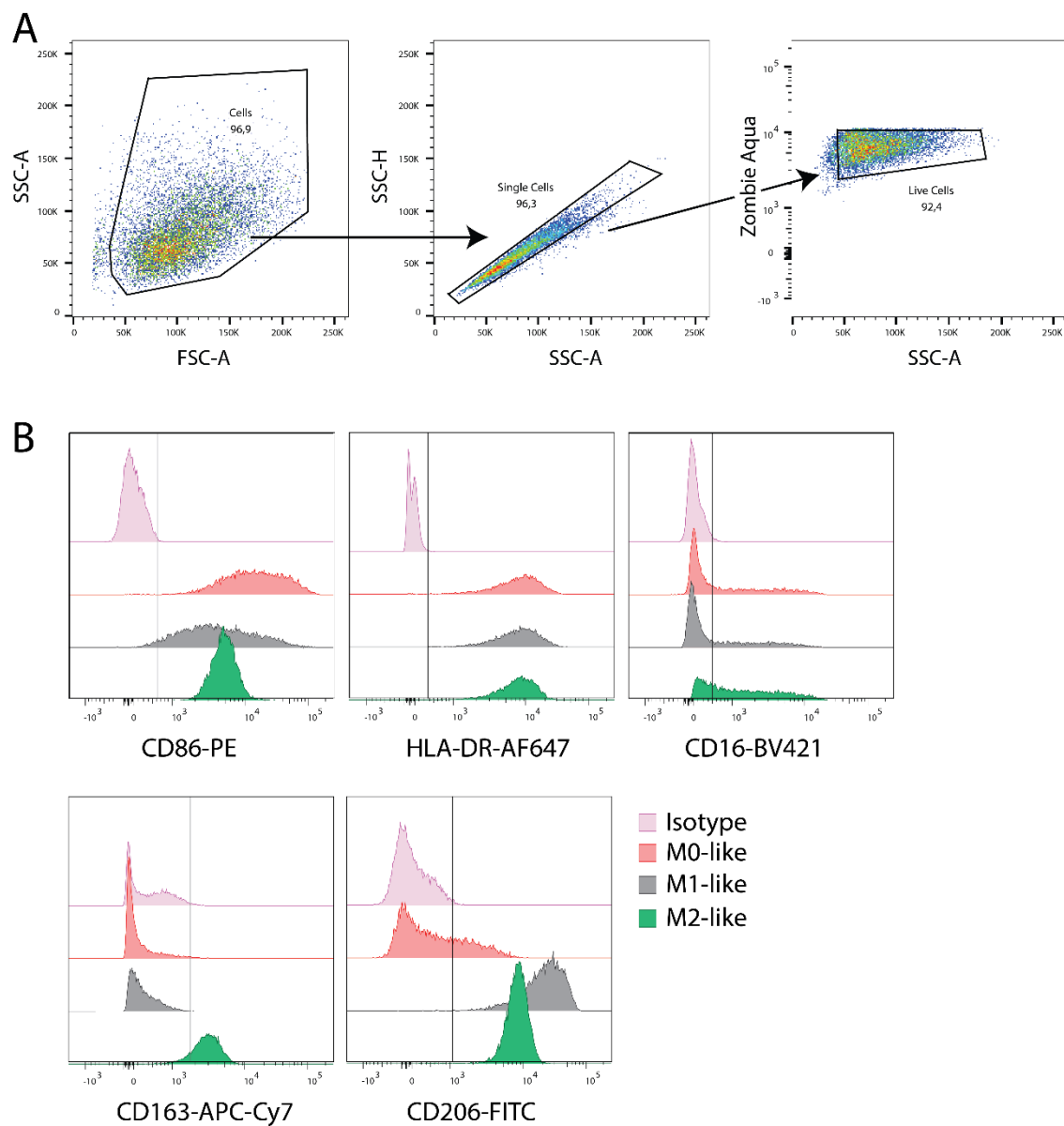


Figure 3-4: Characterisation of monocyte-derived macrophages by flow cytometry. Human monocyte-derived macrophages were stained with different cell markers (see labels) and expression levels determined using flow cytometry. **A)** Live cells were selected by indicated gating strategy. **B)** Representative histograms of 1 out of 3 donors.

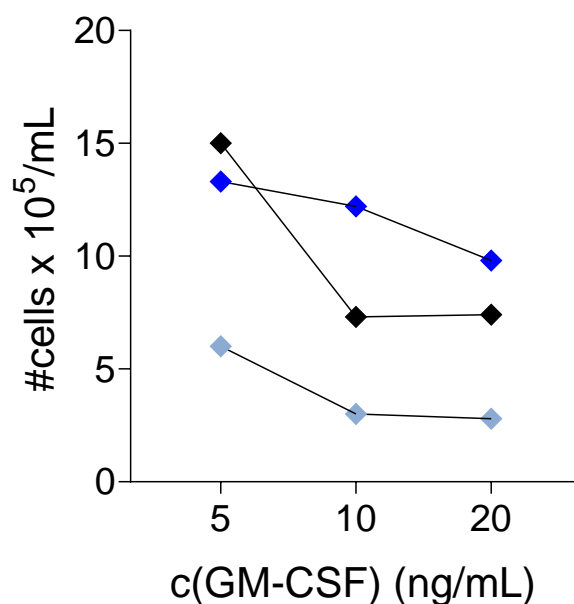


Figure 3-5: Optimising the amount of GM-CSF to generate M1-like macrophages. Blood-derived monocytes were cultured for 8 days in RPMI supplemented with 10% FBS and GM-CSF. The amount of GM-CSF was varied (5, 10 or 20 ng/mL) and the number of cells per millilitre determined with 0.5×10^6 monocytes per mL seeded at the beginning. n = 3 donors and experiments.

Taken together, four human macrophage types were compared. Lung macrophages were used fresh, directly after isolation from lung resections and purified via adherence. M0-like, M1-like and M2-like macrophages were generated by culturing monocytes for 8 days. M0-like macrophages were spreading wide and expressed high levels of CD86 and MHC class II and low levels of CD163 and CD206. M1-like macrophages had a round morphology and also expressed high levels of CD86 and MHC class II and low levels of CD163. However, they did also express high levels of CD206. M2-like macrophages displayed an elongated morphology and expressed high levels of CD163 and CD206 as well as CD86 and MHC class II. Finally, 5 ng/mL GM-CSF was found to differentiate monocytes into M1-like macrophages while showing best growth.

3.3.2 Activating Macrophages on IgG Coated Surfaces

During an immune response, pathogens may get opsonized to facilitate targeted phagocytosis for example by macrophages. In this project we set out to investigate the phagocytic synapse formed when a macrophage encounters an opsonized target. Therefore, macrophages were activated on IgG-coated glass slides or IgG-containing lipid bilayers, presenting a 2D model of the phagocytic synapse. Macrophages are investigated in non-activating and activating condition. In the case of glass slides, this is achieved by coating microscopy slides with PLL only (non-activated) or PLL and IgG (activated). To confirm the ability of the PLL+IgG coating to activate macrophages, secretion of TNF α and IL-10 was assessed in cell supernatants of all four macrophages incubated for 20 h on glass slides coated with PLL and different concentrations of IgG. TNF α is a major pro-inflammatory cytokines produced by activated macrophages²⁶⁹. In addition, Lacey et al. showed that GM-CSF differentiated macrophages secrete high levels of TNF α while M-CSF treated macrophages secrete high levels of IL-10⁷⁹. However, in both cases cells were activated with LPS, and not, like here, with IgG-coated surfaces.

All four macrophage types secreted TNF α in response to IgG in a dose dependent manner (Figure 3-6A-B). The higher the IgG concentration, the higher the amount of secreted TNF α . In the absence of IgG, cells did not secrete the cytokine, which shows that macrophages do not get activated in non-activating conditions. However, as little as 1 μ g/mL IgG was already sufficient to induce cytokine secretion showing that small amounts of IgG are sufficient to activate macrophages. 10 and 100 μ g/mL induced a more significant activation. Surprisingly, M2-like macrophages also secreted high levels of TNF α and even higher levels than M1-like macrophages. The cytokine IL-10 on the other hand was solely secreted by M2-like macrophages (Figure 3-6C-D). For further experiments, 10 μ g/mL IgG was used to activate macrophages as it induced significant levels of activation.

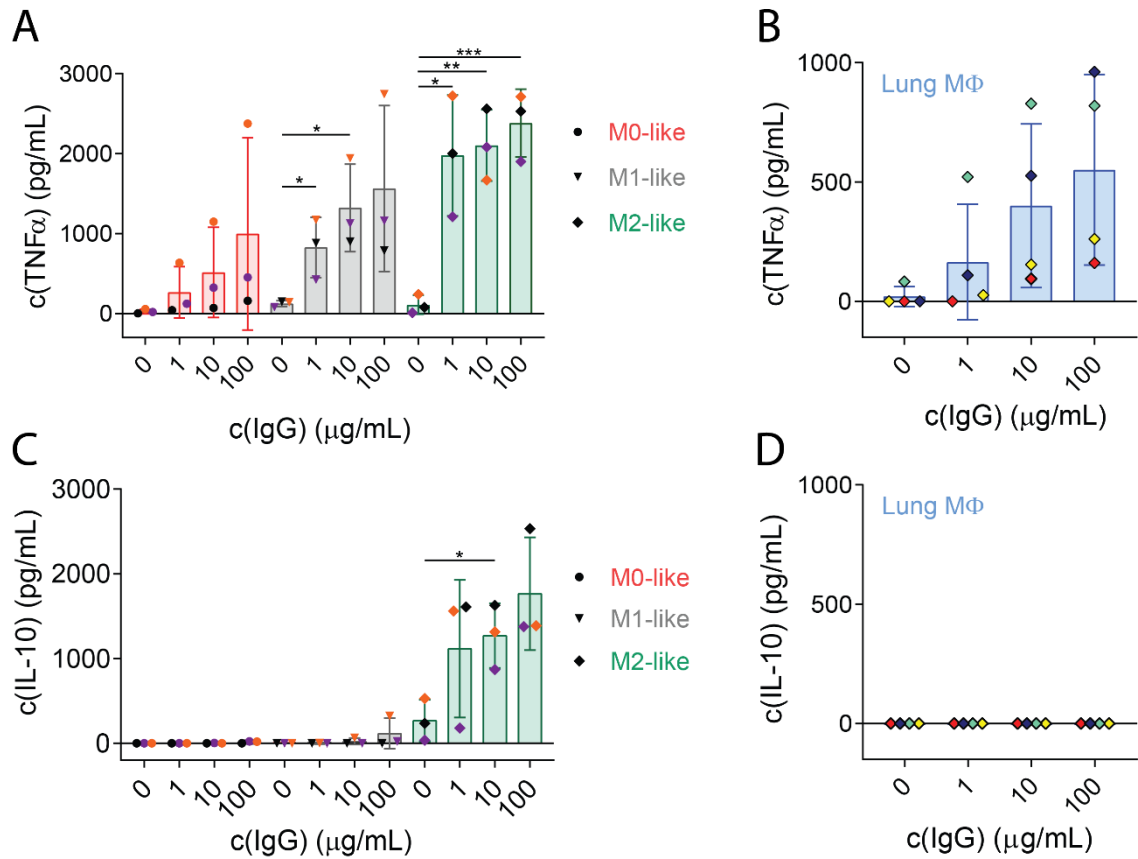


Figure 3-6: Incubation of macrophages on IgG-coated glass slides induces cytokine secretion. M0-like, M1-like, M2-like and lung macrophages were incubated on glass slides coated with PLL and different concentrations of IgG (1, 10 or 100 µg/mL) for 20 h and TNFα (**A** for monocyte-derived macrophages; **B** for lung macrophages) or IL-10 (**C** for monocyte-derived macrophages; **D** for lung macrophages) was measured in cell supernatants using Human DuoSet ELISA kits. Each dot represents 1 donor for which they are colour coded. Bars show the geometric mean \pm SD of $n = 3$ different donors. *, $p \leq 0.1$; **, $p \leq 0.01$; ***, $p \leq 0.001$; Mann-Whitney or unpaired t test where appropriate using GraphPad Prism.

Another indication for cell activation is cell spreading. Thus, the cell spreading of all four macrophage types was determined in non-activating and activating conditions. Therefore, macrophages were incubated for 15 min on glass slides coated with PLL only or PLL and 10 µg/mL IgG, fixed and imaged with interference reflection microscopy (IRM). All four cell types displayed increased spreading in activated compared to non-activated conditions (Figure 3-7). Interestingly, there are great differences between the cell types. Lung macrophages spread the least with a mean of $431 \pm 473 \mu\text{m}^2$ for activating conditions. The spreading of monocyte-derived macrophages slightly increased from M0-like macrophages with $670 \pm 533 \mu\text{m}^2$ and M1-like macrophages

with $843 \pm 550 \mu\text{m}^2$ to M2 like macrophages with $1473 \pm 859 \mu\text{m}^2$ in activated conditions. Despite the discrepancies between the cell types, all of them spread significantly larger upon incubation with IgG, indicating the activation of the cells.

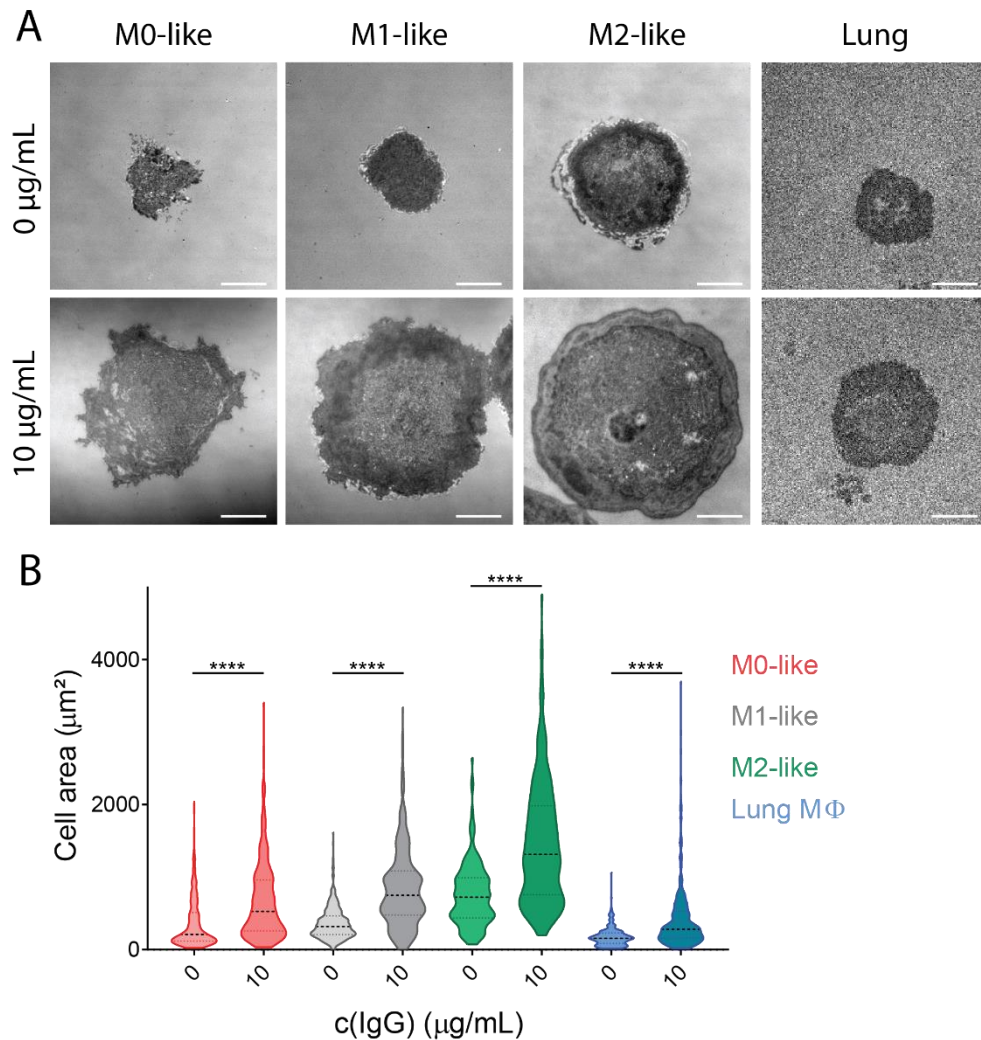


Figure 3-7: Activation of macrophages via IgG coated glass slides induces cell spreading. M0-like, M1-like, M2-like and lung macrophages were incubated on microscopy slides coated with PLL only (non-activated conditions) or PLL and IgG (10 $\mu\text{g/mL}$; activated conditions) for 15 min and fixed. **A)** Representative interference reflection microscopy (IRM) images of non-activated and activated conditions. Scale bar 10 μm . **B)** Violin plots of cell areas. $n = 158 - 675$ cells per condition from 3 individual donors and experiments. ****, $p \leq 0.0001$; Kruskal-Wallis test using GraphPad Prism.

To study the phagocytic synapse in a more biological relevant system, cells were incubated on planar lipid bilayers. This represents more closely an opsonized target compared to glass slides. In addition, macrophages could be detached from bilayers after activation. When utilising immobile bilayers this allowed the investigation of cellular secretions without them diffusing away. The correct formation of the bilayer was tested with fluorescence recovery after photobleaching (FRAP) experiments. Therefore, bilayers were prepared as usual and stained with AF488. Small regions of interest (ROI) were photobleached and fluorescence images taken over time to monitor fluorescence recovery. In the case of an immobile bilayer, bleached areas should not recover their fluorescence intensity, which would result in a relatively constant value (or straight line). In case of a mobile bilayer, the fluorescence intensity of the bleached area would recover to values close to 1. Indeed, photobleaching of ROIs did not result in fluorescence recovery as the normalised intensity of the ROI stays at about 0.5, confirming the immobility of the bilayer (Figure 3-8). Thus, it will be able to capture secretions without them diffusing away.

Next, to test the activation of macrophages on immobile bilayers, macrophages were incubated on bilayers containing different amounts of IgG and their cytokine secretion was investigated. Similar to macrophages activated on glass slides, macrophages activated on bilayers secreted TNF α in a dose-dependent manner (Figure 3-9). However, in the case of monocyte-derived macrophages, M0-like macrophages secreted only very low levels of TNF α while M1-like and M2-like macrophages secreted relatively high levels. In addition, M1- and M2-like macrophages secreted relatively high levels of TNF α in non-activated conditions, possibly indicating the activation of macrophages. Nevertheless, overall all macrophages were activated on IgG-containing lipid bilayers in a dose-dependent manner.

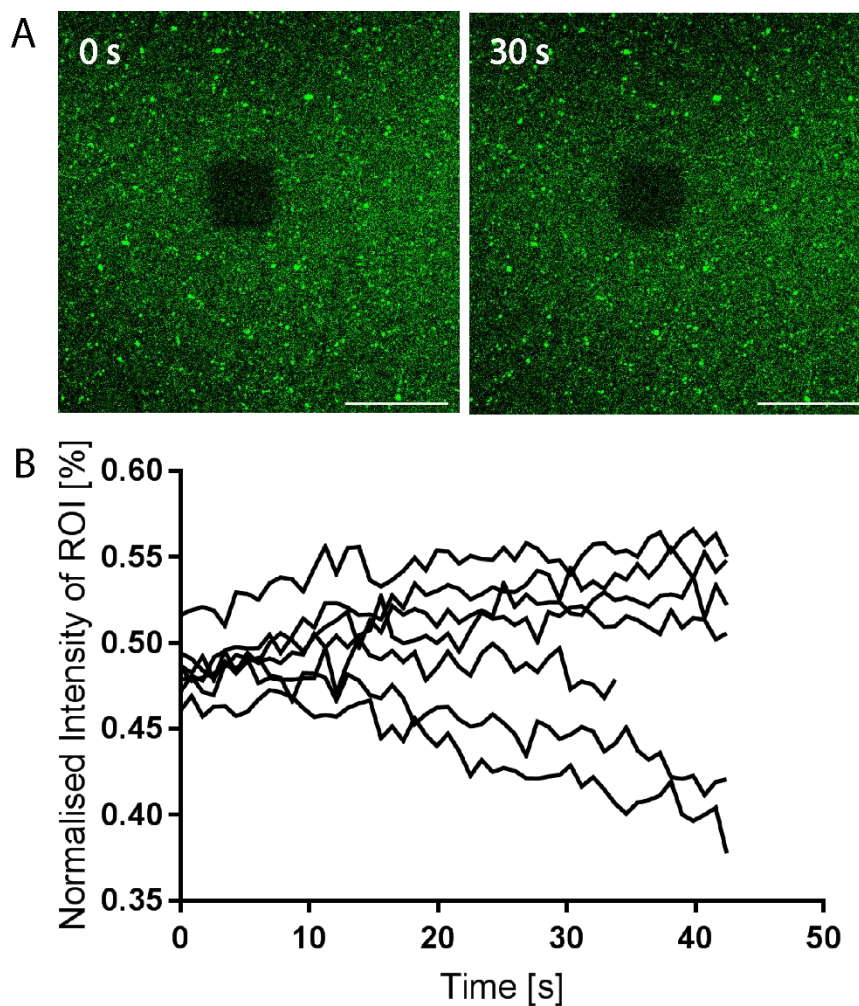


Figure 3-8: Planar lipid bilayers are immobile. Biotin-containing lipid bilayers were stained with streptavidin-AF488 for 5 min, washed and fluorescence recovery after photobleaching (FRAP) experiments conducted using the LAS AF FRAP wizard (Leica Microsystems). Small regions of interest (ROI) were photobleached and fluorescence images taken before and after bleaching. **A)** Representative images at 0 and 30 seconds after photobleaching. Scale bar 20 μm . **B)** Normalised mean fluorescence intensities of bleached vs. non-bleached regions over time. Each line represents one ROI. Data representative for $n = 3$ experiments. s, seconds.

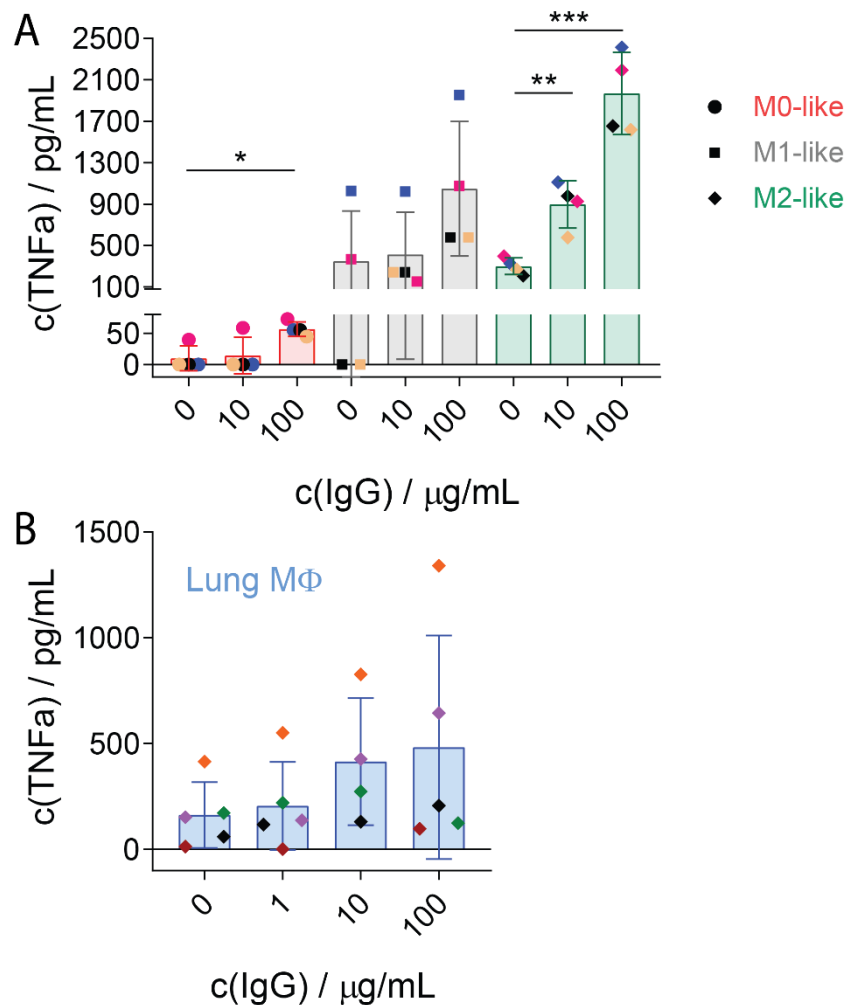


Figure 3-9: Incubation of macrophages on IgG-containing lipid bilayers introduces cytokine secretion of macrophages. A) M0-like, M1-like, M2-like or **B)** lung macrophages were incubated on lipid bilayers containing different concentrations of IgG (0, 1, 10 or 100 μg/mL) for 20 h and TNFα was measured in cell supernatants using Human TNFα DuoSet ELISA kits. Each dot represents 1 donor with dots being colour coded according to the donors. Bars show the geometric mean ± SD of n = 4 - 5 different donors. *, p ≤ 0.1; **, p ≤ 0.01; ***, p ≤ 0.001; Mann-Whitney or unpaired t test where appropriate using GraphPad Prism.

Taken together, all four macrophage types were activated on IgG-coated glass slides, leading to the secretion of TNFα in a dose dependent manner and increased spreading compared to non-activated conditions. M2-like macrophages also secreted high levels of IL-10 in a dose dependent manner. The incubation of monocyte-derived macrophages on IgG-containing immobile bilayers also led to the dose-dependent secretion of TNFα though M1-like and M2-like macrophages also secreted the cytokine

in non-activating conditions. Overall, 10 µg/mL was sufficient to activate human macrophages and is thus used for further experiments.

3.3.3 Imaging Autofluorescent Human Lung Macrophages

The lung tissue used in this study originates from lung cancer resections. Therefore, the donors are very often (ex-)smokers. In fact, only one out of 18 donors has never smoked, 3 stopped smoking at least 1 year ago and 14 were current smokers (Table 3-1). Tissue macrophages in general, but especially lung macrophages are known to emit high levels of intrinsic fluorescence, which is exacerbated for smoking individuals¹²⁹. They are often termed 'smoker cells'. Thus, lung macrophages obtained from these tissues were likely to be highly autofluorescent, potentially interfering with fluorescent labels used in light microscopy. Therefore, the spectral range of unstained lung macrophages was recorded, to investigate the nature of autofluorescence of lung macrophages obtained from these tissue samples and to determine the ideal spectral range for fluorescent microscopy. For this, cells isolated from lung tissue were plated onto PLL-coated microscopy slides at 5×10^4 macrophages/well. Cells were incubated for 15 min at 37°C and 5% CO₂. Unattached cells were washed off with PBS, adherent cells fixed, blocked and imaged with a scanning confocal microscope (Leica TCS SP8). To cover most of the spectrum of visible light, the excitation laser was set at 470 nm (the lowest possible wavelength for this microscope) and emission was detected in windows of 35 nm with a total of 7 steps and a λ -detection step size of 45 nm starting at 480 nm (Figure 3-10A). Figure 3-10B shows representative 3D-images of unstained lung macrophages and their mean intensity was quantified in Figure 3-10C. Both demonstrate clearly that the autofluorescence peaks in the green and yellow channel and gets weaker in the far red range. In the very last detection window, basically no signal was detected. This means, fluorophores emitting in the far red spectrum are best for imaging lung macrophages.

Table 3-1: Patient data of all lung tissues used in this chapter. Patient ID, gender, age on the day of surgery and smoking history is displayed. In order for a patient to be classed as an ex-smoker they must have stopped smoking more than 1 year ago.

Patient ID	Gender	Age	Smoking history
W004962	Male	71	Current smoker
W005070	Female	66	Current smoker
W005159	Female	38	Current smoker
W005197	Male	69	Current smoker
W005600	Male	44	Current smoker
W005628	Female	78	Ex-smoker
W005645	Female	72	Ex-smoker
W005652	Female	80	Never smoked
W005653	Female	78	Ex-smoker
W005972	Female	75	Current smoker
W006031	Male	54	Current smoker
W006115	Male	63	Current smoker
W006128	Male	63	Current smoker
W006221	Male	63	Current smoker
W006253	Female	63	Current smoker
W006281	Male	62	Current smoker
W006286	Female	63	Current smoker (electronic cigarettes)
W006321	Female	67	Current smoker

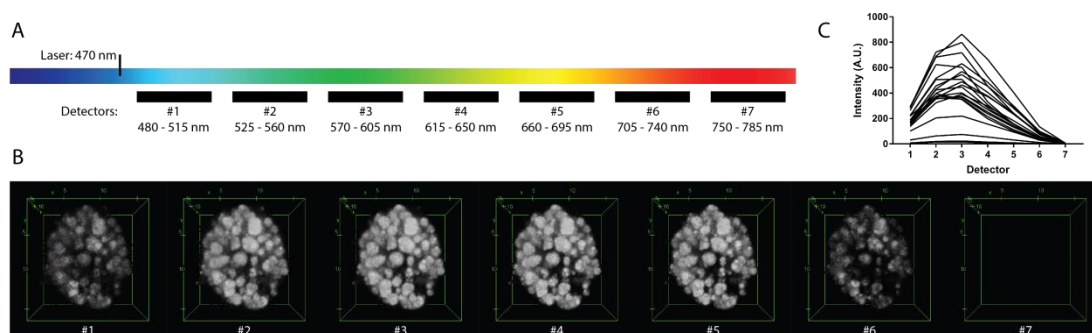


Figure 3-10: Spectral range of unstained lung macrophages. Z-stacks of unstained human lung macrophages (donor W006128; current smoker) were recorded at different wavelengths by confocal microscopy (Leica TCS SP8). **A)** The excitation laser was set at 470 nm and emission was detected in windows of 35 nm with a total of 7 steps and a λ -detection step size of 45 nm starting at 480 nm. **B)** Representative 3D-images of lung macrophages incubated for 15 min on slides coated with PLL at different wavelengths. Coordinate box indicates μm . **C)** Mean intensity of unstained lung macrophages at different wavelengths. Mean intensities were calculated from the sums of the z-stacks. Each line represents one cell. $n = 35$ cells from 4 individual donors and experiments.

3D-images further indicate that puncta inside the cell are the origin of the autofluorescence. This is in agreement with a clinical study which suggests that human lung macrophage autofluorescence derives from tobacco tar¹²⁹. Macrophages that patrol the airways remove particles and microorganisms from the air spaces which include tar, in the case of smokers. These particles are then stored in vacuoles or so-called inclusion bodies inside the cell¹⁴⁹.

Even though autofluorescence from lung macrophages was found to be low in the red spectrum using confocal microscopy (Figure 3-10), STORM requires different image settings, including very high laser powers. Thus, the effect of autofluorescence could differ significantly in STORM settings. However, before imaging lung macrophages with STORM, merging parameters for used antibodies had to be determined to ensure robust imaging. More precisely, STORM takes advantage of stochastic switching of fluorophores in combination with computational post-processing to localize single molecules within the cell. The final STORM image is built up from calculated coordinates that arise from a series of thousands of blinking events. The blinking characteristics of

the used fluorophore strongly influence the re-construction of the final image and need to be determined in order to ensure robust imaging. Dyes can for example re-blink which leads to repeated detections. This is corrected by merging repeated detections within a certain distance and time (or frame). For all single colour STORM the dye AF647 was used. Thus, the blinking characteristics of AF647 dyes was determined. Therefore, LILRB1 mAbs conjugated in house to AF647 were seeded onto PLL coated microscopy slides and imaged in the same way as cells. This means 300 – 400 μ L of oxygen scavenging buffer was added to each well shortly before acquisition and the 8000 acquired frames were processed using ThunderSTORM¹⁵². Antibodies were seeded highly diluted so that individual antibodies could be determined. Figure 3-11 shows a single localisation visualised in MatLab (MathWorks) before (left) and after (right) merging. Here, x-axis shows the x-coordinate of the selected region and the y-axis the acquisition frame in which events were detected; the y-coordinate is colour coded. It can be seen clearly that repeated detections occur (Figure 3-11, No merging). By merging all events that occur within 40 nm and 20 off-frames, these bursts of re-detections could be eliminated. Here, the high dilution ensured the imaging of individual antibodies. However, it has to be kept in mind that one antibody can be labelled with several fluorescent molecules. More precisely an average of approximately 3 fluorophores per antibody was found. The aim of the merging is to combine all events originating from one fluorophore. Thus, in an ideal situation an average of 3 detections should be found. The example in Figure 3-11 shows 5 detections after merging which can be explained by the variability of the degree of labelling between individual antibodies. Nevertheless, the merging all events within 40 nm and 20 off-frames successfully eliminated bursts of detections occurring within close distance and short time, indicating that these burst originated from individual fluorophores (Figure 3-11, With merging). Therefore, these merging parameters were applied to all STORM images taken.

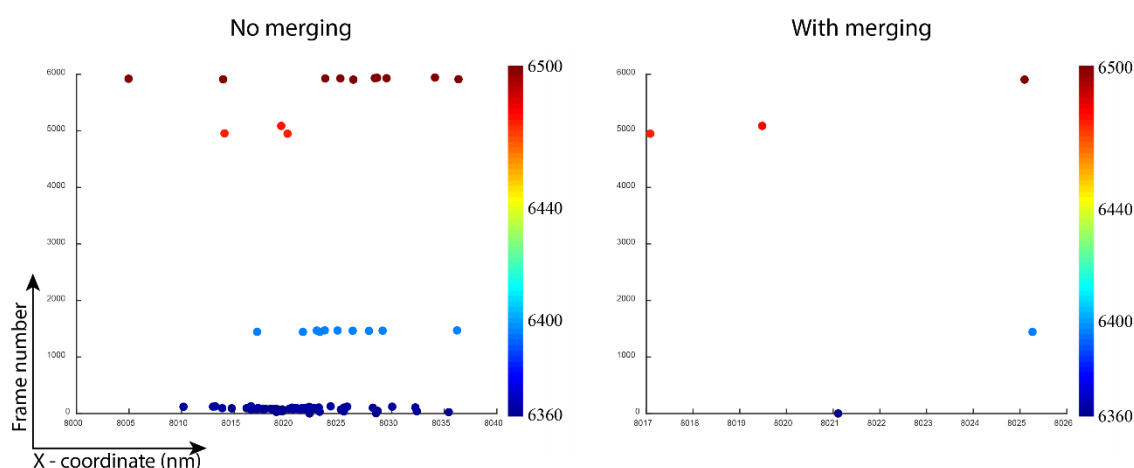


Figure 3-11: Imaging sparse antibodies on glass. A highly diluted solution of LILRB1 mAbs conjugated in house to AF647 were seeded onto glass slides and individual Abs were imaged via STORM. Data was processed using ThunderSTORM with and without merging repeated detections. Individual Abs were visualised using MatLab and recorded frames are plotted against x-coordinate of the detections. The y-coordinates are colour coded. Representative plots of an Ab with and without merging of all events that occur within 40 nm and 20 off-frames are displayed. n = 4 individual experiments.

Next, to investigate the effect of autofluorescence in STORM, single-colour STORM imaging was performed. Therefore, cells were prepared as before and stained for 1 h at RT with anti-human HLA-A,B,C mAb (W6/32) labelled with AF647. The fluorophore AF647 was chosen as autofluorescence is weakest in the red spectrum and HLA-A,B,C was chosen due to its importance for antigen presentation and wide expression on macrophages. Cells were imaged in TIRF mode by acquiring 10000 frames and analysed to generate reconstructed images (using ThunderSTORM¹⁵²).

In STORM, individual blinks of fluorophores are recorded (for more detail see 1.7.2). However, looking at the data sets of stained lung macrophages, bright, autofluorescence spots can be observed which don't blink but stay on over time (Figure 3-12A, blue arrows). Signals originating from the staining don't stay on but disappear in adjacent frames (Figure 3-12A, yellow and orange circles). In addition, autofluorescent areas are generally much bigger and not as well defined as blinks originating from an extrinsic fluorophore. The autofluorescence signal is very bright and saturates the blinks of the fluorophores (Figure 3-12B-C). In the post-acquisition analysis, the software then

fails to detect these blinks and the information is lost. Figure 3-12B shows the reconstructed STORM images of the data set shown in Figure 3-12A. It can be seen clearly that reconstructed images comprise artefacts where there has been autofluorescence in the data set. Even though cells were stained with AF647 (where autofluorescence was found to be relatively weak), they display autofluorescence which results in big white spots on the surface membrane (unfiltered). These spots are so bright that they saturate the signal (Figure 3-12C, unfiltered) while only a low signal was found in the red channel when recording the spectral range of unstained lung macrophages (Figure 3-10). It has to be kept in mind though, that a lower laser power was used to record the spectral range. Whereas for STORM, high laser powers are required. When vesicles containing tar and other particles are close to the surface of the cell they may give rise to unwanted fluorescence, even though STORM is operated in TIRF mode (which yields a penetration depth of the excitation laser of only 150 nm – 200 nm).

During post-processing of acquired images big, bright spots of autofluorescence were removed yielding empty areas on the cell surface (Figure 3-12B, filtered) thereby losing information about receptor organisation. The line profile of the filtered cell dropped down when the unfiltered signal is highest. This demonstrated how big, bright spots of autofluorescence saturate the images and signal arising from the staining was lost. This also showed clearly that the autofluorescence of lung macrophages represents a problem for STORM and has to be overcome in order to properly investigate the surface organisation of lung macrophages.

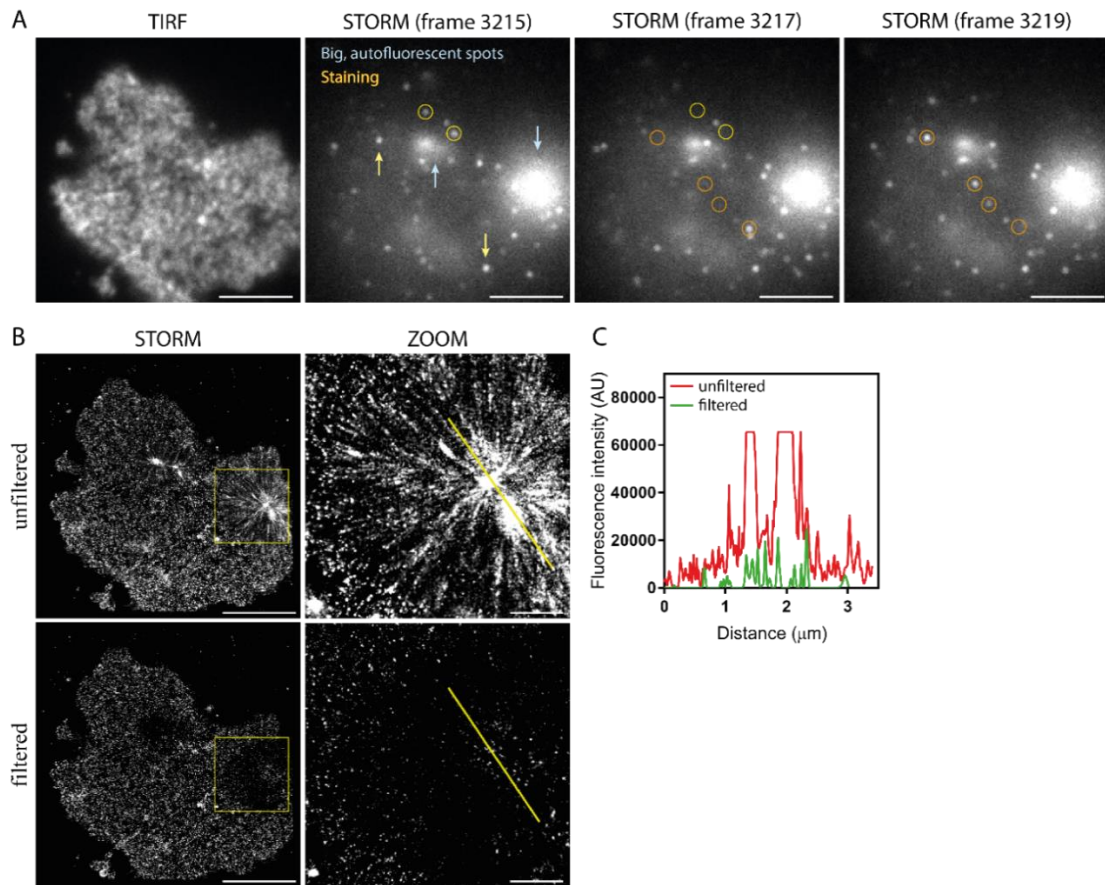


Figure 3-12: The effect of autofluorescence in STORM. Lung macrophages were incubated for 15 min on slides coated with PLL, washed, fixed and stained with anti-human HLA-A,B,C mAb labelled with AF647. **A)** TIRF image and individual frames of the STORM data set 22 ms apart (every other frame). Blue arrows indicate bright autofluorescence spots, yellow arrows and yellow and orange circles indicate signal originating from the staining. Scale bar 5 μm . **B)** Reconstructed STORM images of the data set shown in A) before (up) and after (down) filtering. Scale bar represents 5 μm . Zoomed-in regions (5 μm x 5 μm) with corresponding line profiles are displayed. Scale bar 1 μm . Images are representative of $n = 63$ cells from 8 individual donors and experiments.

One possible approach to address this problem could be to record the autofluorescence of unstained lung macrophages from the same donor (but a different cell) and subtract it from stained cells. This is only possible if cells from the same donor display similar autofluorescence. However, two different lung macrophages from the same donor stained with anti-human HLA-A,B,C mAb labelled with AF647 illustrate that this is not possible (Figure 3-13). Here, similar to the cell in Figure 3-12, cell A is highly autofluorescent displaying bright, saturated spots in the unfiltered image. These are removed during post processing resulting in empty areas on the cell surface (filtered;

line profile). Cell B on the other hand displays less autofluorescence and intensity values of unfiltered and filtered image match in regards to peak position and intensity value itself. While cell A shows high autofluorescence, cell B lacks intense white spots and filtering yields a homogenous resolution throughout the cell. Importantly, cell A and B arise from the same donor which demonstrates clearly that autofluorescence varies from cell to cell. In addition, autofluorescence is not homogenous across the cell membrane. Thus, even for two cells with similar levels of autofluorescence, the spatial appearance of highly autofluorescent areas will be distinct.

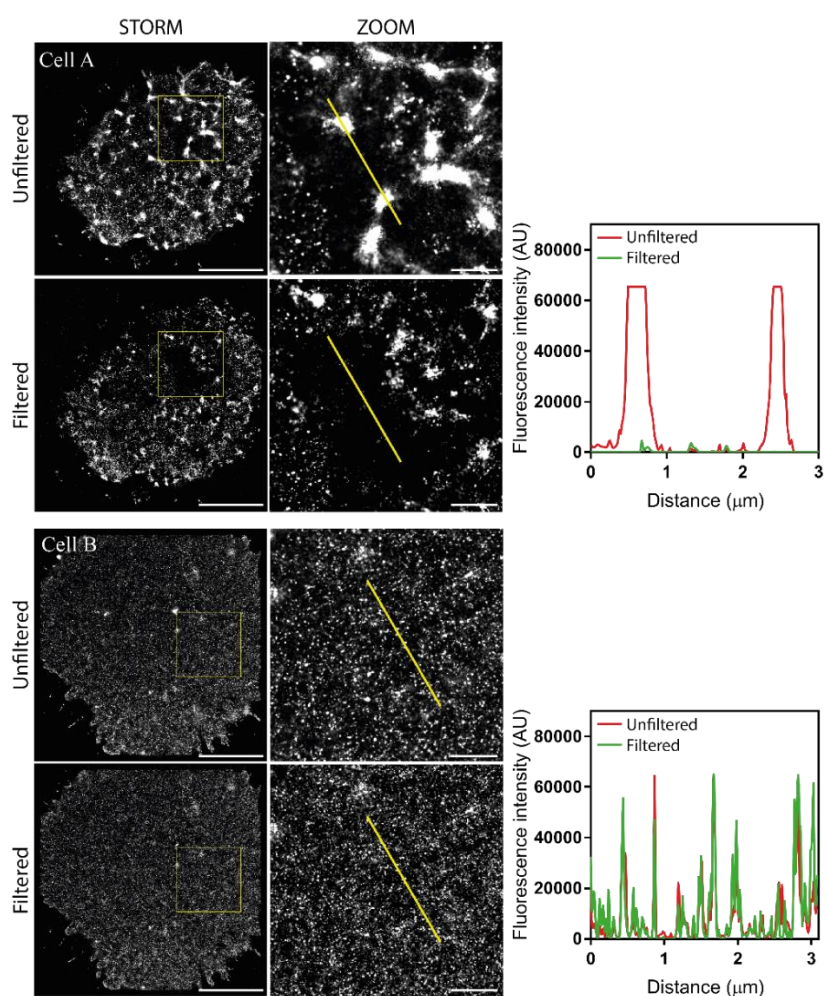


Figure 3-13: Autofluorescence of lung macrophages varies from cell to cell. Cells isolated from lung tissue were plated onto PLL-coated microscopy slides and stained with anti-human HLA-A,B,C mAb conjugated to AF 647. Reconstructed STORM images of two cells from donor #W005118 are shown before and after filtering. Scale bar represents 5 μm. Zoomed-in regions (5 x 5 μm) with corresponding line profiles are displayed. Scale bar 1 μm. Images are representative of n = 63 cells from 8 individual donors and experiments.

To investigate, whether autofluorescence could be bleached, the fluorescence signal of unstained lung macrophages excited at 488 nm with 100% laser power was recorded for approximately 45 min. Here, the autofluorescence of lung macrophages dropped in the first 5 min but reached a stable value or increases again afterwards (Figure 3-14). This makes it difficult to bleach them sufficiently prior to staining and does not provide an adequate solution to the problem.

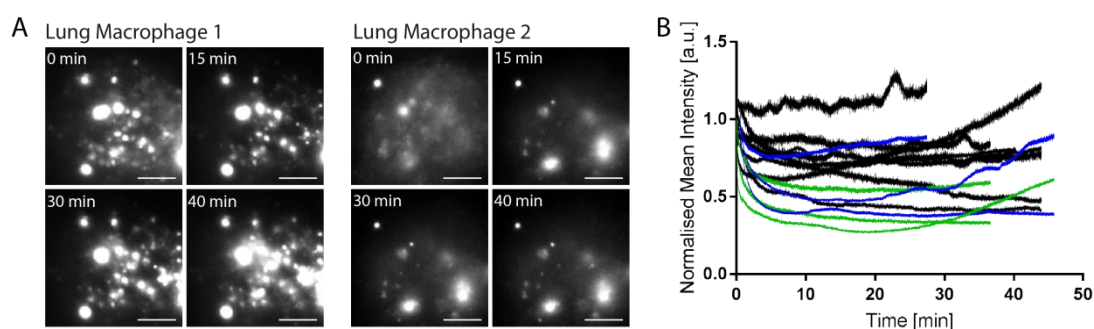


Figure 3-14: Autofluorescence is not bleachable. Fluorescent signal of unstained lung macrophages excited at 488 nm with 100% laser power were recorded over time. Every 11 ms a frame was recorded for up to 45 min. **A)** Representative images of a STORM data set of unstained lung macrophages at 0 min, 15 min, 30 min and 40 min. Scale bar 5 μm . **B)** Normalised mean fluorescence intensity of unstained lung macrophages plotted against time. Each line represents one cell which are colour coded according to the donor. $n = 14$ cells from 3 individual donors and experiments.

Overall, autofluorescence of lung macrophages is a problem for STORM resulting in big white spots in unfiltered and empty areas in filtered images. In addition, autofluorescence varies from cell to cell and cannot be bleached. To investigate the nanometer-scale organisation of cell surface receptors on lung macrophages this problem must be overcome.

3.4 Discussion

3.4.1 Summary of Results

The aim of this chapter was to establish an imaging system to study the nano-scale organisation of human monocyte- and lung-derived macrophages at the phagocytic synapse. Therefore, four different macrophage types were investigated: M0-like, M1-like and M2-like macrophages which were generated from monocytes and lung macrophages. The latter were used fresh, directly after isolation from the lung tissue. Cells were activated on IgG-coated surfaces, presenting a 2D-model of the phagocytic synapse. Finally, the intrinsic autofluorescence of human lung macrophages was examined in the context of STORM. The main findings of this investigation can be summarised as follows:

- M0-, M1- and M2-like macrophages display distinct morphologies and surface marker expression
- Human lung macrophages can be purified via adhesion from lung immune cell suspensions isolated from human lung resections
- All four cell types can be activated through their FcγRI with IgG-coated glass slides or IgG-containing lipid bilayers which induced the secretion of TNFα in a dose-dependent manner and cell spreading
- Natural autofluorescence of human lung macrophages peaks in the green and yellow channel and is weakest in the far red spectrum
- High laser powers used in STORM severely enhance autofluorescence which cannot be photobleached

3.4.2 Morphology and Phenotype of Macrophages

Macrophages from different tissues and origins display great phenotypical and functional diversity¹. To fully understand their biology, it is important to study macrophages with different phenotypic features. Therefore, four different macrophage types were investigated and compared in this project: M0-like, M1-like, M2-like and lung macrophages (Figure 3-1). M0-like, M1-like and M2-like macrophages were generated by culturing monocytes. After 8 days they displayed distinct morphologies

with M0-like macrophages spreading wide, M1-like macrophages being roundish and M2-like macrophages elongated (Figure 3-2). Indeed, macrophages are known to display different morphologies and several studies conclude that there is a link between morphology and phenotype^{260–262}. In fact, McWhorter and co-workers showed that the elongation itself induced the expression of M2 markers including arginase-1 and CD206 but not the M1 marker iNOS²⁶⁰. They used micropatterned substrates to control the cell geometry of bone marrow-derived mouse macrophages. They further showed that cell elongation enhanced the effects of the M2-cytokines IL-4/IL-13 while it hampered the effect of M1-inducing IFN γ /LPS. Rostam et al. developed an imaging assay that was able to identify human M1, M2 as well as naïve macrophages and monocytes with an accuracy of approximately 90% solely by analysing their morphology²⁶³. In addition, Rey-Giraud et al. showed that the morphology of monocyte-derived macrophages depended on the cytokine stimulation used²⁷⁰. Similar to results reported in this project, for cells differentiated in RPMI/10% FBS, they found a roundish cell shape when stimulated with GM-CSF and an elongated shape when stimulated with M-CSF. However, when they changed the media to X Vivo 10, this was reversed. This means, that in X Vivo 10 media, M1 macrophages displayed an elongated and M2 macrophages a roundish cell shape. Nevertheless, in RPMI/10% the M2 phenotype was connected to an elongated shape while M1 macrophages were more roundish. Thus, the morphologies observed for monocyte-derived macrophages are in accordance with the literature and indicate accurate differentiation of the macrophages.

Macrophage phenotypes also display distinct expression of surface molecules. However, due to the great diversity of macrophages, identifying clear phenotype markers is challenging. Oversimplified, the M1 phenotype is classically linked to expression of CD86, MHC class II and CD16 while M2 macrophages express high levels of CD163 and CD206^{59,61,261,266}. However, dependent on the differentiation and activation protocol, results vary. For example, Rey-Giraud et al. found similar levels of CD86 for expression between M1 (RPMI/10%FBS/GM-CSF) and M2 (RPMI/10%FBS/M-CSF) macrophages²⁷⁰. In the current project M1 marker CD86 was highly expressed in all three macrophage types though there was a different distribution for M0-like and

M1-like macrophages compared to M2-like macrophages. M0-like and M1-like macrophages displayed a broader range and slightly higher expression of CD86 than M2-like macrophages (Figure 3-4B, CD86-PE).

Further, M1 macrophages are known to express high levels of MHC class II²⁶⁶. This was true for data presented here, however, M0-like and M2-like macrophages expressed MHC class II in similar levels. In addition, Jaguin et al. found no difference of CD206 expression between M1 (RPMI/M-CSF/IFN γ /LPS) and M2 (RPMI/M-CSF/IL-4) macrophages⁷⁷. In the current project, M1-like as well as M2-like macrophages expressed high levels of CD206 while M0-like macrophages displayed only low levels (Figure 3-4B, CD206-FITC). In fact, M1-like macrophages expressed even more CD206 than M2-like macrophages. Similar results were found by Rey-Giraud and co-workers where M1 macrophages (RPMI/10%FBS/GM-CSF) expressed higher levels of CD206 than M2 macrophages (RPMI/10%FBS/M-CSF)²⁷⁰. They found that the absence of M2 marker CD163 in M1 macrophages was more reliable to identify M1/M2 subsets. This is in agreement with findings of the current project. Here, the scavenger receptor CD163 was found to be high in M2-like macrophages while M0- and M1-like macrophages were negative (Figure 3-4B, CD163-APC-Cy7). In addition they found that M2 macrophages express higher levels of CD16 which was also observed in the current project. These similarities are not surprising as macrophages were differentiated in the same way (and not activated).

This highlights how sensitive macrophages are to the differentiation protocol and that it is difficult to define a clear M1/M2 phenotype independent of the differentiation protocol used. Crucially it shows that macrophages studied in this project were successfully differentiated with all three macrophage types showing distinct expression of surface markers which are in accordance with the literature when differentiated in the same way.

Lung macrophages were not cultured but used fresh directly after isolation. Therefore, immune cells were isolated from the airways of lung tissue resections via perfusion. Due to macrophages being the most abundant cell type in the healthy lung, immune cell suspension is expected to mainly contain macrophages^{90,271}. In fact, macrophages consist of over 95% of all cells collected by bronchoalveolar lavage (BAL) in healthy individuals²⁶⁴. Yet, plating immune cell suspensions from lung resections onto tissue culture plates or PLL-coated glass slides revealed a contamination of macrophages, identified by their big size, with other, smaller cells (Figure 3-3, Before Wash). However, because lung macrophages are adherent cells it is common to purify them by adhesion²⁶⁵. Indeed, after 15 min of incubation and a single wash with PBS all small cells were removed and a clean macrophage population was left behind (Figure 3-3, After Wash). Notably, this was also true for PLL-coated glass slides despite the adherence promoting properties of PLL.

Taken together, four macrophage types were investigated in this project. Lung macrophages were used fresh, after isolation from lung tissue resection and could be purified via adhesion. M0-like, M1-like and M2-like macrophages were successfully differentiated from blood monocytes. M0-like macrophages did spread wide and expressed high levels of CD86 and MHC class II and low levels of CD163 and CD206. M1-like macrophages displayed a round morphology and expressed high levels of CD86, MHC class II while being negative for CD163. Surprisingly, they also expressed highest levels of CD206. M2-like macrophages had an elongated cell shape and expressed high levels of CD163 and CD206 as well as CD86 and MHC class II. They were the only cell type expressing CD163.

3.4.3 Model of the Phagocytic Synapse

When a macrophage encounters an opsonized target, it binds IgG with its FcγRI, which leads to cell activation and phagocytosis. This can be modelled by presenting IgG-coated surfaces to macrophages^{170,173,272}. Here, the application of TIRF microscopy allows the investigation of the contact between the surface (representing the opsonized target) and the macrophage. By applying STORM, the nano-scale organisation of this interphase can be studied⁵. Therefore, to establish an imaging system to study the phagocytic synapse of human macrophages interacting with opsonised targets, macrophages were incubated on IgG-coated glass slides or IgG-containing lipid bilayers, leading to the activation of the macrophages and cell spreading.

The chosen 2D-model of the phagocytic synapse is an excellent tool to study the nanoscale organisation within the membrane. However, it has to be kept in mind, that the process of phagocytosis is normally a 3D-process and therefore the chosen 2D-model has its limitations. In the 2D-model, the macrophage tries to phagocytose the coated glass slide. It is therefore likely that the macrophage spreads much wider than when phagocytosing a much smaller pathogen. This could influence the nanoscale organisation of molecules within the membrane. In addition, in the 2D-model the process of phagocytosis is 'never ending'. The macrophages keep trying to phagocytose the glass slide while in real phagocytosis the process 'ends' by internalising and degrading the pathogen. This again could influence the nanoscale organisation within the membrane. For example, it is likely that the nanoscale organisation within the membrane changes in a time dependent manner, e.g. once the particle is fully internalised. These time-sensitive changes, especially at later timepoints, may be lost in the chosen 2D-model. Nevertheless, the 2D-model is a great tool to study the initial contact of macrophages with opsonized targets and accompanying changes within the phagocytic synapse. Further, the model successfully activated the macrophages which led to the secretion of cytokines and cell spreading.

TNF α is a major pro-inflammatory cytokines produced by activated macrophages²⁶⁹. IL-10 on the other hand is a major anti-inflammatory cytokine, produced by macrophages and many other cell types^{273,274}. Upon activation, M1 macrophages are thought to secrete higher levels of TNF α while M2 macrophages secrete IL-10. Thus, to test the ability of IgG-coated surfaces to activate the macrophages and further characterise the different macrophage types, levels of TNF α and IL-10 were determined in supernatants of macrophages incubated overnight on IgG-containing surfaces. In the case of glass slides, the PLL-coating failed to induce the secretion of TNF α while all four macrophage types did secrete the cytokine in a dose dependent manner when coated with IgG (Figure 3-6A-B). The higher the IgG concentration was, the higher the amount of detected TNF α . Surprisingly, M2-like macrophages secreted the highest levels of TNF α . Lacey et al. investigated the cytokine secretion of human monocyte-derived M1 (RPMI/10%FBS/GM-CSF) and M2 (RPMI/10%FBS/M-CSF) macrophages with and without stimulation with LPS⁷⁹. When stimulated with LPS, both macrophages secreted TNF α with M1 macrophages secreting approximately three times more TNF α than M2 macrophages. Compared to the TNF α secretion detected in the current study, amounts were 10 – 30 times higher. In unstimulated conditions no TNF α was detected. These discrepancies likely are caused by the different stimulations of the macrophages (LPS vs. IgG-coating). Further, they detected high levels of IL-10 for M2 macrophages activated with LPS and lower levels for M1 macrophages. Interestingly, they also detected IL-10 secretion for M2 but not M1 macrophages in unstimulated conditions. M2-like macrophages in the current study also secreted high levels of IL-10 while all other cell types didn't secrete the cytokine (Figure 3-6C-D). Similar to glass slides, macrophages incubated on IgG-containing lipid bilayers secreted TNF α in a dose-dependent manner (Figure 3-9). However, TNF α levels were very low for M0-like macrophages and M1- and M2-like macrophages secreted relatively high levels in activated conditions. The latter could indicate the activation of the macrophages in non-activating conditions. Nevertheless, the amount of TNF α detected increased with the addition of IgG.

Overall, macrophages were successfully activated by IgG-coated surfaces. This led to the secretion of TNF α , and in the case of M2-like macrophages also IL-10, in a dose-dependent manner. Even though 1 μ g/mL IgG was sufficient to activate macrophages on glass slides, 10 μ g/mL was used for further experiments as it induced a more significant cytokine secretion. In addition, all four cell types significantly increased their cell size upon incubation on glass slides coated with 10 μ g/mL IgG (Figure 3-7). As cell spreading is a sign for activation, this confirms the successful activation of human macrophages on surfaces coated with 10 μ g/mL IgG.

3.4.4 The Natural Autofluorescence of Human Lung Macrophages

Imaging human lung macrophages is thought to be challenging, due to their high levels of intrinsic fluorescence. Indeed, the natural autofluorescence of human lung macrophages was observed and found to be brightest in the green channel (Figure 3-10). Therefore, unstained lung macrophages were excited at 470 nm and the emission spectrum was detected in seven 35 nm-wide windows starting at 480 nm and a 10 nm gap between detection windows (Figure 3-10A). The autofluorescent signal was highest in the detection windows 525 – 560 nm and 570 – 605 nm. This is in accordance with the literature. J.D. Edelson et al. identified already in 1985 the emission maximum of unstained alveolar macrophages at 541 nm with a shoulder at 580 nm¹⁰⁹. This was confirmed by Pauly and co-workers who imaged unstained touch imprints of lung tissue with emission maxima lying between 500 and 600 nm, when excited at 405 nm¹²⁹. They further showed that the intensity of autofluorescence depends highly on the donor's smoking history, with current smokers emitting approximately 4 times higher intensities than ex- or never smokers. Tobacco tar has long been discussed as source of autofluorescence in human lung macrophages. In fact, Pauly et al. showed that lung macrophages incubated with human serum treated with cigarette smoke displayed similar emissions to those by lung macrophages derived from a current smoker¹²⁹. In addition, the fluorescence spectra of autofluorescent lung macrophages has been shown to match that of tobacco tar elements^{129,132,133}. In addition, sections of unstained lung macrophages showed that autofluorescence originates from cytoplasmic inclusion

bodies with levels of autofluorescence being retained in long-term culture^{129,132}. This paints a picture of macrophages patrolling the airways taking up autofluorescent particles and storing them long-term within the cell which is exaggerated in smoking individuals, leading to high autofluorescence, originating from cytoplasmic inclusion bodies.

Acquired 3D-stacks of unstained lung macrophages support this theory (Figure 3-10B). Particles taken up by the macrophage may be stored in vacuoles inside the cell for a long time, if the material cannot be degraded easily. In 1994, Streck and co-workers cultured lung macrophages after isolation for over 6 weeks and reported retained levels of autofluorescence throughout, further showing the longevity of autofluorescence¹³². They also present laser-generated optical sections of living lung macrophages, displaying vesicular structures inside the cell with similar appearance than acquired 3D-stacks. This has been confirmed by Pauly and co-workers in 2005¹²⁹. They as well optically sectioned live lung macrophages and imaged isolated sections, displaying circular structures throughout the cell. These cytoplasmic inclusion bodies were retained in long-term culture (>10 days). With autofluorescence seemingly originating from vacuoles within the cell, this could give hope of little interference of autofluorescence with TIRF microscopy and therefore STORM (which is operated in TIRF mode). In TIRF, the sample is only illuminated within 150 – 200 nm from the glass slide. Therefore, most of the cell is not excited. It was thus surprising that STORM of lung macrophages was severely impaired by autofluorescence (Figure 3-12).

Nevertheless, other sources for autofluorescence were reported. Different cellular components and metabolites including flavins, nicotinamide-adenine dinucleotide (NAD), aromatic amino acids and collagen are known to emit intrinsic natural fluorescence^{114,115,275}. Flavins and NAD are most intensively studied as they are thought to be responsible for most of the cytoplasmic autofluorescence. However, autofluorescence from these compounds normally shows a low quantum yield which does not correspond to observations made with lung macrophages¹¹⁷. In fact, when

imaging stained lung macrophages using STORM, autofluorescence greatly distorted the signal (Figure 3-12). More precisely, data sets of lung macrophages displayed regions or spots of high autofluorescence which saturated the signal of the exogenous marker. The fact that autofluorescence is displayed in spots rather than across the whole membrane may also correspond to autofluorescence originating from inclusion bodies. They could still be excited if they are at close proximity to the imaged cell membrane. This leads to the saturation of the signal, making the detection of the fluorescence emitted by the exogenous marker impossible, leaving blank areas in the reconstructed, filtered STORM image (Figure 3-12B). This highlights the need to accurately correct for unwanted autofluorescence signal.

Different possible solutions for the problem of autofluorescence have been proposed in the past. The simplest of all solutions discussed in the literature is to avoid the spectral region where autofluorescence occurs¹⁰⁹. However, this does not take into account that autofluorescence of lung macrophages covers nearly the whole visible range (Figure 3-10B-C)¹²⁹. In addition, many techniques rely on commercially available fluorophores which binds the researcher to work in a specific spectral range. STORM for example depends highly on the fluorophore used and its blinking characteristics. More precisely, AF647 yielded best results for single colour STORM and was thus chosen for all STORM imaging in this project. In addition, autofluorescence proved to be lowest in the red spectrum (Figure 3-10B-C). Nevertheless, the autofluorescence of lung macrophages severely interfered with the spectra of AF647, demanding a different correction method.

Another potential solution discussed in the literature is to photobleach samples prior to fluorescent staining. Kumar and co-workers irradiated formalin fixed paraffin embedded human lung tissue for 15 min with a mercury arc lamp at 20 cm distance in combination with fluotar objective 40X (NA 0.70) and observed a reduction of tissues autofluorescence of almost 80%¹⁴⁴. Similar results were achieved when photobleaching autofluorescent slide-mounted human brain tissue sections with white light emitting

diode (LED) array for up to 48h¹⁴⁵. However, bleaching single cells was less successful^{129,133}. Indeed, the attempt to photobleach lung macrophages at 488 nm with 100 % laser power for approximately 45 min failed (Figure 3-14). Autofluorescence dropped in the first 5 min, quickly reaching a plateau with some cells' autofluorescence increasing again with time. This highlights that lung macrophages obtained in this project are not photobleachable.

Chemical quenching has been reported to significantly reduce autofluorescence of lung macrophages enabling flow cytometry analysis^{146–149}. Here, fixed and permeabilized cells were treated with dyes like crystal violet or trypan blue prior to staining to quench intracellular autofluorescence. However, this has been mainly described for flow cytometry rather than microscopy. In addition, it has to be kept in mind that flow cytometry operates with lower laser powers than STORM, making it more difficult to achieve similar quenching effects.

As STORM is a computational heavy technique, background may be corrected digitally after acquisition. Most simply, the autofluorescent signal could be recorded at a different wavelength than the extrinsic marker used to stain the sample and subtracted¹⁵¹. However, the autofluorescence of one cell was found to vary at different wavelength, potentially leading to the subtraction of either 'too much' or 'not enough' background (Figure 3-10). More precisely, STORM samples were stained with AF647, leaving the green and yellow channel to record the autofluorescent signal, as the microscope used for this project had 3 lasers available (488 nm, 532 nm and 647 nm). However, autofluorescence was found to be highest in these channels (Figure 3-10B-C). Therefore, this may led to over correction and subtraction of 'real' signal. Nevertheless, the autofluorescent signal in STORM is distinct from that of extrinsic fluorophores in that it constantly emits light while extrinsic fluorophores blink on and off (Figure 3-12A). This was exploited for developing a novel background correction technique.

In summary, autofluorescence of lung macrophages was brightest in the green and yellow spectral range. It seemed to originate from inclusion bodies inside the cell which severely interfered with STORM. The signal saturated that of extrinsic markers, leaving big blank areas in the reconstructed STORM image. Autofluorescence could not be photobleached, nor the spectral range avoided. As most lung tissues used in this chapter are derived from smoking donors (14 out of 18 were current smokers (Table 3-1)), where autofluorescence is exacerbated, the need for a reliable correction technique arises.

3.4.5 Conclusions

In summary, the results indicate that M0-like, M1-like and M2-like macrophages were successfully generated by culturing blood monocytes. In agreement with the literature, they displayed distinct morphologies with M0-like macrophages spreading wide, M1-like macrophages being round and M2-like macrophages being elongated. All three cell types expressed high levels of MHC class II and CD86 while only M2-like macrophages expressed CD163 and only M0-like macrophages expressed low levels of CD206. Lung macrophages were used fresh upon isolation from the lung tissue and purified by adhesion. The activation of macrophages on IgG-coated surfaces led to increased cell spreading and the secretion of TNF α in a dose dependent manner. Only M2-like macrophages also secreted IL-10. Imaging human lung macrophages showed that their intrinsic autofluorescence originated from cytoplasmic inclusion bodies and covered a broad range of the visible spectrum, peaking in the green and yellow channel. It severely interfered with STORM, making the investigation of lung macrophages impossible. Therefore, the next chapter will focus on a novel background correction technique that enables the application of STORM for autofluorescent samples like human lung macrophages.

Chapter 4 – Establishment of a novel background correction technique to study the nanoscale organisation of the membrane of human lung macrophages

4.1 Introduction

Our understanding of biological processes that occur in cells is widely built up on direct visualization of these processes using different microscopy techniques. In recent years, several new techniques that can overcome Abbe's diffraction limit were developed and provide tools with which to gain new insights on nanoscale processes that happen in cells²⁷⁶. They helped to establish that many receptor molecules organise in distinct nanoclusters on the surface of immune cells and that their organisation impacts signal integration as well as cellular activation^{139,277–280}. For example, Lopes et al. studied the nanometer-dynamics of inhibitory receptor SIRP α and activating receptor Fc γ RI on the surface of macrophages, showing their segregation upon activation⁵. These results underline the importance of studying the nanoscale organisation of the immune cell membrane – helping us to better understand how immune cells communicate.

Macrophages display a large repertoire of membrane receptors, playing a key role in initiating and coordinating immune responses. Thus, it is especially important to understand the nanoscale dynamics of macrophage cell surface receptors. In addition, macrophages are highly plastic, with their phenotype strongly depending on their surroundings, highlighting the need to study macrophages derived from different tissues^{2,47,90}. Lung macrophages constitute for example the most abundant immune cell type in the healthy lung. Here, they are key players in regulating homeostasis as well as inflammation and are the primary cell type to encounter pathogens^{281,282}. They play a vital role in presenting antigens to T cells, thereby activating the adaptive immune system^{283,284}. In this process, the antigen is taken up by the macrophage, broken down into small peptides and presented to T cells on MHC molecules^{285–289}. T cell and

macrophage form a tight synapse, where adhesion and receptor molecules rapidly rearrange, which directly links to function²⁹⁰. This highlights the importance of understanding the nanometer-scale organisation of membrane molecules, including MHC molecules.

Another way of communication, rather than engaging receptors through cell-cell contact or soluble factors, is the transfer of information through extracellular vesicles (EVs)¹⁷⁹. They are released by all cells and vary in size (30 – 2000 nm in diameter), composition and function^{183,291}. Interestingly, EVs derived from pulmonary structural and immune cells were found to play a role in lung diseases^{292–295}. For example, EVs derived from lung epithelial cells were shown to activate macrophages *in vitro* and promote inflammation *in vivo*, with increased amount immunomodulatory cells detected in the bronchoalveolar lavage fluid (BALF)²⁹⁶. Usually, vesicles are studied in bulk, after isolation. However, the isolation process is harsh and comes with many caveats^{187,297,298}. Isolation of vesicles using ultracentrifugation for example goes in hand with co-purification of non EV-associated proteins, including protein aggregates and lipoproteins^{186,187}. Nevertheless, ultracentrifugation is the most applied isolation process, according to a research market analysis by GenReports. Here, over 56% of users in the field described ultracentrifugation as the gold standard for EV isolation¹⁸⁵. It is thus vital, to find a better way of studying EVs, especially without the isolation process. Here, STORM offers the opportunity to study vesicles directly upon secretion, allowing analysis on a cell-by-cell basis and in a near native state.

Despite their importance, very little studies imaged tissue-derived human macrophages, which are highly autofluorescent. High laser powers used in STORM proved to be especially potent to bring forth autofluorescence, making an investigation by STORM challenging. Yet, the nanoscale investigation of receptor molecules on tissue-derived cells like human lung macrophages is greatly needed. It is thus vital, to improve super-resolution imaging techniques for autofluorescent samples, like human lung macrophages.

Here, we hypothesised that the high autofluorescence of lung macrophages could be corrected post acquisition by estimating and subtracting the background. Therefore, this chapter aimed to develop a background correction technique that enables STORM of human lung macrophages followed by rigours testing and application. Finally, this allowed the investigation of MHC class I as well as the vesicle marker CD81 on a nanometre-scale at the membrane of human lung macrophages.

4.2 Summary of Chapter Aims

- a) Development of a background correction technique to correct for autofluorescence of human lung macrophages in STORM
- b) Detailed validation of background correction technique with simulated and acquired data
- c) Investigation of MHC I and CD81 in the membrane of lung macrophages made possible by application of the background correction technique

4.3 Results

4.3.1 Background Correction Technique

Imaging human lung macrophages in STORM proved to be challenging. The high laser powers applied in STORM especially brought forth the autofluorescent signal that was not photo-bleachable. Therefore, a background correction technique was developed that utilises post-acquisition analysis to address the problem of autofluorescence. The correction technique takes advantage of the fact that the signal intensity of autofluorescence is high and constant while fluorophores blink. The principle of this technique is illustrated in Figure 4-1. A STORM image is built up from blinking events occurring at different time points (or in different frames). The autofluorescence signal on the other hand is constant over many frames. Thus, in regions of autofluorescence, where high intensities of light are continuously emitted, the median intensity will be similar to the autofluorescence itself. In contrast, a blink is detected only for a short amount of time (or only in few frames) and the fluorescence of this will increase the pixel intensity beyond the autofluorescence signal. Therefore, determining the median intensity of each pixel in the stack (that consists of several thousand frames which in total give rise to the final STORM image) and subtracting this value afterwards yields a 'cleaned' stack which can be analysed as usual.

With 1 frame being recorded every 11 ms, it takes approximately 2 min to acquire 10000 frames. Within this time, the intensity of autofluorescence drops and reaches a constant level afterwards (Figure 3-14). To account for this, the median intensity is determined for every n frames of the original stack rather than the whole stack. In the example of 10000 original frames and a group size of $n = 200$ frames this yields 50 median intensity frames with decreasing intensity. Then, in order to be able to subtract these median intensity frames from the original stack they have to be expanded to the same number of frames as the original stack. Thus, each median intensity frame is multiplied by n (here 200). A bicubic interpolation is applied for the expansion which means the new frames smoothly transition between each other. This means, the intensity of the median intensity frames is dropping continuously rather than stepwise.

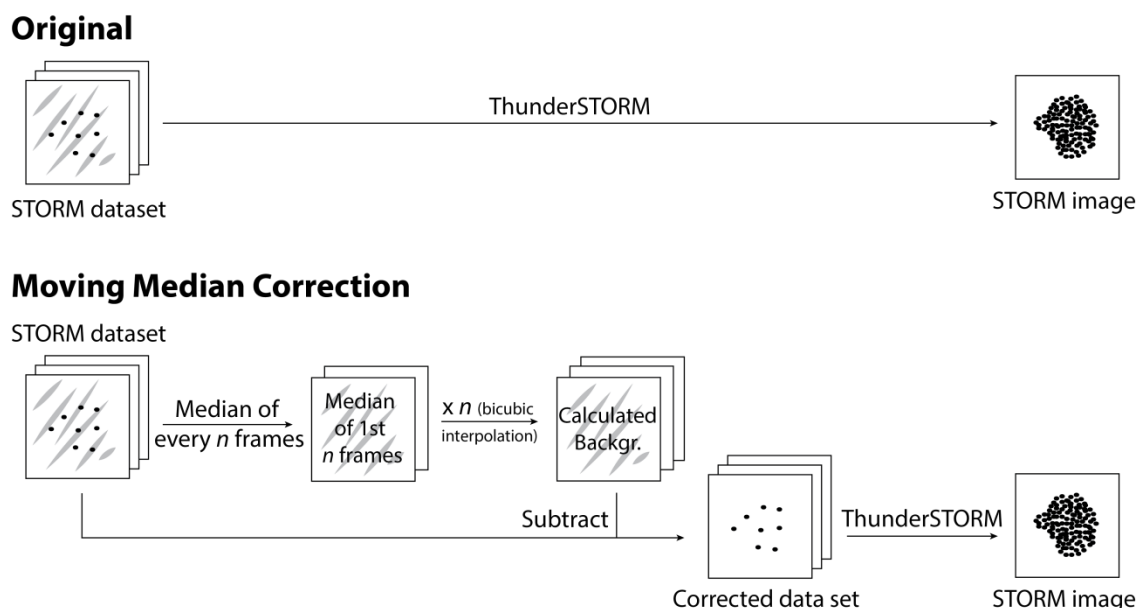


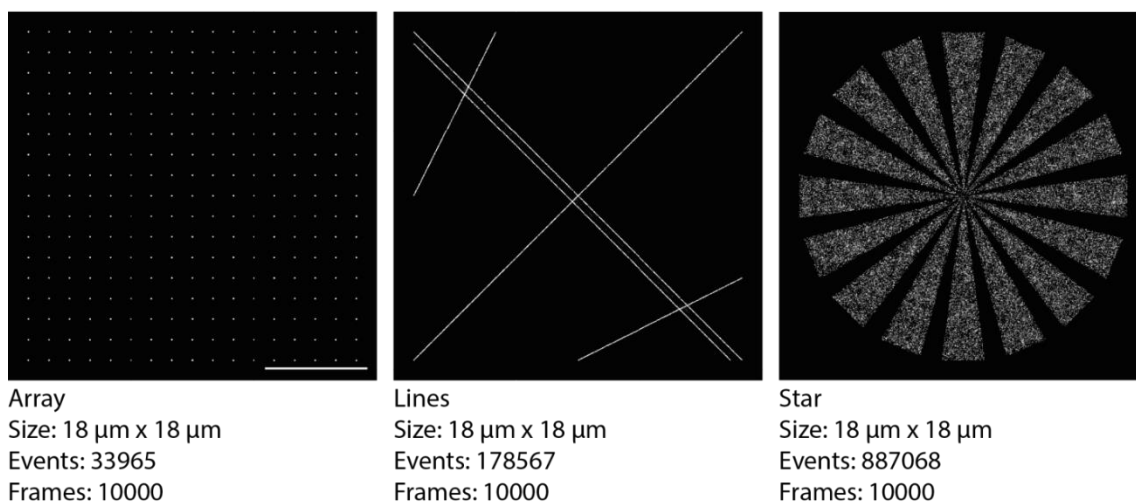
Figure 4-1: Principle of background correction technique. The median fluorescence intensity of every n frames of the originally recorded stack is determined and expanded to the same number of frames as the original stack applying a bicubic interpolation. Subtraction from the original yields a corrected set of stacks that can be processed as usual using the ThunderSTORM software.

4.3.2 Validation of Background Correction Technique

4.3.2.1 Simulated Data

In order to validate the performance of the designed background correction technique, simulated data was used. In total, 3 different ground truths and 4 different backgrounds were simulated. Ground truths were simulated using TestSTORM, an open-source plugin for MatLab²⁵². These STORM data sets contained uniform blinks with known localisations in the resulting picture. Simulated backgrounds were generated using FIJI with different shapes presenting different challenges to the correction technique (Figure 4-2, i-iv). Both, background and STORM data sets were 18 x 18 μm in size and consisted of 10000 frames.

Simulated Ground Truths



Simulated Backgrounds

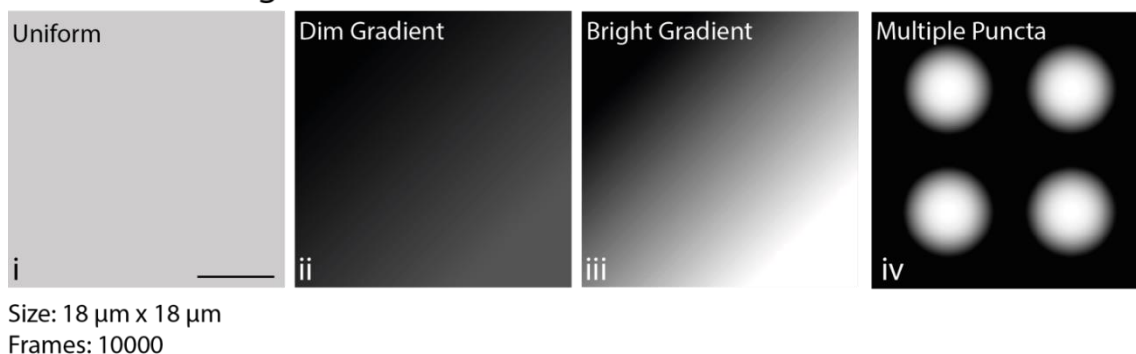


Figure 4-2: Overview of simulated data used to validate the background correction technique. 3 different ground truths were simulated using TestSTORM²⁵² yielding STORM data sets with uniform blinks and known localisations in the resulting STORM image. Shown are the reconstructed STORM images (top) with according parameters. Scale bar 5 μm . Simulated backgrounds were generated using FIJI. Shown is the first frame of a 10000-frame strong data set of identical images of each background data set (bottom).

To ensure that the simulated ground truths are comparable to normal, acquired STORM data sets, blink characteristics were analysed and compared (Figure 4-3). Therefore, a single frame of each data set was chosen randomly and the intensity profile of individual localisations was determined. This was compared to an acquired data set where blood-derived macrophages were plated onto PLL-coated slides for 15 min at 37°C, fixed and stained with anti-human MHC class I mAb conjugated with AF647. As can be seen in Figure 4-3A, the size of the simulated blinks matched those of recorded localisations very well. All line profiles of 1 μm length show the intensity profile of the

blinks which peak at about 0.5 μm . As expected, actual data was noisier than simulated one, resulting in a higher base level of fluorescence intensity. Thus, line profiles of simulated data started at about 200 AU while acquired data started at about 700 AU. To better compare the intensity profiles regardless of the background noise, the peak heights were calculated (Figure 4-3B). Here, example blinks in the ground truths Array and Lines showed similar peak heights than dim blinks of the acquired data while Star intensities matched with bright blinks. However, these were only example localisations, randomly chosen. To compare the whole data sets, intensities of all pixels from all frames were measured and the histograms are shown in Figure 4-3C. Confirming observations from single frames, Array and Lines pixels had their base level at approximately 200 AU and high signals at approximately 700 – 800 AU while pixel intensities of Star ranged from 0 to over 3800 AU. The recorded data set of monocyte-derived macrophages had their base level at approximately 350 AU and high values ranged from 700 to over 1540 AU. This demonstrated that the three simulated ground truths reflect the natural variety of signals observed in actual data sets. They are thus suitable comparison data sets.

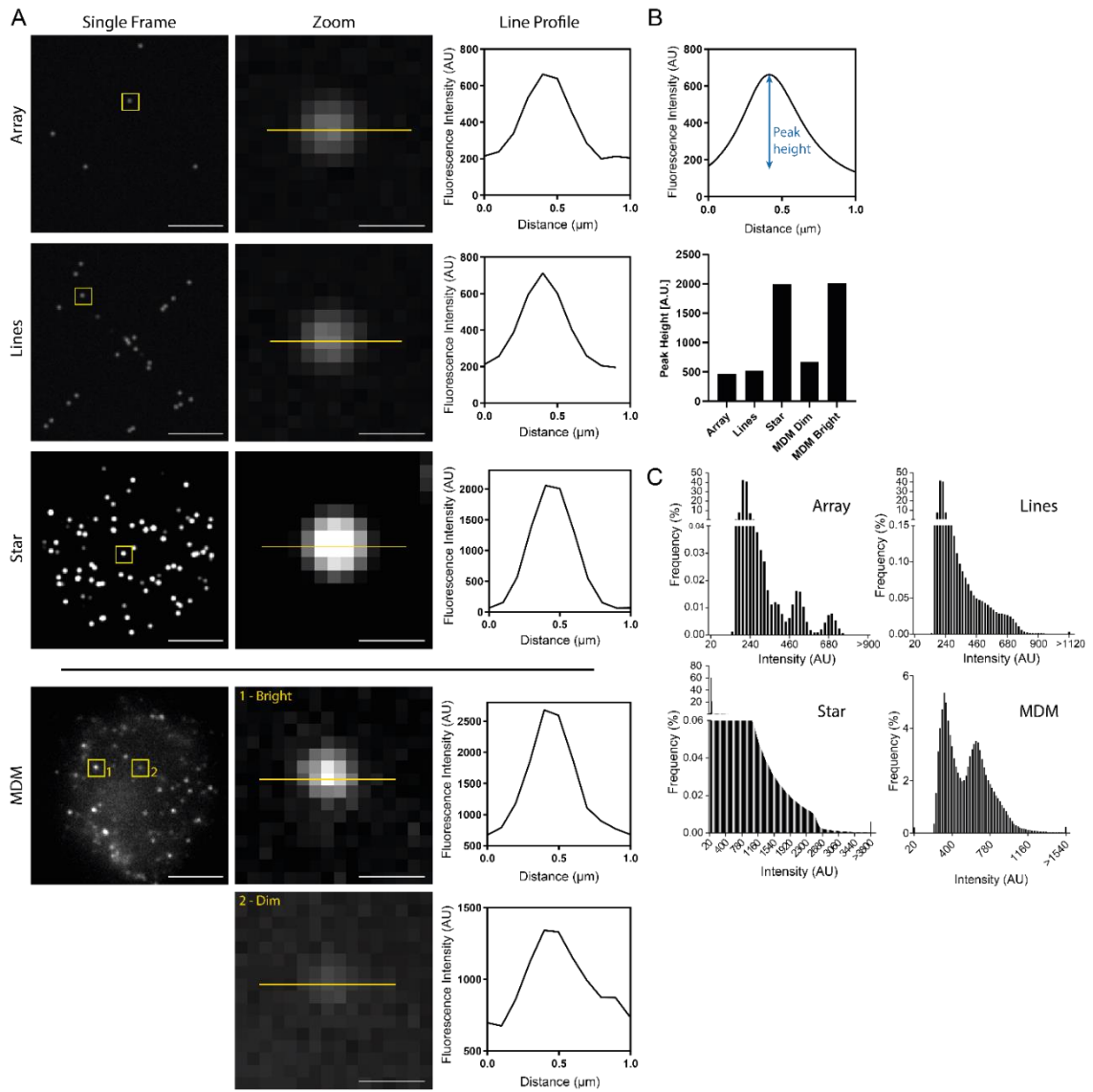


Figure 4-3: Intensity profiles of simulated ground truth and acquired data. A) Single frame, zoom and line profile of simulated ground truth (Array, Lines, Star) or an acquired data set (monocyte-derived macrophages; MDM). For the latter, human monocyte-derived macrophages were plated onto PLL coated microscopy slides for 15 min at 37°C, fixed and stained with anti-human MHC class I mAb conjugated with AF647. Scale bars 5 μm and 0.5 μm (Zoom). **B)** Schematic of the peak height (top). Calculated peak heights of line profiles shown in A (bottom). **C)** Histograms of intensities of all pixels from each data set (10,000 frames).

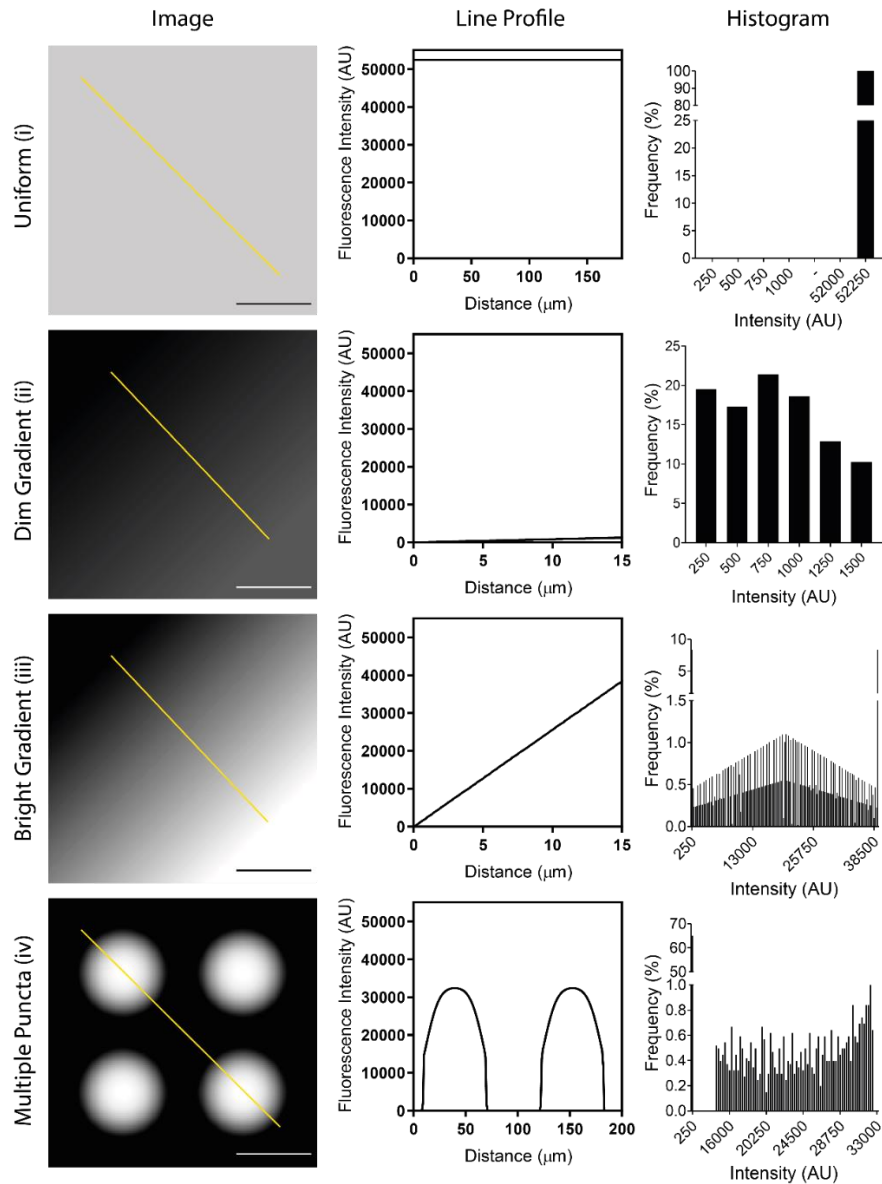


Figure 4-4: Intensity profiles of simulated backgrounds. Images (single frame; left), line profiles (middle) and intensity histograms of the whole stack (10000 identical frames; right) of the 4 different simulated backgrounds. Scale bars 5 μm .

Further, the characteristics of the simulated backgrounds were assessed. Figure 4-4 shows their intensity profiles. As can be seen in the line profiles, the intensities varied greatly in relation to their absolute values but also their trajectory. While Uniform had the highest intensity value (52428 AU), the intensity in all other backgrounds varied regarding to position. The Dim Gradient had much lower intensities (highest point 1304 AU) compared to the other backgrounds. Histograms of intensities of all pixels and all frames confirmed these observations with the Uniform background

displaying only one very intense signal while other backgrounds had an array of intensities with the Dim Gradient covering much smaller numbers.

Next, signal intensities of ground truths and backgrounds were directly compared. For backgrounds, the mean intensity of the whole image was measured, whereas for ground truths, the mean intensity of 100 – 150 blinks was determined. All backgrounds apart from Dim Gradient were much brighter than localisations in simulated data (Figure 4-5). This is also reflected in the histograms in Figure 4-3 and Figure 4-4. Here, all backgrounds apart from Dim Gradient displayed intensities over 30000 AU (Figure 4-4 Histogram) while high ground truth values reach approximately 1000 - 3000 AU (Figure 4-3C). The high background values represent a desired challenge as they will show if the designed background correction technique is capable of correcting severe backgrounds.

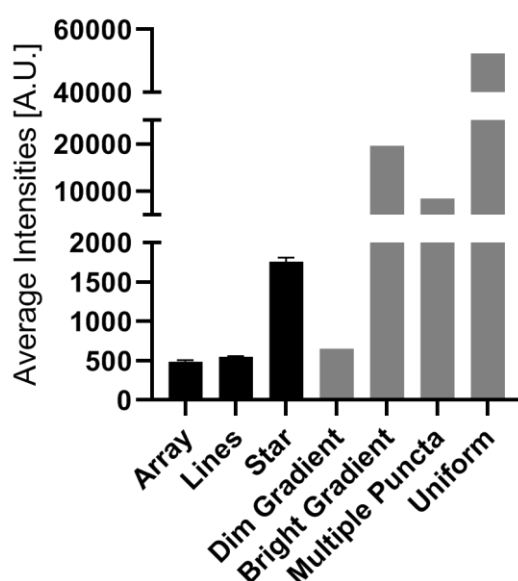


Figure 4-5: Comparing intensities of simulated ground truths and backgrounds. Black columns show the mean intensity of 100 - 150 localisations from ground truth data sets. Error bars; \pm SD. Grey columns show mean intensity of the whole background image.

4.3.2.2 Correcting Simulated Data

To test the performance of the correction technique, the 4 simulated backgrounds and the 3 simulated ground truths were combined (every possible combination; $n = 12$) to form ‘dirty’ data sets; in the following labelled ‘No Correction’. Combined data sets were corrected using the described background correction method and a group size of $n = 200$; in the following referred to as ‘Corrected’. The corrected stack (consistent of 10000 corrected frames) was then analysed in ThunderSTORM, yielding a reconstructed STORM image and compared to the ground truth image.

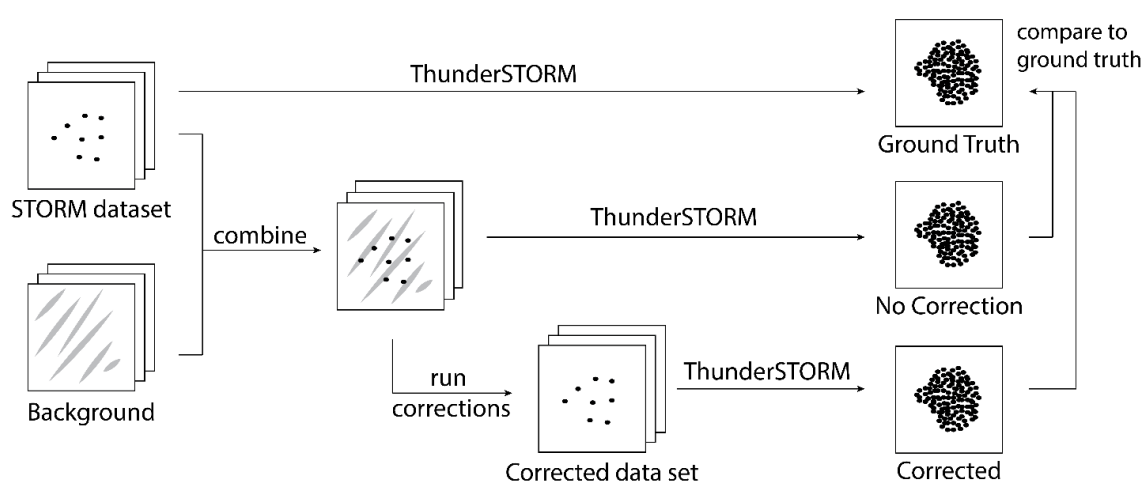


Figure 4-6: Principle of the validation of the correction technique. A perfectly ‘clean’ simulated STORM data set was combined with simulated background to form a ‘dirty’ STORM data set. The combined stack was either directly reconstructed or corrected using the described background correction method and then reconstructed in ThunderSTORM yielding the final STORM images “No Correction” and “Corrected” respectively. Comparison of corrected and not corrected STORM image to the ground truth was used to validate the performance of the correction technique.

Several parameters were measured before and after correction in order to evaluate the performance of the correction method; all in relation to the ground truth: the percentage of events detected, coordinate based co-localisation (CBC), nearest neighbour distance (NND), Manders overlap and Pearsons correlation coefficient. CBC and Pearsons correlation coefficient have a value of 1 for perfect co-localisation and -1 for complete separation. Manders overlap coefficient ranges from 1 for perfect overlap to 0 for no overlap.

As can be seen in Table 4-1, the different simulated backgrounds have different effects on the ground truths (No Correction). Surprisingly, even so the Uniform background (i) had the highest intensity values; much higher than simulated localisations (Figure 4-5), it had very little effect on the simulated ground truth image. The Dim Gradient (ii) on the other hand had much lower intensities but caused more severe problems. This suggests that image filtering included in ThunderSTORM can identify and subtract uniform backgrounds while it struggles to remove structured backgrounds.

However, the intensity of the background still played a role. This is demonstrated with the Bright Gradient (iii) that differed from the Dim Gradient only in intensity. While 99.7% of events were detected for the Dim Gradient, not even one third of events were detected for the Bright Gradient. In addition, CBC dropped from 0.96 ± 0.03 to 0.44 ± 0.43 and NND increased from 0.48 ± 0.30 nm to 11.09 ± 9.16 nm. Manders and Pearsons coefficients also decreased from 0.95 ± 0.04 and 0.80 ± 0.09 to 0.73 ± 0.22 and 0.61 ± 0.53 respectively.

The highest impact however had the Multiple Puncta (iv). Here, basically no events were detected ($0.5 \pm 0.8\%$), CBC is lowered to 0.40 ± 0.55 while NND increased to 22.40 ± 35.80 nm and Manders and Pearsons co-efficient were 0.65 ± 0.56 and -0.10 ± 0.16 respectively. This highlighted the fact that standard processing with ThunderSTORM is sufficient to remove uniform but not complex backgrounds. In summary, the intensity values as well as the structure of the background influenced the quality of the reconstructed STORM image and were not sufficiently accounted for by ThunderSTORM.

When correcting the combined data sets, the reconstruction of STORM images was much improved, resulting in increased event detection ($100.6 \pm 0.9\%$), higher CBC (0.99 ± 0.01), Manders (1.00 ± 0.001) and Pearsons coefficients (0.99 ± 0.01) as well as reduced NND (0.20 ± 0.06 nm), in the case of Multiple Puncta (Table 4-1, Corrected, iv).

It is surprising that corrected parameter have the same mean values for all 4 backgrounds, though their errors differ marginally (not shown). However, differences between data sets even out as each value represents the mean value of all 3 ground truths. In addition, backgrounds are constant over time meaning the stack of one background consists of 10000 identical images. Thus, it is likely that the correction method has the same ability to detect the background in all cases, resulting in very similar mean values.

Table 4-1: Removing simulated backgrounds from simulated SMLM data. Simulated backgrounds (Figure 4-2, i – iv; and Figure 4-4) were combined with the 3 simulated ground truths (Figure 4-2, top) and corrected or not (No Correction) before processing in ThunderSTORM, yielding the final STORM images. The latter were assessed relative to the ground truth for percentage of detected events, coordinate based co-localisation (CBC), nearest neighbour distance (NND), Manders overlap and Pearsons correlation coefficient. Each value is the mean value of the 3 ground truths combined with indicated background.

	Backgr.	% events	CBC	NND [nm]	Manders Co-efficient	Pearsons Co-efficient
Ground Truth	-	100.0	1.00	0.00	1.00	1.00
No Corrections	i	99.8	0.98	0.18	1.00	0.99
	ii	99.7	0.96	0.48	0.95	0.80
	iii	29.8	0.44	11.09	0.73	0.61
	iv	0.5	0.40	22.40	0.65	-0.10
Moving Median	i	100.6	0.99	0.20	1.00	0.99
	ii	100.6	0.99	0.20	1.00	0.99
	iii	100.6	0.99	0.20	1.00	0.99
	iv	100.6	0.99	0.20	1.00	0.99

100% / 0 nm

90% / 10 nm

Percentage of Grund Truth / Neares Neighbour Distance

4.3.2.3 Correcting Ground Truth Images with no Background

Within a series of experiments, all images should be processed in the same way, in order to be comparable. However, backgrounds may vary greatly from image to image, as it is the case for autofluorescence (Figure 3-13). Therefore, a correction method needs to be able to identify unwanted background but not interfere with the actual signal in case of low background noise. To test this, we corrected ground truth images without adding any background. The reconstructed images were compared to the ground truth without correction (Figure 4-7A).

There was no optical difference between ground truth and corrected image and line profiles match perfectly (Figure 4-7B). When assessing images quantitatively, only very subtle differences were found. The percentage of events and mean NND were increased to $100.6 \pm 0.9\%$ and 2.02 ± 0.57 nm while the mean CBC, Manders and Pearsons co-efficient decreased slightly to 0.99 ± 0.01 , 1.00 ± 0.01 and 0.99 ± 0.001 respectively. This shows that the background correction is not detrimental to data sets without background and is thus suitable for application to all images.

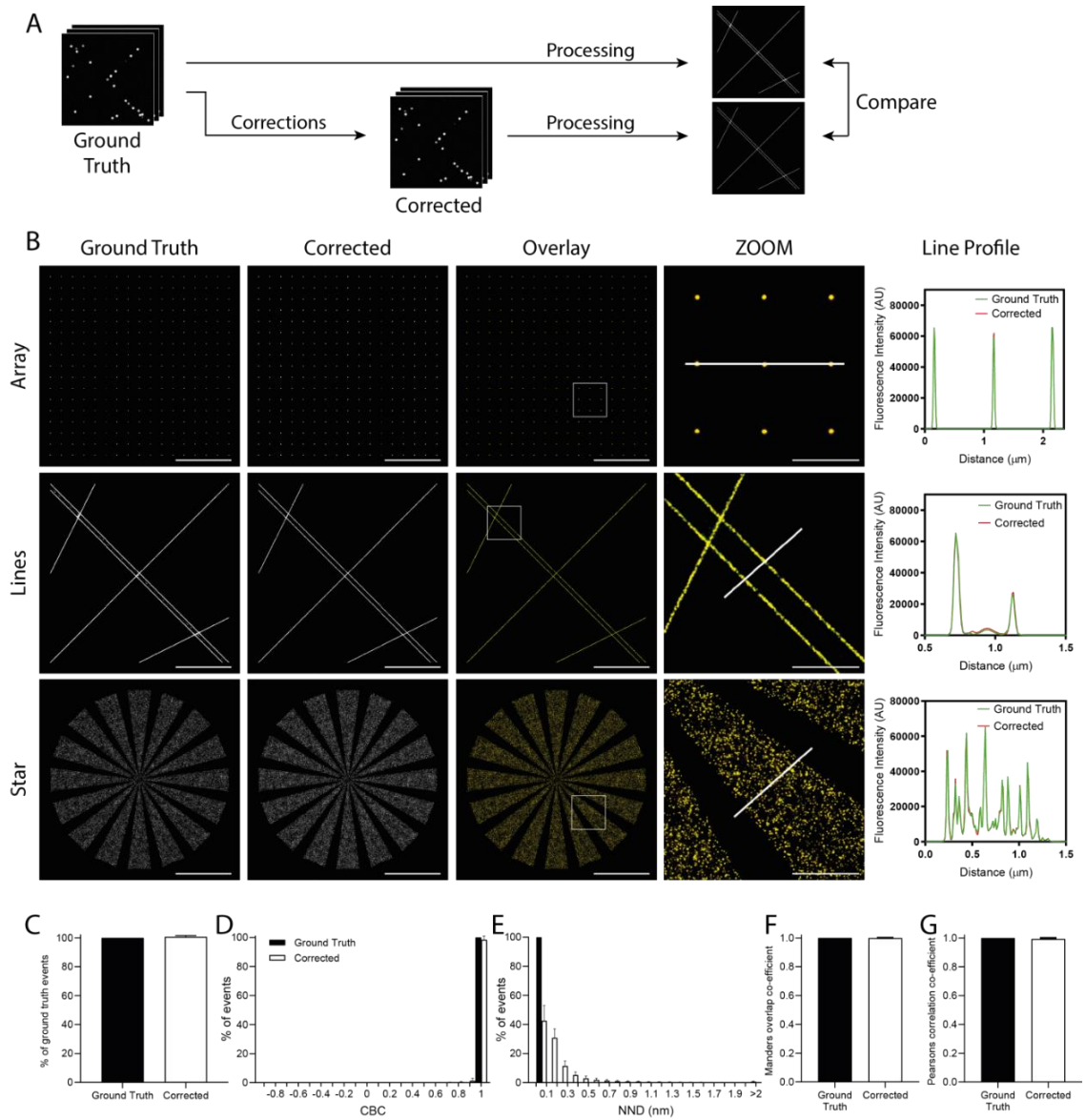


Figure 4-7: Correction method does not aggravate data sets without background. **A)** Ground truth data sets were corrected or not and processed using ThunderSTORM. Reconstructed images were compared. **B)** STORM images of ground truths (without correction) and corrected data sets, overlay, zoom ($3 \times 3 \mu\text{m}$) and corresponding line profiles. Scale bars: $5 \mu\text{m}$ and $1 \mu\text{m}$ (zoom). **C-G)** Quantification of reconstructed images shown in **B)** relative to uncorrected ground truth images. **C)** Number of events detected. **D)** Coordinate based co-localisation (CBC). **E)** Nearest neighbour distance (NND). **F)** Manders overlap coefficient. **G)** Pearson's correlation coefficient. Error bars; $\pm\text{SD}$.

4.3.2.4 Constant Background

To test the ability of the background correction technique to remove constant simulated background, the Star ground truth was combined with the Bright Gradient background. Corrected and not corrected data sets were processed (in ThunderSTORM) and compared to the ground truth. The background data set Bright Gradient consisted of 10000 identical images representing a background with constant intensity (Figure 4-8A). The addition of the background to the ground truth data set had severe impact on the original data set as single frames demonstrate (Figure 4-8C, Single Frame). Dim events were entirely lost when the background was added (No Correction) while the corrected data set was optically identical to the ground truth data set. The effect of the background was also visible in the reconstructed STORM image which was especially distorted where the gradient was highest. Upon correction, the image was nearly perfectly restored. The percentage of events relative to the ground truth increased from 46.8% to 99.7% (Figure 4-8D). The mean CBC increased from 0.002 to 0.97 (Figure 4-8E) and the NND decreased from 4.38 nm to 0.22 nm (Figure 4-8F). In addition, Manders overlap and Pearsons correlation coefficients increased from 0.82 to 1.00 (Figure 4-8G) and 0.001 to 0.99 (Figure 4-8H). This showed that the moving median correction was able to correct for simulated, constant backgrounds where ThunderSTORM failed to do so.

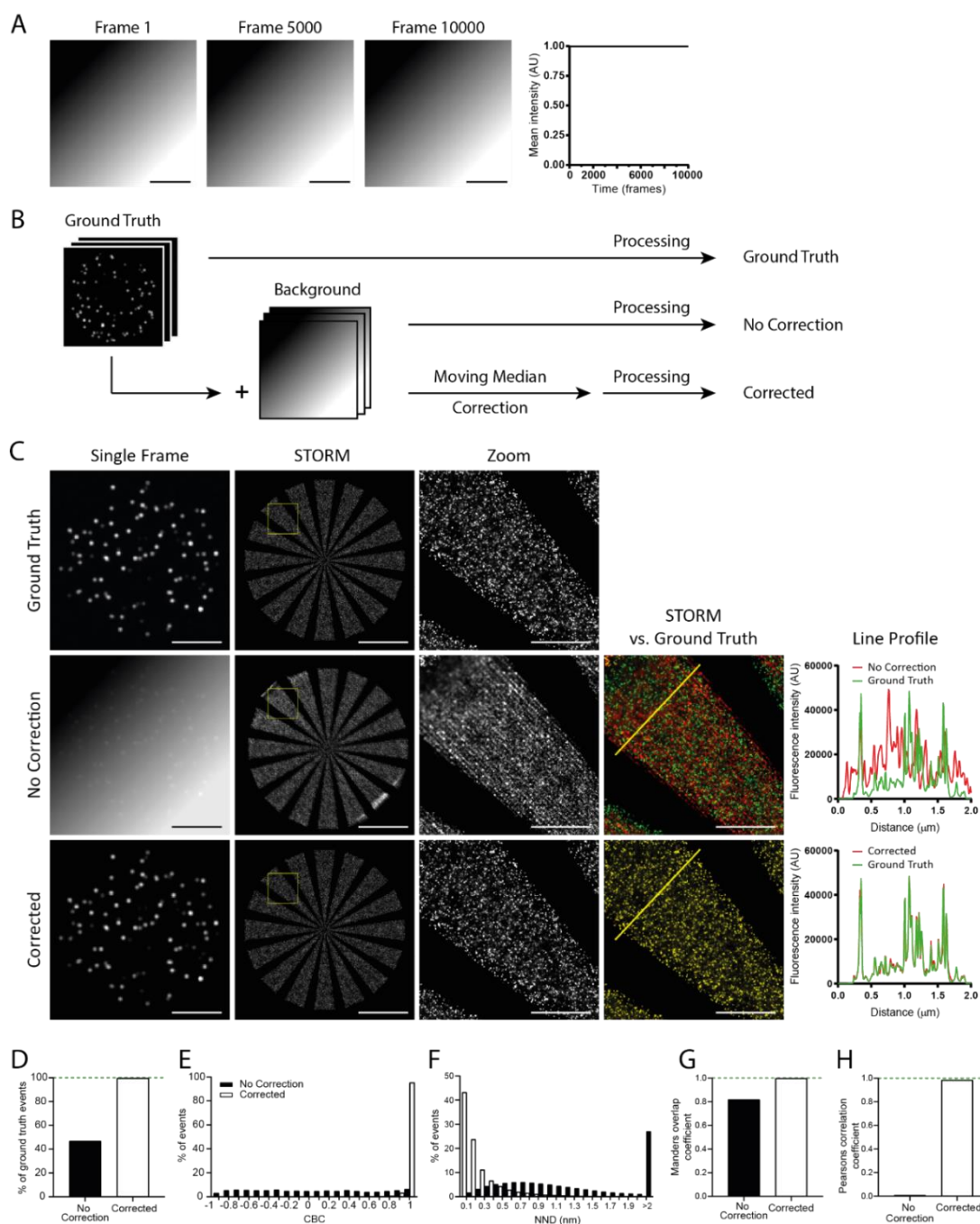


Figure 4-8: Moving median correction prior to image processing successfully corrects simulated, constant backgrounds. **A)** Frame 1, 5000 and 10000 of simulated background Bright Gradient and intensity profile of all frames. **B)** The simulated ground truth data set Star was combined or not with the Bright Gradient background data set. The combined data set was either corrected or not and reconstructed STORM images were assessed relative to the ground truth. **C)** Single frame, STORM image, zoom (3 x 3 μm) and overlay (vs. ground truth) with line profiles shown from the ground truth, not corrected and corrected data. Scale bars: 5 μm and 1 μm (Zoom). **D-H)** Quantification of reconstructed images shown in B) relative to ground truth, shown in green. **D)** Number of events detected. **E)** Coordinate based co-localisation (CBC). **F)** Nearest neighbour distance (NND). **G)** Manders overlap coefficient. **H)** Pearson's correlation coefficient.

4.3.2.5 Linearly Decaying Background

So far, the correction method was only challenged with constant backgrounds. This means that background stacks consisted of 10000 identical images which were added to the simulated ground truth data sets (Figure 4-8A). However, real backgrounds may decay over time. Therefore, the 4 simulated backgrounds (Figure 4-2, i - iv) were altered so that their intensity reduced in a linear manner. Representative images and line profile of the Dim Gradient are shown in Figure 4-9A. Backgrounds were then added to simulated ground truths, resulting in 12 new data sets, each with a linearly decaying background. Data sets were corrected or not and reconstructed STORM images were compared to the respective ground truth image (Figure 4-9B-C). As can be seen in Figure 4-9C addition of the Dim Gradient to the ground truth Array changed the data set drastically. Without correction, the background disturbed individual frames, with dim events entirely lost. The effect can be seen in the reconstructed STORM image where localisations were misplaced resulting in the distortion of the array. However, correction of the data set prior to image processing was able to restore individual frames and the reconstructed STORM image which then perfectly matched the ground truth.

Figure 4-9D-H displays the quantitative assessment of all 3 ground truth and all 4 backgrounds ($n = 12$). Following correction, the percentage of events increased from $63.9 \pm 40.1\%$ to $100.0 \pm 0.7\%$. The mean CBC value improved from 0.57 to 0.98 while the NND decreased from $16.63 \text{ nm} \pm 31.30 \text{ nm}$ to $0.33 \text{ nm} \pm 0.21 \text{ nm}$. Manders and Pearsons coefficients increased from 0.81 ± 0.33 to 1.00 ± 0.01 and $0.65 \text{ nm} \pm 0.46 \text{ nm}$ to $0.96 \text{ nm} \pm 0.04 \text{ nm}$ respectively. This demonstrates that the moving median correction prior to image processing was capable of correcting constantly decaying backgrounds that would otherwise cause severe problems.

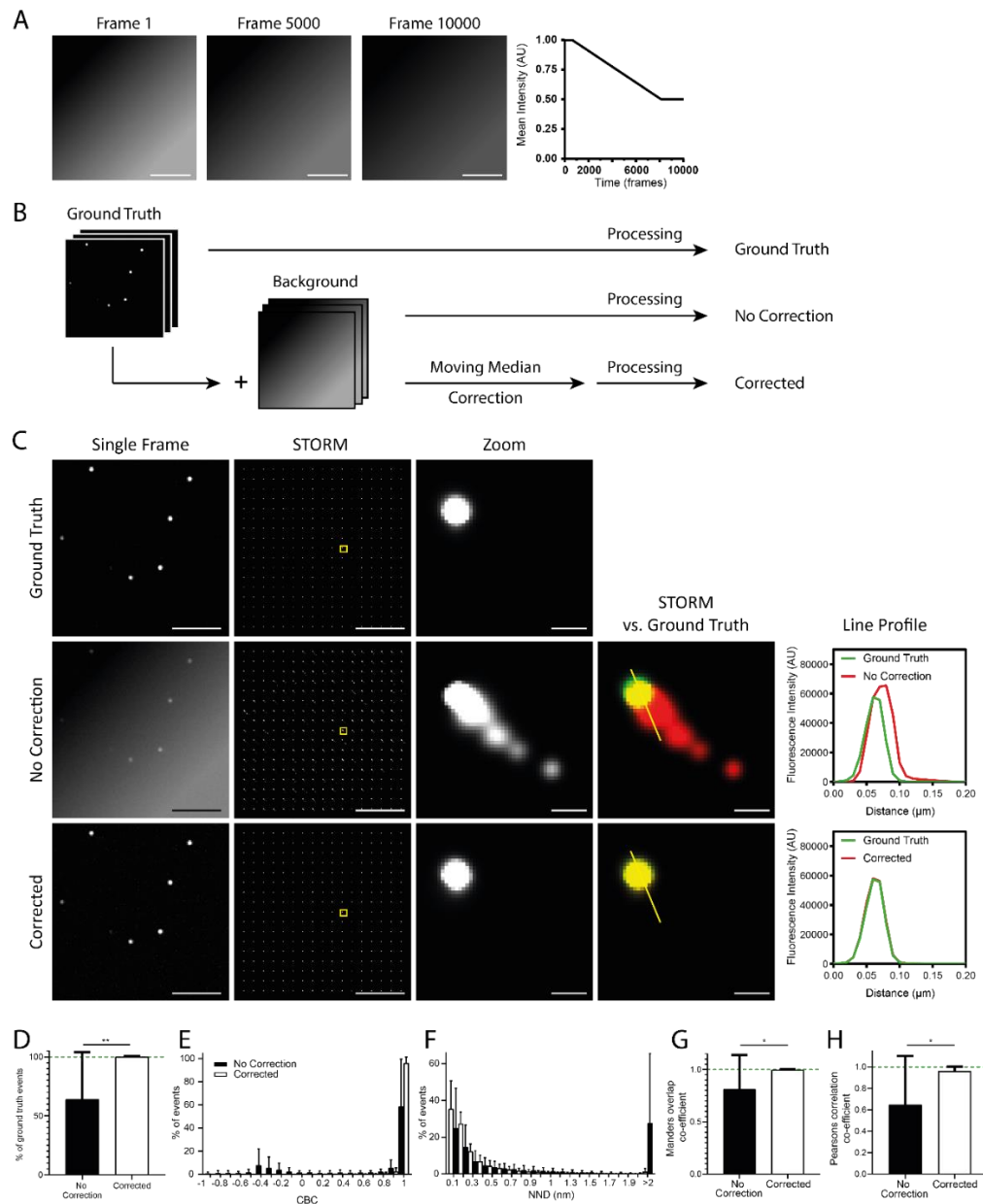


Figure 4-9: Moving median correction successfully corrects simulated, linearly decaying backgrounds.

A) Frame 1, 5000 and 10000 of simulated background Dim Gradient and intensity profile of all frames.

B) Simulated ground truth data sets were combined or not with linearly decaying background data sets.

The combined data sets were either corrected or not and reconstructed STORM images were assessed relative to the ground truths. **C)** Single frame, STORM image, zoom (0.5 x 0.5 μm) and overlay (vs. ground truth) with line profiles shown of ground truth, not corrected and corrected data. Here, the linearly decaying Dim Gradient background was combined with the ground truth Array. Scale bars: 5 μm and 100 nm (Zoom).

D-H) Quantification of reconstructed images relative to the ground truth (shown in green). Data from all 3 ground truths and all 4 backgrounds (as defined in Figure 4-2) combined (n = 12). **D)** Number of events detected. **E)** Coordinate based co-localisation (CBC). **F)** Nearest neighbour distance (NND). **G)** Manders overlap coefficient. **H)** Pearson's correlation coefficient. Error bars; ±SD. **, P ≤ 0.01; *, P ≤ 0.05; Paired t-test or Wilcoxon test using GraphPad Prism.

4.3.2.6 Non-Linearly Decaying Background – Simulating Autofluorescence

In the case of autofluorescence, signal intensity decays in a non-linear way (Figure 3-14). It drops within the first 5 min of acquisition and reaches a plateau. To mimic this, we generated backgrounds with similar intensity profiles. Representative images and line profile of Multiple Puncta is shown in Figure 4-10A. All 4 backgrounds and 3 ground truths as defined in Figure 4-2 were combined to create 12 new data sets, each with a non-linearly decaying background. Data sets were corrected or not and reconstructed STORM images were compared to the respective ground truth image (Figure 4-10B-C). The addition of the decaying background Multiple Puncta to the ground truth Lines had severe consequences (No Correction). The mean intensity of the background was much higher compared to the mean intensity of ground truth localisations (8444 AU vs. 552 AU; Figure 4-5). Without correction, this led to no localisations visible in the example frame and a distorted STORM image and line profile. After moving median correction, the single frame as well as the STORM image and line profile were near enough identical to the ground truth showing that the moving median correction is able to correct for very strong, non-linearly decaying backgrounds.

This is also reflected when assessing all 12 data sets relative to the ground truths (Figure 4-10D-H). Following correction, the mean percentage of events increased from $64.9 \pm 39.5\%$ to $100.0 \pm 0.7\%$. CBC improved from 0.57 ± 0.49 to 0.98 ± 0.02 while the NND decreased from 16.59 ± 30.33 nm prior correction to 0.33 ± 0.24 nm afterwards. Manders and Pearsons coefficients also greatly ameliorated from 0.81 ± 0.33 to 0.99 ± 0.01 and 0.65 ± 0.46 to 0.96 ± 0.04 respectively. This demonstrated that the moving median correction successfully corrects for simulated, non-linearly decaying backgrounds.

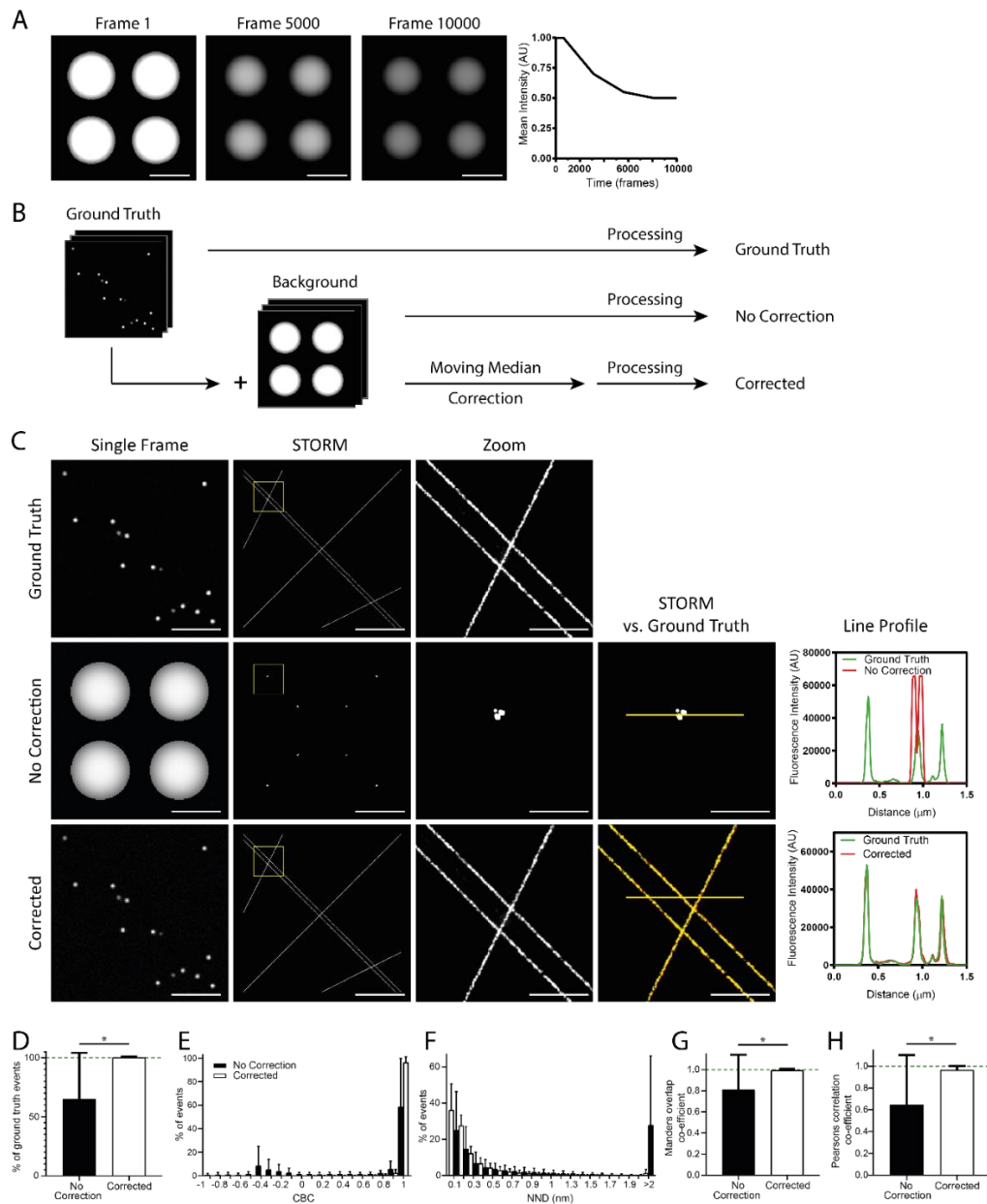


Figure 4-10: Moving median correction successfully removes simulated, non-linearly decaying backgrounds. **A)** Frame 1, 5000 and 10000 of simulated background Dim Gradient and intensity profile of all frames. **B)** Simulated ground truth data sets were combined or not with linearly decaying background data sets. The combined data sets were either corrected or not and reconstructed STORM images were assessed relative to the ground truth. **C)** Single frame, STORM image, zoom (3 x 3 μm) and overlay (vs. ground truth) with line profiles shown of ground truth, not corrected and corrected data. Here, the linearly decaying Dim Gradient background was combined with the ground truth Array. Scale bars: 5 μm and 1 μm (Zoom). **D-H)** Quantification of reconstructed images relative to ground truth, shown in green. Data from all 3 ground truths and all 4 backgrounds (as in Figure 4-2) combined (n = 12). **D)** Number of events detected. **E)** Coordinate based co-localisation (CBC). **F)** Nearest neighbour distance (NND). **G)** Manders overlap coefficient. **H)** Pearson's correlation coefficient. Error bars; ±SD. *, P ≤ 0.05; Paired t-test or Wilcoxon test using GraphPad Prism.

4.3.2.7 Determining the Ideal Group Size

This far, the moving median background correction was operated with a group size of $n = 200$. This means, the median intensity of every 200 frames was calculated, then interpolated to the same number of frames as the original stack and subtracted. When acquiring a STORM data set, one frame is recorded every 11 ms. Thus, it takes 2.2 s to record 200 frames. Therefore, the calculated median was adjusted every 2.2 s which allows addressing rapidly changing backgrounds. However, to thoroughly test this, the 4 simulated backgrounds (Figure 4-2, bottom) were combined with the 3 ground truths (Figure 4-2, top) and corrected using different group sizes (50, 100, 200, 500, 1000 and 2000). Backgrounds consisted of either 10000 identical frames (Figure 4-11A) or the intensity was altered in a linearly (Figure 4-11B) or non-linearly decaying (Figure 4-11C) way. Not corrected and corrected data sets were processed using ThunderSTORM and resulting STORM images were compared to the retrospective ground truth regarding the percentage of events detected, CBC, NND, Manders overlap and Pearsons correlation coefficient. Each value represents the mean of the 12 possible combinations of 3 ground truth and 4 backgrounds.

As can be seen in Figure 4-11A, the group size had no significant influence on the quality of correction when facing a constant background. This was expected as the difference between groups solely lies in the ground truths data which the correction method should separate; leaving a constant background. However, the group size plays an important role when facing a decaying background. For both, linearly and non-linearly decaying backgrounds, it was effective to calculate the background every 50, 100 or 200 frames (Figure 4-11B-C). There were only very little differences between the three groups with 50 performing best. The bigger group sizes of 500, 1000 and 2000 on the other hand failed to accurately correct decaying backgrounds. This is not surprising, as the calculated median is adjusted in longer time intervals for bigger group sizes. With one frame recorded every 11 ms, the median is calculated every 11 s at a group size of 1000. For a group size of 100 on the other hand, it is calculated every 1.1 s. Thus, it was expected that smaller group sizes better correct for backgrounds that change over time.

Taking together, smaller group sizes proved to better to address complex backgrounds and for all further analysis, the group size of 50 frames was used.

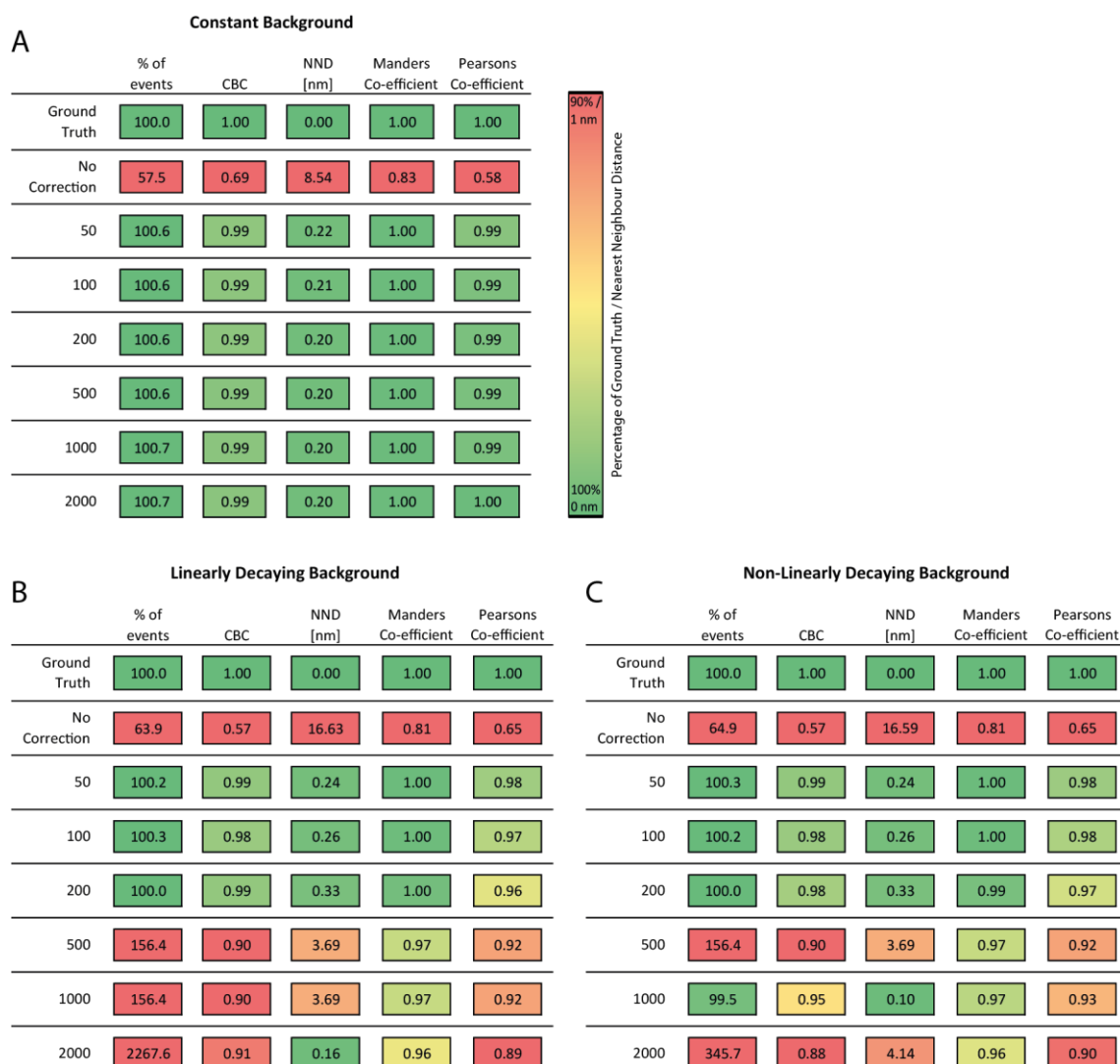


Figure 4-11: 50 frames is the ideal group size for the moving median correction. Ground truth data sets were combined or not with simulated background data sets. The combined data sets were either corrected with the moving median correction or not. For correction, different group sizes were applied: 50, 100, 200, 1000 and 2000. Reconstructed STORM images were assessed relative to the ground truth regarding the percentage of events detected, CBC, NND, Manders overlap and Pearsons correlation coefficient. Displayed are mean values of all 3 ground truths and all 4 backgrounds (as defined in Figure 4-2; n = 12 for each value). Backgrounds did either have **A**) constant, **B**) linearly decaying or **C**) non-linearly decaying intensity.

4.3.2.8 Recorded Autofluorescence

The moving median correction proved to be effective to remove complex simulated backgrounds. However, idealised simulated data cannot reflect fluctuations observed in real data. Therefore, unstained lung macrophages derived from a smoking individual were imaged. Cells isolated from human lung tissue were plated onto PLL-coated microscopy slides for 15 min, washed, fixed and 10000 frame-strong STORM data sets were recorded. Then, 4 data sets displaying highest autofluorescence, termed α , β , γ and δ , were selected for further analysis, ensuring a maximal challenge for the correction technique. Notably, most lung macrophages actually display less autofluorescence; especially when derived from a non- or ex-smoker. Images and line profiles of recorded backgrounds displayed big white spots of autofluorescence (Figure 4-12A). The mean intensity of these backgrounds dropped to approximately 50% within the first 2000 frames and stayed then relatively stable (Figure 4-12B). In the following, these 4 recorded backgrounds got combined with the 3 simulated ground truth (as defined in Figure 4-2, top) to test whether the moving median correction is sufficient in removing recorded autofluorescence. Beforehand, signal intensities of ground truths and backgrounds were directly compared. Therefore, for backgrounds, the mean intensity of the whole image (first frame) was measured, whereas for ground truths, the mean intensity of 100 – 150 blinks was taken. As can be seen in Figure 4-12C, the 4 recorded backgrounds cover the spectrum of the intensities of ground truths localisations. To compare individual pixels, histograms of the intensities of all pixel in the recorded stack were measured (Figure 4-12D). Depending on the background, highest values range from approximately 2000 to 7000 AU. Therefore being mostly lower than simulated backgrounds (high values over 30000 AU; Figure 4-4) and higher than simulated ground truth (high values approximately 2000 – 3000 AU; Figure 4-3). They thus presented a suitable challenge for the background correction technique.

Combined data sets ($n = 12$) were corrected or not and reconstructed STORM images were compared to the ground truths (Figure 4-13A). The addition of the autofluorescence background α to the ground truth Star had severe consequences for

the data set (Figure 4-13B, No Correction). In the example frame, autofluorescence spots were saturating the signal and thereby strongly impairing the precise detection of ground truth localisations. The consequences were big white spots in the resulting STORM image. Notably, the background α had such strong impact on the ground truth Star even though its mean intensity was much lower than localisations in the ground truth (Figure 4-12C). Upon moving median correction, these spots were removed and the STORM image as well as the according line profile closely matched the ground truth.

Quantitative assessment of all 12 data sets relative to the ground truths confirmed this observation (Figure 4-13C-G). Values represent the mean of all 12 data sets. Here, the mean percentage of events detected was $87.3 \pm 11.4\%$ for corrected images and $613.7 \pm 623.6\%$ for data without correction. In addition, CBC improved from 0.10 ± 0.31 to 0.90 ± 0.08 upon correction. NND decreased from 50.44 ± 49.25 nm to 4.52 ± 3.55 nm and Manders and Pearsons coefficients increased from 0.43 ± 0.42 to 0.89 ± 0.14 and 0.19 ± 0.23 to 0.83 ± 0.08 respectively. Thus, all metrics were significantly improved. At first it may seem that the correction was less successful than with simulated data (Figure 4-8 and Figure 4-10). However, simulated backgrounds had less severe effects on the ground truth in general. In addition, highest autofluorescent backgrounds were chosen, representing a worst case scenario.

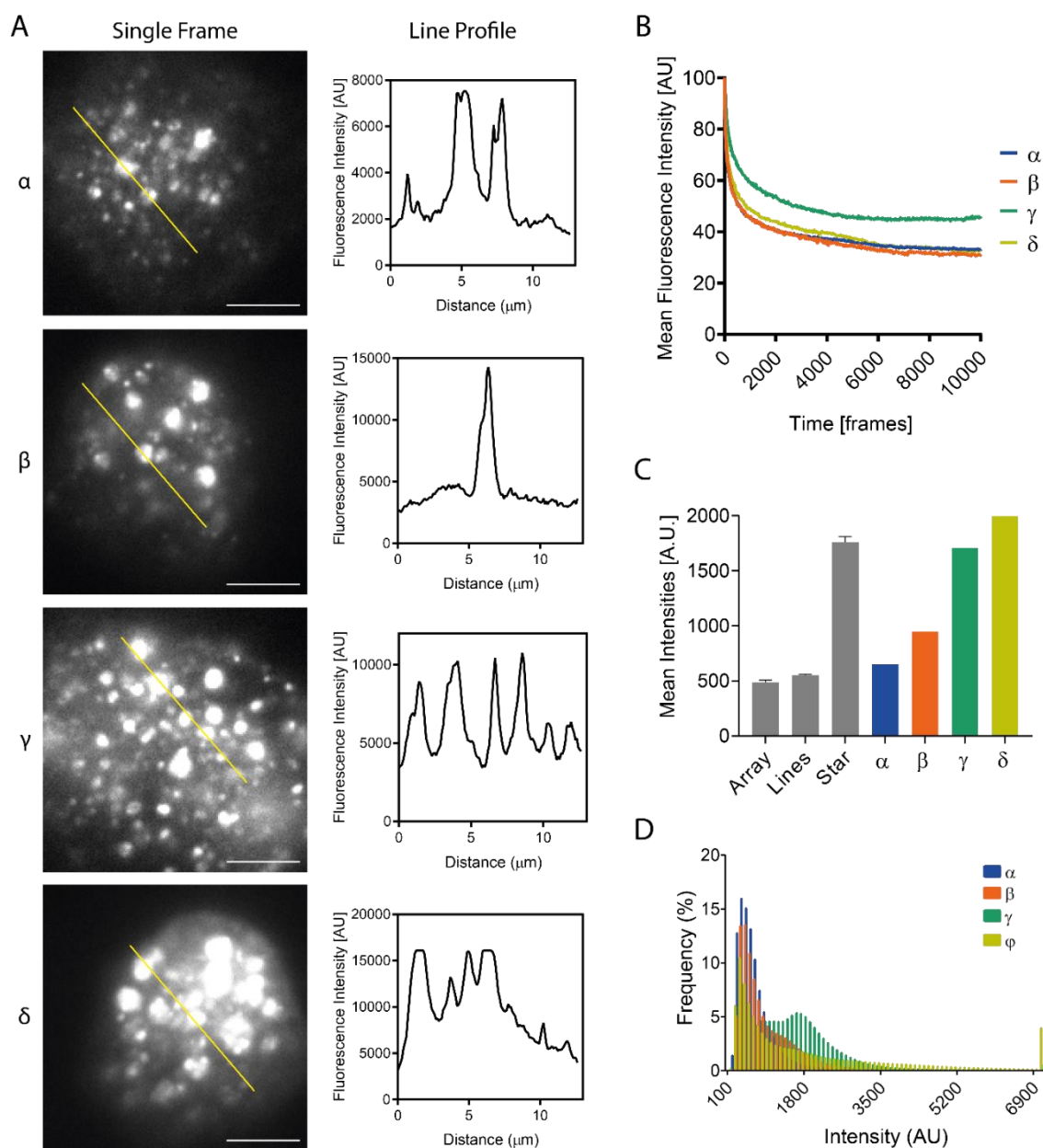


Figure 4-12: Intensity profiles of unstained, autofluorescent lung macrophages. Cells isolated from human lung tissue were plated onto PLL-coated microscopy slides for 15 min, washed, fixed and a 10000 frame-strong STORM data set was recorded. **A)** Single frame and according line profile of recorded data sets. Scale bar 5 μm . **B)** Normalised intensity profiles over time. The mean intensity of the whole frame was measured for the whole data set. **C)** Comparison of mean intensities of simulated ground truths and autofluorescence backgrounds. Grey columns show the mean intensity of 100 - 150 blinks from ground truth data sets. Coloured columns show mean intensity of recorded data sets. **D)** Histogram of intensities of all pixels from each data set (10,000 frames).

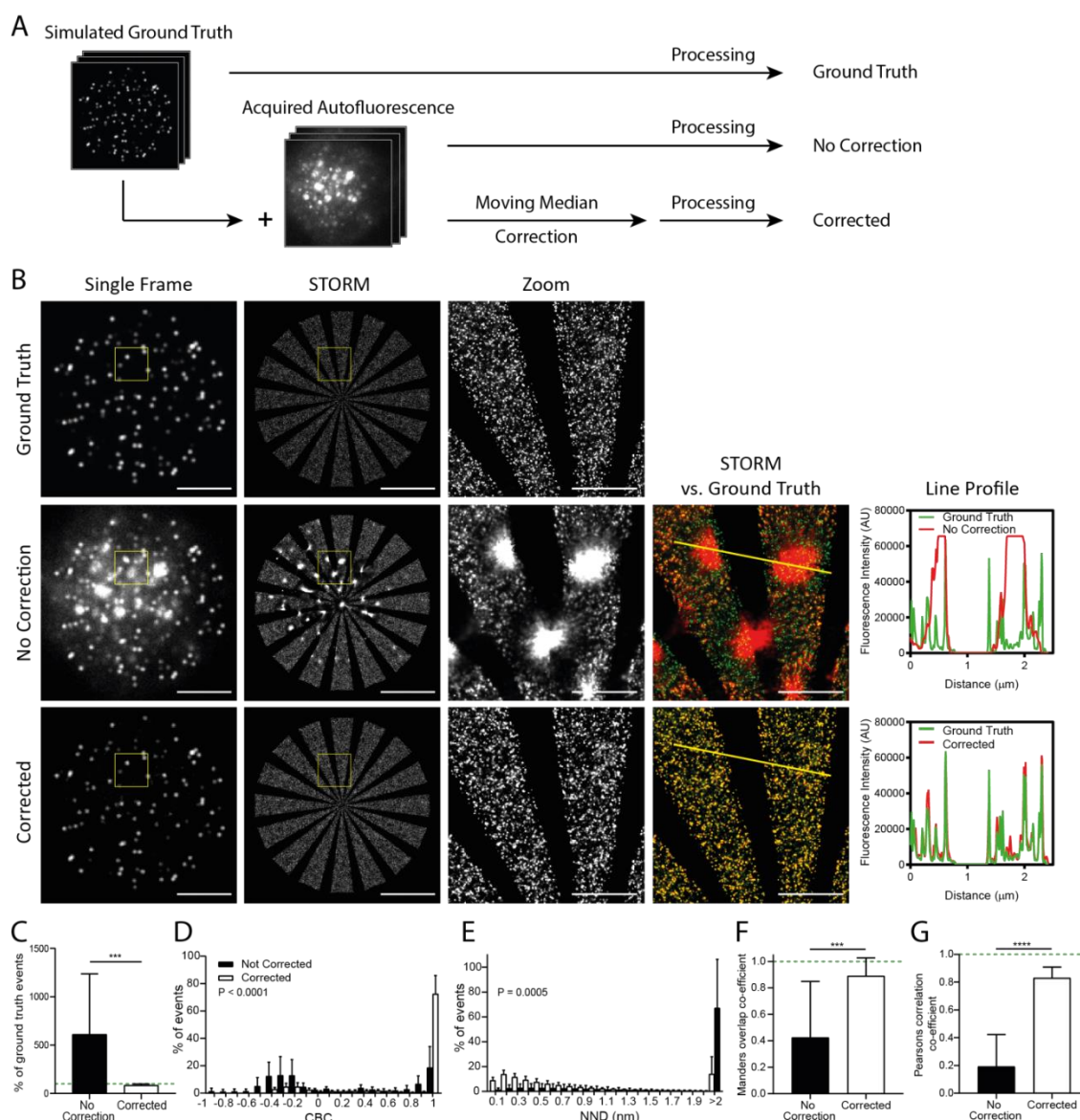


Figure 4-13: Application of moving median filter successfully corrects recorded autofluorescence.

A) Simulated ground truth data sets ($n = 3$; as defined in Figure 4-2, top) were combined with autofluorescence data sets from unstained lung macrophages ($n = 4$; as defined in Figure 4-12), yielding 12 separate data sets (No Correction). Combined data sets were corrected or not and reconstructed STORM images were assessed relative to the ground truths. **B)** Single frame, STORM image, zoom ($3 \times 3 \mu\text{m}$) and overlay (vs. ground truth) with line profiles of ground truth, not corrected and corrected data. Here, the background α was combined with the ground truth Star. Scale bars: $5 \mu\text{m}$ and $1 \mu\text{m}$ (Zoom). **C-G)** Quantification of reconstructed images relative to the ground truth, shown in green. Data from all 3 ground truths and all 4 backgrounds combined ($n = 12$). **C)** Number of events detected. **D)** Coordinate based co-localisation (CBC). **E)** Nearest neighbour distance (NND). **F)** Manders overlap coefficient. **G)** Pearsons correlation coefficient. Error bars; $\pm\text{SD}$. ***, $P \leq 0.001$; ****, $P \leq 0.0001$; Paired t-test using GraphPad Prism.

Further, the autofluorescence background could be calculated, showing that precise detection of ground truth events occurred upon correction. Therefore, the simulated ground truth Star was joined together with the background β (Figure 4-14, No Correction). As expected, the autofluorescence background severely distorted the ground truth data set and the reconstructed STORM image contained big white spots in regions of high autofluorescence. Alternating example frames with detected localisations circled demonstrate the poor precision in detection with most events being positioned in the centre of autofluorescence. Subtraction of the calculated background shown in the 3rd column yielded a corrected data set where STORM and single frames matched the ground truth data (Figure 4-14, Corrected). Compared to the ground truth data, corrected example frames were more pixelated or still show a low level of background fluorescence. However, when processing in ThunderSTORM, all ground truth events were precisely detected. It also has to be kept in mind that the background was chosen on the premise of extraordinary high autofluorescence and therefore represents an especially severe scenario. Taken together, the moving median correction successfully removed acquired severe autofluorescence from simulated SMLM data.

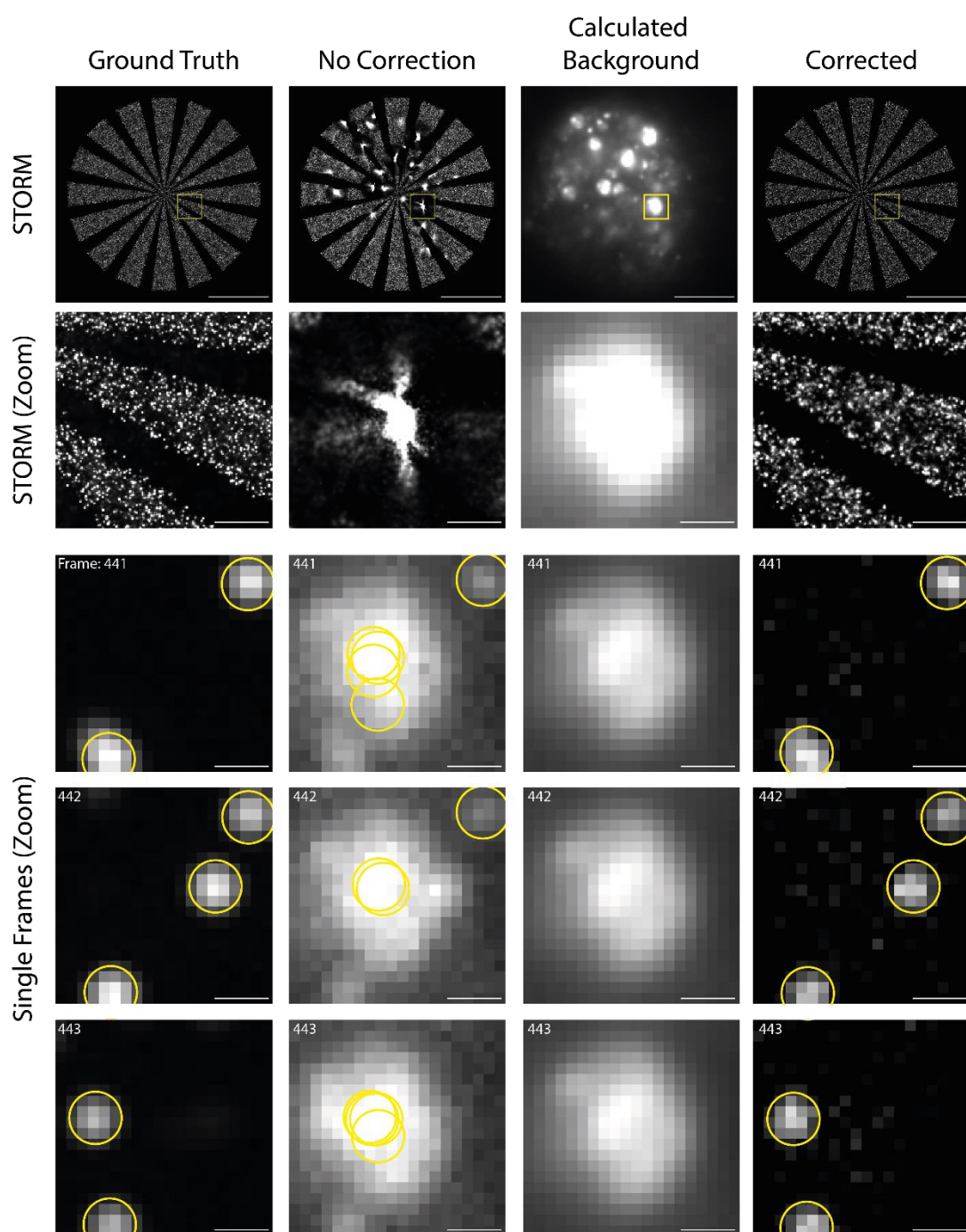


Figure 4-14: Displaying calculated autofluorescence background. The simulated ground truth Star was joined with the background β , a data set recorded from unstained lung macrophages. The combined data set was corrected or not and processed using ThunderSTORM. Shown are reconstructed STORM images with a $2 \times 2 \mu\text{m}$ zoom region and 3 alternating frames from the same region. Detected localisations are circled. The third column shows the calculated moving median which is subtracted from the combined data to yield the corrected data set, displayed in column 4. Scale bars: $5 \mu\text{m}$ and 500 nm (Zoom).

4.3.2.9 Recorded Ground Truth

To test a scenario even closer to normal imaging condition, data sets acquired from stained cells were combined with autofluorescence backgrounds recorded separately from unstained lung macrophages (as defined in Figure 4-12). Therefore, blood-derived macrophages or HEK293T cells were plated onto PLL coated microscopy slides for 15 min, fixed, stained and imaged. As expected, the addition of autofluorescence backgrounds severely distorted the acquired ground truth data sets (Figure 4-15B, No Correction). Single frames displayed bright autofluorescent spots which resulted in empty areas in the processed and filtered STORM image. Upon moving median correction, autofluorescence is no longer visible in the example frames and STORM images were restored. Notably, the corrected data set looks even ‘cleaner’ than the ground truth data set (Single Frame of Ground Truth vs. Corrected). This is, because all cells display some level of autofluorescence. Consequently, during correction, not only the added background but also ground truth noise was subtracted leading to differences between the data sets. Therefore, a quantitative analysis was not possible. However, the correction method was able to restore cellular structures like the actin filaments that were completely lost with the addition of the autofluorescence background (Figure 4-15B, bottom). This showed, that the moving median correction technique was able to successfully separate severe autofluorescence backgrounds and acquired STORM data sets, enabling precise and accurate event detection.

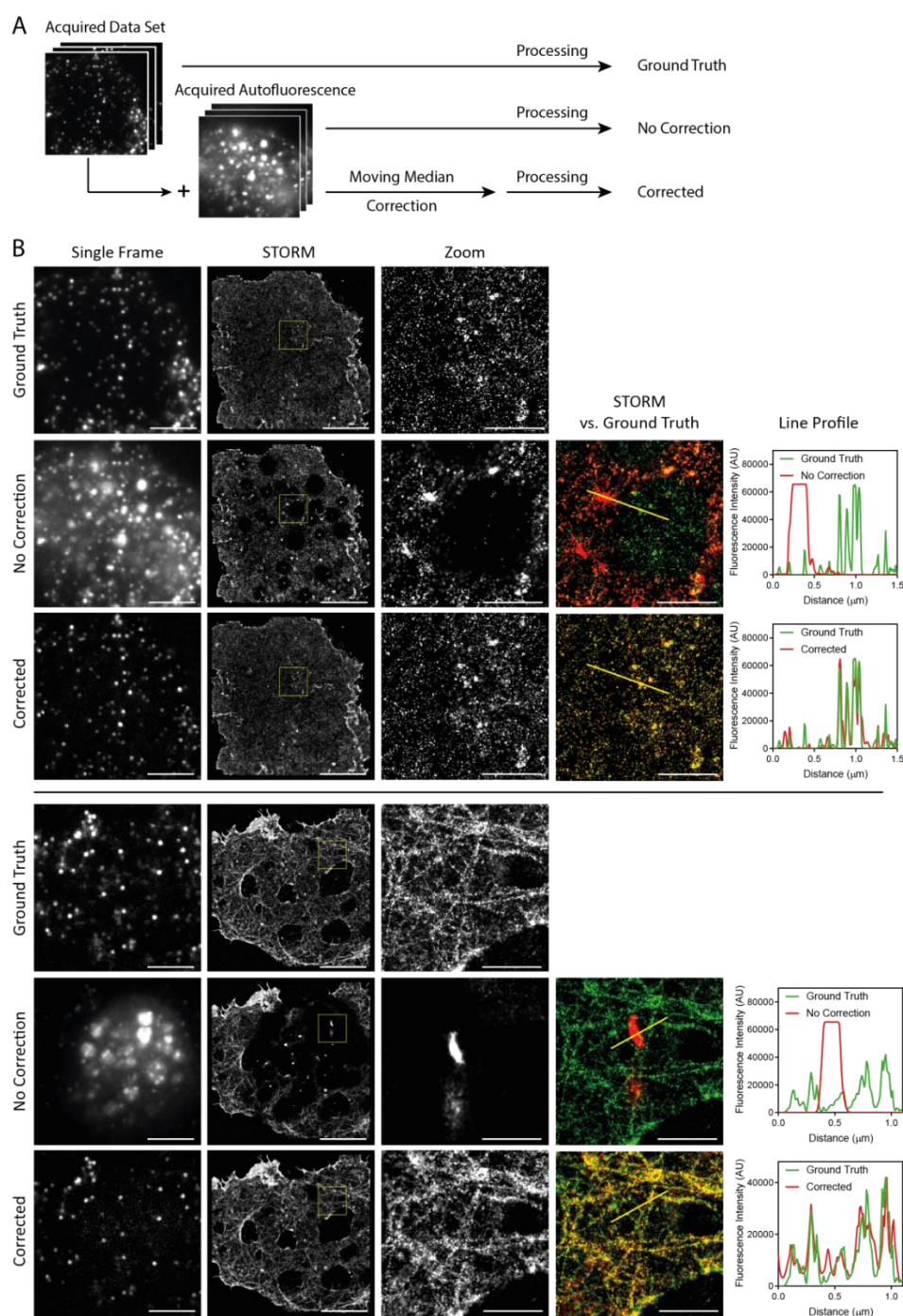


Figure 4-15: Correcting recorded STORM data sets from separately acquired, severe autofluorescence.

A) Ground truth data sets were acquired from stained cells and combined with autofluorescence backgrounds recorded separately from unstained lung macrophages. Combined data sets were corrected or not and compared to the ground truth. **B)** The autofluorescence background γ was combined with a STORM data set of blood-derived macrophages stained for MHC class I with an AF647 conjugated mAb (top) and the background δ was combined with a data set of HEK293T cells stained for filamentous actin with phalloidin-AF647 (bottom). Displayed are single frame, STORM image, zoom (3 x 3 μm) and overlay (vs. ground truth) with line profiles of ground truth, not corrected and corrected data. Scale bars: 5 μm and 1 μm (Zoom).

4.3.3 Applying Correction Technique to Stained Lung Macrophages

Finally, the correction technique was applied to recorded stacks of stained, autofluorescent lung macrophages in order to test its performance on real data. Therefore, cells isolated from human lung tissue were plated onto PLL-coated microscopy slides for 15 min, washed, fixed and stained for actin (Figure 4-16, top) or MHC class I (Figure 4-16, bottom). 10000 frame-strong STORM data sets were recorded and either corrected or not prior to reconstruction. In both cases, actin and MHC class I, single frames of not corrected data sets displayed big white puncta which resulted in blank areas in the reconstructed STORM image. Upon correction, autofluorescence was removed and blank areas were filled. Importantly, the background correction was able to visualise the filamentous structure of actin that could not be observed in uncorrected images. This demonstrated that the correction technique can successfully remove high autofluorescent backgrounds, enabling the investigation of previously unusable samples, such as auto-fluorescent lung macrophages.

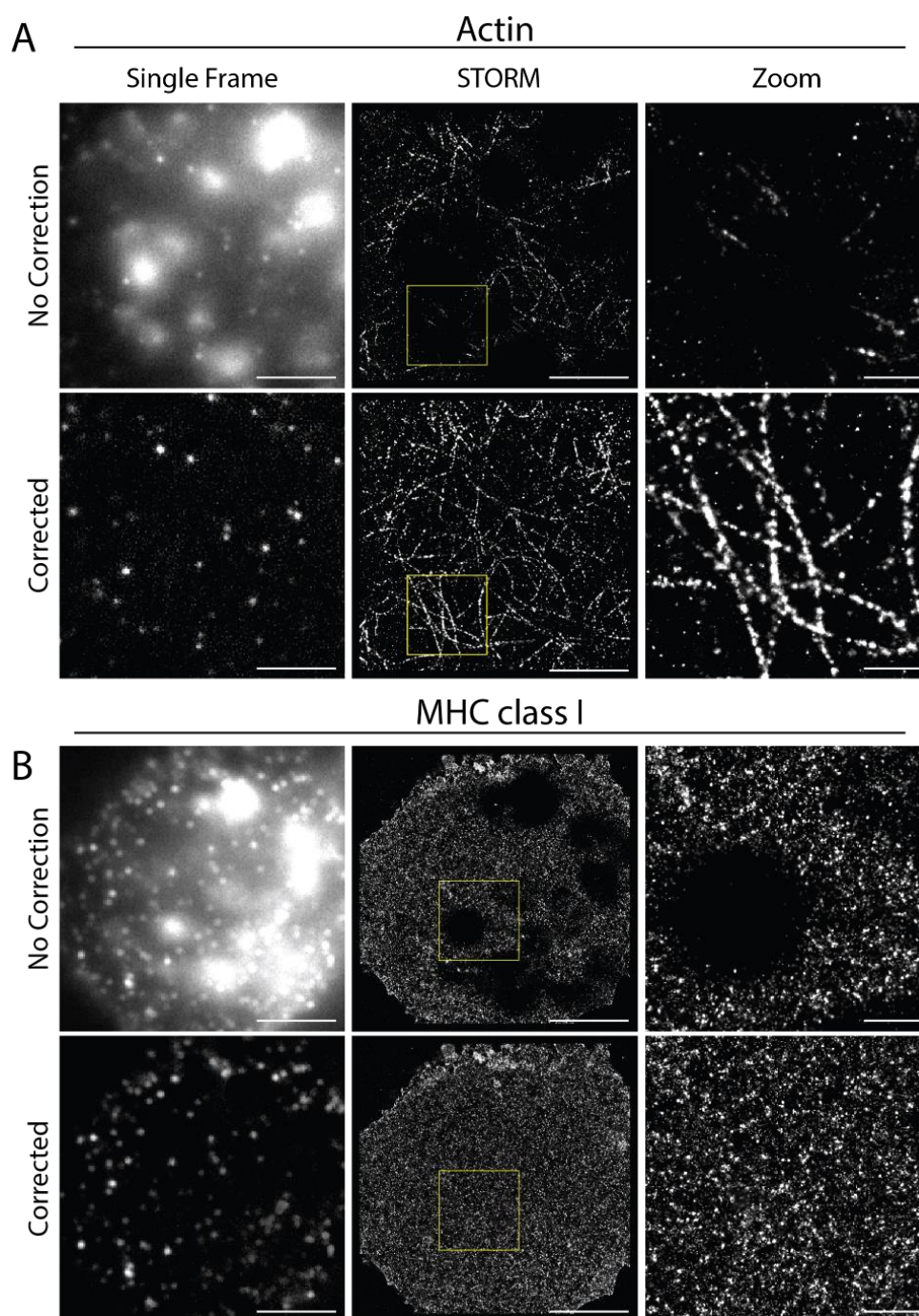


Figure 4-16: Successfully correcting autofluorescent lung macrophages using moving median filter. Human lung macrophages were plated onto PLL-coated glass slides for 15 min, blocked and stained with phalloidin-AF647 (**A**) or anti-human MHC class I mAb conjugated with AF647 (**B**). Data sets were either corrected prior to image processing or not. Shown are single frame, STORM image and zoom (5 x 5 μm). Scale bars: 5 μm and 1 μm (Zoom). Images representative for n = 3 individual donors and experiments.

4.3.4 Observation of Protrusion-Like Structures on the Surface of Human Lung Macrophages

The background correction allowed detailed investigation of the membrane of human lung macrophages. Therefore, cells isolated from the human lung were allowed to settle for 15 min, washed, fixed and stained for MHC class I and wheat germ agglutinin (WGA). WGA binds N-acetyl-glucosamine, a glycoprotein of the cell membrane and can thus be used to label the plasma membrane^{299,300}. First, samples were investigated using TIRF microscopy. Here, WGA visualises the surface topology of the membrane and allows to distinguish between the reorganisation of molecules within the membrane and topological changes of the cell membrane itself.

In non-activating conditions, MHC class I as well as WGA stain showed a homogenous distribution and perfect overlay (Figure 4-17A; top). When activated through FcγRI, the membrane topology of lung macrophages changed, forming protrusion-like structures with MHC class I accumulating at the tips (Figure 4-17A; bottom). Line profiles demonstrated the ring-like structure of WGA with MHC class I concentrated in the middle (Figure 4-17B). To quantify this observation the cell area covered by MHC class I stain, relative to the total cell was determined by thresholding on 75% of its maximum grey value (Figure 4-17C). It reduced from $92.4 \pm 13.2\%$ to $68.6 \pm 24.2\%$ of the total cell area following stimulation, demonstrating that this occurred across many cells.

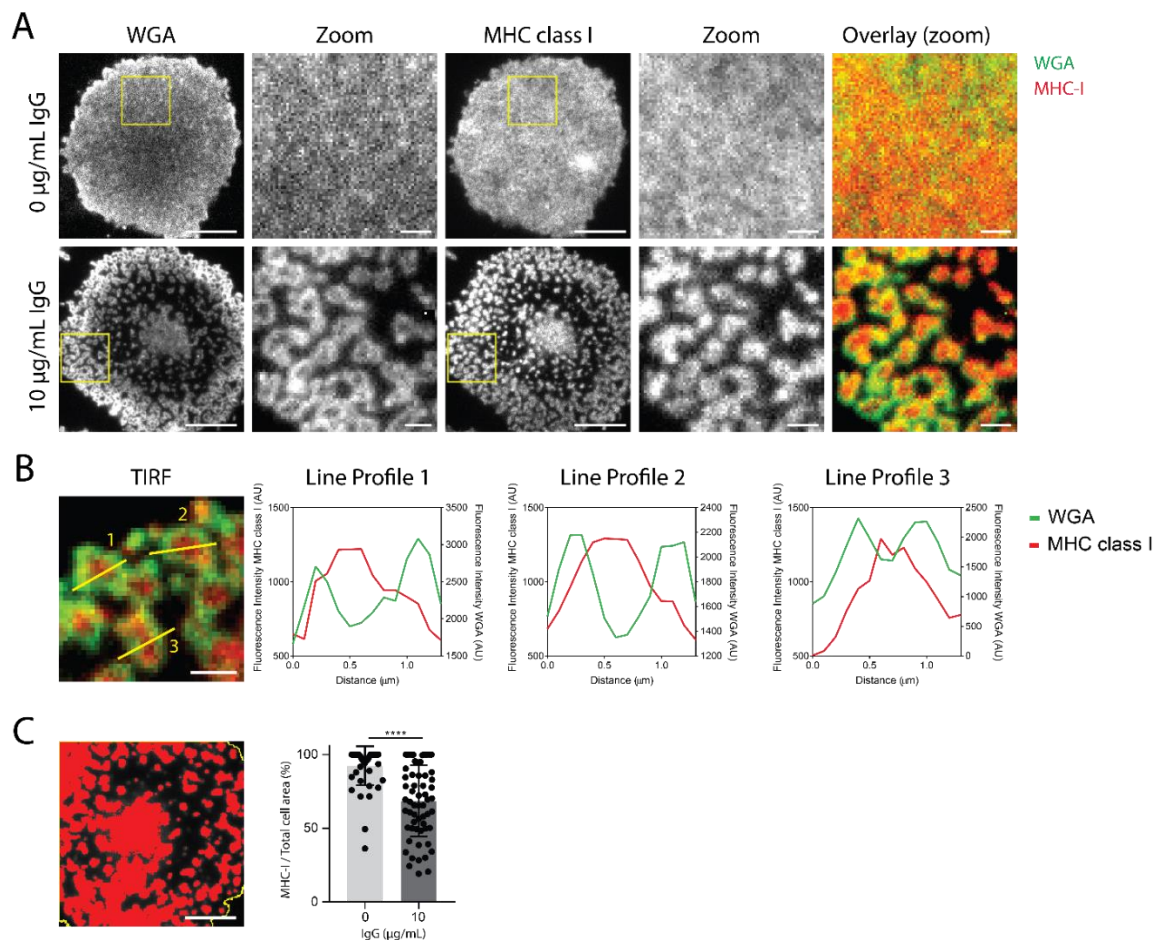


Figure 4-17: Lung macrophages form protrusions upon activation through Fc receptors. Lung macrophages were plated onto PLL (0 $\mu\text{g/mL}$ IgG) or PLL and human IgG (10 $\mu\text{g/mL}$ IgG) coated glass slides for 15 min and stained with wheat germ agglutinin (WGA)-AF488 and anti-MHC class I mAb conjugated to AF647. **A)** Representative TIRF images with zoomed regions. Scale bar 5 μm and 1 μm (Zoom). **B)** Zoomed region with line profiles. Scale bar 1 μm . **C)** Percentage of area covered by staining for MHC class I protein relative to total cell area. Top: example image. MHC class I stain in red (thresholded at 75% of max grey value) and total cell area indicated by yellow line. Scale bar 5 μm . Bottom: Quantitative assessment. Each dot represents a single cell, $n = 4$ individual donors and experiments. Error bars; $\pm\text{SD}$. ****, $P \leq 0.0001$; unpaired t-test using GraphPad Prism.

Next, the nanoscale organisation of MHC class I at the membrane of lung macrophages was investigated, made possible by the correction method. Therefore, the samples from TIRF microscopy were used to record STORM data sets which were either corrected or not. In non-activated conditions, cells displayed empty areas typical for autofluorescence when not corrected, making it impossible to accurately assess the nanoscale structure (Figure 4-18, 0 $\mu\text{g/mL}$, left column). Upon correction, events from

these areas were regained and a homogenous distribution emerged, matching the observations made in TIRF microscopy (Figure 4-17).

In activating conditions protrusion-like structures were formed (Figure 4-18, 10 $\mu\text{g/mL}$). These were visible regardless of the correction and also correlate with observations made in TIRF microscopy. It seems there was less autofluorescence present in activating conditions. This is likely because of the cell body and thus autofluorescent particles being further away from the cover slip due to the formation of the protrusions. Once beyond the TIRF evanescent field, their signal won't be detected anymore.

Event density and NND of corrected vs. not corrected STORM images in activating and non-activating conditions were determined to assess the nanoscale organisation quantitatively (Figure 4-18B-D). In both, activating and non-activating condition, the event density increased significantly upon correction, changing the outcome of the analysis. As a result, the event density of activating and non-activating conditions was significantly different without correction while it was non-significant for corrected data (Figure 4-18B; $p = 0,0073$ (No Correction) vs. $p = 0,0577$ (Corrected)). Similarly, the NND decreased upon activation with the decrease being much less significant after correction (Figure 4-18; $p = 0.0005$ (No Correction) vs. $p = 0.0326$ (Corrected)). The comparison of all NND of one autofluorescent region in non-activated condition clearly demonstrated the effect of the correction method. After correction, more than double of the events were detected (6332 (No Correction) vs. 13528 (Corrected)) and the mean NND was reduced (2.18 nm (No Correction) vs. 1.87 nm (Corrected)).

Taken together, this highlights the necessity of the background correction method for accurate assessment of the nanoscale organisation of data sets distorted by high backgrounds like autofluorescence. Without this method, nanoscale investigation of MHC class I at the surface of human lung macrophages would not be possible.

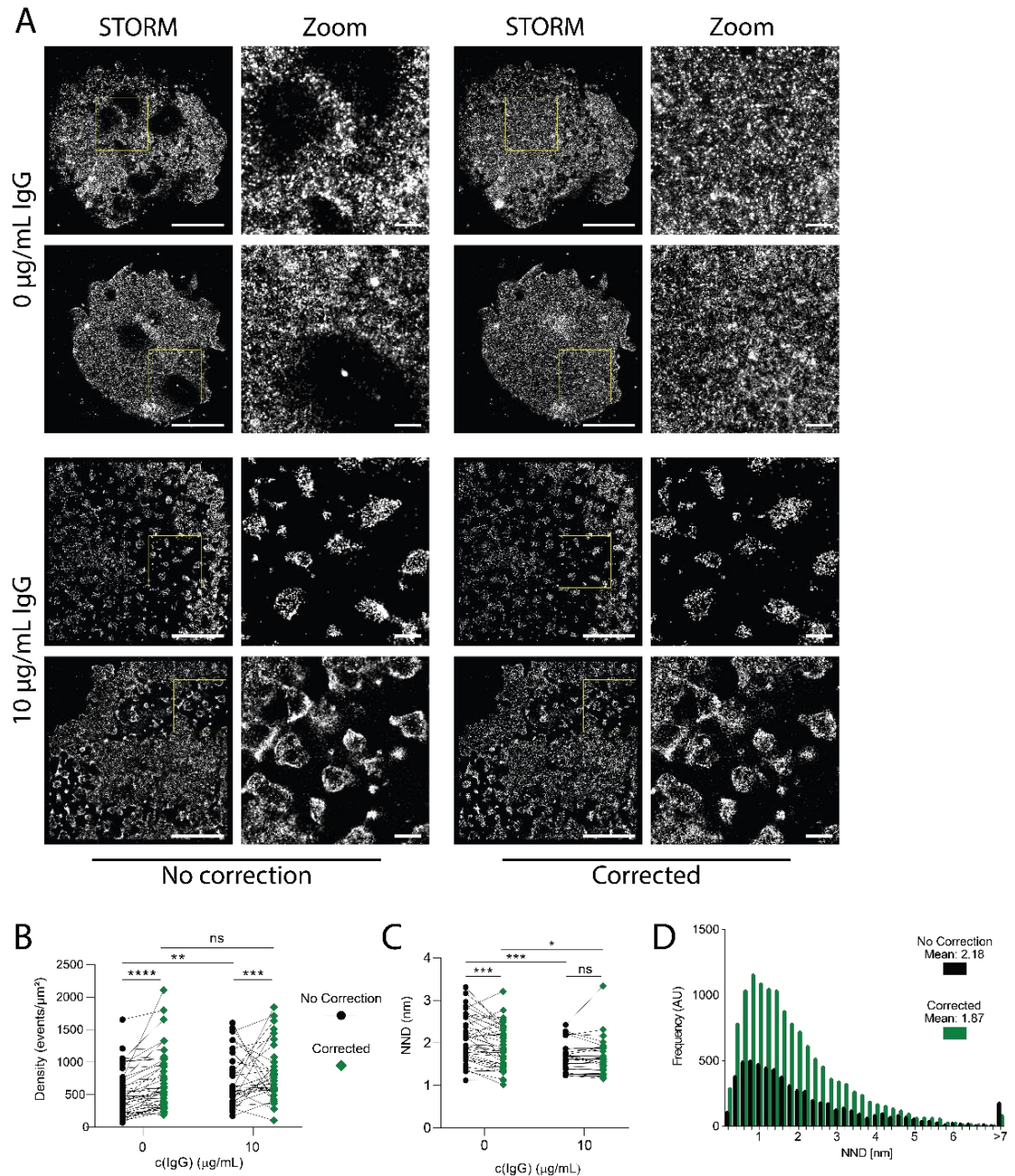


Figure 4-18: Nanoscale investigation of macrophage protrusions. A) STORM images and zoomed regions (5 x 5 μm) of corrected and not corrected data set s of human lung macrophages stained for MHC class I. Cells were plated onto PLL (0 $\mu\text{g/mL}$; top) or PLL and IgG (10 $\mu\text{g/mL}$; bottom) for 15 min and stained with anti-human MHC class I mAb conjugated with AF647. Two examples per condition. Scale bars 5 μm or 1 μm (Zoom). **B)-C)** Quantitative analysis of not corrected and corrected STORM images in non-activated (0 $\mu\text{g/mL}$ IgG; left) and activated (10 $\mu\text{g/mL}$ IgG; right) conditions. Each data point represents the density of an auto-fluorescent region (5 x 5 μm) with a single region per cell. 5 individual donors and experiments for 0 $\mu\text{g/mL}$ IgG and 4 for 10 $\mu\text{g/mL}$. **B)** Density defined as number of events/ μm^2 . **C)** NND. **D)** Histogram of all NND of one 5 x 5 μm region (non-activating condition; 0 $\mu\text{g/mL}$); corrected (green); not corrected (black). *, $p \leq 0.05$; **, $p \leq 0.01$; ***, $p \leq 0.001$; ****, $p \leq 0.0001$; Unpaired T-test, Mann Whitney or Wilcoxon Test as appropriate.

4.3.5 Background correction reveals nanometre-scale ring structures at the membrane of human lung macrophages

Lung macrophages were plated onto PLL (0 $\mu\text{g/mL}$ IgG; non-activating conditions) or PLL and human IgG (10 $\mu\text{g/mL}$ IgG; activating conditions)-coated glass slides for 15 min, fixed and stained for the tetraspanin and exosome marker CD81. Figure 4-19A shows corrected and not corrected data sets; two examples per condition (activated vs. non-activated). As expected, autofluorescence was evident in not corrected data sets as bright white spots and underlying haze in the single frame and empty areas in the reconstructed STORM image. Upon correction, autofluorescence was removed, regaining localisations in the single frame and events in the empty areas. In non-activated conditions (0 $\mu\text{g/mL}$ IgG), CD81 was distributed homogenously with no structure visible. However, upon activation CD81 formed into nanometer-scale ring structures (Figure 4-19A, 10 $\mu\text{g/mL}$, Corrected). In regions of high autofluorescence, these structures were completely absent, highlighting the necessity of the correction technique (Figure 4-19A, 10 $\mu\text{g/mL}$, No Correction). In contrast, ring structures were visible before and after correction in low background regions, demonstrating that observations are not artefacts created by the correction method (Figure 4-19A, 10 $\mu\text{g/mL}$, second example, Zoom 1).

To visualise the ring nature of the observed structures, a representative zoom with line profiles is shown in Figure 4-19B. In all 3 line profiles, intensity peaked either end of the structure with a drop in the middle, highlighting their circularity. A detailed investigation and quantification of these nanometre-scale ring structures at the membrane of macrophages can be found in the following chapter (Chapter 3).

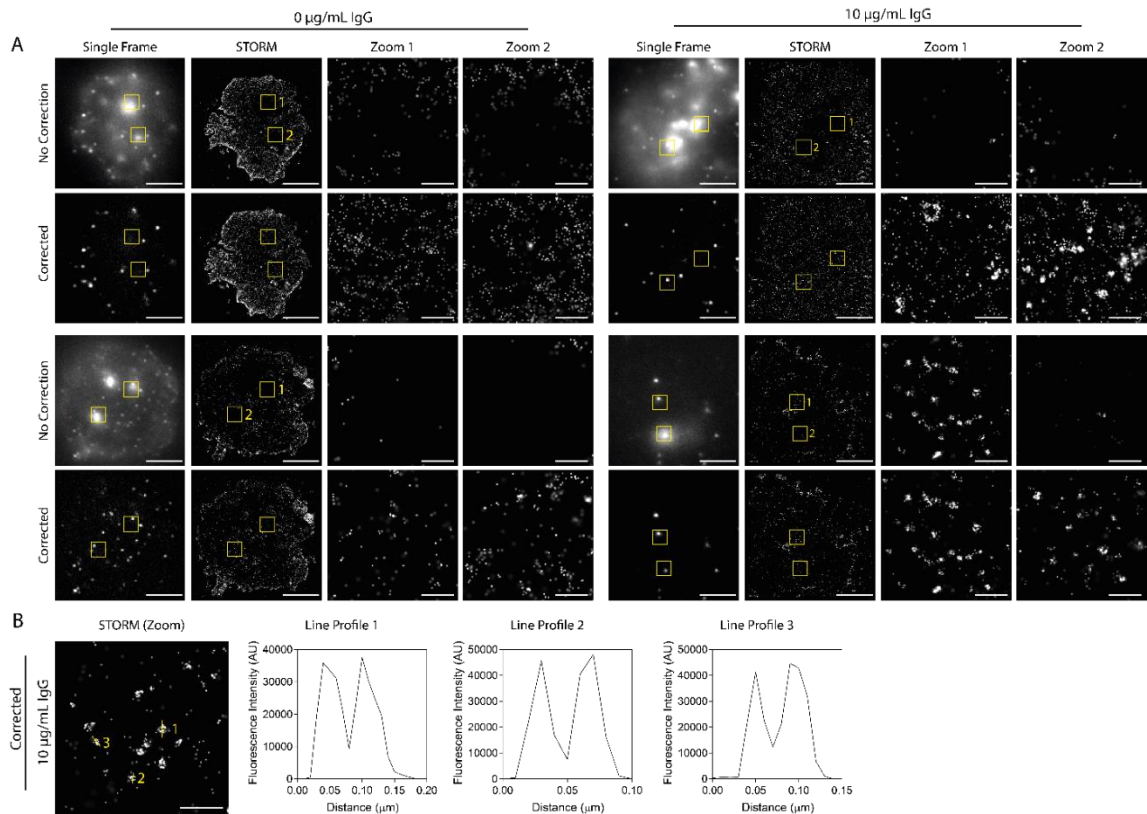


Figure 4-19: CD81 forms into nanometer-scale ring structures at the membrane of IgG-activated lung macrophages. A) Lung macrophages were seeded onto PLL (0 µg/mL IgG; non-activating conditions; left) or PLL and human IgG (10 µg/mL IgG; activating conditions; right)-coated glass slides for 15 min, fixed and stained with anti-humanCD81 mAb conjugated in house with AF647. Single frame, STORM and zoomed regions of corrected (top) and not corrected (bottom) data sets and two examples per condition (activated vs. non-activated). Scale bar 5 µm or 500 nm (Zoom). **B)** Representative zoomed region (2 x 2 µm) in activating condition with 3 line profiles. Scale bar 500 nm.

Taken together, it could be demonstrated, with simulated and real data, that the described correction technique accurately corrects severe backgrounds such as autofluorescence and allows for precise assessment of the nanoscale organisation of otherwise lost samples. It allowed the nanoscale investigation of human lung macrophages for the first time and revealed the formation of protrusions tipped with MHC class I as well as CD-81 ring structures at their membrane. From now on, all data sets of lung macrophages were corrected prior reconstruction.

4.4 Discussion

4.4.1 Summary of Results

The aim of this chapter was to enable the use of STORM for autofluorescent samples like human lung macrophages. Therefore, a novel background correction technique was developed and validated. This allowed the investigation of MHC class I and the tetraspanin CD81 on a nanometre-scale at the membrane of human lung macrophages. The main findings of this investigation can be summarised as follows:

- Severe autofluorescent backgrounds can be corrected post acquisition by subtracting a moving median filter
- Human lung macrophages form protrusion-like structures with MHC class I accumulating at their tips when activated through its FcγRI
- Tetraspanin CD81 forms into nanometer-scale ring structures at the membrane of activated human lung macrophages

4.4.2 Background Correction Technique

A novel background correction technique was developed to correct for autofluorescence of lung macrophages in STORM. The method separates foreground signal from unwanted backgrounds. It determines the background by calculating the median intensity of each pixel. Subtracting the background from the original image (which holds back- and foreground signal) yields a corrected image. This is possible because autofluorescence is emitting constantly while extrinsic fluorophores blink (Figure 3-12A). More clearly, in areas of high autofluorescence, the overall emission will be constant over many frames and thus, the median calculated over n frames will be similar to the autofluorescence itself. A blink on the other hand is only detected for a short amount of time (or only in few frames), having little influence over the median calculated for n frames. In fact, the blinks present like outliers compared to the relatively constant background signal. Due to the nature of the median being “the middle” value within a given data set, it is not as susceptible to being skewed by a small

number of very large or very small values as for example the mean^{301,302}. Thus, the median was expected to work well to estimate backgrounds in STORM.

As a starting point, a group size of $n = 200$ frames was chosen. Because one frame is recorded every 11 ms, a group size of $n = 200$ frames means that the calculated median is adjusted every 2.2 s ($200 \times 11 \text{ ms} = 2.2 \text{ s}$), which allows addressing rapidly changing backgrounds.

One STORM data set consists of several thousand individual frames. Each of these frames need to be corrected prior to image reconstruction. Thus, the median fluorescence intensity of every 200 frames is determined and expanded to the same number of frames as the original stack applying bicubic interpolation. This yields a 'background stack', consisting of the same number of frames as the original. Subtraction of this 'background stack' from the original yields a corrected data set that can be processed and reconstructed as usual (Figure 4-1).

Utilising median filtering for image processing is not a new concept. B. R. Frieden suggested already in 1976 a simple median filter for image processing³⁰³. Since then, many improved algorithms have been proposed to advance the performance of median filtering^{304–307}. More recently, Hoogendoorn et al. successfully applied a temporal median filter implemented in Python to acquired and simulated STORM data sets¹⁵³. Even though their correction method was demonstrated to work well, a detailed quantitative assessment is missing. In addition, basic knowledge of the programming language Python is necessary for its application. This temporal median filter has also never been tested for the autofluorescence of lung macrophages, which is much brighter than regular cellular background addressed in their work.

The novel background correction technique developed for this project was rigorously tested with simulated and recorded data. Simulated data consisted of 3

different ground truth STORM data sets and 4 different backgrounds with varying shapes and intensities (Figure 4-2 to Figure 4-5). Backgrounds were added to ground truth data sets and the combined data sets were either corrected or not prior to image reconstruction (Figure 4-6). After reconstruction, corrected and not corrected images were compared to the original ground truth images. For detailed quantitative analysis, several metrics were investigated: the percentage of events detected, coordinate based co-localisation (CBC), nearest neighbour distance (NND), Manders overlap and Pearsons correlation coefficient. The method proved to be precise and robust for constant as well as linearly and non-linearly decaying backgrounds while it is not distorting images with no background (Figure 4-7 to Figure 4-10). All metrics investigated were significantly improved upon correction. Notably, all discrepancies of corrected vs. ground truth images were smaller than the theoretical 20 nm resolution of STORM²³⁴. In fact, 99.97 % of all events in corrected reconstructions were within 10 nm of the ground truth localisations (combined data from Figure 4-8 to Figure 4-10).

So far, a group size of $n = 200$ frames was applied for median calculation. As mentioned above, 200 frames are equivalent to 2.2 s of acquisition time, with 1 frame being recorded every 11 ms. Despite the small time frame, the group size chosen was bigger than other techniques reported. Hoogendoorn et al. was for example utilising a median filter with a group size of 101 frames¹⁵³. Baddeley and co-workers proposed a temporal mean filter with a group size of 10 frames and Cremer et al. simply subtracted the succeeding from the preceding frame, which represents a group size of 1 frame^{308,309}. All methods work reasonably well. However, with a smaller frame size it is more likely to subtract foreground signal, especially with a high density image or high signal to noise data. In fact, Hoogendoorn et al. compared their 101-group size technique to Baddeley et al.'s 10-group size technique and found that Baddeley et al.'s methods subtracted up to four times as much signal, thereby losing foreground signal¹⁵³. It has to be kept in mind though, that here, a median and mean based background estimation was compared. The comparison of different group sizes would be more meaningful when tested for the same technique.

Therefore, to ensure the optimal group size for the newly developed correction method, 6 different group sizes ranging from 50 – 2000 frames were tested for constant, linearly decaying and non-linearly decaying backgrounds (Figure 4-11). As expected, the group size only marginally influenced the quality of correction for constant backgrounds (Figure 4-11A). Constant backgrounds consisted of 10000 identical frames, leading to the same calculated median across any group size. The slight differences between group sizes may be due to the different foreground signal across different group sizes and the bicubic interpolation applied for expansion.

Decaying backgrounds on the other hand clearly perform better with smaller group sizes (Figure 4-11B-C). Both, linearly and non-linearly decaying backgrounds were best corrected with group sizes of 50 – 200 frames. Between these groups, the quality of correction differs only slightly with 50 frames performing best. In contrast, group sizes of 500 – 2000 frames failed to accurately correct the data. This was expected as the median of larger group sizes will differ more greatly within one stack, bearing a greater challenge to accurately interpolate. For example, for a decaying background and a group size of 2000, the median intensity of the first 2000 frames will be significantly different to the median intensity of the second 2000 frames. When expanding the calculated median frames to match the number of frames of the original stack (as there is only one median frame calculated per 2000 original frames), a bicubic interpolation is applied. The greater the difference between two adjacent median-frames, the more difficult is an accurate estimation of missing intensities. This leads to the subtraction of ‘not enough’ background in some frames and ‘too much’ in others, resulting in loss of signal but also the creation of artefacts. This is especially evident in the number of events detected. At large group sizes and decaying backgrounds, more events were detected than in the original as well as the not corrected image. In the case of a group size of 2000 frames, $2267.6 \pm 7047.3\%$ and $345.7 \pm 860.0\%$ of events relative to the ground truths were detected for linearly and non-linearly decaying background respectively. Even though most of these artefacts presumably can be accounted for by filtering the reconstructed STORM image due to their much lower intensity values compared to ‘real’ events, this is still an enormous amount of artefacts and shows how

heavily STORM relies on accurate background estimation. For all further image correction, a group size of 50 was applied.

The simulated data was necessary to verify precision and robustness of the designed correction method. It provided ground truth data sets with known localisations, event densities and intensities etc., allowing a detailed quantitative assessment of the performance of the correction method. However, real background differs from the defined shapes and intensity values of simulated backgrounds. Thus, in the next step the correction method with optimised frame size was applied to acquired data. Therefore, the autofluorescence of unstained lung macrophages displaying a range of shapes and intensities was recorded (Figure 4-12). The optimised correction method proved to be effective to correct simulated as well as separately recorded ground truth data for real autofluorescence (Figure 4-13, Figure 4-15). In addition, the correction of real autofluorescence proved to be similar to correcting simulated backgrounds, with 98.8% of all events in corrected reconstructions being within 10 nm of the ground truth localisations (data from Figure 4-13). In addition, the accurately calculated background was displayed for one example (ground truth: Star, background: β ; Figure 4-12). The estimated background perfectly matched the added background (compare Figure 4-12A, β and Figure 4-14 top row, Calculated Background), confirming accurate performance of the correction method.

Finally, the method was applied to stained lung macrophages (Figure 4-16). Therefore, human lung macrophages were incubated on PLL-coated glass slides for 15 min, fixed, blocked and stained for actin or MHC class I. Both data sets showed similar results: in not corrected data sets, bright saturated spots were evident which resulted in blank areas in the reconstructed STORM images. These spots were removed in the corrected data sets and reconstructed images displayed no blanks anymore. The precision of the correction technique is especially evident in the case of actin, where the filamentous structure is an indication of accurate background subtraction.

Taken together, the novel background correction technique successfully corrected simulated and acquired STORM data sets for complex backgrounds containing different structures and with varying intensities over space and time. The method was applied to accurately correct STORM data sets of stained lung macrophages which enabled the nanometer-scale investigation of their membrane.

4.4.3 Protrusion-like Structures Tipped with MHC class I

The novel background correction technique was applied to investigate the membrane topology of human lung macrophages and the nanometer-scale organisation of MHC class I protein in the membrane. The topology was visualised utilising TIRF microscopy by staining macrophages with the membrane stain wheat germ agglutinin (WGA). Upon activation with IgG, the formation of protrusion-like structures was observed (Figure 4-17). WGA stain concentrated in a ring-like fashion around the edges of these protrusions while MHC class I accumulated in the middle (Figure 4-17B).

Many cells are known to form protrusions. In the case of macrophages, these could be for example a way of 'reaching out' to phagocytic targets, which has been reported for serum-opsonized bacteria³¹⁰. Here, macrophages surrounded the bacteria with protrusions before phagocytosis to maintain the directional entry of the parasite. Another possible function may be antigen presentation. Junt and co-workers showed that in mice, specialised macrophages captured viral particles in lymph nodes with subsequent presentation to follicular B cell by extending protrusion-like structures across lymph node compartments³¹¹. Thus, the fact that MHC class I accumulated at the tip of observed protrusions may indicate a role in specialised antigen presentation to T cells. Therefore, a more detailed investigation of MHC class I in STORM was carried out. Here, the event density at the surface of human lung macrophages did not change upon activation with IgG (Figure 4-18B). However, the mean NND decreased significantly, indicating denser packing of MHC class I proteins for activated macrophages (Figure 4-18C). In the past, denser clusters of membrane proteins have been reported to

potentiate cellular signalling^{6,159,280}. This may suggest a functional importance for densely packed MHC class I proteins at the tips of macrophage protrusions to activate T cells. It is unclear though, how many of these MHC class I proteins bear an antigenic peptide and how clustering impacts this.

4.4.4 CD81 at the Membrane of Human Lung Macrophages

Further investigation of the membrane of human lung macrophages showed that the tetraspanin and vesicle marker CD81 forms into ring structures in IgG-activated macrophages (Figure 4-19). Notably, the novel background method was necessary for this observation as in regions of high autofluorescence precise reconstruction failed otherwise (Figure 4-19A, 10 µg/mL IgG, example 1, Zoom 1-2, and example 2, Zoom 2). Importantly, observed ring structures were not artefacts of the correction technique as regions with low autofluorescence displayed them with and without correction (Figure 4-19A, 10 µg/mL IgG, example 2, Zoom 1). In addition, line profiles confirmed their circular structure (Figure 4-19B).

As mentioned above, CD81 is commonly used as extracellular vesicle (EV) marker^{192,193}. EVs are lipid bound vesicles which are classically divided into 3 subgroups: exosomes, microvesicles and apoptotic bodies. These subgroups differ in size, composition and function. Microvesicles and apoptotic bodies are considered to be larger than 100 nm and directly released from the cell surface (from living and dying cells respectively)¹⁸¹. Exosomes on the other hand are the smallest of these subtypes of vesicles ranging from 30 – 150 nm in diameter³¹². Line profiles in Figure 4-19B indicate a diameter of approximately 80 nm for observed ring structures. This may suggest the observation of exosomes secreted by human lung macrophages activated through their FcγRI. However, a detailed qualitative and quantitative analysis of these structures is necessary for a reliable conclusion.

Nevertheless, studying vesicles and other secretions using STORM bears many advantages. In fact, vesicles are usually studied in bulk after isolation for example via ultracentrifugation, leading to co-purification of non EV-associated proteins and other caveats^{186,187,297,298}. STORM on the other hand presents a tool to study vesicles on a cell-by-cell basis directly upon secretion, avoiding caveats caused by the isolation process. Indeed, it has been utilised in the past to study EVs. Chen and co-workers studied the composition and uptake of cancer-derived exosomes using PALM and STORM²³⁴. A similar study was conducted by Nizamudeen et al. imaging stem cell-derived EVs and their uptake by live stem cells in culture²³⁵. However, in both studies, EVs were isolated prior to imaging, thereby making them subject to the disadvantages of the harsh isolation process, possibly changing their composition and function.

Thus, utilising STORM to capture EVs directly upon secretion could advance the field, giving new insight on secretory behaviour of cells. In addition, the application of the correction method allows investigation of so far unusable samples.

4.4.5 Conclusions

In summary, a novel background correction technique to account for the autofluorescence of human lung macrophages was suggested and validated. It precisely and robustly corrected simulated as well as acquired data. Most importantly, it enabled the nanometer-scale investigation of the membrane of human lung macrophages for the first time. This led to the discovery of MHC class I tipped protrusions, possibly suggesting a tissue specific mechanism for activating T cells. In addition, nanometer-scale ring structures of EV marker CD81 were observed at the membrane of IgG-activated human lung macrophages. Their approximate diameter of 80 nm may suggest them being exosomes. Here, STORM presents the unique possibility to study vesicles directly upon secretion, allowing analysis on a cell-by-cell basis and in a near native state. Crucially, this was only made possible by the correction method which enables the investigation of so far unusable samples. However, a detailed analysis of CD81-rings

at the membrane of activated macrophages is missing. Therefore, the next chapter focused on CD81 in the membrane of macrophages derived from blood and lung.

Chapter 5 – Macrophages Secrete Distinct Populations of Extracellular Vesicles upon Stimulation through their Fcγ receptor I

5.1 Introduction

Macrophages are phagocytic cells that can be found all through the body. They play a vital role in homeostasis as well as inflammation. Interestingly, their phenotype is strongly influenced by their environment. This means macrophages residing in different tissues display great structural and functional diversity. For example, in the healthy lung, alveolar macrophages are sessile, highly suppress inflammation and responsible for the clearance of alveolar surfactant^{88,90,313}. Cardiac macrophages on the other hand facilitate and modulate electrical conduction in the heart via connexin-43-containing gap junctions between macrophages and cardiomyocytes³¹⁴. In the last decade, many tissue-specific macrophage functions have been identified and investigated. Thus, macrophage responses should be studied with macrophages originating from different tissues or displaying different phenotypes. Classically, macrophages were described in two distinct subsets, namely M1 and M2 macrophages, where M1 macrophages display pro-inflammatory features and M2 macrophages mainly immune-suppressive features¹⁰. Nowadays, macrophage phenotype is thought to be a spectrum rather than distinct populations. Nevertheless, studies using differently differentiated macrophages shed new light on macrophage function and phenotype delivering information crucial for understanding macrophage plasticity. In addition, there is a paucity of studies with human cells compared to animals, due to restricted availability of human tissue samples, yet they are greatly necessary.

Needless to say, some properties are shared across all macrophages including phagocytic functions, the ability to initiate an immune response and shared surface markers including the Fcγ receptor I (FcγRI; CD64)^{315–319}. The engagement of FcγRI leads to the activation of the macrophage and mediates a number of immunological

responses including the production of cytokines, phagocytosis and the induction of cytolytic activity^{320,321}. This can lead to the initiation of an immune response.

Macrophages may initiate an immune response through the secretion of cytokines and chemokines. However, other forms of communication are possible. In recent years, more and more attention is paid to extracellular vesicles (EV). EV are secreted by all cells and thought to play a role in cell-to-cell communication¹⁷⁹. They vary in size (30 – 2000 nm in diameter), composition and function¹⁸³. An accurate definition of EV subsets is therefore not obvious. In general, the field distinguishes between three types of EV: exosomes, microvesicles (MVs; also microparticles, MPs) and apoptotic bodies³²². All three types of vesicles consist of a phospholipid bilayer with a spheroidal shape which contains DNAs, RNAs, a great variety of proteins and lipids from their cell of origin¹⁷⁹. MVs and apoptotic bodies are considered to be larger than 100 nm and directly released from the cell surface (from living and dying cells respectively)¹⁸¹. Exosomes on the other hand are the smallest of these subtypes of vesicles ranging from 30 – 150 nm in diameter³¹². Inward budding of late endosomal membranes leads to the formation of exosomes within large multivesicular bodies (MVBs)³²³. The fusion of these MVBs with the plasma membrane results in the release of exosomes into the extracellular space.

Due to the phagocytic nature of macrophages, they are very likely to uptake EV. In fact, exosomes derived from pro-inflammatory macrophages were taken up very selectively by macrophages and dendritic cells in the lymph node of mice after subcutaneous injection³²⁴. Similarly, Saunderson and co-workers showed that B-cell derived EV co-localised with macrophages in the spleen and lymph node of mice after intravenously injection³²⁵. Macrophages are also a key cell type to secrete vesicles. For example, the macrophage marker CD68 was strongly increased in EV isolated from BALF of LPS-challenged mice, identifying macrophages as main source of EV³²⁶. Further, the isolation of these EV and subsequent intratracheal delivery into wild type mice led to the induction of a pro-inflammatory phenotype in lung macrophages highlighting their

ability to induce inflammation. In addition, exosomes derived from M1 macrophages have been reported to reverse the quiescent phase of breast cancer cells within the bone marrow stroma³²⁷. These studies highlight the importance of macrophage vesicles and their ability to influence immunological processes.

In recent years, many functions and characteristics of macrophage vesicles were identified and investigated. However, EV are classically studied after isolation, often by ultracentrifugation. This comes with several caveats including the co-purification of non-EV-associated proteins^{186,187}. In addition, the isolation process is usually based on physical properties like the vesicle size. However, EV subpopulations overlap in size and composition. This makes the isolation of a pure EV population very challenging. Studying EV after isolation also makes single cell analysis impossible. Here, Stochastic Optical Reconstruction Microscopy (STORM) could offer a great tool to overcome these problems, by directly imaging the secretion of different vesicles cell-by-cell.

STORM has a theoretical resolution of 20 nm and should therefore be able to resolve even the smallest of vesicles²³⁴. Here, members of the tetraspanin family including CD81, CD9 and CD63 are commonly used as extracellular vesicle (EV) markers^{192,193}. Cells were stimulated on microscopy slides and the release of vesicle studied directly upon secretion. This allowed analysis on a cell-by-cell basis. STORM has been used in the past to study EV. For example, human breast cancer cell-derived exosomes and their interaction with normal cells was studied using PALM and STORM²³⁴. Similarly, Nizamudeen and co-workers applied STORM to characterise stem cell-derived EV and their uptake by live stem cells in culture²³⁵. However, in both studies, EV were isolated prior to imaging, thereby not avoiding the harsh isolation process. Their uptake and interaction with other cells was studied but not the direct secretion.

Taken together, the hypothesis was that the secretion of EV could be captured by STORM when imaging the EV marker CD81 and that different macrophages may display

different vesicle characteristics. Thus, this chapter aimed to investigate CD81 nanometer-scale ring structures at the synapse of human macrophages. Here, we set out to determine their vesicular nature and differences between M0-like, M1-like, M2-like and lung macrophages. Utilising STORM allowed to study vesicles directly upon secretion on a single cell basis and detailed proteomics analysis revealed discrete contents for vesicles of different macrophages.

5.2 Summary of Chapter Aims

- e) Determine the characteristics of CD81 ring structures at the synapse of M0-like, M1-like, M2-like and lung macrophages activated on IgG-coated glass slides and IgG-containing planar lipid bilayers on a cell-by-cell basis utilising STORM
- f) Investigate the vesicular nature of CD81 ring structures by imaging the secretions of macrophages and isolated vesicles
- g) Determine the involvement of actin remodelling at the site of vesicle secretion
- h) Determine contents of vesicles secreted by different macrophages by proteomics analysis and different microscopy techniques

5.3 Results

5.3.1 CD81 forms into nanometer-scale ring structures at the membrane of activated, human macrophages

The previous chapter has shown that the tetraspanin and exosome marker CD81 formed into nanometer-scale ring structures at the membrane of IgG-activated, human lung macrophages (Figure 4-19). However, tissue-specific macrophages are known to have specialised functions and thus, may behave different to monocyte-derived macrophages. Therefore, the observation of CD81-ring structures was expanded to several different types of monocyte-derived macrophages: M0-like, M1-like and M2-like macrophages. A detailed characterisation and the differentiation protocol of the different macrophage populations can be found in Chapter 3 and the methods section (2.1.1).

Monocyte- and lung-derived macrophages were plated onto microscopy slides coated with PLL (0 $\mu\text{g}/\text{mL}$ IgG, non-activating condition) or PLL and IgG (10 $\mu\text{g}/\text{mL}$ IgG, activating condition) for 15 min, washed, fixed and stained with anti-CD81 mAb labelled in house with AF647. STORM data sets were recorded and corrected with the moving median filter (described in Chapter 4). Activated conditions, where glass slides are coated with PLL and IgG, represent a 2-D model of the phagocytic synapse (Figure 5-1A). STORM images capture this synapse. For all four cell types, TIRF as well as STORM of non-activated conditions displayed a relatively homogenous distribution of CD81 (Figure 5-1B, 0 $\mu\text{g}/\text{mL}$ IgG). In activated conditions on the other hand, CD81 concentrated in spots appearing as bright dots in the TIRF images (Figure 5-1B, 10 $\mu\text{g}/\text{mL}$, top row). These dots were resolved into nanometer-scale ring structures in the STORM images. Notably, CD81-rings observed at M0-like macrophages seem to be bigger than those of M1-, M2-like and lung macrophages.

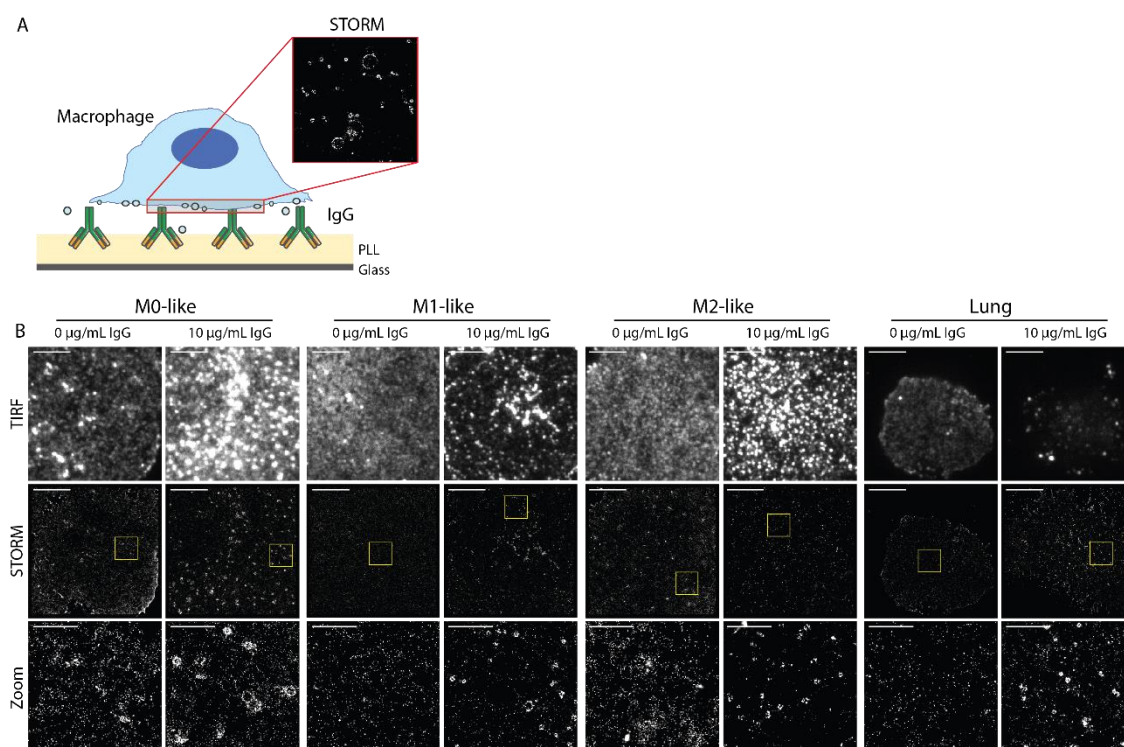


Figure 5-1: CD81 forms into nanometer-scale ring structures at the synapse of activated macrophages.

A) Macrophages were incubated on PLL- (0 µg/mL IgG, non-activating condition) or PLL- and IgG- (10 µg/mL IgG, activating condition, coated glass slides for 15 min, fixed and stained with human anti-CD81, labelled with AF647. **B)** TIRF, STORM and Zoom (3 x 3 µm) images of non-activating and activating conditions. Scale bar 5 µm, Zoom 1 µm. Images are representative for n = 30 – 43 cells per condition from 4 – 6 individual donors and experiments.

All line profiles showed two clear peaks on the edges with a dip in the middle. This is in accordance with the structure being vesicular (Figure 5-2). Interestingly, the dimensions of the line profiles also confirmed observations of M0-like macrophages displaying bigger ring structures than the other cell types. In fact, line profiles of M0-like macrophages showed a diameter of approximately 200 nm (Figure 5-2, top row, line profile 1 and 3) while all other cell types had diameters half this size.

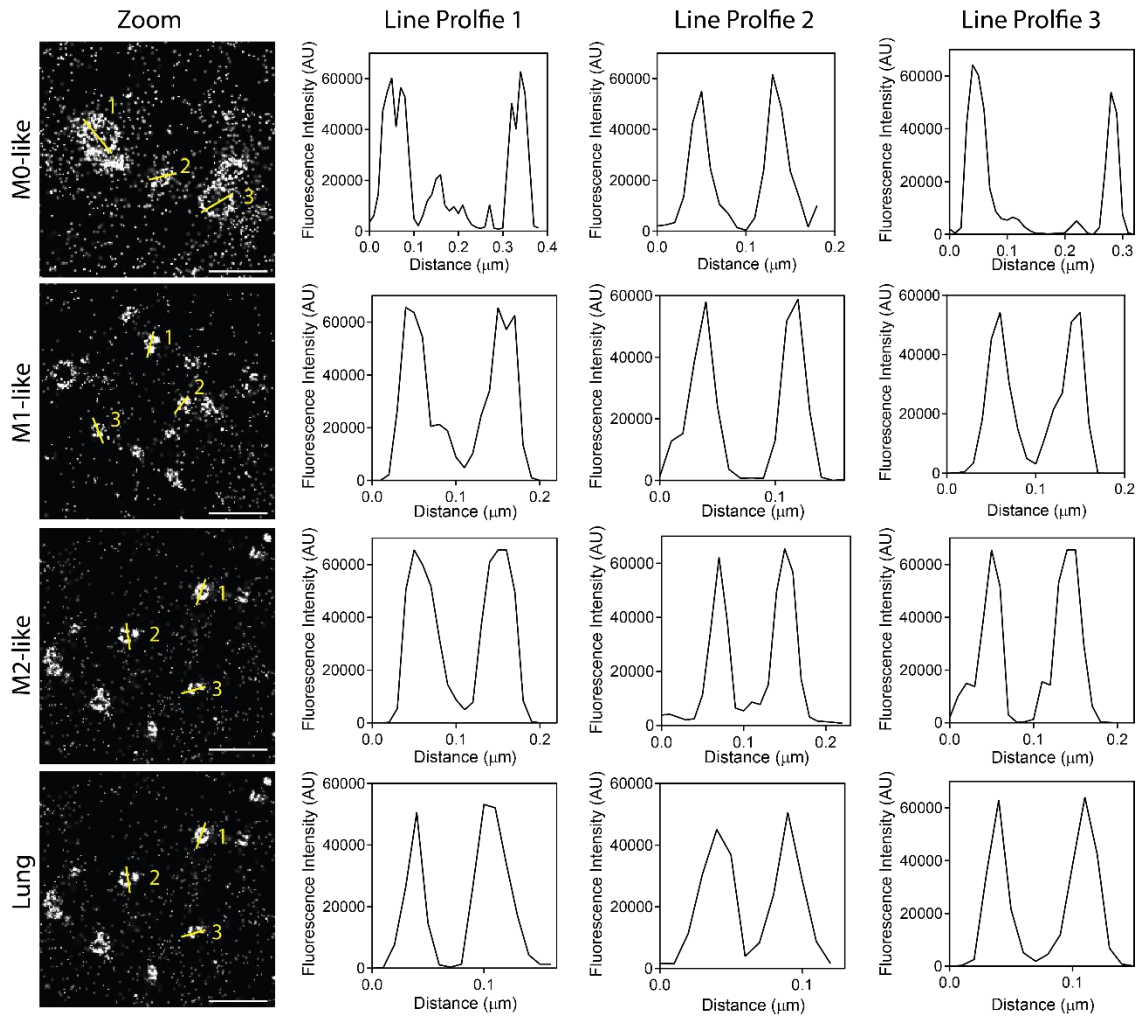


Figure 5-2: Line profiles of CD81-ring structures confirm circular nature of observations. Macrophages were incubated on glass slides coated with PLL and 10 $\mu\text{g}/\text{mL}$ IgG for 15 min, fixed and stained with anti-CD81 labelled with AF647. Zoom STORM images ($2 \times 2 \mu\text{m}$) with according line profiles are shown. Scale bar 0.5 μm . Images are representative for $n = 30 - 43$ cells per condition from 4 – 6 individual donors and experiments.

To quantitatively assess these observations, the ring density defined as number of rings per μm^2 was determined (Figure 5-3). In accordance to earlier observations, the ring density was significantly lower in non-activated compared to activated conditions. In all four cell types, the stimulation of the macrophages with IgG induced the formation of ring structures. Interestingly, M1- and M2-like macrophages have higher densities than M0-like and lung macrophages in activated condition.

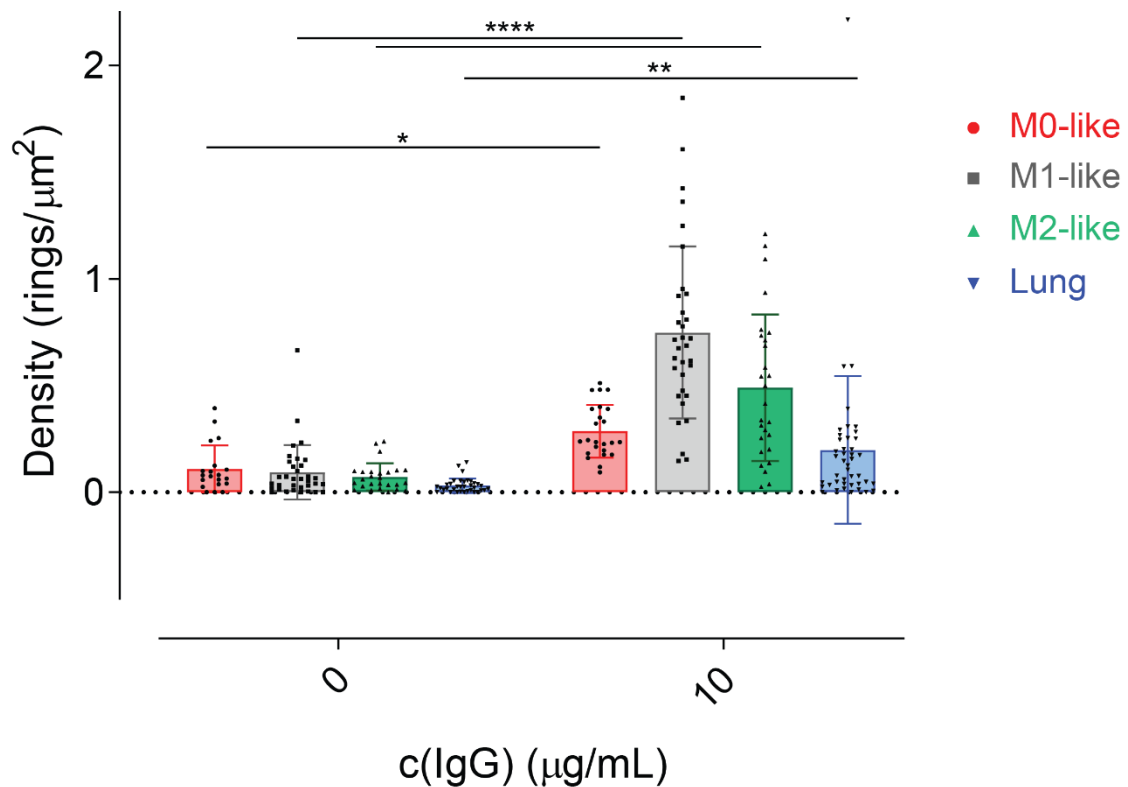


Figure 5-3: Activation through FcγRI induces the formation of rings. Macrophages were incubated on glass slides coated with PLL only (0 µg/mL IgG, non-activating condition) or PLL and IgG (10 µg/mL IgG, activating condition) for 15 min, fixed and stained with anti-CD81 labelled with AF647. Ring density defined as number of rings per µm² was determined for both conditions. One dot represents one cell. Bars show the geometric mean ± SD of n = 20 – 43 cells per condition from 3 – 6 individual donors and experiments. *, p ≤ 0.05; **, p ≤ 0.01; ****, p ≤ 0.0001; One-way ANOVA using GraphPad Prism.

Further, the nanoscale diameters of observed ring structures were measured and compared (Figure 5-4). As expected, ring structures at the synapse of M0-like macrophages displayed bigger diameters with a mean of 182 ± 95 nm compared to 92 ± 47 nm for M1-like macrophages, 75 ± 41 nm for M2-like macrophages and 93 ± 50 nm for lung macrophages. Interestingly, the size distribution of M0-like macrophage rings was also much wider (Figure 5-4B, red data). All other cell types showed a similar distribution with a relatively narrow range. In fact, most diameters measured were within ± 25 nm of their mean diameter (51.3% for M1-like macrophages, 77.3% for M2-like macrophages, 66.5% for lung macrophages). For M0-like macrophages on the other hand, only 23.8 % of all ring structures fall within ± 25 nm of its mean diameter.

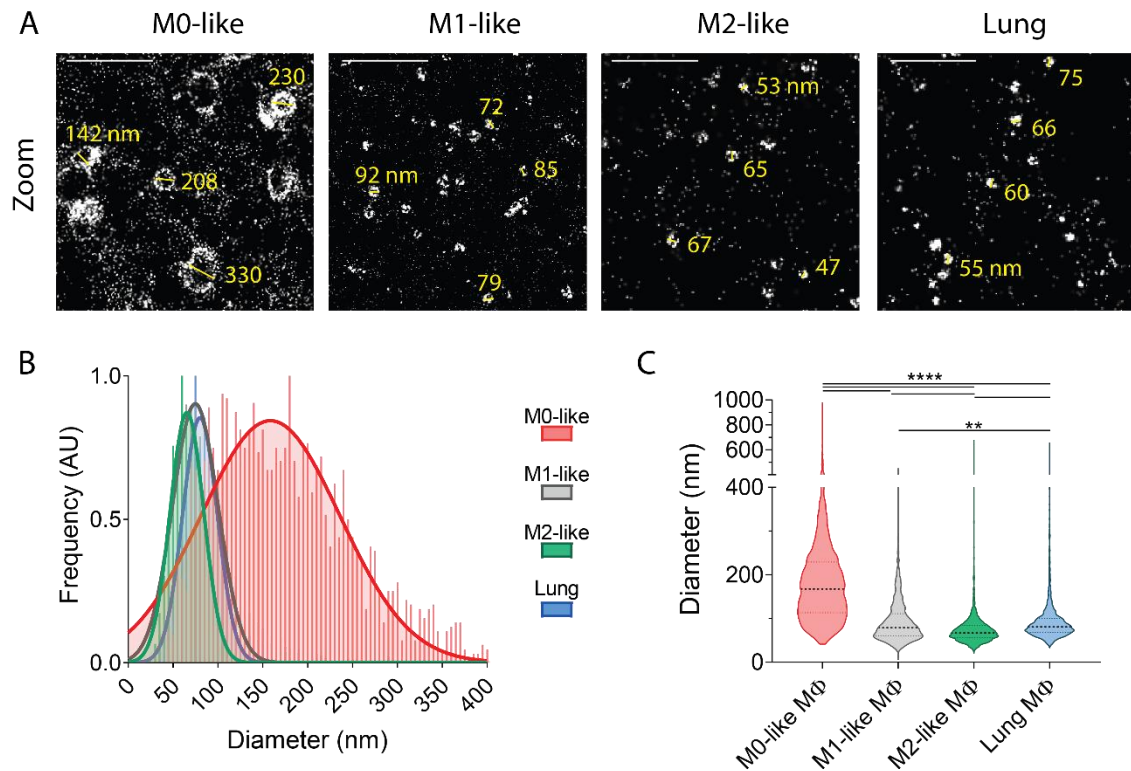


Figure 5-4: Different macrophage populations show distinct characteristics for nanometer-scale ring structures. Macrophages were incubated on glass slides coated with PLL and 10 $\mu\text{g}/\text{mL}$ IgG IgG for 15 min, fixed and stained with anti-CD81 labelled with AF647. **A)** Zoom STORM images (2 x 2 μm) with example measurements are shown. Scale bar 0.5 μm . Ring diameters were measured using ImageJ. **B)** Normalised histogram and **C)** violin plots are shown. n = 20 – 43 cells per condition from 3 – 6 individual donors and experiments. **, p \leq 0.01; ****, p \leq 0.0001; Kruskal-Wallis test using GraphPad Prism.

Taken together, CD81 formed into nanometer-scale ring structures at the synapse of M0-like, M1-like, M2-like and lung macrophages when activated through their Fc γ RI. Line profiles confirmed the circular nature of these structures. Upon activation, ring density increased significantly for all four cell types with M1-like and M2-like macrophages showing higher densities than M0-like and lung macrophages. Interestingly, M0-like macrophages displayed distinct characteristics in that their rings were larger and their size distribution much wider than that of the other cell types. This shows that observed ring structures have distinct characteristics for different macrophages, possibly hinting distinct functions and mechanisms underlying this phenomenon.

5.3.1.1 Spatial Characteristics and Timing of Ring Formation

Not only the characteristics of the ring structures themselves, but also their location at the synapse might differ between different cell types. To assess this, we compared secretion in three different areas of the synapse: the centre, the periphery or across the whole synapse. TIRF images of activated macrophages stained for CD81 were scored for the frequency of secretion within these three regions (Figure 5-5).

Macrophages were incubated on glass slides coated with PLL and 10 µg/mL IgG for 15 min, fixed and stained with anti-CD81 labelled with AF647. Interestingly, M0-like and lung macrophages, who both showed low ring densities (Figure 5-3) formed ring structures mostly across the whole synapse (16 out of 31 cells for M0-like macrophages; 20 out of 33 cells for lung macrophages). M1-like and M2-like macrophages on the other hand formed rings in the centre of the cell (21 out of 33 cells for M1-like macrophages; 28 out of 29 cells for M2-like macrophages). This means, M1-like and M2-like macrophages both spread widely with rings forming in the centre of the synapse and at a great density while M0-like and lung macrophages spread less widely and form ring structures across the whole synapse at lower density.

We next set out to test whether or not the formation of ring structures changed over time (Figure 5-6). For this, monocyte-derived macrophages were incubated on glass slides coated with PLL only (0 µg/mL IgG, non-activating condition) or PLL and IgG (10 µg/mL IgG, activating condition) for 15, 30, 60 and 120 min, fixed and stained with anti-CD81 labelled with AF647. STORM images were recorded and corrected prior to reconstruction. Ring densities significantly increased for all cell types after 15 min of incubation with IgG while levels remained low for non-activating conditions (Figure 5-6B-D). The ring density is enhanced at longer incubation times; however, this is also true for non-activating conditions and leads to the reduction of significance between activated and non-activated conditions. As 15 min was sufficient to induce a significant increase in ring density in activating conditions while keeping levels low in non-activating conditions, this time span was used for all further experiments.

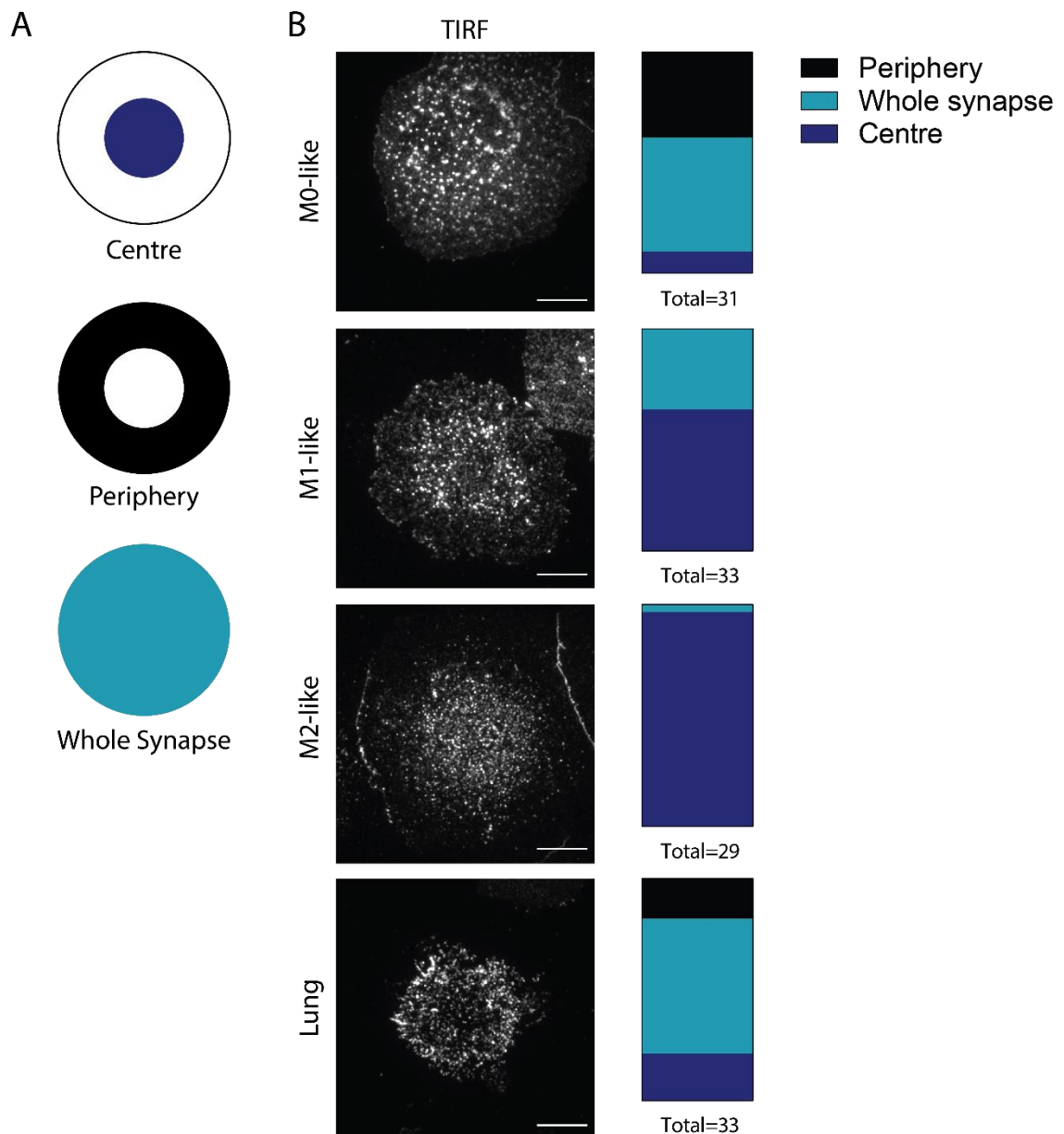


Figure 5-5: Ring structures appear in different areas across the synapse. Macrophages were incubated on glass slides coated with PLL and 10 $\mu\text{g}/\text{mL}$ IgG for 15 min, fixed and stained with anti-CD81 labelled with AF647. **A)** Ring structures were observed in the centre, the periphery or across the whole synapse. **B)** Representative TIRF images with according quantification of the proportions of where ring structures were observed. Scale bar 10 μm . $n = 29 - 33$ cells per condition from 3 individual donors and experiments.

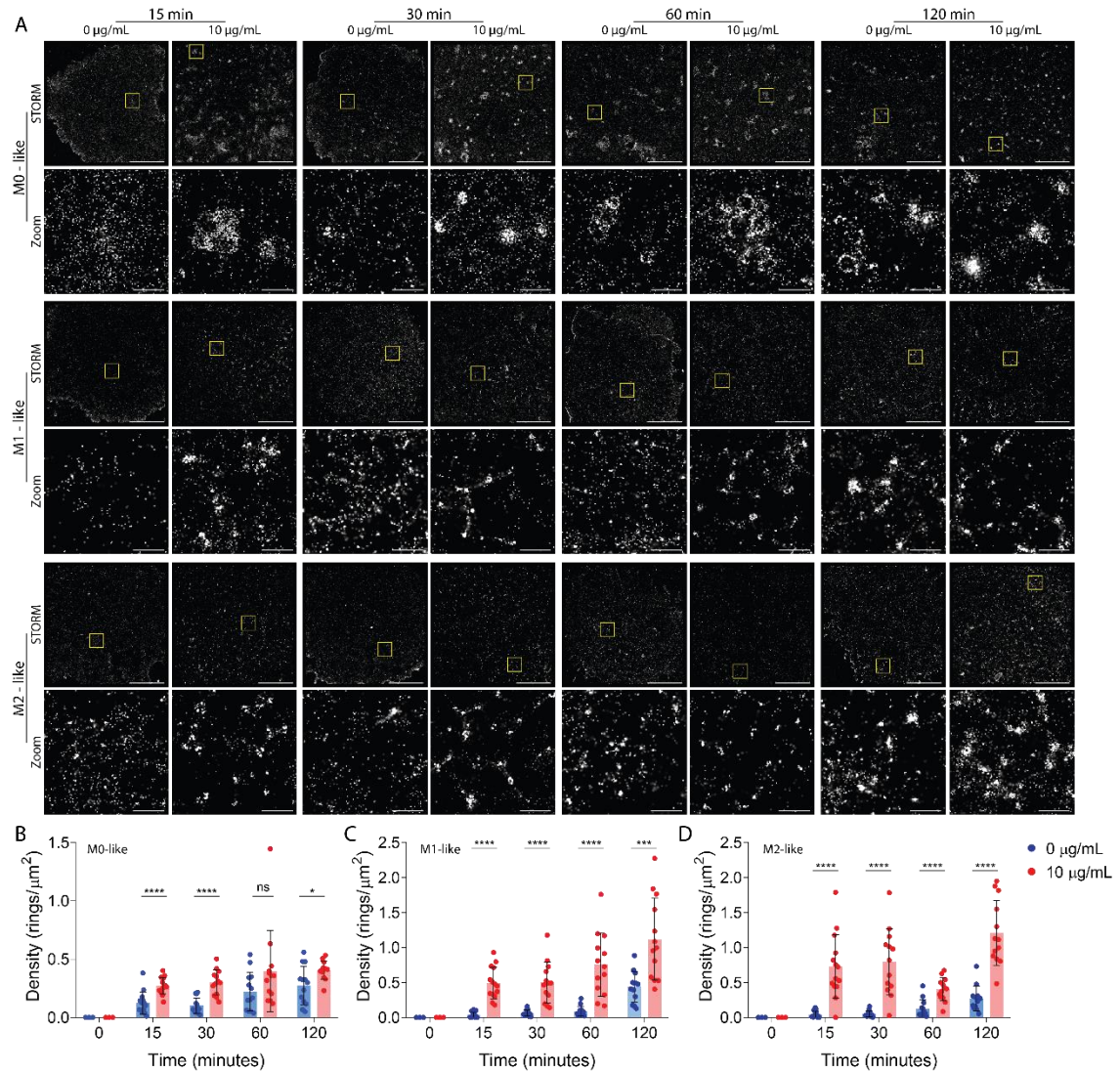


Figure 5-6: Formation of CD81 nanometer-scale ring structures over time. Macrophages were incubated on glass slides coated with PLL only (0 µg/mL IgG, non-activating condition) or PLL and IgG (10 µg/mL IgG, activating condition) for 15, 30, 60 or 120 min, fixed and stained with anti-CD81 labelled with AF647. **A)** Representative STORM and Zoom (2 x 2 µm) images for activated and non-activated conditions at all time points. Scale bar 5 µm, Zoom 0.5 µm. **B)** Ring density defined as number of rings per µm² for activated and non-activated conditions at different time points. One dot represents one cell. Bars show the geometric mean ± SD of n = 12 – 14 cells per condition from 2 individual donors and experiments. ns, not significant; *, p ≤ 0.05; ***, p ≤ 0.001; ****, p ≤ 0.0001; unpaired t-test using GraphPad Prism.

5.3.1.2 Culturing Human Lung Macrophages Influences Ring Characteristics

As established earlier, monocyte-derived macrophages generated using different differentiation protocols showed distinct ring characteristics. In particular, M0-like macrophages displayed significantly larger rings than M1-like and M2-like macrophages with M2-like macrophages displaying the smallest rings. However, all of these macrophages were generated by culturing blood monocytes for approximately 8 days (details see 2.1.1). Lung macrophages on the other hand are used fresh, directly upon isolation from the lung tissue. Therefore, to test the effect of the differentiation protocol on ring formation, lung macrophages were isolated, and half of the cells were used fresh while the other half was cultured like M0-like macrophages (Figure 5-7A). The protocol of M0-like macrophages was chosen to not influence the polarisation of the lung macrophages. In addition, characteristics of M0-like macrophage rings showed the biggest difference to fresh lung macrophages and was thus considered a good test.

As can be seen in Figure 5-7B-E culturing lung macrophages did influence the ring characteristics. Surprisingly, ring density was very high in non-activating as well as activating conditions suggesting the macrophages being activated without stimulation (Figure 5-7C). In addition, cultured lung macrophages displayed rings with bigger diameters. Similar to M0-like macrophages, the histogram of cultured lung macrophages was much broader than that of fresh lung macrophages (Figure 5-7D). This was also evident in their mean diameter that significantly increased from 94 ± 70 nm for fresh to 133 ± 82 nm for cultured lung macrophages.

Taken together, this could indicate that CD81 ring formation may be influenced by the polarisation status of the cell in question. However, it is surprising that cultured lung macrophages were activated without stimulation. It has to be kept in mind though that lung macrophages need their tissue environment to function properly. Removing them from this environment could potentially lead to the cell being stressed and activated. Within the tissue, lung macrophages face an environment with a high antigen load and are in constant contact with the extracellular matrix as well as other cells.

These interactions are missing in a sterile *ex vivo* model like the one used here, possibly leading to a different reaction of cultured vs. freshly used macrophages.

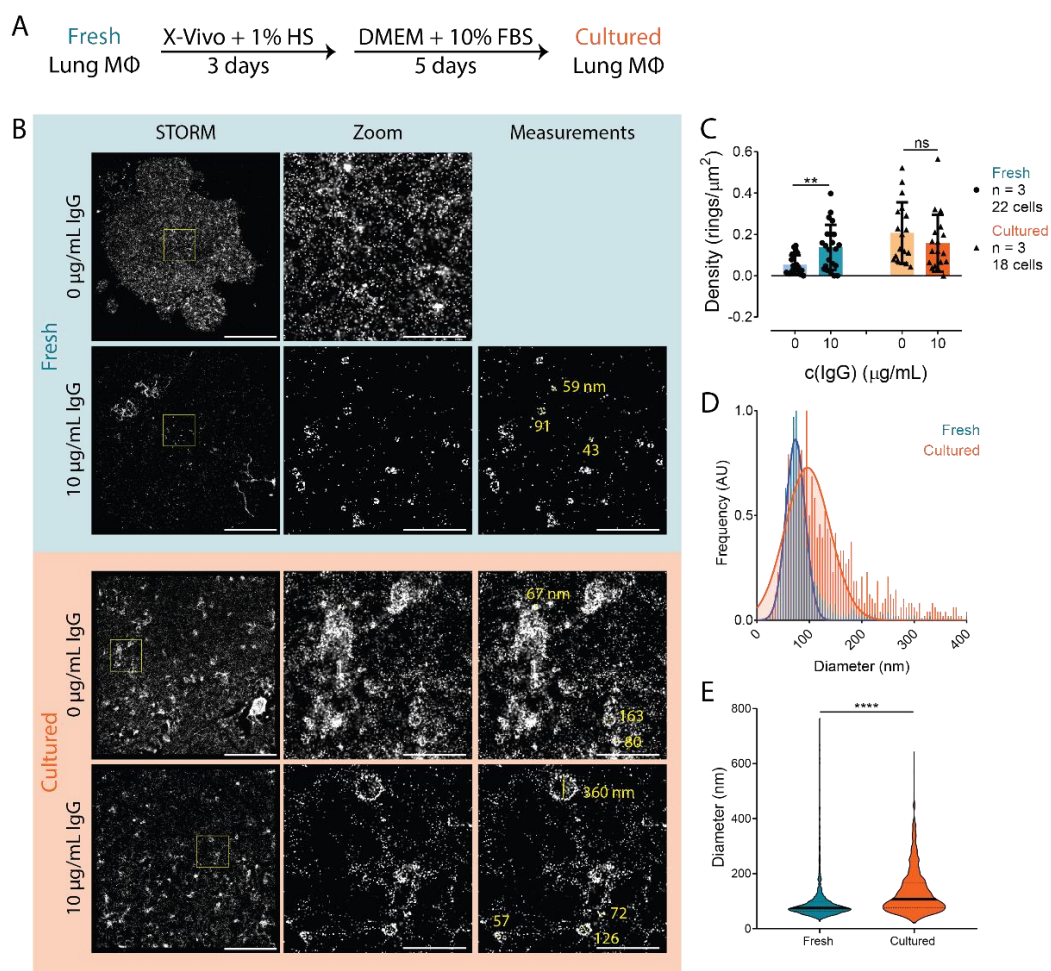


Figure 5-7: Culturing lung macrophages influences their CD81 ring characteristics. Human lung macrophages were isolated and half of the cells were used fresh. The other half was cultured for 3 days in X-Vivo media supplemented with 1% HS followed by 5 days in DMEM media supplemented with 10% FBS, 1% L-glutamine, 1% Penicillin/Streptomycin and 10 mM HEPES buffered saline (**A**). Macrophages were incubated on glass slides coated with PLL only (0 µg/mL IgG, non-activating condition) or PLL and IgG (10 µg/mL IgG, activating condition) for 15 min, fixed and stained with anti-CD81 labelled with AF647. **B**) Representative STORM and Zoom (3 x 3 µm) images for activated and non-activated conditions for fresh and cultured cells and Measurements where applicable. Scale bar 5 µm, Zoom 1 µm. **C**) Ring density for both conditions for fresh and cultured cells. Each dot represents one cell. Bars show the geometric mean \pm SD of n = 18 – 22 cells per condition from 3 individual donors and experiments with matching donors for fresh and cultured cells. **D**) Normalised histogram of ring diameters for activated conditions for fresh and cultured cells with a Gaussian curve fitted for the data. **E**) Violin plots of ring diameters for activated conditions for fresh and cultured cells with mean diameter. ****, $p \leq 0.0001$; Mann-Whitney test using GraphPad Prism.

5.3.2 Formation of CD81-Rings at the Membrane of Human Macrophages Incubated on Activating Lipid Bilayers

So far, macrophages were incubated on coated glass slides which proved to be a reliable model that is especially compatible with imaging the immune synapse. However, glass represents an artificial system, which may influence cellular response. To study the formation of CD81-rings in a more biological relevant scenario, macrophages were incubated on planar lipid bilayers instead of glass slides. Bilayers contained 10 µg/mL IgG to activate the macrophages, being physiologically more similar to an opsonised target compared to glass slides. After 20 min of incubation, cells were fixed and stained with anti-CD81 mAb labelled with AF647 (Figure 5-8A). As expected, nanometer-scale ring structures formed and appeared similar to those on macrophages activated on glass slides (Figure 5-1, Figure 5-8B). Line profiles confirmed their circular structure, with two main peaks on the outside and a dip in the middle (Figure 5-9). In contrast to ring structures observed on macrophages activated on IgG-coated glass slides, M0-like macrophages seem to display slightly smaller diameter. In the images, there is no obvious difference evident. In addition, line profiles show similar diameters for all four cell types. However, for a reliable interpretation, the quantitative comparison of ring characteristics of the different cell types is necessary.

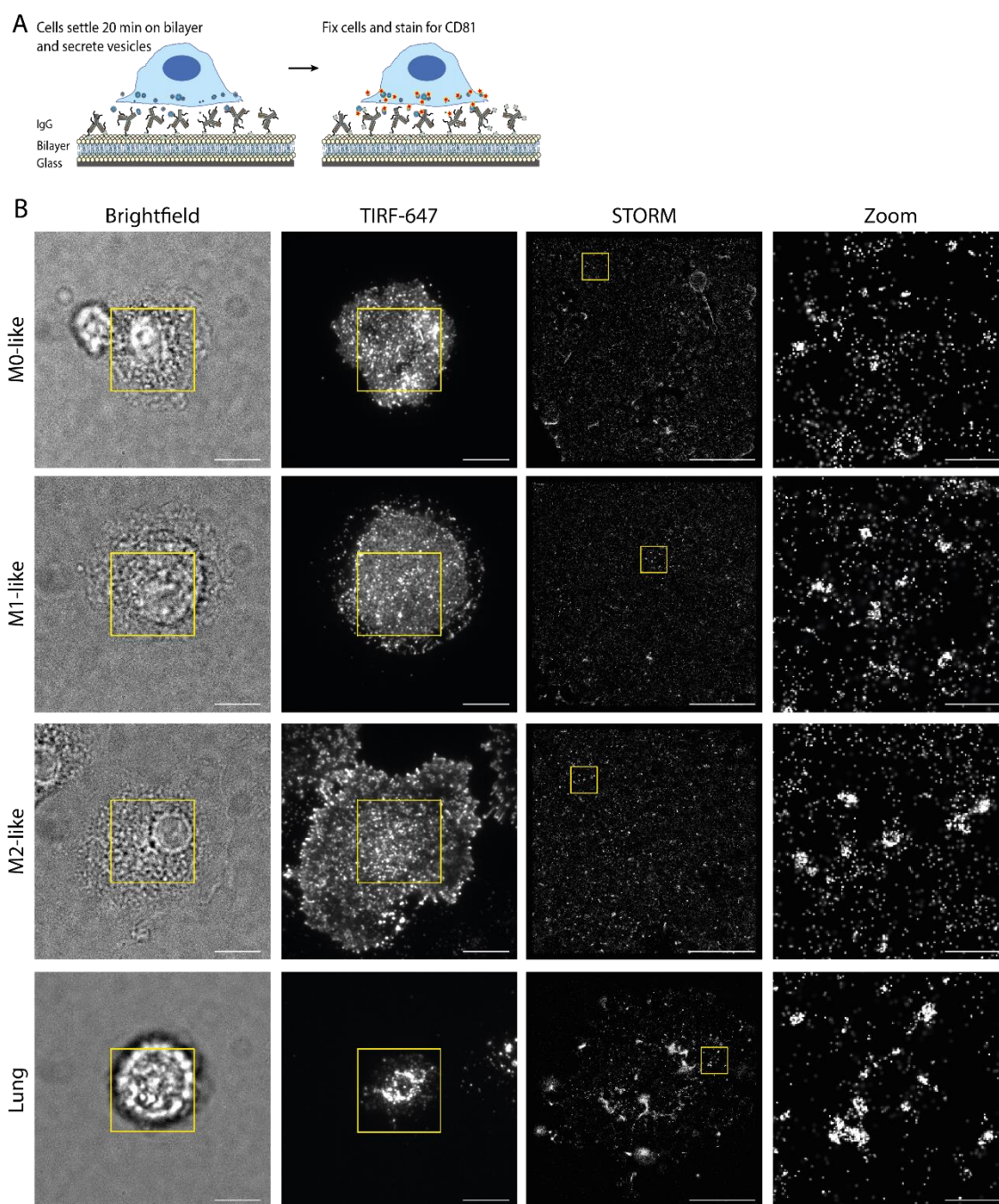


Figure 5-8: CD81 forms into nanometer-scale ring structures at the membrane of macrophages incubated on planar lipid bilayers containing IgG. **A)** Macrophages were plated onto bilayers containing 10 $\mu\text{g}/\text{mL}$ IgG for 20 min, then fixed and stained with anti-CD81 mAb labelled with AF647. **B)** Representative Brightfield, TIRF, STORM and Zoom ($2 \times 2 \mu\text{m}$) images. Scale bar 10 μm for Brightfield and TIRF images, 5 μm for STORM images and 0.5 μm for Zoom images. $n = 18 - 22$ cells per condition from 3 independent donors and experiments.

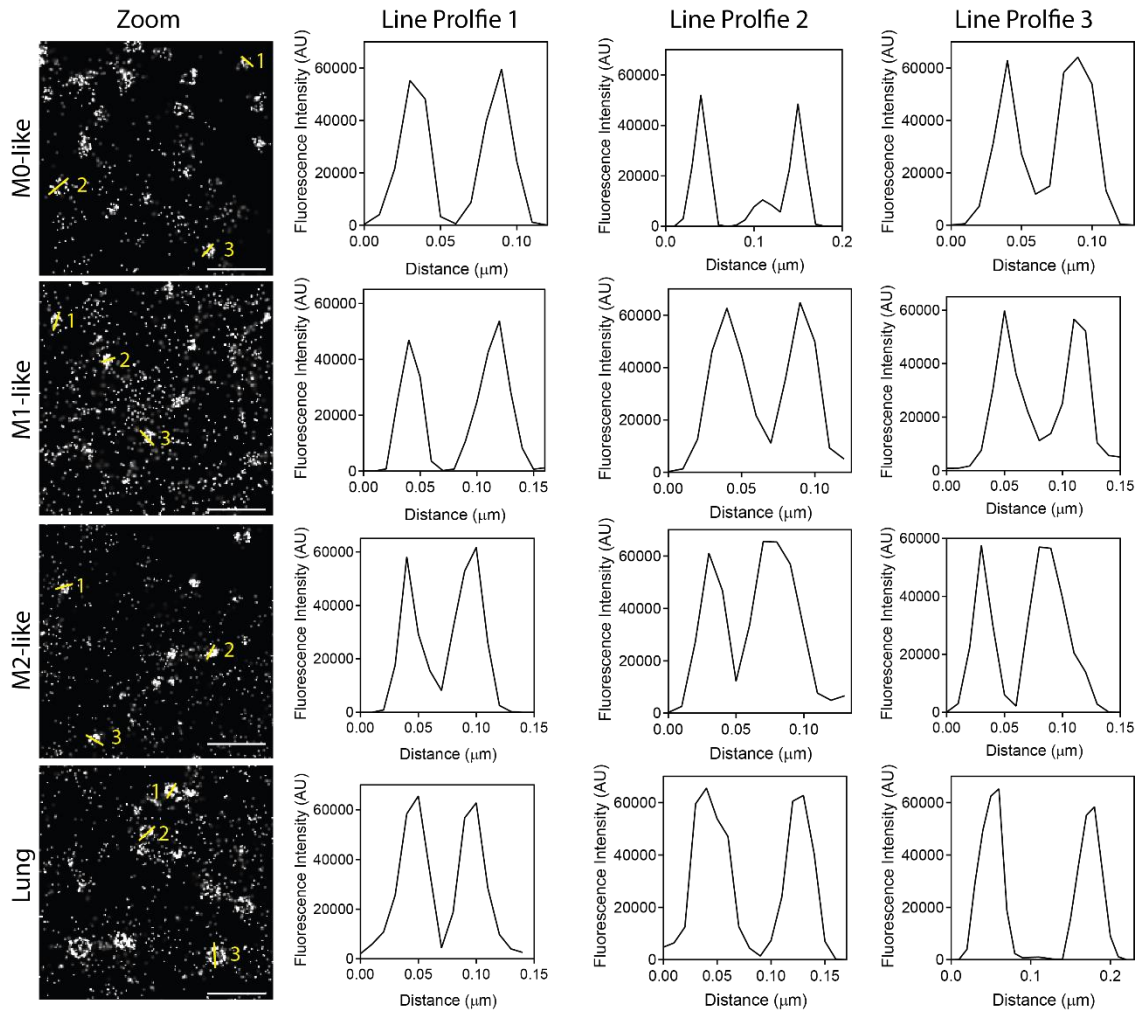


Figure 5-9: Line profiles of CD81-ring structures at the membrane of macrophages activated on planar lipid bilayers. Macrophages were incubated on lipid bilayers containing 10 $\mu\text{g/mL}$ IgG for 20 min, fixed and stained with anti-CD81 labelled with AF647. Zoom STORM images ($2 \times 2 \mu\text{m}$) with according line profiles are shown. Scale bar $0.5 \mu\text{m}$. Images are representative for $n = 18 - 22$ cells per condition from 3 independent donors and experiments.

To analyse ring characteristics on a cell-by-cell basis, the density defined as rings per μm^2 was determined and compared to that of macrophages activated on IgG coated glass slides (Figure 5-3 vs. Figure 5-10). The density of secretions for macrophages activated on lipid bilayers was slightly higher than that for coated glass slides for all cell types but M1-like macrophages. More precisely, the ring density increased from 0.285 ± 0.124 rings/ μm^2 to 0.389 ± 0.290 rings/ μm^2 for M0-like macrophages, from 0.490 ± 0.343 rings/ μm^2 to 0.878 ± 0.482 rings/ μm^2 for M2-like macrophages and from 0.198 ± 0.346 rings/ μm^2 to 0.877 ± 0.997 rings/ μm^2 for lung macrophages. The density of M1-like macrophage vesicles decreased from 0.748 ± 0.404 rings/ μm^2 to $0.703 \pm$

0.746 rings/ μm^2 . Interestingly, the ring densities for macrophages activated on lipid bilayers displayed no significant differences. For glass slides on the other hand, M0-like and lung macrophages displayed significantly lower ring densities than M1- and M2-like macrophages. Thus, M0-like and lung macrophages show the biggest increase in ring density on bilayers compared to glass slides.

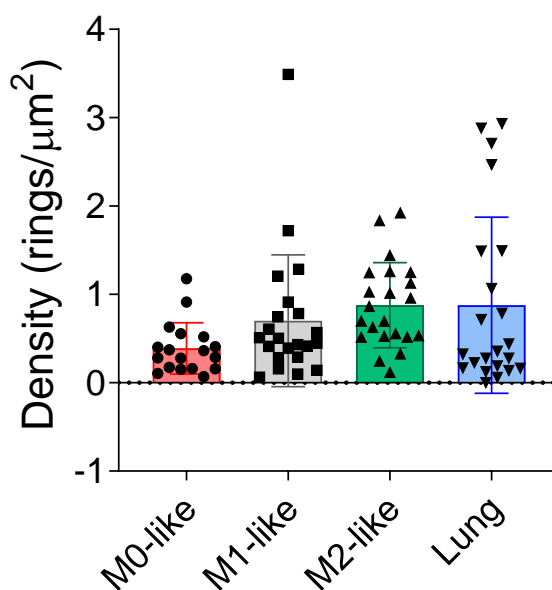


Figure 5-10: Incubation of macrophages on activating planar lipid bilayers induced CD81-ring formation. Macrophages were plated onto bilayers containing 10 $\mu\text{g}/\text{mL}$ IgG for 20 min, then fixed and stained with anti-CD81 labelled with AF647. Shown is the ring density of macrophages incubated on bilayers containing 10 $\mu\text{g}/\text{mL}$ IgG. Each dot represents one cell. Bars show the geometric mean \pm SD of $n = 18 - 22$ cells per condition from 3 independent donors and experiments.

Next, the diameters of CD81-rings were measured (Figure 5-11). Interestingly, diameters of the four different cell types were less heterogeneous than those measured on cells activated on coated glass slides (Figure 5-4). Especially M0-like macrophages were less distinct compared to the other cell types. This was also obvious in that their mean diameter was more similar compared to the other cell types. In fact, on bilayers the mean diameter decreased for three out of four cell types. M0-like macrophages showed the biggest decrease from 182 ± 95 nm on glass to 114 ± 75 nm on bilayers. M1-like and lung macrophages showed smaller changes from 92 ± 47 nm to 83 ± 54 nm and 93 ± 50 nm to 81 ± 69 nm respectively. Only for M2-like macrophages the diameter

increased from 75 ± 41 nm to 91 ± 64 nm. Nevertheless, M0-like macrophages still displayed larger ring structures than all other cell types following the same trend observed on glass slides.

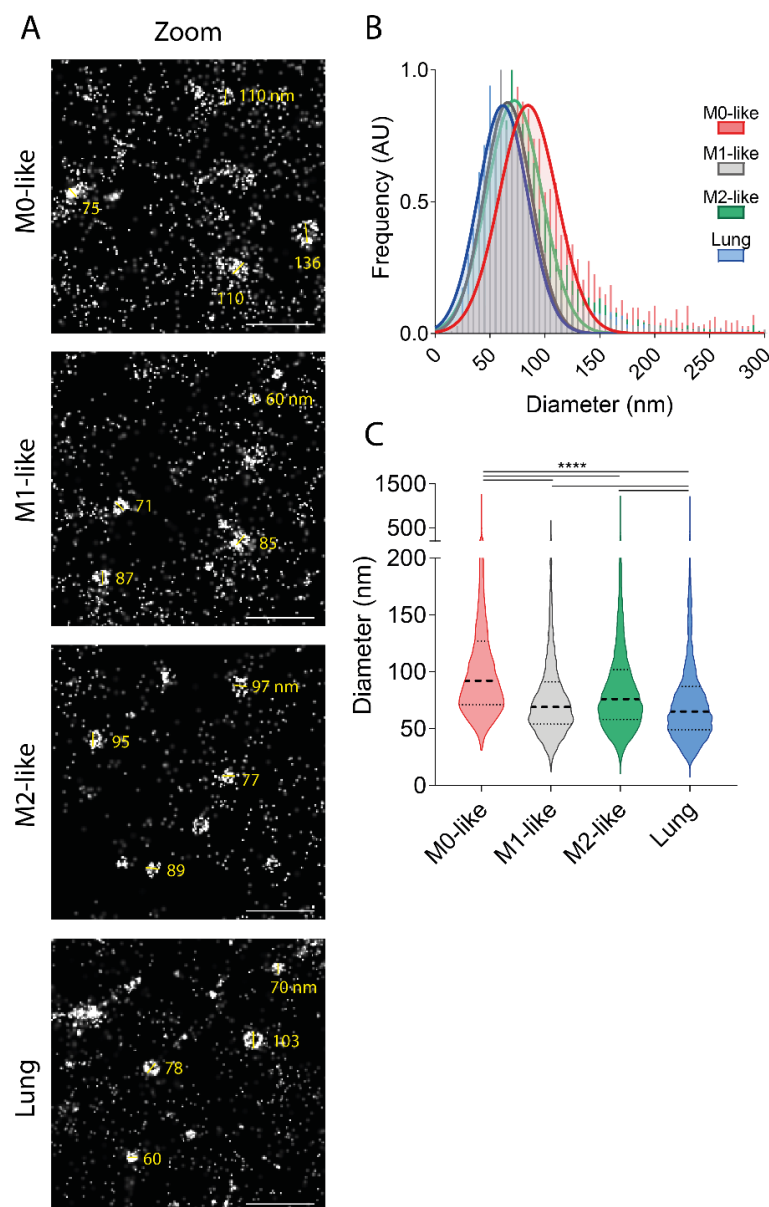


Figure 5-11: Characteristics of CD81-rings at the membrane of macrophages activated on lipid bilayers.

Macrophages were plated onto bilayers containing 10 $\mu\text{g/mL}$ IgG for 20 min, then fixed and stained with anti-CD81 labelled with AF647. **A)** Representative Zoom (STORM; $2 \times 2 \mu\text{m}$) images. $0.5 \mu\text{m}$. **B)** Histogram and **C)** violin plots of ring diameters. $n = 18 - 22$ cells per condition from 3 independent donors and experiments. ; ****, $p \leq 0.0001$; Kruskal-Wallis test using GraphPad Prism.

Taken together, the formation of nanometer-scale ring structures of CD81 was observed at the membrane of macrophages activated on planar lipid bilayers containing IgG, similar to those observed when activating macrophages on IgG-coated glass slides. Ring density on lipid bilayers was comparable for all four cell types but slightly higher compared to glass slides, possibly indicating a better interaction of the cells with the bilayer compared to the glass slide. Interestingly, ring diameters decreased for all but M2-like macrophages on lipid bilayers with the overall trend staying the same as on glass slides: M0-like macrophages display bigger ring-diameters than the other three cell types.

5.3.3 Macrophages Secrete Extracellular Vesicles across the Immune Synapse

CD81 is part of a protein super family called tetraspanins. Tetraspanins are known to play a role in protein trafficking and membrane compartmentalization and are used as marker for extracellular vesicles^{192,193,328}. Thus, observed CD81-ring structures could be extracellular vesicles, captured directly upon secretion at the base membrane of macrophages. To test this hypothesis, macrophage secretions were imaged using a recently developed imaging technique termed 'shadow imaging'³²⁹. Therefore, macrophages were incubated on lipid bilayers containing biotinylated IgG for 20 min followed by a pulsed stain with streptavidin-AF488 (Figure 5-12A). When detaching the cells afterwards, a shadow was left behind, indicating the area where the cells had interacted with the bilayer and its ligands (Figure 5-12B, TIRF-488). Additional staining of CD81-AF647 visualised vesicles that were secreted by the macrophages prior to attachment (Figure 5-12B, TIRF-647, STORM and Zoom).

As can be seen in Figure 5-12B, vesicles that were left behind by the macrophages were captured in the bilayer and resolved in nanometer-scale ring structures similar to those observed when cells were not detached (Figure 5-1 and Figure 5-8). Importantly, brightfield images ensured that the cells were fully detached (Figure 5-12B; Brightfield). In fact, this is also evident in the STORM images of vesicles that display much lower levels of background than images of the cell membrane. When imaging the membrane,

the signal does not only arise from extracellular vesicles but also the membrane itself, as CD81 is a normal part of the cell membrane. Line profiles of secreted vesicles confirmed the circular nature and similar diameters compared to CD81-rings observed before (Figure 5-13).

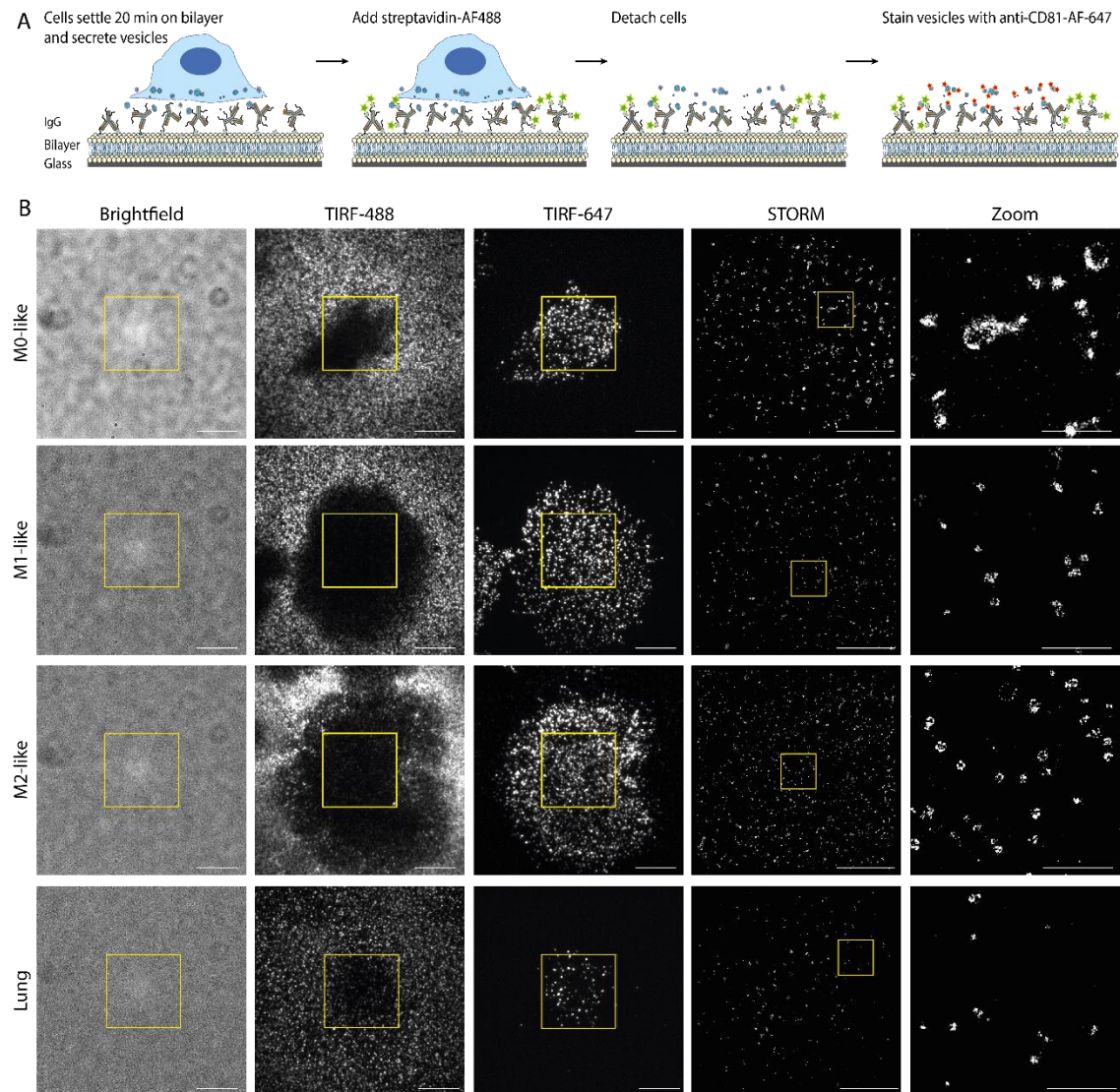


Figure 5-12: Shadow imaging reveals the secretion of extracellular vesicles by IgG-activated macrophages. A) Macrophages are incubated on lipid bilayer containing 10 $\mu\text{g}/\text{mL}$ biotinylated IgG for 20 min, then pulsed with streptavidin-AF488 followed by the detachment of the cells, fixation of the remains and final staining with anti-CD81 labelled with AF647. **B)** Representative Brightfield, TIRF, STORM and Zoom images. Scale bar 10 μm for Brightfield and TIRF images, 5 μm for STORM images and 1 μm for Zoom images. $n = 21 - 24$ cells per condition from 3 individual donors and experiments.

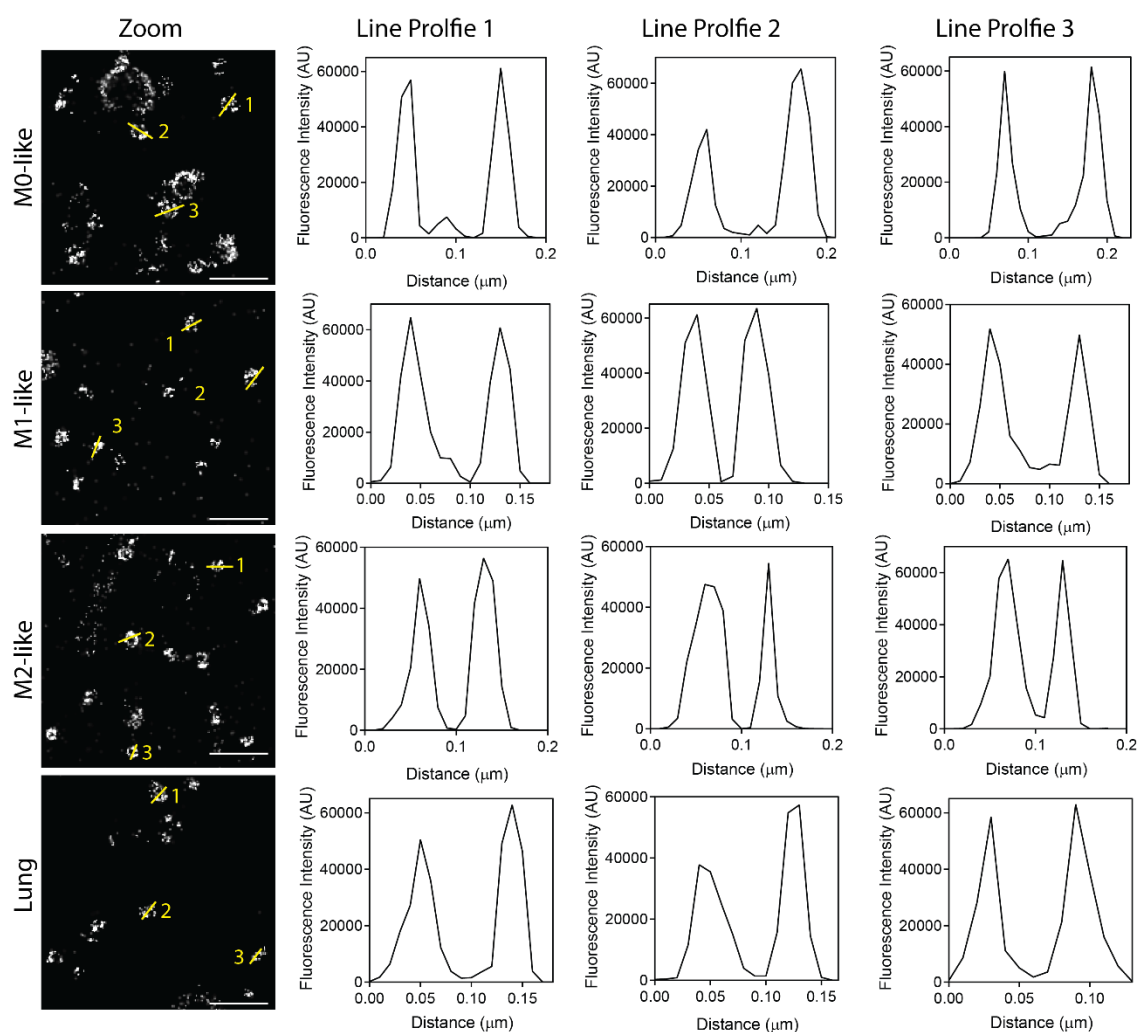


Figure 5-13: Line profiles of extracellular vesicles secreted by macrophages onto activating lipid bilayers. Macrophages were incubated on lipid bilayers containing 10 $\mu\text{g/mL}$ IgG for 20 min, cells detached and remains fixed and stained with anti-CD81 labelled with AF647. Zoom STORM images (2 x 2 μm) with according line profiles are shown. Scale bar 0.5 μm . Images are representative for $n = 3$ individual donors and experiments.

So far, the characteristics of observed ring structures were obtained manually, by counting and measuring rings using ImageJ. Due to images of vesicles displaying much lower backgrounds than images of the cell membrane, an automated analysis is possible. This would ensure robust data collection and avoid subjectivity. Thus, background corrected STORM images of extracellular vesicles left behind on lipid bilayers were analysed using a custom-made macro in ImageJ. The macro was able to detect, count and measure the area of vesicles (Figure 5-14A, Example 1). However, in few occasions, the macro missed a vesicle (Figure 5-14A, Example 2) or divided bigger

vesicles into several small ones (Figure 5-14A, Example 3). All images were checked manually and mistakes corrected. Vesicle diameters were calculated from measured areas with the following equation:

$$d = 2 \sqrt{\frac{A}{\pi}} \quad (4)$$

Here, d is the diameter and A the area of the ring structure. To ensure correct performance, a portion of cells were analysed with the macro as well as manually and compared (Figure 5-14B-E). Because larger vesicles were more challenging for the macro to detect, data from M0-like macrophages was chosen. The number of vesicles detected on the individual cells varied slightly with no trend visible (Figure 5-14B). More importantly, the mean diameter of vesicles detected on individual cells was established correctly (Figure 5-14C). In addition, the diameters of all vesicles measured showed similar distributions, regardless of the detection via macro or manually (Figure 5-14D-E).

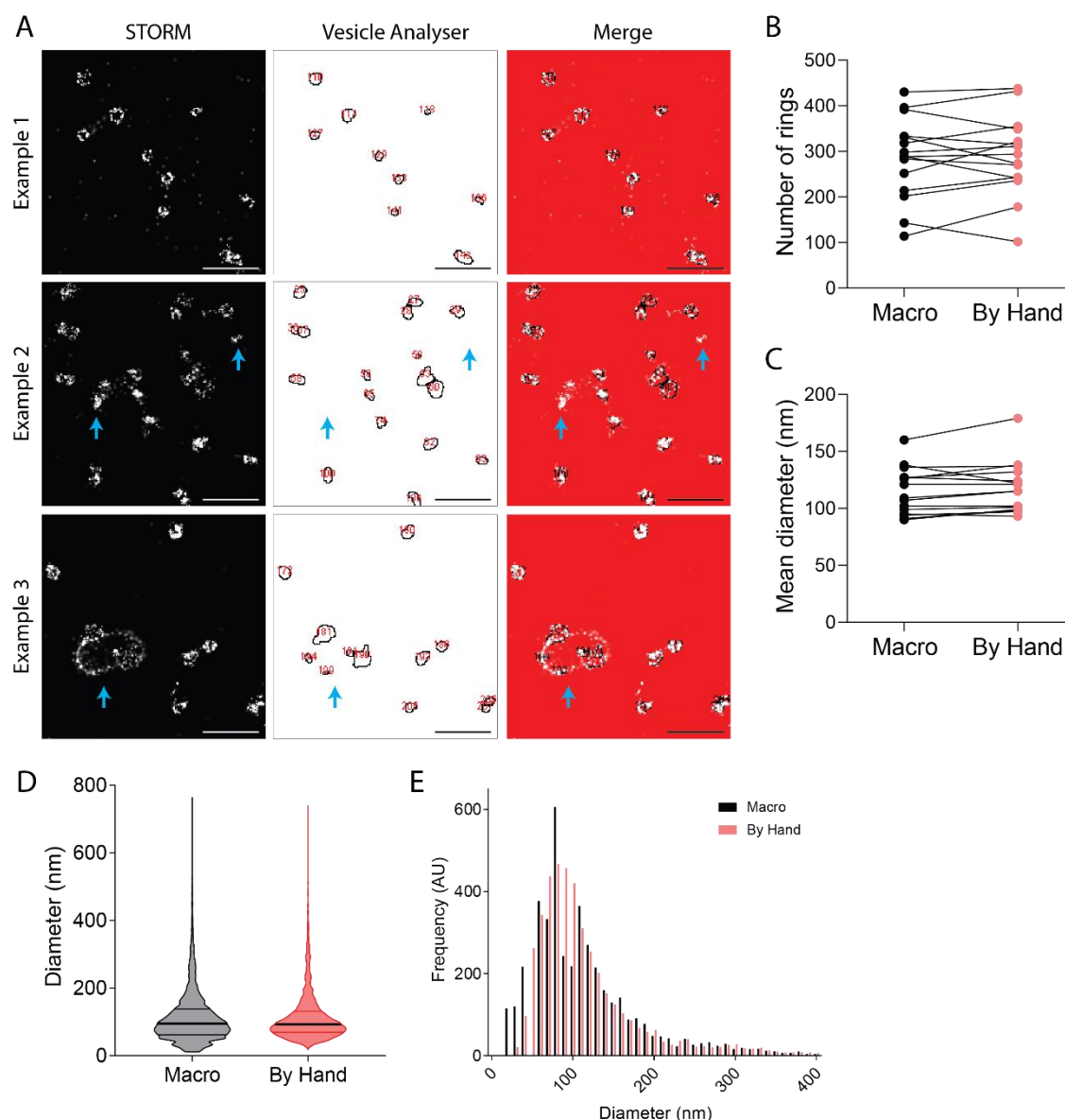


Figure 5-14: Automated analysis of vesicle characteristics using a custom-made macro. Images from secretions in Figure 5-12 were analysed using a custom made macro. All results were checked and in few occasions where the macro failed, corrected. **A)** Example STORM images with according results of the vesicle analyser and overlay. Scale bar 0.5 μ m. **B-E)** Data from M0-like macrophages analysed by the macro was compared to manual analysis to verify correct performance. One dot represents one cell with $n = 3$ individual donors and experiments and 15 cells analysed in total. **B)** Number of vesicles counted. **C)** Mean diameters of vesicles per cell analysed by the macro and by hand. **D)** Diameters of all vesicles measured by the macro and by hand. **E)** Histogram of diameters analysed with the macro and manually.

However, small differences are evident. For example, the data obtained manually presents 'smoother' than that by the macro, which shows gaps in the diameter distribution (Figure 5-14D-E). This can be explained by the different ways to establish the diameter and the pixel size. STORM images have a pixel size of $1 \times 10^{-4} \mu\text{m}$ (or 0.1 nm). When obtained manually, diameters were measured directly, with a maximum resolution of 0.1 nm. The macro on the other hand utilises the area to calculate the diameter (equation (4)). The area is measured with a resolution of $1 \times 10^{-4} \mu\text{m}^2$ (or 100 nm^2), which is equivalent to a diameter of 11 nm. Anything smaller than this cannot be detected. In addition, diameters calculated from areas have a certain step size. For example, $1 \times 10^{-4} \mu\text{m}^2$ corresponds to a diameter of 11 nm, $2 \times 10^{-4} \mu\text{m}^2$ to a diameter of 16 nm, $3 \times 10^{-4} \mu\text{m}^2$ to a diameter of 20 nm and so forth. This step size is much smaller for manually measured diameters, which leads to no obvious gaps in the diameter distribution and smoother data. Nevertheless, despite these discrepancies none of the parameters measured was significantly different for the different detection methods. In fact, the mean diameter of all vesicles measured was $115 \pm 75 \text{ nm}$ for manual and $114 \pm 78 \text{ nm}$ for automated analysis. Thus, with only 1 nm difference, the macro proved to be precise and robust and ensures a non-subjective analysis. In the following, it was applied to determine the vesicle characteristics of all four cell types.

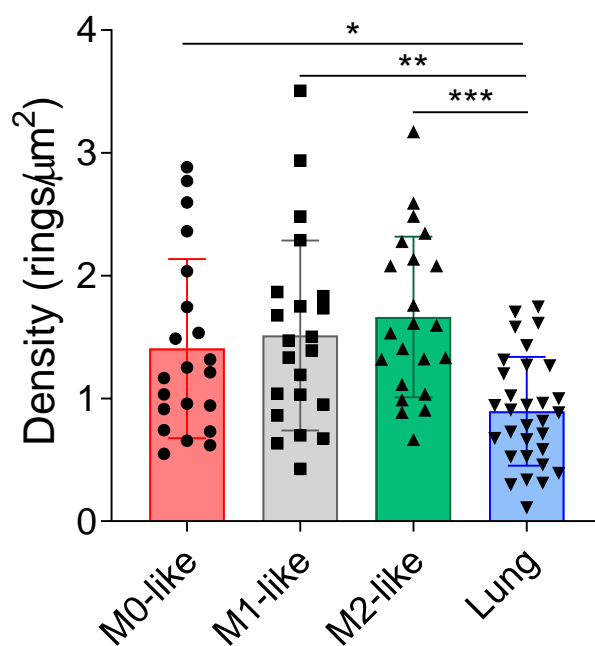


Figure 5-15: Macrophages secrete vesicles when activated on lipid bilayers containing IgG. Macrophages were incubated on lipid bilayers containing 10 μg/mL IgG for 20 min, detached and the remains fixed and stained with anti-CD81 labelled with AF647. Ring density defined as number of rings per μm² was determined. One dot represents one cell. Bars show the geometric mean ± SD of n = 21 – 31 cells per condition from 3 – 4 individual donors and experiments. *, p ≤ 0.05; **, p ≤ 0.01; ***, p ≤ 0.001; One-way ANOVA using GraphPad Prism.

As already established, macrophages activated through their FcγRI secrete vesicles that appear as nanometer-scale ring structures in STORM images. These images can be used to determine vesicle characteristics like the density defined as vesicles per μm² on a cell-by-cell basis. However, when detaching cells and imaging the secretions, the cell area cannot be measured, and thus, the density not calculated. This was addressed with the application of the ‘shadow’ imaging technique, which marks the area where the cell interacted with the bilayer prior to attachment (Figure 5-12A). Thus, vesicle density was determined for M0-like, M1-like, M2-like and lung macrophage secretions utilising a custom macro in ImageJ (Figure 5-15). Interestingly, the density was significantly increased in secretions compared to images taken with the cell still attached (Figure 5-3, Figure 5-10 and Figure 5-15). This may be explained by the ‘cleaner’ images from secretions. It is easier to identify a vesicle in a low background

image. When cells are still present, vesicles need to be identified amongst the signal arising from the membrane itself.

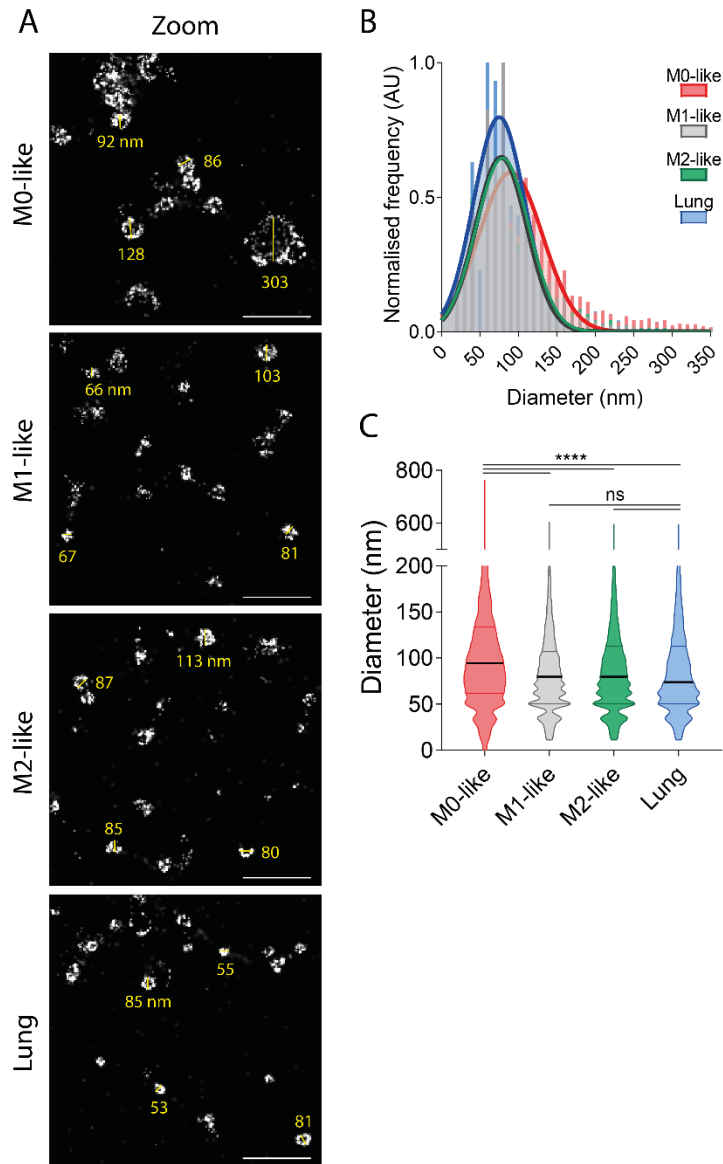


Figure 5-16: Characteristics of vesicles left behind on lipid bilayers. Macrophages were incubated on lipid bilayers containing 10 µg/mL IgG for 20 min, detached and the remains fixed and stained with anti-CD81 labelled with AF647. **A)** Representative Zoom (STORM) images (2 x 2 µm) with example measurements. Scale bar 0.5 µm. Ring diameters were measured using ImageJ. **B)** Histogram and **C)** violin plots of diameters. n = 21 – 31 cells per condition from 3 – 4 individual donors and experiments. ns, not significant; ****, p ≤ 0.0001; Kruskal-Wallis test using GraphPad Prism.

From all four cell types, lung macrophages have the lowest density. This was also the case for cells activated on glass slides (Figure 5-3, Lung data). However, the densities differ greatly with a mean of 0.198 ± 0.346 rings/ μm^2 for cells activated on IgG coated glass and 0.895 ± 0.442 rings/ μm^2 for secretions captured on lipid bilayers. Densities of monocyte-derived macrophages increase slightly but not significantly from M0- via M1- to M2-like macrophages.

Next, the vesicle diameters were determined (Figure 5-16). Histograms as well as violin plots were very similar to those of macrophages activated on bilayers without attachment of the cells (Figure 5-11B-C and Figure 5-16B-C). This was expected as cells were activated in the same way. However, when detaching the cells the biggest diameters measured lied between 600 - 800 nm while they ranged to up to 1300 nm when cell were still there. This may indicate that very few, very big vesicles were detached with the cells. However, it could also mean, that membrane folds or protrusions were mistaken for vesicles and detaching the cells yields more accurate data. In any case, the mean diameters were strikingly similar with 114 ± 75 nm and 112 ± 79 nm for M0-like macrophages, 83 ± 54 nm and 85 ± 49 nm for M1-like macrophages, 91 ± 64 nm and 89 ± 54 nm for M2-like macrophages and 81 ± 69 nm and 91 ± 59 nm for lung macrophages for cells still present and cells detached respectively. This showed that vesicle characteristics were reproducible independent of cell detachment and analysis technique, as data with cells still present was obtained manually while secretions were analysed using the macro.

Taken together, the detachment of macrophages activated on IgG-containing lipid bilayers revealed vesicles left behind. These vesicles appeared as nanometer-scale ring structures when imaged with STORM and line profiles could confirm their circular structure. Images of vesicles alone displayed less background than images of membranes which enabled their automated analysis. This may also explain the higher vesicle density found for secretions. Vesicle diameters of macrophages activated on

planar lipid bilayers did not change upon detachment of the cells, highlighting the reproducibility of the phenomenon as well as the robustness of the automated analysis.

5.3.4 Isolation of Extracellular Vesicles via Ultracentrifugation

In recent years, the interest to study extracellular vesicles increased enormously. Thus, several techniques on how to isolate them are known. One of the most common techniques is differential ultracentrifugation. In fact, vesicles are mostly studied after isolation. Therefore, to further validate that observed ring structures are in fact extracellular vesicles, the latter were isolated and imaged. Macrophages were stimulated in solution with beads coated with 10 $\mu\text{g/mL}$ IgG for 90 min and cells, large and small extracellular vesicles were isolated using differential ultracentrifugation (Figure 5-17A). Isolated fractions were then incubated on PLL-coated microscopy slides for 20 min, fixed and stained with anti-CD81 labelled with AF647.

As expected, vesicles appeared as nanometer-scale ring structures when imaged with STORM (Figure 5-17B). Images with cells still present also displayed higher backgrounds than images of vesicles (Figure 5-17B, Cells vs. Large EV and Small EV). This is in accordance with observations made so far. In addition, line profiles could confirm the circular structure and similar sizes to ring structures observed before. Thus, CD81-ring structures forming at the membrane of macrophages are likely to be extracellular vesicles, secreted upon activation through their Fc γ RI.

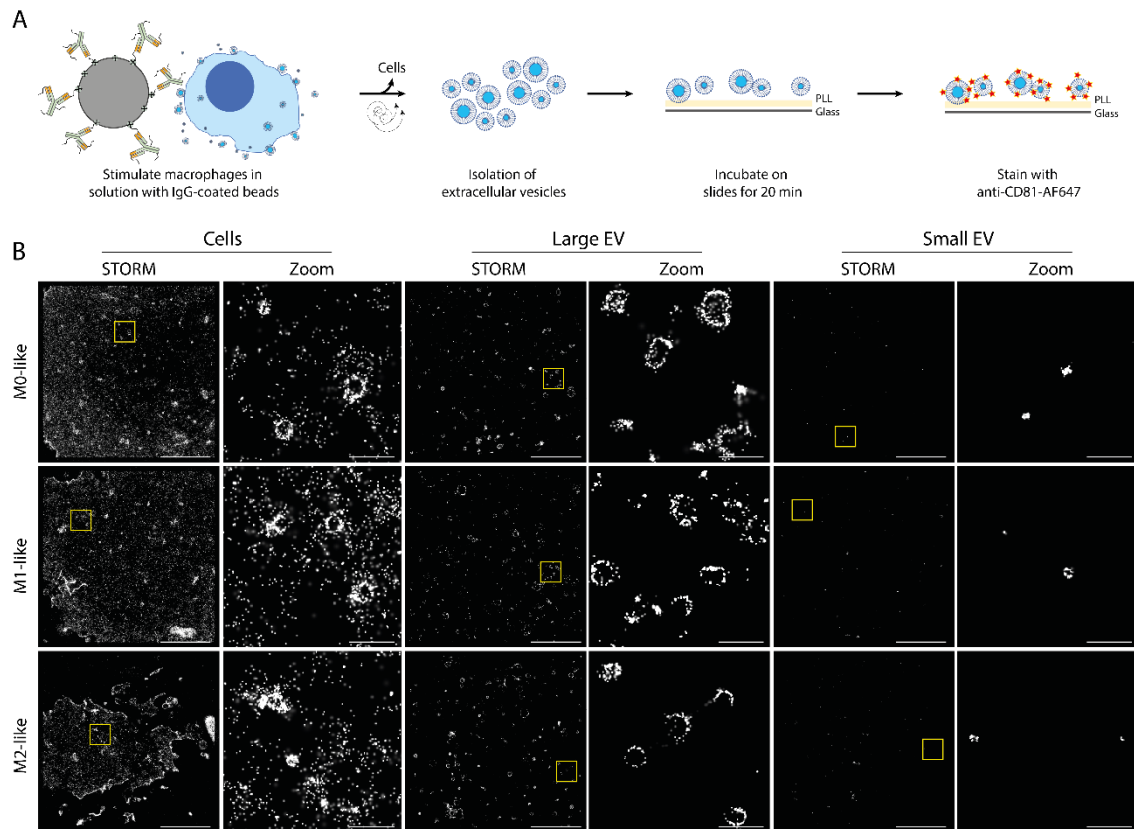


Figure 5-17: Vesicles isolated via ultracentrifugation appear as nanometer-scale ring structures when imaged with STORM. A) Macrophages were stimulated in solution with beads coated with 10 $\mu\text{g}/\text{mL}$ IgG for 90 min and cells, large and small extracellular vesicles were isolated using differential ultracentrifugation. Isolated fractions were incubated on PLL-coated microscopy slides for 20 min, fixed and stained with anti-CD81 labelled with AF647. **B)** Representative STORM and Zoom ($2 \times 2 \mu\text{m}$) images. Scale bar 5 μm , Zoom 0.5 μm . $n = 18 - 20$ images per condition from 3 individual donors and experiments. EV, extracellular vesicles.

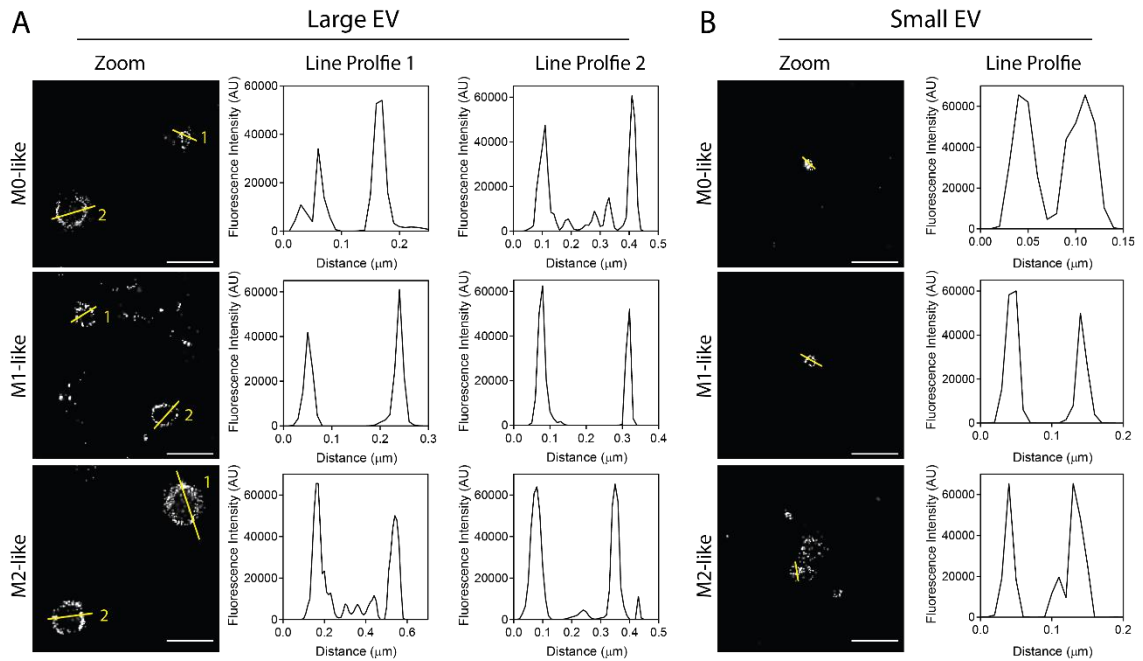


Figure 5-18: Line profiles of extracellular vesicles (EV) isolated with differential ultracentrifugation. Macrophages were stimulated in solution with beads coated with 10 $\mu\text{g/mL}$ IgG for 90 min and large and small EV were isolated using differential ultracentrifugation. Isolated fractions were incubated on PLL-coated microscopy slides for 20 min, fixed and stained with anti-CD81 labelled with AF647. Zoom STORM images ($2 \times 2 \mu\text{m}$) with according line profiles of large (A) and small (B) EV are shown. Scale bar $0.5 \mu\text{m}$. Images are representative for $n = 18 - 20$ images per condition from 3 individual donors and experiments.

5.3.5 Macrophage Vesicles are being secreted through Holes in the Actin Mesh at the Immune Synapse

The cytoskeleton regulates vital processes like cell migration, division and homeostasis³³⁰. Its main component is actin, a small protein which can form into filaments that build up more complex structures such as branched networks, cross-linked meshworks and bundles³³¹. The actin network has been shown to play a role in various membrane trafficking pathways and exocytosis^{206,332–335}. It is also known that a dense actin mesh is forming at the lytic synapse of T and NK cells, for example coordinating receptor rearrangements^{336,337}. Thus, it is very likely that the actin network also plays a role in the secretion of extracellular vesicles observed in this project.

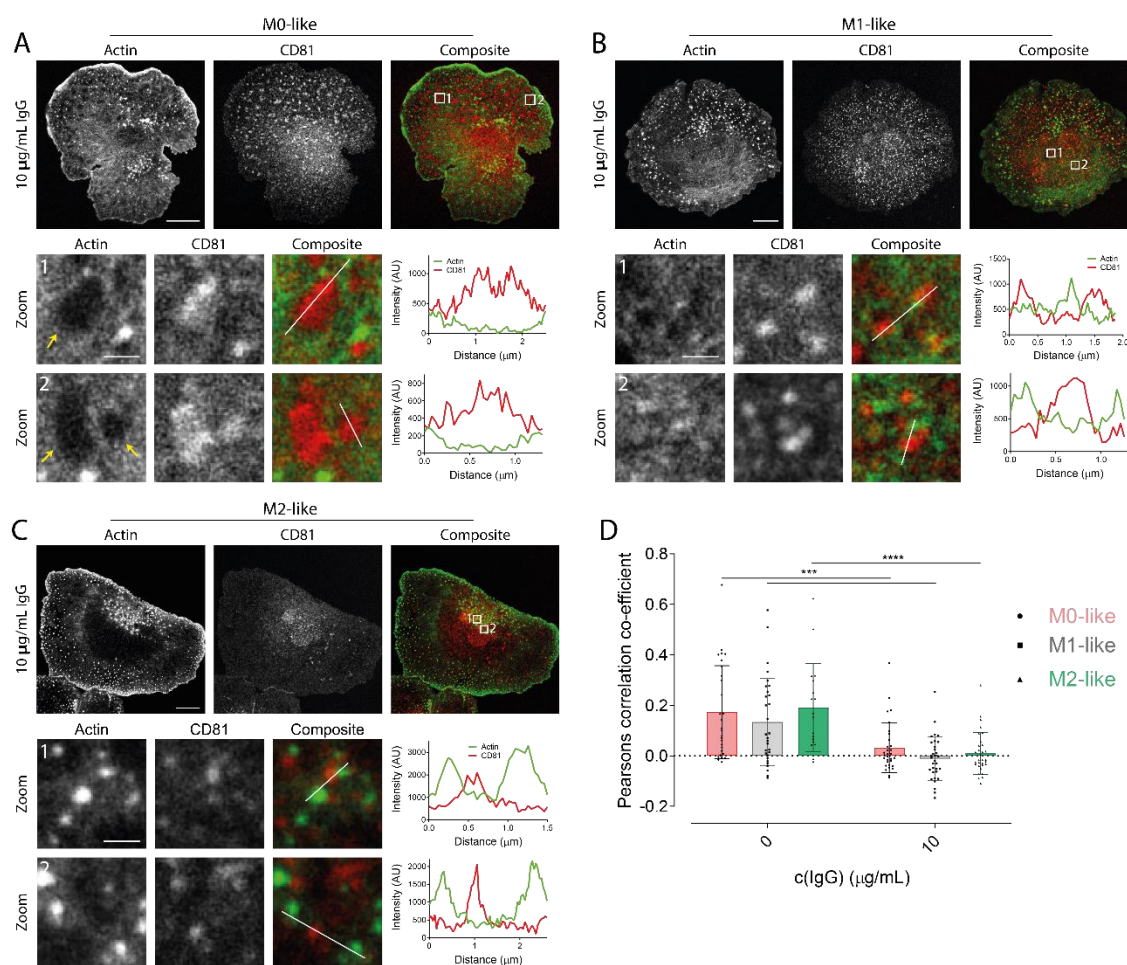


Figure 5-19: Macrophage vesicles are secreted through holes in the actin mesh. Macrophages were incubated on glass slides coated with PLL only (0 µg/mL IgG, non-activating condition) or PLL and IgG (10 µg/mL IgG, activating condition) for 15 min, permeabilised, fixed and stained with phalloidin-AF488 and anti-CD81 labelled with AF647. **A-C**) Representative STED (Actin), confocal (CD81), Zoom and Composite images with according line profiles of M0-like (**A**), M1-like (**B**) and M2-like (**C**) macrophages in activating conditions. **D**) Pearson's correlation co-efficient in activating and non-activating conditions. Each dot represents one cells. Bars show the geometric mean \pm SD of $n = 21 - 32$ cells per condition from 4 individual donors. ***, $p \leq 0.001$; ****, $p \leq 0.0001$; Mann Whitney or unpaired t test where appropriate using GraphPad Prism.

To test this hypothesis, macrophages were incubated on glass slides coated with PLL only (0 µg/mL IgG, non-activating condition) or PLL and IgG (10 µg/mL IgG, activating condition) for 15 min, permeabilised, fixed and stained with phalloidin-AF488 and anti-CD81 labelled with AF647 (Figure 5-19). The actin network was imaged with STED and CD81 with confocal microscopy. Thus, vesicles will not be resolved in detailed ring structures but will appear as blurred spots. However, this resolution is sufficient to

define the location of the vesicles across the synapse. Interestingly, vesicles co-localised with holes in the actin mesh which was most obvious for M0-like macrophages (Figure 5-19A, Zoom, yellow arrows). This was expected because vesicles from M0-like macrophages are more than double the size of vesicles from M1- and M2-like macrophages when activated on glass slides (Figure 5-4). Thus, holes in the actin mesh will be bigger and easier visible. However, line profiles confirmed this observation for all three cell types. Here, the intensity of actin was low when CD81 was high (Figure 5-19A-C, line profiles).

To determine the correlation of actin and CD81 across and all cell types and donors, Pearsons correlation coefficients were calculated (Figure 5-19D). Pearsons values can range from -1 (no correlation at all) to +1 (perfectly co-localised). And indeed, Pearsons correlation coefficients decreased significantly from non-activated to activated conditions for all cell types. This means that upon activation, actin and CD81 move apart, maybe indicating the re-organisation of the actin network, away from the vesicles, to enable their fusion with the cell membrane.

5.3.6 Proteomics Analysis of Macrophage Vesicles Reveal Distinct Contents for Different Macrophages

So far, M0-like, M1-like, M2-like and lung macrophages were found to secrete extracellular vesicles upon activation through their FcγRI. The different cell types displayed distinct secretion densities and vesicle diameters. This raises the question if vesicles derived from different macrophages also contain different material. In general, extracellular vesicles contain different biological material including, proteins, lipids and miRNAs and their composition is thought to reflect the state of the cell of origin³³⁸. This would mean that vesicles derived from M1-like macrophages contain pro-inflammatory proteins while M2-like macrophages act anti-inflammatory. To test this, monocyte-derived macrophages were stimulated to secrete vesicles in solution with IgG-coated beads for 90 min, and vesicles were isolated using differential ultracentrifugation (Figure 5-20A). Then, label-free proteomics analysis was performed on isolated

fractions. For all cell types, large and small extracellular vesicles were isolated from matching donors (Figure 5-20B).

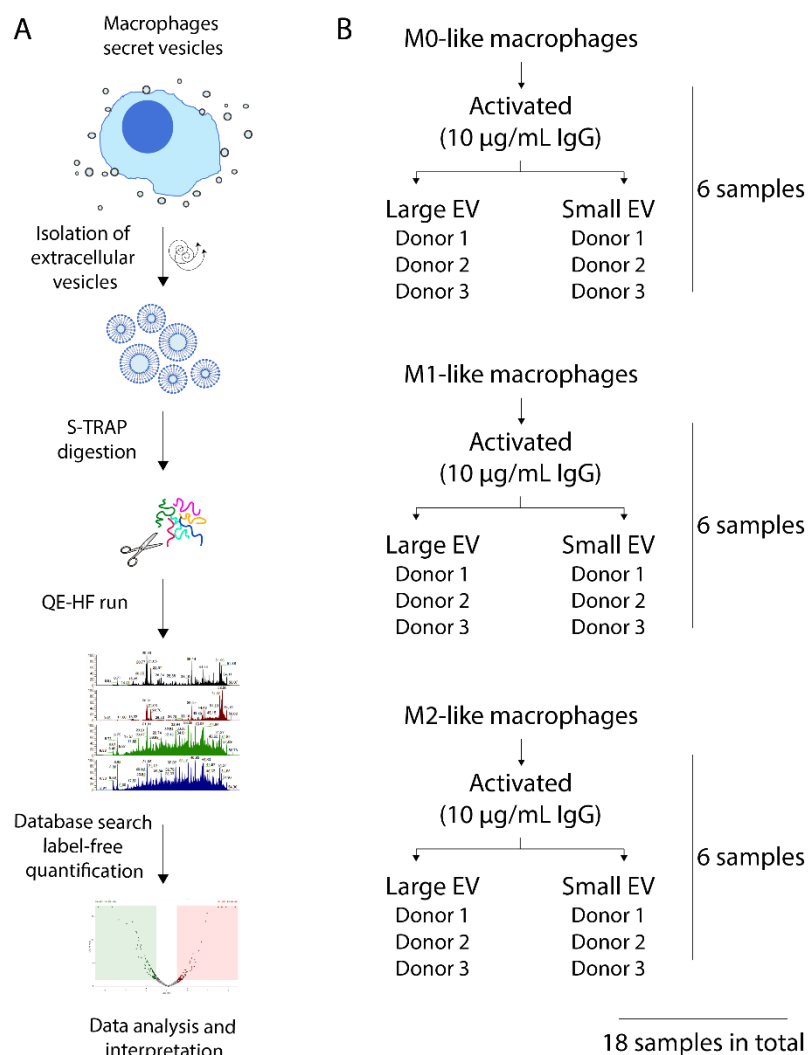


Figure 5-20: Schematic of macrophage preparation for proteomics analysis. **A)** Macrophages were stimulated in solution with beads coated with 10 µg/mL IgG for 90 min and large and small extracellular vesicles were isolated using differential ultracentrifugation. Isolated fractions were digested using S-TRAP™ technology and run on a QE-HF mass spectrometer. Raw data was analysed using the software Proteome Discoverer for label-free quantification. **B)** Overview of samples used for proteomics analysis. Large and small extracellular vesicles (EV) were isolated for matching donors for all cell types, yielding a total of 18 samples.

Hierarchical clustering analysis of all identified proteins from all samples revealed distinct protein contents for small and large vesicles from all three cell types (Figure 5-21A). Interestingly, M1- and M2-like macrophage vesicles form different clusters in both, small and large extracellular vesicles. Vesicles derived from M0-like macrophages on the other hand cluster together with M1-like macrophages for small vesicles and with M2-like macrophages for large vesicles. This makes sense as M0-like macrophages are differentiated so that they are polarised neither towards M1- nor M2-like macrophages. In fact, they likely contain markers from both cell types and thus are prone to cluster with both of them.

Further, principal component analysis (PCA) was performed (Figure 5-21B). Similar to the hierarchical clustering analysis, small and large extracellular vesicles cluster in separate, clear clusters. These can further be divided in the three different cell types. The overall clustering of the different fractions and cell types is also an indication that the isolation process and proteomics analysis was carried out correctly. If samples would have been contaminated during the preparation process this would be visible.

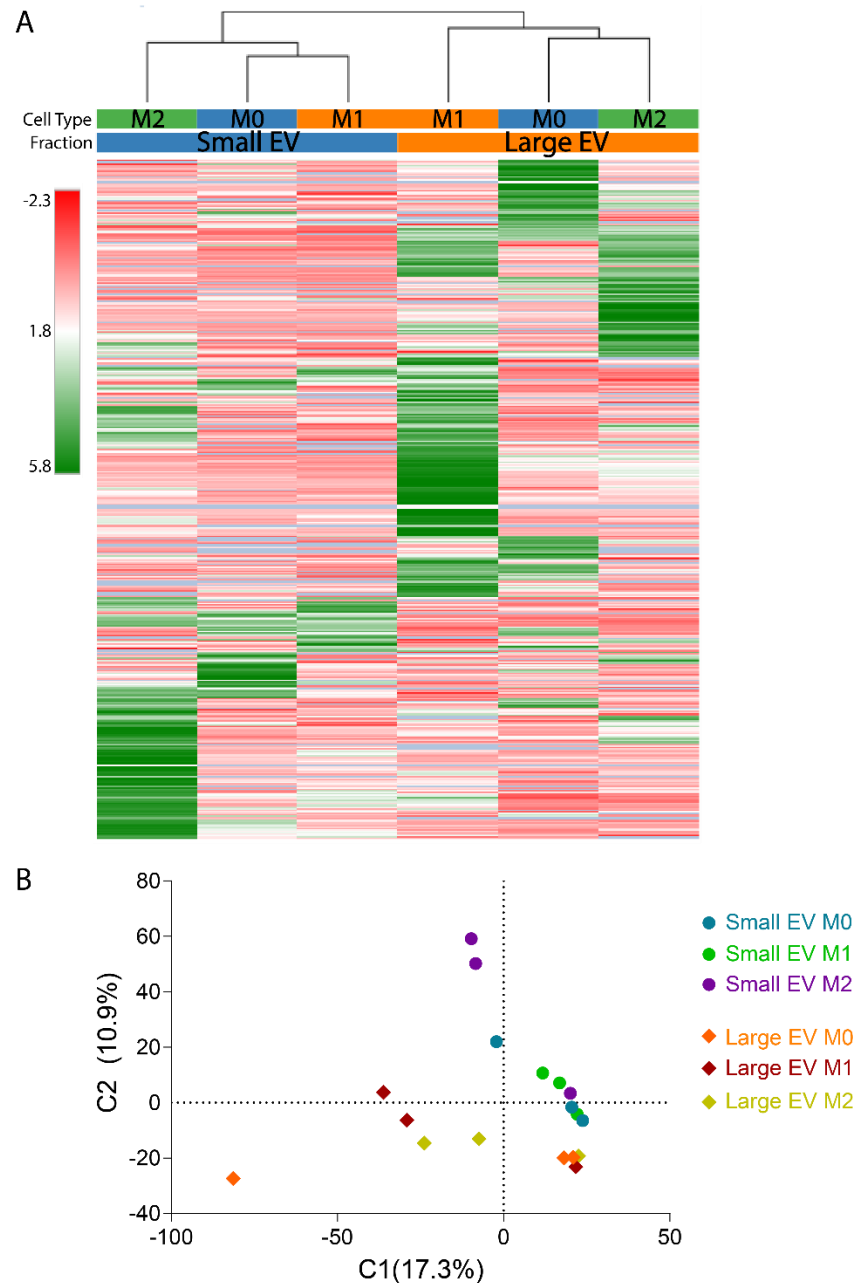


Figure 5-21: Extracellular vesicles (EV) from different macrophages show distinct protein contents. Macrophages were stimulated in solution with beads coated with 10 $\mu\text{g}/\text{mL}$ IgG for 90 min and large and small extracellular vesicles were isolated using differential ultracentrifugation and label-free proteomics analysis was performed. **A)** Heatmap of all samples using normalised and grouped abundances, the distance function Pearson and complete linkage method; created in Proteome Discoverer. Columns were scaled before clustering. **B)** Principal component analysis (PCA) plot showing clusters of samples based on their similarity. Each data point represents one donor. $n = 3$ individual donors and experiments.

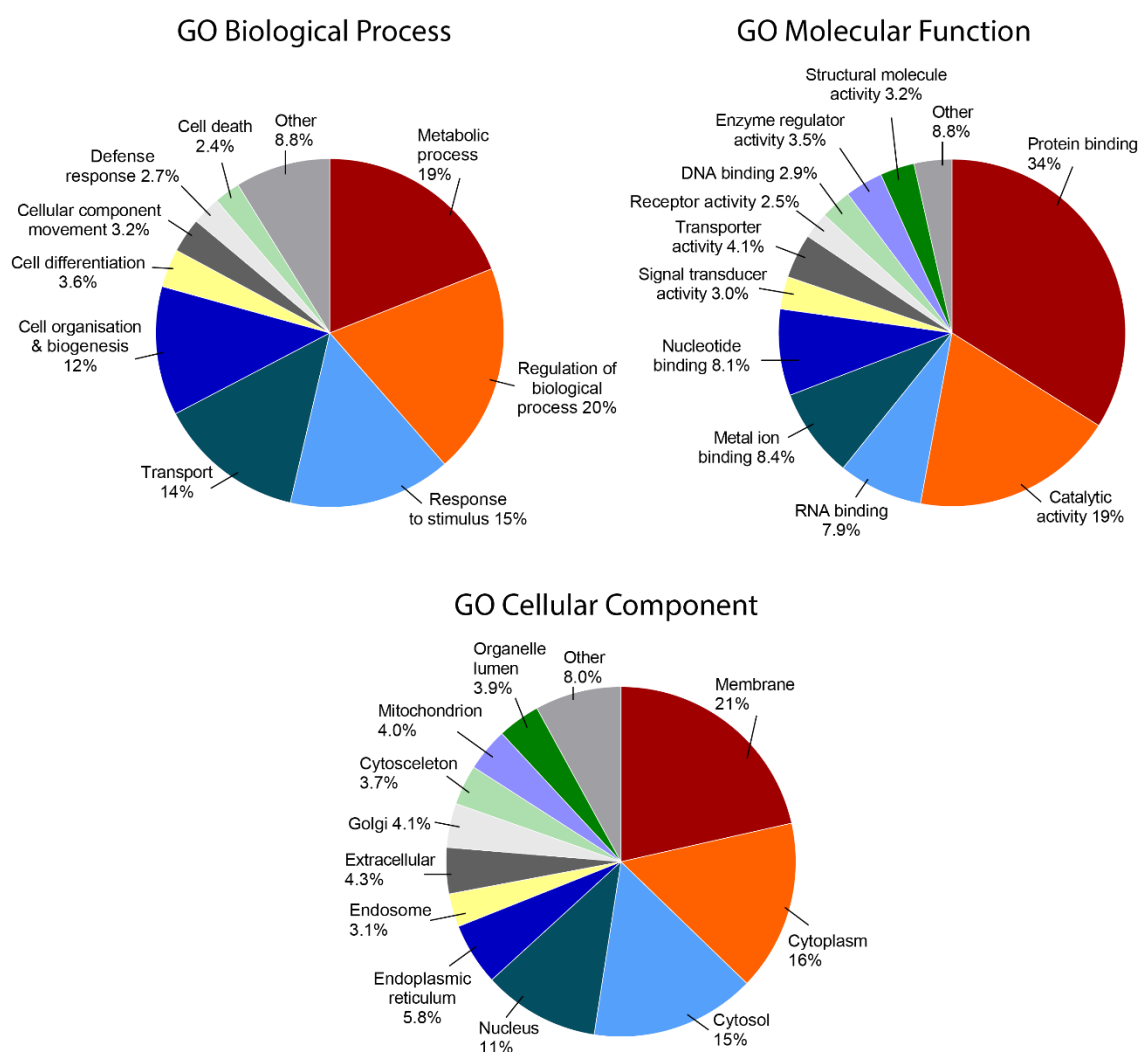


Figure 5-22: Gene Ontology (GO) annotation of all proteins identified in proteomics analysis. GO terms for cellular biological process (top left), molecular function (top right), and cellular component (bottom) of all identified proteins from the proteomics analysis.

Gene Ontology (GO) information for cellular biological processes, molecular functions, and cellular components of all identified proteins were retrieved from Proteome Discoverer (Figure 5-22). As expected, most identified proteins were of membranous, cytoplasmic or cytosolic origin. Their major functions were protein binding and catalytic activities and they could be linked to processes of metabolism, response to stimulus and transport. This is all coherent with analysing extracellular vesicles. Vesicles consist of a phospholipid bilayer with a spheroidal shape containing a variety of biomolecules including proteins, nucleic acids, lipids and metabolites¹⁷⁹. Their biogenesis takes place in the cytoplasm and cytosol and they are released from the

membrane. This explains GO annotation observed for isolated vesicles. More importantly, it shows no notable contamination of the samples and therefore confirms again the correct isolation and processing of the samples.

The first step of mass spectrometer analysis is to identify the peptides from the raw data. The peptides are then used to identify the proteins that fragmented into these peptides. Finally, identified proteins are matched with retention times to quantify their amount. However, these processes are influenced by the data set that's being analysed. This means, once the software identified a peptide or protein in one sample, it 'looks' for this peptide in the other samples. Therefore, slight differences can occur depending on the sample pool. Thus, in order to identify differences between the three different cell types in small vesicles, only data from small vesicles was analysed.

As can be seen in Figure 5-23A, hierarchical clustering of all regulated proteins identified in small vesicles confirmed observations seen when analysing the whole data set: small vesicles derived from M0-, M1- and M2-like macrophages show distinct protein contents. Interestingly, HLA class II molecule is under the most abundant proteins for M0- and M1-like macrophage vesicles but not M2-like macrophage vesicles (Figure 5-23B). In fact, when investigating all MHC class II proteins that were identified in small extracellular vesicles, M1-like macrophage vesicles contain relatively high levels compared to M0- and M2-like macrophages (Table 5-1). Inhibitory receptor LILRB2 on the other hand was found to be high on M2-like macrophage vesicles while it was not detected in vesicles derived from M0- and M1-like macrophage. However, M0-like macrophages vesicles contained high levels of LILRB2 (Table 5-2). This means that pro-inflammatory M1-like macrophages secreted vesicles containing MHC class II molecules, in accordance with their importance in antigen presentation. Anti-inflammatory M2-like macrophages on the other hand contain the inhibitory receptor LILRB2.

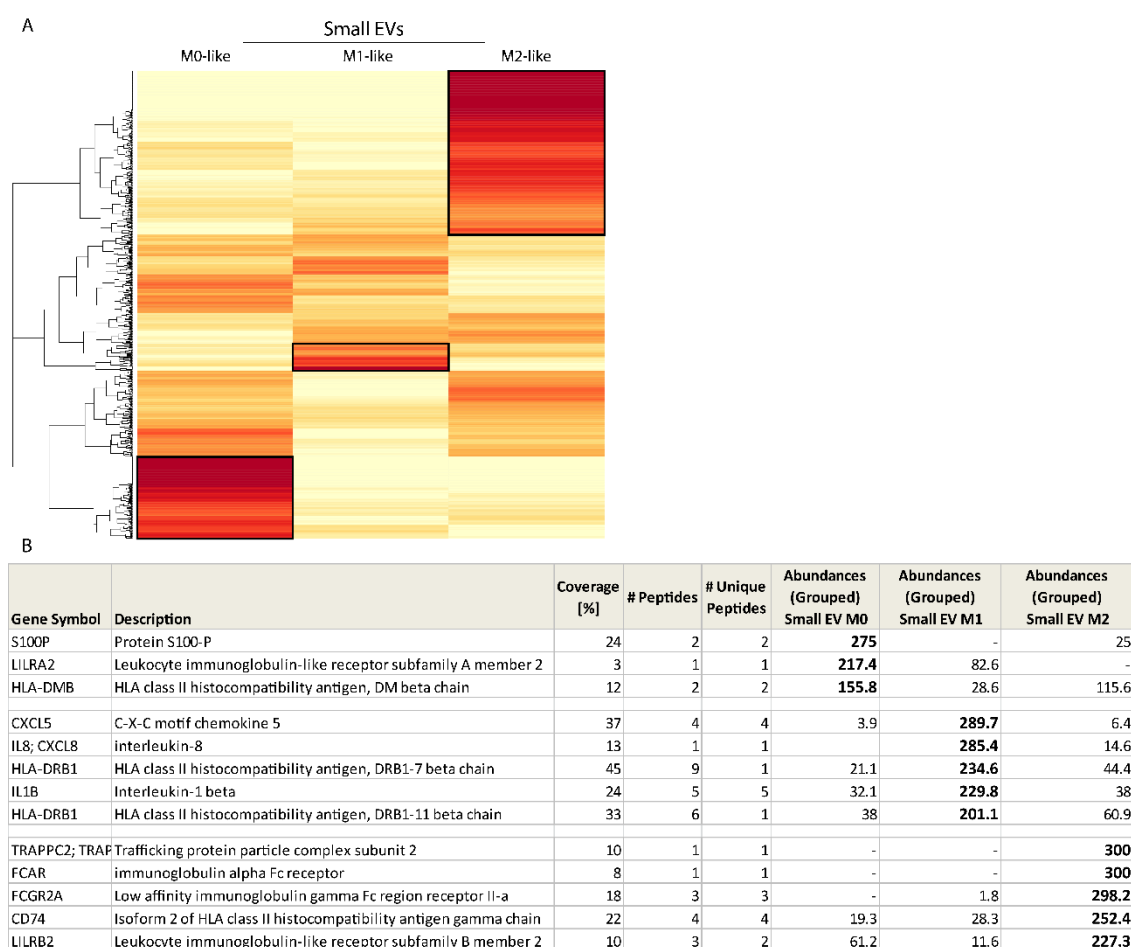


Figure 5-23: Hierarchal clustering reveals distinct populations of small extracellular vesicles (EV) for M0-, M1- and M2-like macrophages. A) Heatmap of all significantly changed proteins of small EV; created in R using the standard *heatmap* function with no scaling applied. Abundant proteins highlighted for M0-, M1- and M2-like macrophages (black boxes). **B)** Table of selected proteins with high abundance in M0-like (top), M1-like (middle) and M2-like (bottom) macrophages. Gene Symbol, a description, percentage of gene covered by identified peptides, number of peptides and unique peptides identified and grouped abundances are shown.

Table 5-1: Small extracellular vesicles (EV) of M1-like macrophages contain high levels of HLA-DR. List of all HLA class II proteins identified in the proteomics analysis of small EV. Gene Symbol, a description, percentage of gene covered by identified peptides, number of peptides and unique peptides identified and grouped abundances are shown. Abundances are colour coded according to their values.

Gene Symbol	Description	Coverage [%]	# Peptides	# Unique Peptides	Abundances (Grouped) Small EV M0	Abundances (Grouped) Small EV M1	Abundances (Grouped) Small EV M2
HLA-DRB3	HLA class II histocompatibility antigen, DRB1-7 beta chain	45	9	1	21.1	234.6	44.4
HLA-DRB1	HLA class II histocompatibility antigen, DRB1-11 beta chain	33	6	1	38	201.1	60.9
HLA-DRB1	HLA class II histocompatibility antigen, DRB1-12 beta chain	35	6	1	72.3	177.2	50.5
HLA-DRB5	HLA class II histocompatibility antigen, DR beta 5 chain	35	6	2	88.9	137.1	74
HLA-DPA1	HLA class II histocompatibility antigen, DP alpha 1 chain	5	1	1	50.1	135.8	114.2
HLA-DPB1	HLA class II histocompatibility antigen, DP beta 1 chain	19	4	3	9.2	134	156.8
HLA-DRA	HLA class II histocompatibility antigen, DR alpha chain	32	6	6	46	130.9	123
HLA-DMB	HLA class II histocompatibility antigen, DM beta chain	12	2	2	155.8	28.6	115.6
CD74	Isoform 2 of HLA class II histocompatibility antigen gamma chain	22	4	4	19.3	28.3	252.4

265
0
Abundance values

Table 5-2: Small extracellular vesicles (EV) of M1-like macrophages contain low levels of Leukocyte immunoglobulin-like receptors (LILRs). List of all LILR proteins identified in the proteomics analysis of small EV. Gene Symbol, a description, percentage of gene covered by identified peptides, number of peptides and unique peptides identified and grouped abundances are shown. Abundances are colour coded according to their values.

Gene Symbol	Description	Coverage [%]	# Peptides	# Unique Peptides	Abundances (Grouped) Small EV M0	Abundances (Grouped) Small EV M1	Abundances (Grouped) Small EV M2
LILRB2	Leukocyte immunoglobulin-like receptor subfamily B member 2	10	3	2	61.2	11.6	227.3
LILRA2	Leukocyte immunoglobulin-like receptor subfamily A member 2	3	1	1	217.4	82.6	0

265
0
Abundance values

Similar to small vesicles, large vesicles also displayed distinct protein contents for the three different cell types analysed (Figure 5-24A). In fact, MHC class II was again under highest abundant proteins identified for M0-like and M1-like macrophage vesicles (Figure 5-24B). When taking a closer look at all MHC class II molecules identified in large extracellular vesicles, it was highest in vesicles derived from M1-like

macrophages though it was also found in M0-like and M2-like macrophage vesicles (Table 5-3). MHC class I on the other hand was found to be high especially in M2-like but also M0-like macrophage vesicles and lowest in vesicles derived from M1-like macrophages (Table 5-4). Similar to findings in small vesicles, the inhibitory receptors LILRB1 and 2 were high in M2-like macrophage vesicles (Table 5-5).

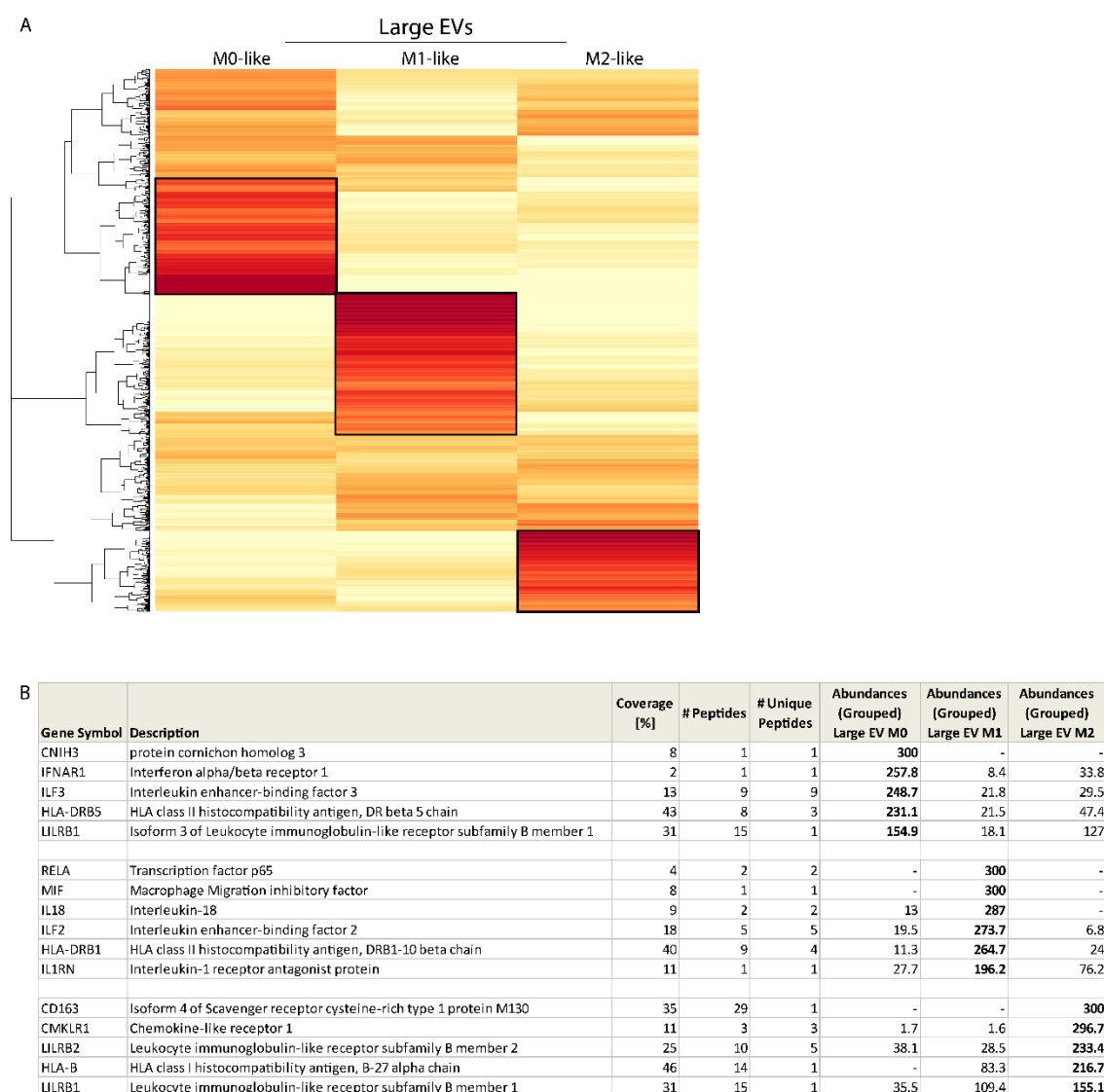


Figure 5-24: Hierarchal clustering reveals distinct populations of large extracellular vesicles (EV) for M0-, M1- and M2-like macrophages. A) Heatmap of all significantly changed proteins of large EV; created in R using standard *heatmap* function. No scaling applied and abundant proteins highlighted for M0-, M1- and M2-like macrophages (black boxes). **B)** Table of selected proteins with high abundance in M0-like (top), M1-like (middle) and M2-like (bottom) macrophages. Gene Symbol, a description, percentage of gene covered by identified peptides, number of peptides and unique peptides identified and grouped abundances are shown.

Table 5-3: Large extracellular vesicles (EV) of M1-like macrophages contain high levels of HLA class II.

List of all HLA class II proteins identified in the proteomics analysis of large EV. Gene Symbol, a description, percentage of gene covered by identified peptides, number of peptides and unique peptides identified and grouped abundances are shown. Abundances are colour coded according to their values.

Gene Symbol	Description	Coverage [%]	# Peptides	# Unique Peptides	Abundances (Grouped) Large EV M0	Abundances (Grouped) Large EV M1	Abundances (Grouped) Large EV M2
HLA-DRB1	HLA class II histocompatibility antigen, DRB1-10 beta chain	40	9	4	11.3	264.7	24
HLA-DRB3	HLA class II histocompatibility antigen, DR beta 3 chain	33	6	1	39.3	257.8	3
HLA-DRB1	HLA class II histocompatibility antigen, DRB1-9 beta chain	45	10	2	60.8	230.3	8.9
HLA-DRB1	HLA class II histocompatibility antigen, DRB1-8 beta chain	38	7	1	51.7	223.5	24.8
HLA-DQA1	HLA class II histocompatibility antigen, DQ alpha 1 chain	11	3	2	16.7	222.4	60.9
HLA-DPB1	HLA class II histocompatibility antigen, DP beta 1 chain	31	6	5	31.2	173.4	95.5
HLA-DRB1	HLA class II histocompatibility antigen, DRB1-11 beta chain	45	10	3	47.6	158.8	93.7
HLA-DQA2	HLA class II histocompatibility antigen, DQ alpha 2 chain	14	3	1	0	141.3	158.7
HLA-DPA1	HLA class II histocompatibility antigen, DP alpha 1 chain	20	4	4	8.6	123.9	167.5
HLA-DMA	HLA class II histocompatibility antigen, DM alpha chain	8	1	1	82.4	69.3	148.3
HLA-DRB4	HLA class II histocompatibility antigen, DR beta 4 chain	50	9	6	106.3	35.6	158.1
HLA-DRB5	HLA class II histocompatibility antigen, DR beta 5 chain	43	8	3	231.1	21.5	47.4

265 0

Abundance values

Table 5-4: Large extracellular vesicles (EV) of M2-like macrophages contain high levels of HLA class I.

List of all HLA class I proteins identified in the proteomics analysis of large EV. Gene Symbol, a description, percentage of gene covered by identified peptides, number of peptides and unique peptides identified and grouped abundances are shown. Abundances are colour coded according to their values.

Gene Symbol	Description	Coverage [%]	# Peptides	# Unique Peptides	Abundances (Grouped) Large EV M0	Abundances (Grouped) Large EV M1	Abundances (Grouped) Large EV M2
HLA-B	HLA class I histocompatibility antigen, B-27 alpha chain	46	14	1	0	83.3	216.7
HLA-E	HLA class I histocompatibility antigen, alpha chain E	19	5	1	146	0	154
HLA-C	HLA class I histocompatibility antigen, Cw-1 alpha chain	41	16	4	80.8	85.2	134
HLA-B	HLA class I histocompatibility antigen, B-51 alpha chain	59	17	1	133.3	38.2	128.5
HLA-B	HLA class I histocompatibility antigen, B-49 alpha chain	62	18	2	79.3	94.5	126.2
HLA-B	HLA class I histocompatibility antigen, B-37 alpha chain	62	19	2	148.4	48.9	102.7
HLA-B	HLA class I histocompatibility antigen, B-44 alpha chain	56	18	4	58	194.6	47.4



Table 5-5: Inhibitory leukocyte immunoglobulin-like receptors (LILRs) LILRB1 and LILRB2 increased detected in M2-like macrophages.

List of all LILR proteins identified in the proteomics analysis of large EV. Gene Symbol, a description, percentage of gene covered by identified peptides, number of peptides and unique peptides identified and grouped abundances are shown. Abundances are colour coded according to their values.

Gene Symbol	Description	Coverage [%]	# Peptides	# Unique Peptides	Abundances (Grouped) Large EV M0	Abundances (Grouped) Large EV M1	Abundances (Grouped) Large EV M2
LILRB2	Leukocyte immunoglobulin-like receptor subfamily B member 2	25	10	5	38.1	28.5	233.4
LILRB1	Leukocyte immunoglobulin-like receptor subfamily B member 1	31	15	1	35.5	109.4	155.1
LILRB1	Isoform 3 of Leukocyte immunoglobulin-like receptor subfamily B member 1	31	15	1	154.9	18.1	127



Taken together, small and large extracellular vesicles were successfully isolated using differential ultracentrifugation and their protein contents analysed with mass spectrometry. Hierarchical clustering of all proteins revealed distinct contents for small and large vesicles of M0-, M1- and M2-like macrophages which was confirmed by principal component analysis. As expected most proteins were of membranous and cytoplasmic origin with functions linked to transport and protein binding. Analysing only the regulated genes for small and large vesicles confirmed discrete clusters for different

cell types with MHC class II being highest in M1-like macrophages while inhibitory receptors of the LILR family were highest in M2-like macrophages.

5.3.7 Preliminary Data Confirms LILRB1 in M0-like and M2-like Macrophage Vesicles

To validate observations made in proteomics analysis, macrophages were allowed to settle on activating lipid bilayers for 20 min, then detached, fixed and stained for CD81-AF488 and LILRB1-AF647 (Figure 5-25A). TIRF images of M0-like and M2-like macrophages showed a bright signal with similar levels for CD81 and LILRB1 (Figure 5-25B). Interestingly, most but not all CD81-positive vesicles were also found to be positive for LILRB1 highlighting the heterogeneity of cellular secretions. M1-like macrophage vesicles on the other hand displayed nearly no signal at all (Figure 5-25B, M1-like). Notably, TIRF images of M1-like macrophage secretions not only displayed low signal for LILRB1 but also CD81. This suggests that no vesicles were present and thus no strong conclusion can be drawn from the data. Nevertheless, TIRF imaging revealed the presence of LILRB1 in EV derived from M0-like and M2-like macrophages, which is consistent with the proteomics analysis. This was confirmed when calculating the mean fluorescent intensity of TIRF images of LILRB1 normalised to the signal of CD81 (Figure 5-25C). Interestingly, the amount of LILRB1 differs from cell to cell within one donor, further highlighting the heterogeneity of cellular secretions.

To determine whether LILRB1-containing vesicles could be captured, directly upon secretion, M0-like macrophages were analysed using single and two colour STORM. First, to ensure correct application of two colour STORM, a positive control was imaged. Therefore, M0-like macrophages were incubated on PLL-coated microscopy slides for 15 min, fixed and stained with anti-LILRB1 mAb labelled with AF647 followed by a secondary Ab labelled with AF488. As expected, STORM images of both channels matched each other which is highlighted by line profiles (Figure 5-26A). This was confirmed by coordinate based co-localisation (CBC) analysis, where acquired data trended towards the value 1 while randomised data was more evenly distributed (Figure 5-26B). This confirms correct application of two colour STORM.

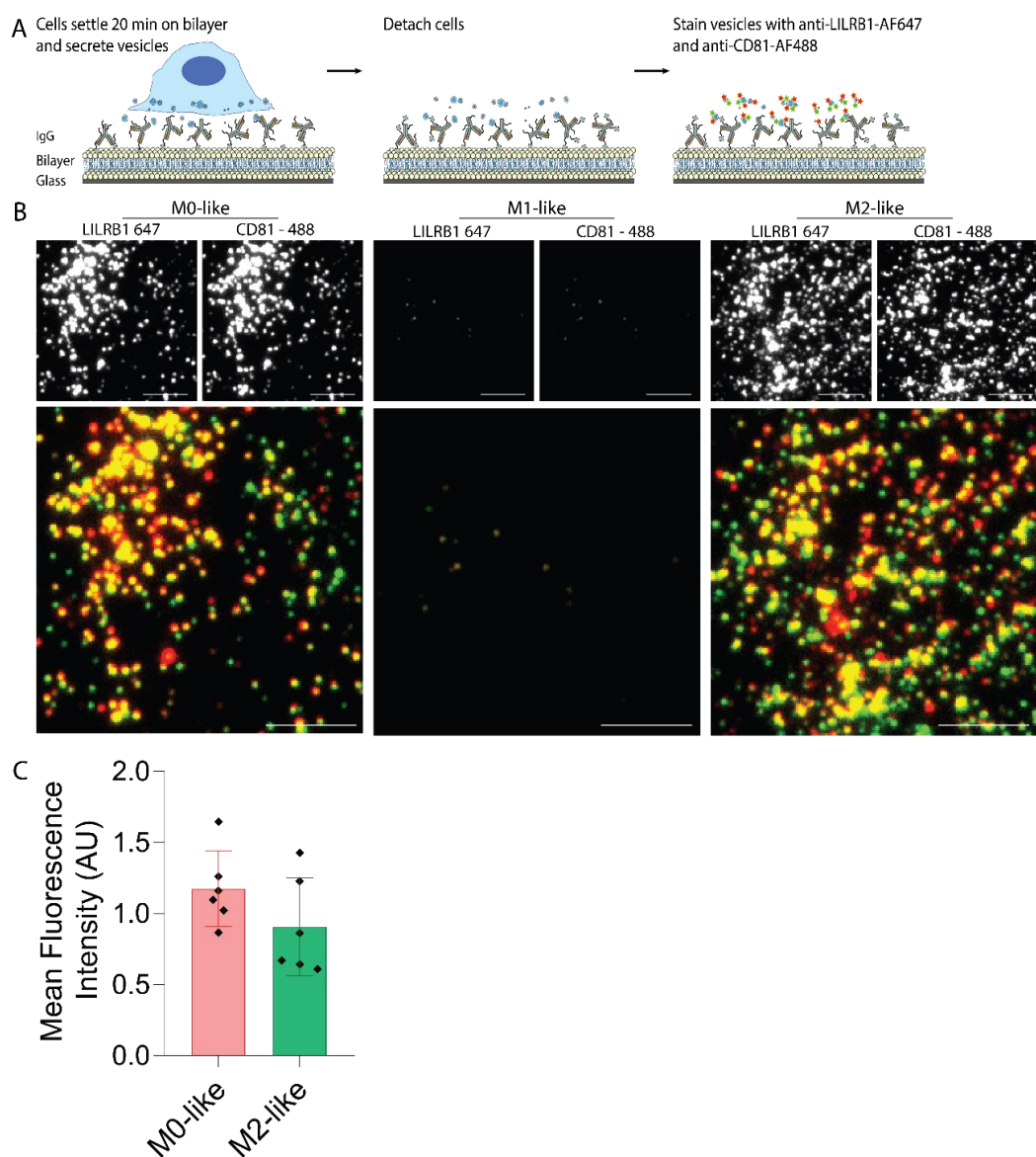


Figure 5-25: M0- and M2-like macrophage vesicles contain inhibitory receptor LILRB1. **A)** Macrophages were incubated on planar lipid bilayers containing 10 $\mu\text{g}/\text{mL}$ biotinylated IgG for 20 min, detached, the remains fixed and stained with anti-CD81 labelled with AF488 and anti-LILRB1 labelled with AF647. **B)** Representative TIRF and overlay images for M0-, M1- and M2-like macrophages. Scale bar 10 μm . **C)** Normalised mean fluorescence intensity of LILRB1 TIRF images of M0-like and M2-like macrophage secretions. One point presents one cell and bars show the geometric mean \pm SD. Preliminary analysis of $n = 6$ cells per condition from 1 individual donor.

Then, the synapse of M0-like macrophages was investigated for LILRB1. Therefore, M0-like macrophages were incubated on microscopy slides coated with PLL and 10 $\mu\text{g}/\text{mL}$ IgG for 15 min, fixed and stained with anti-LILRB1 labelled with AF647. As expected, vesicles appeared as nanometer-scale ring structures in STORM images

(Figure 5-27A). Line profiles confirmed their circular structure and their approximate diameters match those of M0-like macrophages activated on glass slides (Figure 5-27A, Line Profiles).

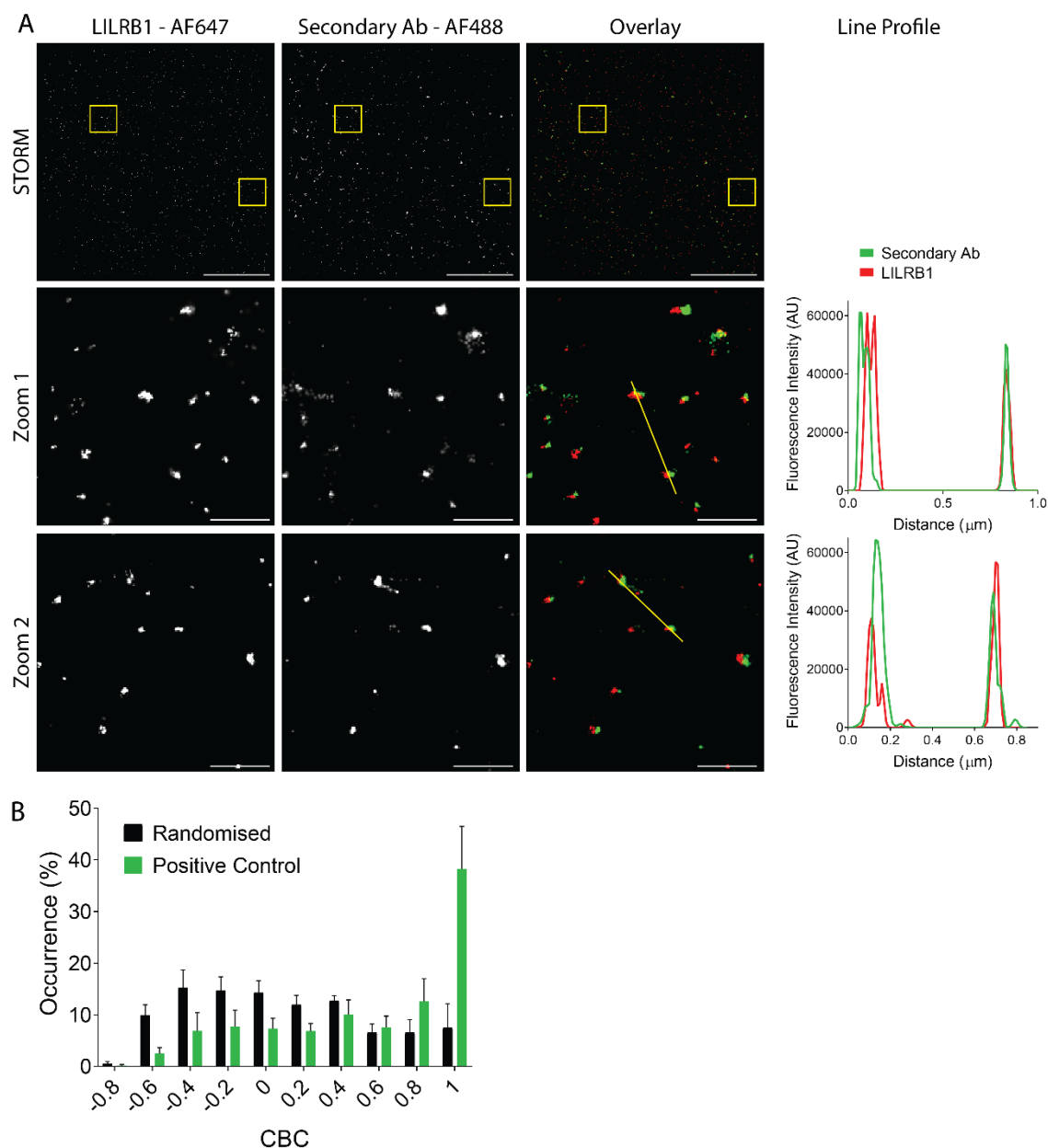


Figure 5-26: Positive control for two colour STORM. M0-like macrophages were incubated on PLL-coated glass slides for 15 min, fixed and stained with anti-LILRB1 mAb labelled with AF647 followed by a secondary Ab labelled with AF488. **A)** Representative STORM and Zoom ($2 \times 2 \mu\text{m}$) images are shown with according line profiles. **B)** Coordinate based co-localisation (CBC) between primary and secondary channel for acquired and randomised data. Bars show the geometric mean \pm SD of $n = 14$ cells from 3 donors.

According to the proteomics data analysed, LILRB1 as well as MHC class I are contained in M0-like macrophage vesicles. To see whether both molecules are contained in the same vesicles, two colour STORM was performed. Therefore, macrophages were incubated on glass slides coated with PLL and IgG for 15 min, fixed and stained with anti-LILRB1 mAb labelled with AF488 and anti-MHC-class-I mAb conjugated with AF647. As expected, nanometer-scale ring structures were detected for both, LILRB1 and MHC class I. More interestingly, LILRB1 co-localised with MHC class I molecules at vesicles of M0-like macrophages (Figure 5-27B). All LILRB1-positive vesicles were also MHC-class-I-positive, however, not all MHC-class-I-positive vesicles were also positive for LILRB1 (Figure 5-27B, Cell C, yellow arrows). This highlights again the heterogeneity and complexity of cellular secretions.

To quantitatively assess this observation two colour TIRF images were analysed. Therefore, M0-like macrophages were plated onto microscopy slides coated with PLL (0 µg/mL IgG, non-activated conditions) or PLL and IgG (10 µg/mL IgG, activated conditions) for 15 min, fixed and stained with anti-LILRB1 mAb labelled with AF488 and MHC class I mAb conjugated with AF647. Manders as well as Pearsons correlation coefficient did display similar values as the control sample in non-activated conditions and did not change upon activation (Figure 5-27C-D). This indicates the co-localisation of LILRB1 and MHC class I at the membrane of M0-like macrophages.

Taken together, preliminary data confirmed LILRB1 being contained in M0-like and M2-like macrophage vesicles. These resolve into nanometer-scale ring structures when investigated in STORM. In addition, two colour STORM of M0-like macrophages showed the co-localisation of LILRB1 and MHC class I molecules in vesicles, though not all vesicles contained both molecules. These investigations should be expanded to M1-like, M2-like and lung macrophages. Nevertheless, the data shown supports observations made in the proteomics experiment. It demonstrates that cellular secretions are heterogeneous and dependent on the cell type.

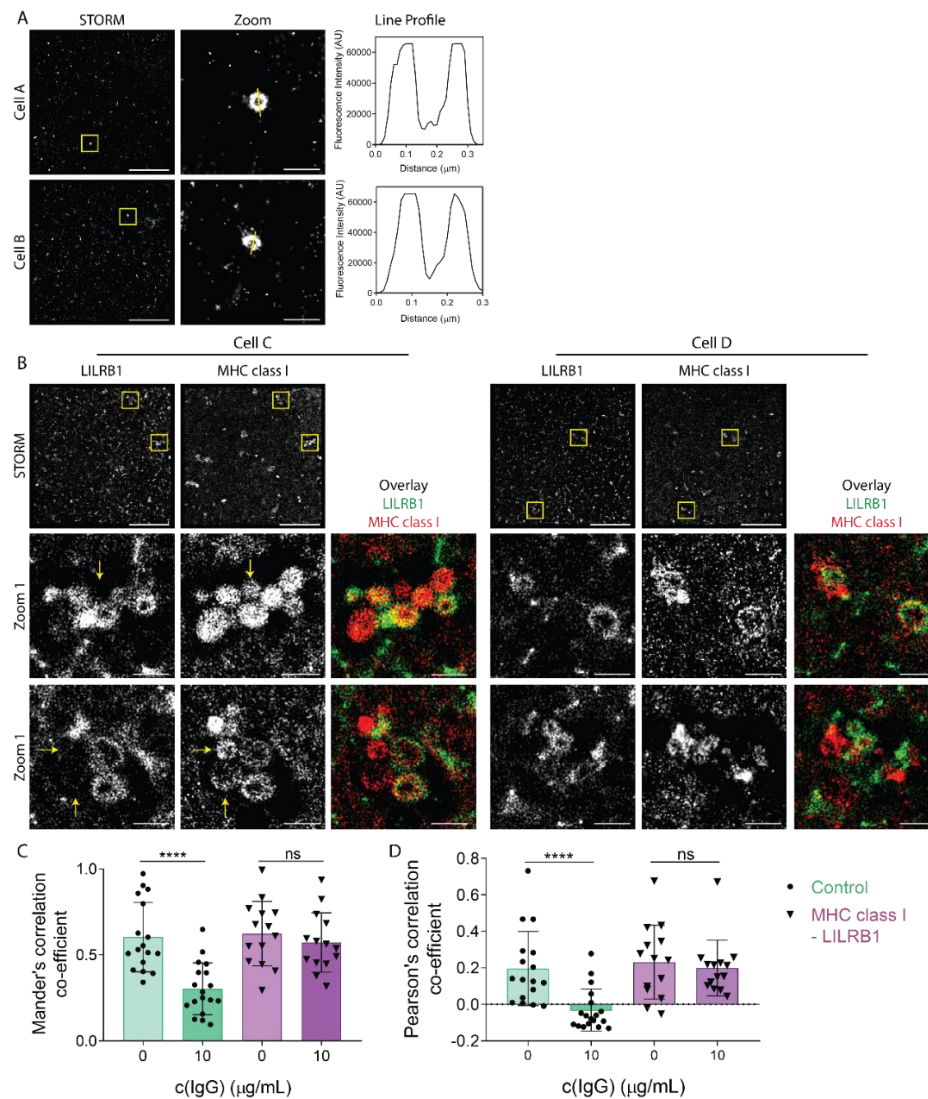


Figure 5-27: Inhibitory receptor LILRB1 and MHC class I co-localise at the membrane of M0-like macrophages. **A)** Macrophages were incubated on glass slides coated with PLL and 10 $\mu\text{g/mL}$ IgG for 15 min, fixed and stained with human anti-LILRB1 labelled with AF647. STORM and Zoom (2 x 2 μm) images with according line profiles shown for two examples. Images representative for 26 cells from $n = 4$ individual donors and experiments. Scale bar 10 μm , Zoom 0.5 μm . **B)** Macrophages were incubated on glass slides coated with PLL and 50 $\mu\text{g/mL}$ IgG for 15 min, fixed and stained with human anti-LILRB1 mAb labelled with AF488 and anti-MHC-class-I mAb conjugated with AF647. STORM, Zoom (2 x 2 μm) and overlay images. Two cells shown. $n = 13$ cells from 2 individual donors and experiments. Scale bar 10 μm , Zoom 0.5 μm . **C-D)** Macrophages were incubated on glass slides coated with PLL only or PLL and 10 $\mu\text{g/mL}$ IgG for 15 min, fixed and stained with human anti-LILRB1 labelled with AF488 and MHC class I conjugated with AF647. Control samples were stained with anti-SIRP α mAb labelled with AF647 and AF488-conjugated anti-CD64 mAb. TIRF images were taken. **C)** Manders and **D)** Pearsons correlation coefficients of TIRF images. Each dot represents one cell. Bars show the geometric mean \pm SD of $n = 14 - 18$ cells from 1 individual donor and experiment. ****, $p \leq 0.0001$; ns, non-significant; Unpaired t-test or Mann-Whitney test where appropriate using GraphPad Prism.

5.4 Discussion

5.4.1 Summary of Results

This chapter aimed to investigate the formation of CD81 nanometer-scale ring structures at the synapse of IgG-activated human macrophages. In total, four cell types were compared: M0-like, M1-like, M2-like and lung macrophages. Here, STORM was utilised to study the phenomenon on a cell-by-cell basis. The main findings of this chapter can be summarised as follows:

- CD81 forms into nanometer-scale ring structures at the synapse of all four macrophage types when activated through their FcγRI
- M0-like, M1-like, M2-like and lung macrophages display distinct ring characteristics which differ slightly if activated on IgG-coated glass slides or IgG-containing planar lipid bilayers
- Nanometer-scale ring structures are extracellular vesicles, secreted by the macrophages and captured directly upon secretion
- Extracellular vesicles are secreted through holes in the actin mesh
- Proteomics data reveals discrete contents of vesicles isolated from different macrophages
- Preliminary imaging experiments confirm hits in the proteomics data: LILRB1 is present in M0- and M2-like macrophage vesicles
- MHC class I co-localises with LILRB1 on M0-like macrophage vesicles

5.4.2 CD81 Nanometer-scale Ring Structures at the Synapse of IgG-activated Macrophages are Extracellular Vesicles

In this chapter, the formation of CD81 nanometer-scale ring structures at the synapse of IgG-activated macrophages was investigated. These structures have been observed for M0-like, M1-like, M2-like and lung macrophages after incubation on IgG-coated glass slides as well as activating lipid bilayers (Figure 5-1, Figure 5-8). Line profiles confirmed their round structure (Figure 5-2, Figure 5-9). The ring density defined as number of rings per μm^2 increased significantly upon activation for all cell types

incubated on glass slides, highlighting the fact that the formation of ring structures is induced after engagement of FcγRI (Figure 5-3). Importantly, STORM enabled the analysis of these ring structures and on a single-cell basis. Indeed, ring densities differed greatly from cell to cell. For macrophages activated on IgG-coated glass slides, M1-like macrophages showed the highest average ring density with 0.748 ± 0.404 rings/ μm^2 and also had the greatest variation between single cells (Figure 5-3, M1-like). This means, some cells displayed many rings while others displayed only very few, which may indicate that some cells are activated stronger than others. However, it has to be kept in mind that one $18 \times 18 \mu\text{m}$ big area per cell was imaged and analysed. When cells exceeded this size, not the whole cell was analysed. Thus, the data could be skewed towards a higher or lower density depending on which area of the cell was analysed. Nevertheless, the heterogeneity between images and cells highlights the importance of single cell analysis. The differences between single cells can for example give clues on detailed mechanisms of cellular activation.

Further, lung macrophages displayed the lowest average ring density with 0.198 ± 0.346 rings/ μm^2 . Interestingly they also spread the least on IgG-coated glass slides, possibly indicating lower levels of activation. In addition, lung macrophages are thought to be highly immunosuppressive and may have a higher threshold of activation. However, for macrophages incubated on activating lipid bilayers lung macrophages displayed the highest average ring density with 0.877 ± 0.997 rings/ μm^2 (Figure 5-10). In general, ring densities were higher and more similar between cell types on activating bilayers. The bilayers present a more biological relevant system, mimicking the interaction with another cell. Thus, the macrophages may better interact with the bilayer compared to the glass slide. However, macrophages showed similar levels of cytokine secretion on both substrates with secreting slightly more on glass slides (Figure 3-6 and Figure 3-9). In addition, macrophages detached easier from lipid bilayers compared to glass slides possibly indicating a weaker interaction with the bilayers.

Taken together, the density of CD81 nanometer-scale rings at the synapse of IgG-activated macrophages differs from cell to cell. In general, the ring density was higher for macrophages incubated on activating bilayers compared to glass slides but no trend between the different cell types was obvious. However, only a limited amount of donors and cells was imaged. Differences between cell types may be visible when studying more donors and cells. Nevertheless, it shows that the stimulation with IgG does induce the formation of CD81 ring structures and that there is a heterogeneity between individual cells within one cell type.

Interestingly, ring structures of different macrophages display distinct characteristics. While ring structures of M1-like, M2-like and lung macrophages display relatively similar mean diameters (92 ± 47 nm, 75 ± 41 nm and 93 ± 50 nm respectively) M0-like macrophage rings are much bigger (182 ± 95 nm) for macrophages activated on IgG-coated glass slides (Figure 5-4). Not only the diameters but also where at the synapse ring structures are forming differs between the cell types. M0-like and lung macrophages tend to form ring structures across the whole synapse while M1- and M2-like macrophages form them at the centre of the synapse (Figure 5-5).

CD81 is a member of the tetraspanin super family. Their main function is thought to be the organisation of membrane proteins. As a molecular scaffold they facilitate the formation of so-called tetraspanin enriched microdomains (TEMS), containing adhesion, signalling and receptor proteins¹⁹⁰. Thus, it is not surprising that tetraspanins have also been reported to play a role in immune responses^{339–341}. CD81 was shown to accumulate at the synapse formed between T cells and APCs where it co-localised with CD3³⁴². However, tetraspanin ring structures were only reported when imaging extracellular vesicles (EV) after isolation from for example media of cell cultures or tissues^{235,343,344}. In fact, tetraspanins are well-known to be enriched in EV and are commonly used as EV marker^{192–194}. Thus, CD81-rings observed in this project likely are extracellular vesicles, captured directly upon secretion. Indeed, the ring diameters observed lay within the expected range for EV. Classically, EV are divided into 3 main

subgroups which are overlapping in size: exosomes (30 – 150 nm), microvesicles and apoptotic bodies (both > 100 nm)³¹². According to these categories, rings observed at the synapse of M1-like, M2-like and lung macrophages would be exosomes and ring structures observed at the membrane of M0-like macrophages microvesicles. However, this characterisation cannot be done solely on the size of the vesicles. In addition, M0-like macrophage rings were much smaller on activating bilayers (114 ± 75 nm), thereby losing more than one third of their size compared to rings observed on glass slides and falling into the range of exosomes (Figure 5-11). M1-like and lung macrophages also slightly decreased their mean diameter while the mean diameter of M2-like macrophage rings increased on bilayers compared to glass slides. Nevertheless, M0-like macrophage rings were bigger than those of M1-like, M2-like and lung macrophages who displayed more similar diameters. However, similar to the ring densities, no obvious trend between cell types emerged from the data collected but different results presented themselves when activating the macrophages on IgG-coated glass slides or IgG-containing lipid bilayers.

As mentioned before, the bilayer presents a more biological relevant system, presenting a physiologically more accurate model of an opsonised target. The interaction between the cells and the bilayer might be stronger and thus different results follow compared to glass slides. In addition, glass slides are also coated with poly-L-lysine (PLL) to facilitate adhesion. PLL is a positively charged polymer that can electrostatically interact with negatively charged cell membranes and proteins^{345,346}. However, PLL not only facilitates cell attachments, it may also influences cellular activation and responses. For example, it has been shown to initiate T and B cell signalling and render the activity of membrane proteins as well as their organisation in the membrane³⁴⁷. Here T cell receptor (TCR) clustering and mobility were greatly influenced by PLL. Thus, PLL may also influence the dynamics of FcγRI and therefore activation levels of macrophages which may alter the density of vesicles or their diameter size.

Different sizes of vesicle diameter may also indicate different mechanisms of biogenesis. Larger vesicles of more than 100 nm are thought to bud off the membrane while smaller vesicles are generated through the inward budding of late endosomal membranes. However, this would need to be investigated in more depth, with specific markers and inhibitors identifying different mechanisms of biogenesis.

In any case, vesicle secretion is observed when stimulating macrophages with IgG, thereby engaging FcγRI. The latter is part of the family of Fc receptors for IgG which consists of several receptors balancing activating- and inhibitory signals and thereby controlling innate immune effector cell activation³⁴⁸. FcγRI has a high affinity for IgG and is thought to be an activating receptor, inducing a pro-inflammatory phenotype. Indeed, macrophages stimulated with IgG secreted the pro-inflammatory cytokine TNFα (Figure 3-6 and Figure 3-9). This paints a picture of macrophages being activated on IgG-containing surfaces (glass or bilayer), and secreting extracellular vesicles, possibly containing pro-inflammatory proteins and cytokines to locally boost the immune response. In recent years, the impact of EV on an immune response has gained more and more attention^{349,350}. In an infectious lung model in mice, EV secreted by macrophages were able to induce a pro-inflammatory phenotype in resting macrophages *in vitro* and *in vivo*³²⁶. In addition, exosomes derived from M1-polarised macrophages were successfully used as an immunopotentiator for a cancer vaccine while exosomes of M2-polarised macrophages failed to do so³²⁴. Here, M1 exosomes were mainly taken up by macrophages and dendritic cells after subcutaneous injection in mice and induced the release of pro-inflammatory cytokines. This highlights the role of EV in inflammation and the distinct functions of EV from different cell types.

Studying the secretion of EV at the synapse of macrophages in a time-dependent manner showed that vesicle density increased over time in both, activating and non-activating conditions (Figure 5-6). Therefore, M0-like, M1-like and M2-like macrophages were plated onto glass slides coated with PLL only (non-activating conditions) or PLL and 10 µg/mL IgG (activating conditions) for 15, 30, 60 and 120 min,

fixed and stained with anti-CD81 mAb labelled with AF647. The increased vesicle density over time makes sense as vesicles secreted at an early time point could be trapped between the cell and the glass slide, yet new vesicles could be secreted, thereby increasing the density. Importantly, the increase in vesicle density in non-activating conditions over time may indicate the activation of the macrophages despite the lack of stimulation via IgG. Thus, to avoid the activation of macrophages in non-activating conditions, an incubation time of 15 min was used for further experiments.

5.4.3 Characteristics of Extracellular Vesicles Change with Culture

The blood-derived macrophages used in this project are generated by culturing monocytes. In fact, experiments are generally carried out with matching donors. This means, macrophages were derived from the same pool of monocytes, yet they display different vesicle characteristics. This shows that the differentiation or culturing process influences these characteristics. Lung macrophages on the other hand are used fresh, directly after isolation from human lung tissue. Thus, they are already fully differentiated. To investigate the effect of culturing cells on ring characteristics lung macrophages were cultured like M0-like macrophages. With this protocol, cells are thought to not be polarised towards M1- nor M2-type macrophages. Thus, lung macrophages were not actively polarised towards a phenotype. In addition, the biggest differences in vesicle characteristics were observed with M0-like macrophages. Interestingly, lung macrophage vesicle characteristics did change upon culture (Figure 5-7). The mean diameter increased significantly from 94 ± 70 nm for fresh to 133 ± 82 nm for cultured lung macrophages with vesicles covering a much broader spectrum in general. Surprisingly, cultured lung macrophages displayed a high vesicle density also in non-activated conditions (Figure 5-7C). This means that lung macrophages are activated even without IgG-stimulation. It is well known that tissue macrophages are greatly influenced and regulated by their environment^{47,319,351}. Thus, it is possible, that macrophages are stressed and activated when cultured because they were removed from their specific tissue environment. In fact, Svedberg et al. reported murine alveolar macrophages to be hyporesponsive to the canonical type 2 cytokine IL-4 *in situ*,

however, when cultured outside of the lung they quickly re-gained responsiveness after only 48h³⁵². Nevertheless, the change in vesicle diameter may still indicate a relation between the secretion of EV and polarisation of the cell.

5.4.4 Analysis of Macrophage Secretions

As mentioned before, CD81 is part of the protein super family called tetraspanins which are well-known to be enriched in EV and are commonly used as EV marker^{192–194}. To further test the hypothesis of CD81 ring structures being EV, macrophages were stimulated on IgG-containing lipid bilayers, then detached and their secretions fixed and stained with anti-CD81 mAb labelled with AF647. If ring structures are vesicles, they will be left behind when the cell is detached. Indeed, secretions left behind resolved into nanometer-scale ring structures similar to those observed before (Figure 5-12). Their circular appearance is a strong indication for a spheroidal shape which is typical for extracellular vesicles and could be confirmed with line profiles (Figure 5-13). In addition, all vesicles measured were in the range of EV (Figure 5-16). In fact, 88% were less than 150 nm in diameter, thereby falling into the range of classical exosomes. Thus, these are strong indications that observed ring structures are indeed EV, captured directly upon secretion by the macrophages.

This was also supported by the successful isolation of EV. Therefore, macrophages were stimulated in solution with IgG-coated beads for 90 min and cells, large and small EV were isolated applying differential ultracentrifugation. When imaging isolated EV with STORM, they again appear as nanometer-scale ring structures in 2D-images (Figure 5-17 and Figure 5-18).

Further, characteristics of imaged secretions were compared to ring structures observed when the cells were still present on lipid bilayers. After confirming the correct performance, an ImageJ macro was applied to analyse the secretions left behind by macrophages in an objective and automated way (Figure 5-14 – Figure 5-16).

Interestingly, densities were slightly higher when cells were detached compared to when cells are still present (Figure 5-10 vs. Figure 5-15). This can be explained by the fact that vesicles are easier identified when cells were detached. When cells were still present, CD81 present in the cell membrane may mask the signal arising from CD81 in EV. It is likely that especially small vesicles or vesicles with relatively low levels of CD81 could be overlooked. In images of secretions on the other hand, vesicles are clearly visible without much background noise. Interestingly, an overall trend is visible for monocyte-derived macrophages activated on lipid bilayers. Vesicle densities are very similar but marginally increase from M0-like to M1-like and M2-like macrophages. This was observed in both cases, when cells were still present and when they were detached and is in the same order as the spreading of the macrophages, which may indicate a stronger interaction with the surface possibly leading to higher levels of activation and therefore higher vesicle densities. The density of lung macrophage vesicles also increased slightly from 0.877 ± 0.997 rings/ μm^2 for cells still present to 0.895 ± 0.442 rings/ μm^2 for secretions. However, relative to monocyte-derived macrophages they sometimes display the highest (cells still present) and sometimes the lowest (for secretions and when activated on glass slides) density. In any case, lung macrophage vesicles were significantly smaller than all monocyte-derived macrophage vesicles while there was no significant difference between them. This may indicate tissue-specific roles for vesicles.

5.4.5 Extracellular Vesicles are being secreted through Holes in the Actin Mesh

The actin cortex, a dense meshwork of actin filaments that is attached to the cell membrane, gives cells their shape³⁵³. Therefore it is not surprising that the actin cortex presents an obstacle for exocytosis, which requires active remodelling to facilitate the fusion of EV with the plasma membrane²⁰⁷. This has been described in a variety of cell systems including the delivery of lytic granules for example in NK cells³⁵⁴. Here, Gil-Krzewska and co-worker showed that openings in the cortex actin mesh controlled the delivery of lytic granules, with the secretion of big granules being hindered due to too small openings in the actin mesh.

Thus, to test whether actin remodelling and the opening up of the actin mesh is also required for macrophage vesicle secretion, macrophages were incubated on glass slides coated with PLL only (0 µg/mL IgG, non-activating condition) or PLL and IgG (10 µg/mL IgG, activating condition) for 15 min, permeabilised, fixed and stained with phalloidin-AF488 and anti-CD81 labelled with AF647. STED images of the actin mesh and confocal images of CD81 showed that EV co-localised with holes in the actin mesh, which was especially evident in M0-like macrophages (Figure 5-19A, yellow arrows). This makes sense as vesicles of M0-like macrophage activated on glass slides displayed a diameter of more than double the size of the other macrophages (Figure 5-4). Thus, holes in the actin mesh are likely to be bigger for M0-like macrophages. Line profiles confirmed observations for M1-like and M2-like macrophages, with CD81-rich areas falling within actin holes. In addition, the calculation of the Pearsons overlap co-efficient showed the segregation of CD81 and actin upon activation. Taken together, upon activation through their FcγRI, macrophages secrete vesicles that are delivered through holes in the actin cortex mesh, which correlate with the size of the EV.

5.4.6 Proteomics Data Confirms Discrete Contents for Macrophage Vesicles

EV contain different biological material including proteins, DNAs, RNAs, lipids and cytokines¹⁸². The contents of EV are thought to reflect the state of their parental cell, without being the product of the random sampling of molecules of the parental cell. For example, Garzetti et al. showed that microvesicles secreted by M1- and M2-polarised macrophages displayed distinct mRNA contents compared to whole cells³⁵⁵. Nevertheless, microvesicles could be utilised to identify the activated phenotype of their parental cell and even follow a phenotype switch in real time.

Thus, to test whether EV observed in this project also display distinct contents, monocyte-derived macrophages were stimulated in solution with IgG-coated beads for 90 min, large and small EV were isolated via differential ultracentrifugation and label free proteomics analysis was performed (Figure 5-20). Indeed, hierarchical clustering analysis of all identified proteins revealed distinct protein contents for small and large

EV and all three cell types (Figure 5-21A). This was confirmed by principal component analysis (PCA) where small and large EV cluster separately (Figure 5-21B). This shows no notable contamination of the samples and therefore confirms the correct isolation and processing of the samples. More importantly, it highlights the fact that large and small EV cluster separately, independent of the cell type, possibly revealing a distinct process of biogenesis for small and large EV.

However, to investigate differences between cell types in more detail, small and large EV were analysed separately. Therefore, all significantly changed proteins of small or large EV were exported from Proteome Discoverer 4.0 and imported into R to create a heatmap using the standard *heatmap* function with no scaling (Figure 5-23 and Figure 5-24). In both cases, hierarchical clustering across rows confirmed distinct protein contents for EV derived from M0-like, M1-like and M2-like macrophages. Interestingly, for both, small and large EV MHC class II molecules was found to be enriched in M1-like macrophages vesicles, though also present in M2-like macrophage vesicles and lowest in vesicles derived from M0-like macrophages (Table 5-1 and Table 5-3). MHC class I on the other hand was highest in M2-like macrophage vesicles but also detected in M0-like macrophage vesicles and lowest in vesicles derived from M1-like macrophage vesicles (Table 5-4). Surprisingly, MHC class I was only detected in large but not in small EV.

MHC molecules have long been described in EV. In fact, the first reported EV from immune cells contained high levels of MHC class I and II. They were secreted by B lymphocytes and able to activate CD4⁺ T cells, suggesting a role in antigen presentation by lymphocytes²¹⁷. Along this line, Théry and co-workers showed that the injection of mice with EV containing the peptide-MHC class II complex derived from dendritic cells (DC) were able to activate antigen-specific naïve CD4⁺ T cells³⁵⁶. Nowadays, the importance of EV in antigen presentation is widely appreciated. MHC class I and II was also described in macrophage derived EV^{357,358}. These were able to activate naïve T cells and macrophages. It is thus not surprising that MHC class I and II could be identified in macrophage EV. In addition, M1 macrophages are known to express high levels of MHC

class II which is in accordance with the proteomics data²⁶⁶. Interestingly, MHC class II expression of M0-like, M1-like and M2-like macrophages used in this project was similar (Figure 3-4); however, EV derived from these macrophages displayed higher levels of MHC II for M1-like macrophages. This highlights the fact that contents of EV are not the result of random sampling of the mother cell, but the enrichment of specific molecules occurs. More importantly, it shows that the expression of MHC molecules varies on EV derived from different macrophages, possibly revealing distinct functions for antigen presentation.

The leukocyte immunoglobulin-like receptors (LILR) are a family of receptor molecules that consist of activating (LILRA) and inhibitory (LILRB) receptors. In recent years, the inhibitory receptor LILRB1 was appreciated as possible checkpoint in immunotherapies. Its ligand is MHC class I which is expressed on all nucleated cells in the body. Barkal and co-workers showed that the blockage of LILRB1 increased the ability of primary human macrophages to phagocytose cancer cells *in vitro*³⁵⁹. Further, by using immunodeficient and immunocompetent mouse models they showed that the LILRB1-MHC I checkpoint protects tumours against macrophage phagocytosis. Interestingly, for small as well as large EV the inhibitory receptors LILRB1 and 2 were enriched especially in M2-like macrophage vesicles while they were lower in M0-like and M1-like macrophage vesicles (Table 5-2 and Table 5-5). This is in agreement with M2-like macrophages having an anti-inflammatory phenotype which is imprinted on EV secreted. The activating receptor LILRA2 was detected in small EV derived from M0-like macrophages while it was low in M1-like and not detected in M2-like macrophage vesicles (Table 5-2).

Another immunocheckpoint on macrophages is the CD47-signal regulatory protein α (SIRP α) interaction. Here, SIRP α functions like LILRB1 as inhibitory receptors that suppresses phagocytosis and CD47, like MHC class I, acts as “don’t eat me signal” that is expressed for example by cancer cells to evade immune surveillance^{359,360}. Exosomal CD47 was used as biomarker for diagnosis and prognosis of breast cancer and

shown to inhibit phagocytosis by macrophages^{361–363}. It's expression has also been reported on macrophage EV³⁶⁴. LILRB1 on the other hand has not been described in EV before.

Taken together, small and large EV of M0-like, M1-like and M2-like macrophages were successfully isolated via differential ultracentrifugation and hierarchical clustering revealed distinct contents for small and large EV and all three cell types. This was confirmed by PCA. Analysis of all regulated proteins for small and large EV separately confirmed distinct EV contents for the different cell types. Interestingly, MHC class II was enriched in EV derived from M1-like macrophages while M2-like macrophage vesicles were contained higher levels of MHC class I as well as inhibitory receptor LILRB1 and 2. Strikingly, cellular levels of MHC class II were similar between the cell types yet their expression on EV varied. In the past, MHC class II bearing EV derived from various cell types have been shown to activate lymphocytes, highlighting their role in antigen presentation. Thus, varying levels of MHC molecules on EV could indicate distinct roles in antigen presentation.

5.4.7 MHC class I co-localises with LILRB1 on M0-like Macrophage Vesicles

To test hits from the proteomics data, M0-like, M1-like and M2-like macrophages were incubated on IgG-coated glass slides for 15 min, fixed and stained with anti-LILRB1 mAb labelled with AF647 and anti-CD81 mAb labelled with AF488 and TIRF images were taken (Figure 5-25). Indeed, preliminary data showed that EV from M0-like and M2-like macrophages were stained positive for LILRB1 (Figure 5-25B). Interestingly, not all, but most vesicles were LILRB1 positive, highlighting again the heterogeneity of cellular secretions. Some vesicles stained positive for CD81 but not LILRB1. M1-like macrophages seemed to not have secreted any vesicles, as they didn't display any signal for CD81 or LILRB1. It may be more likely that this was due to a technical error rather than a biological phenomenon. In any case, images of M0-like and M2-like macrophage vesicles confirmed the presence of LILRB1 in EV, which displayed a heterogeneity.

Next, LILRB1 was investigated using STORM. Therefore, M0-like macrophages were incubated on IgG-coated glass slides for 15 min, fixed and stained with anti-LILRB1 mAb labelled with AF647. As expected, vesicles resolved into nanometer-scale ring structures (Figure 5-27A). However, there were only very few rings visible. Many less than the TIRF images suggested. It has to be kept in mind though that LILRB1 might be contained but not enriched in EV compared to the membrane. This would make it more difficult to identify EV within the membrane. In addition, even for CD81, which is enriched in EV the ring density was found to be higher when cells were detached compared to cells still present.

Finally, M0-like macrophages were investigated for LILRB1 and MHC class I with two colour STORM as proteomics data predicted both molecules to be contained in their vesicles. Therefore, M0-like macrophages were plated for 15 min on PLL (non-activating conditions) or PLL and IgG coated (activating conditions, 50 µg/mL IgG) microscopy slides, fixed and stained with anti-LILRB1-AF488 mAb and anti-HLA-A,B,C-AF647 mAb. As expected, both molecules were found in EV in the membrane of activated M0-like macrophages which resolved in nanometer-scale ring structures. More interestingly, LILRB1 co-localised with MHC class I molecules. All LILRB1-positive vesicles were also MHC-class-I-positive but there were some EV that were only MHC-class-I-positive. MHC class I is the ligand of LILRB1 and LILRB1 is known to interact with it in cis-interactions³⁶⁵. The co-localisation of both molecules on the same EV could indicate that LILRB1 is transferred already engaged, actively inhibiting the recipient cell.

5.4.8 Conclusions

In summary, the tetraspanin and extracellular vesicle (EV) marker CD81 was found to form into nanometer-scale ring structures at the synapse of IgG-activated human macrophages. The comparison of M0-like, M1-like, M2-like and lung macrophages revealed distinct characteristics of these ring structures which differed slightly when activating macrophages on IgG-coated glass slides or IgG-containing lipid bilayers. The capture of secretions of macrophages further identified these ring structures as EV,

which could also be isolated. STORM allowed the investigation of EV directly upon secretion on a cell-by-cell basis. Crucially, cellular secretions were found to be heterogeneous in numbers as well as contents. Thus, the vesicle density differed from cell to cell and two colour TIRF and STORM images of EV revealed that only a fraction of all EV secreted by one cell was LILRB1-positive. In addition, LILRB1 was found to co-localise with MHC class I molecules in EV of M0-like macrophages. In the proteomics data, the expression of MHC molecules on EV varied for the different cell types while cellular expression of MHC class II determined by flow cytometry was similar, possibly revealing distinct functions in antigen presentation. Thus, the activation of different macrophages with the same stimulus led to the secretion of distinct EV. These possibly fulfil specialised functions like the activation or inhibition of specific immune cells via according antigen presentation or the incorporation of LILRB1. Importantly, STORM presents a unique technique to study EV directly upon secretion, avoiding the harsh isolation process and allowing single cell analysis. By studying activation-induced EV on a single cell level, novel mechanisms about cellular activation could be discovered.

Chapter 6 – Final Remarks

Macrophages are one of the most plastic cell types known. They can act pro- as well as anti-inflammatory and fulfil a great variety of different functions. To regulate these many different functions and phenotypes, they continuously sense their surroundings and are in constant contact with other cells. One form of cell-to-cell communication is the exchange of extracellular vesicles (EV). EV are spherical membranous structures, containing biologically active material, including for example RNAs and receptors as well as adhesion and signalling molecules. Different subpopulations of EV exist, including exosomes and microvesicles. These display distinct yet overlapping sizes and contents, which makes a clear definition of subpopulations challenging. Since EV have the capacity to induce different cellular functions in the recipient cell, including for example antigen presentation to and activation of T cells²¹⁷, the heterogeneity in which cells secrete which types of EVs is vital to understand. However, EV are classically studied in bulk, after isolation from supernatants or biofluids and current isolation protocols result in a mixed population of EV. This can lead to the fusion of EV in addition to the co-purification of non-EV-associated molecules. Thus, the biggest limitations of the field are the ongoing inability to selectively isolate pure subpopulations of EV and the lack of single-cell and single-vesicle analysis. To address these limitations, the secretion of EV was studied by super-resolution microscopy, capturing vesicles directly upon secretion by different macrophages. Blood- as well as lung-derived macrophages were studied to investigate cell-specific characteristics of EV secretion. Crucially, the high autofluorescence of lung macrophages led to the development of a novel background correction technique to enable STORM for these samples. In summary, this study established that:

1. A moving median filter accurately corrects complex backgrounds, including autofluorescence, in STORM. Simulated as well as real data was used to thoroughly test and validate the novel correction technique. In general, accurate background correction is crucial in STORM, as an insufficient signal-to-noise ratio inhibits the precise detection of localisations, resulting in a distorted STORM image. Thus, the

novel correction technique is a great advance for the field of super-resolution microscopy and can find wide application for a variety of different samples. Crucially, this enabled the investigation of the membrane of human lung macrophages on a nanometer-scale for the first time, which led to the observation of MHC class I tipped protrusions. Macrophages are well-known to present antigens to other immune cells, including T cells, thereby activating the adaptive immune response. Thus, sessile macrophages in the airways and alveoli may extend protrusions tipped with MHC class I to reach cells nearby and present antigens to them.

2. Different macrophages secrete EV with distinct characteristics upon activation with IgG. The engagement of FcγRI leads to the activation of the macrophage, resulting in the secretion of CD81⁺ EV. Vesicles from different macrophages displayed distinct mean diameters, possibly suggesting different biogenesis pathways. This is supported by proteomics analysis of isolated EV from monocyte-derived macrophages (MDM) which revealed the biggest difference between large and small EV, despite the donor or macrophage type. However, for one EV type, vesicles displayed discrete contents for the different cell types highlighting the imprint of the ‘mother cell’ on their EV.

3. Cellular secretions are heterogeneous. This was true for all aspects investigated on a single-cell or single-vesicle level: the number of vesicles secreted per cell, the contents of single vesicles as well as vesicle sizes secreted by one cell differed greatly. Further advances in single-cell analysis could help to understand the detailed mechanisms of cellular activation that so many researchers are trying to entangle.

Taken together, this study advanced the field of super-resolution microscopy by developing a novel background correction technique which enables the investigation of otherwise lost samples, including autofluorescent lung macrophages. It also revealed new aspects of EV secretion, studied on a cell-by-cell basis. Importantly, it highlights the

heterogeneity of cellular secretions and underscores the need to study EV secretion on a single-cell and single-vesicles basis. This will be instrumental in fully understanding cellular activation and responses, which is ultimately needed to manipulate cellular systems and develop new medicines.

References

1. Wynn, T. A., Chawla, A. & Pollard, J. W. Macrophage biology in development, homeostasis and disease. *Nature* **496**, 445–455 (2013).
2. Davies, L. C. & Taylor, P. R. Tissue-resident macrophages: Then and now. *Immunology* **144**, 541–548 (2015).
3. Sherman, E. *et al.* Functional Nanoscale Organization of Signaling Molecules Downstream of the T Cell Antigen Receptor. *Immunity* **35**, 705–720 (2011).
4. Mattila, P. K. *et al.* The Actin and Tetraspanin Networks Organize Receptor Nanoclusters to Regulate B Cell Receptor-Mediated Signaling. *Immunity* **38**, 461–474 (2013).
5. Lopes, F. B. *et al.* Membrane nanoclusters of FcγRI segregate from inhibitory SIRPα upon activation of human macrophages. *J. Cell Biol.* **216**, 1123–1141 (2017).
6. Bálint, Š., Lopes, F. B. & Davis, D. M. A nanoscale reorganization of the IL-15 receptor is triggered by NKG2D in a ligand-dependent manner. *Sci. Signal.* **11**, eaal3606 (2018).
7. Mosser, D. M. & Edwards, J. P. Exploring the full spectrum of macrophage activation. *Nat. Rev. Immunol.* **8**, 958–969 (2008).
8. Gordon, S. & Taylor, P. R. Monocyte and macrophage heterogeneity. *Nat. Rev. Immunol.* **5**, 953–964 (2005).
9. Geissmann, F. *et al.* Development of Monocytes, Macrophages, and Dendritic Cells. *Science (80-.)*. **327**, 656–661 (2010).
10. Mills, C. D., Kincaid, K., Alt, J. M., Heilman, M. J. & Hill, A. M. M-1/M-2 macrophages and the Th1/Th2 paradigm. *J. Immunol.* **164**, 6166–73 (2000).
11. Martinez, F. O. & Gordon, S. The M1 and M2 paradigm of macrophage activation: time for reassessment. *F1000Prime Rep.* **6**, 13 (2014).
12. van Furth, R. *et al.* The mononuclear phagocyte system: a new classification of macrophages, monocytes, and their precursor cells. *Bull. World Health Organ.*

- 46**, 845–852 (1972).
13. Varol, C., Mildner, A. & Jung, S. *Macrophages: development and tissue specialization. Annu Rev Immunol* vol. 33 (2015).
 14. Kuziel, W. A. *et al.* Severe reduction in leukocyte adhesion and monocyte extravasation in mice deficient in CC chemokine receptor 2. *Proc. Natl. Acad. Sci. U. S. A.* **94**, 12053–12058 (1997).
 15. Schönlau, F. *et al.* Monocyte and macrophage functions in M-CSF-deficient *op/op* mice during experimental leishmaniasis. *J. Leukoc. Biol.* **73**, 564–573 (2003).
 16. Munro, D. A. D. & Hughes, J. The origins and functions of tissue-resident macrophages in kidney development. *Frontiers in Physiology* vol. 8 837 (2017).
 17. Sheng, J., Ruedl, C. & Karjalainen, K. Most Tissue-Resident Macrophages Except Microglia Are Derived from Fetal Hematopoietic Stem Cells. *Immunity* **43**, 382–393 (2015).
 18. Palis, J., Robertson, S., Kennedy, M., Wall, C. & Keller, G. Development of erythroid and myeloid progenitors in the yolk sac and embryo proper of the mouse. *Development* **126**, 5073–5084 (1999).
 19. Bertrand, J. Y. *et al.* Three pathways to mature macrophages in the early mouse yolk sac. *Blood* **106**, 3004–3011 (2005).
 20. Kasaai, B. *et al.* Erythro-myeloid progenitors can differentiate from endothelial cells and modulate embryonic vascular remodeling. *Sci. Rep.* **7**, 1–12 (2017).
 21. Guillemins, M. *et al.* Alveolar macrophages develop from fetal monocytes that differentiate into long-lived cells in the first week of life via GM-CSF. *J. Exp. Med.* **210**, 1977–1992 (2013).
 22. Wu, Y. & Hirschi, K. K. Tissue-Resident Macrophage Development and Function. *Front. Cell Dev. Biol.* **8**, 1750 (2021).
 23. Cumano, A. & Godin, I. Ontogeny of the hematopoietic system. *Annual Review of Immunology* vol. 25 745–785 (2007).
 24. Orkin, S. H. & Zon, L. I. Hematopoiesis: An Evolving Paradigm for Stem Cell

- Biology. *Cell* vol. 132 631–644 (2008).
25. Merad, M. *et al.* Langerhans cells renew in the skin throughout life under steady-state conditions. *Nat. Immunol.* **3**, 1135–1141 (2002).
 26. Ajami, B., Bennett, J. L., Krieger, C., Tetzlaff, W. & Rossi, F. M. V. Local self-renewal can sustain CNS microglia maintenance and function throughout adult life. *Nat. Neurosci.* **10**, 1538–1543 (2007).
 27. Ginhoux, F. & Jung, S. Monocytes and macrophages: developmental pathways and tissue homeostasis. *Nat. Rev. Immunol.* **14**, 392–404 (2014).
 28. Bain, C. C. *et al.* Constant replenishment from circulating monocytes maintains the macrophage pool in the intestine of adult mice. *Nat. Immunol.* **15**, 929–937 (2014).
 29. Epelman, S. *et al.* Embryonic and adult-derived resident cardiac macrophages are maintained through distinct mechanisms at steady state and during inflammation. *Immunity* **40**, 91–104 (2014).
 30. Tamoutounour, S. *et al.* Origins and functional specialization of macrophages and of conventional and monocyte-derived dendritic cells in mouse skin. *Immunity* **39**, 925–938 (2013).
 31. Calderon, B. *et al.* The pancreas anatomy conditions the origin and properties of resident macrophages. *J. Exp. Med.* **212**, 1497–1512 (2015).
 32. Scott, C. L. *et al.* Bone marrow-derived monocytes give rise to self-renewing and fully differentiated Kupffer cells. *Nat. Commun.* **7**, 1–10 (2016).
 33. Molawi, K. *et al.* Progressive replacement of embryo-derived cardiac macrophages with age. *J. Exp. Med.* **211**, 2151–2158 (2014).
 34. Serbina, N. V. & Pamer, E. G. Monocyte emigration from bone marrow during bacterial infection requires signals mediated by chemokine receptor CCR2. *Nat. Immunol.* **7**, 311–317 (2006).
 35. Ginhoux, F. *et al.* Fate mapping analysis reveals that adult microglia derive from primitive macrophages. *Science (80-.).* **330**, 841–845 (2010).

36. Hoeffel, G. *et al.* Adult Langerhans cells derive predominantly from embryonic fetal liver monocytes with a minor contribution of yolk sac-derived macrophages. *J. Exp. Med.* **209**, 1167–1181 (2012).
37. Jakubzick, C. V., Randolph, G. J. & Henson, P. M. Monocyte differentiation and antigen-presenting functions. *Nature Reviews Immunology* vol. 17 349–362 (2017).
38. Janssen, W. J. *et al.* Fas determines differential fates of resident and recruited macrophages during resolution of acute lung injury. *Am. J. Respir. Crit. Care Med.* **184**, 547–560 (2011).
39. Ensan, S. *et al.* Self-renewing resident arterial macrophages arise from embryonic CX3CR1 + precursors and circulating monocytes immediately after birth. *Nat. Immunol.* **17**, 159–168 (2016).
40. Lavin, Y. *et al.* Tissue-resident macrophage enhancer landscapes are shaped by the local microenvironment. *Cell* **159**, 1312–1326 (2014).
41. Gautier, E. L. *et al.* Gene-expression profiles and transcriptional regulatory pathways that underlie the identity and diversity of mouse tissue macrophages. *Nat. Immunol.* **13**, 1118–1128 (2012).
42. Gosselin, D. *et al.* Environment drives selection and function of enhancers controlling tissue-specific macrophage identities. *Cell* **159**, 1327–1340 (2014).
43. Van Hove, H. *et al.* A single-cell atlas of mouse brain macrophages reveals unique transcriptional identities shaped by ontogeny and tissue environment. *Nat. Neurosci.* **22**, 1021–1035 (2019).
44. Ydens, E. *et al.* Profiling peripheral nerve macrophages reveals two macrophage subsets with distinct localization, transcriptome and response to injury. *Nat. Neurosci.* **23**, 676–689 (2020).
45. Gibbings, S. L. *et al.* Transcriptome analysis highlights the conserved difference between embryonic and postnatal-derived alveolar macrophages. *Blood* **126**, 1357–1366 (2015).
46. Bruttger, J. *et al.* Genetic Cell Ablation Reveals Clusters of Local Self-Renewing

- Microglia in the Mammalian Central Nervous System. *Immunity* **43**, 92–106 (2015).
47. Guillems, M. & Svedberg, F. R. Does tissue imprinting restrict macrophage plasticity? *Nature Immunology* vol. 22 118–127 (2021).
 48. Hoeffel, G. *et al.* C-Myb⁺ Erythro-Myeloid Progenitor-Derived Fetal Monocytes Give Rise to Adult Tissue-Resident Macrophages. *Immunity* **42**, 665–678 (2015).
 49. Fausto, N., Laird, A. D. & Webber, E. M. Liver regeneration. 2. Role of growth factors and cytokines in hepatic regeneration. *FASEB J.* **9**, 1527–1536 (1995).
 50. Guillems, M. & Scott, C. L. Does niche competition determine the origin of tissue-resident macrophages? *Nature Reviews Immunology* vol. 17 451–460 (2017).
 51. van de Laar, L. *et al.* Yolk Sac Macrophages, Fetal Liver, and Adult Monocytes Can Colonize an Empty Niche and Develop into Functional Tissue-Resident Macrophages. *Immunity* **44**, 755–768 (2016).
 52. Hashimoto, D. *et al.* Tissue-resident macrophages self-maintain locally throughout adult life with minimal contribution from circulating monocytes. *Immunity* **38**, 792–804 (2013).
 53. Gordon, S. Alternative activation of macrophages. *Nature Reviews Immunology* vol. 3 23–35 (2003).
 54. Fleetwood, A. J., Lawrence, T., Hamilton, J. A. & Cook, A. D. Granulocyte-Macrophage Colony-Stimulating Factor (CSF) and Macrophage CSF-Dependent Macrophage Phenotypes Display Differences in Cytokine Profiles and Transcription Factor Activities: Implications for CSF Blockade in Inflammation. *J. Immunol.* **178**, 5245–5252 (2007).
 55. Amici, S. A., Dong, J. & Guerau-de-Arellano, M. Molecular mechanisms modulating the phenotype of macrophages and microglia. *Frontiers in Immunology* vol. 8 1520 (2017).
 56. Arnold, C. E. *et al.* A critical role for suppressor of cytokine signalling 3 in promoting M1 macrophage activation and function *in vitro* and *in vivo*. *Immunology* **141**, 96–110 (2014).

57. Macmicking, J. D. *et al.* Identification of nitric oxide synthase as a protective locus against tuberculosis. *Proc. Natl. Acad. Sci. U. S. A.* **94**, 5243–5248 (1997).
58. Mantovani, A. *et al.* The chemokine system in diverse forms of macrophage activation and polarization. *Trends in Immunology* vol. 25 677–686 (2004).
59. Orecchioni, M., Ghosheh, Y., Pramod, A. B. & Ley, K. Macrophage polarization: Different gene signatures in M1(Lps+) vs. Classically and M2(LPS-) vs. Alternatively activated macrophages. *Frontiers in Immunology* vol. 10 1084 (2019).
60. Murray, P. J. *et al.* Macrophage Activation and Polarization: Nomenclature and Experimental Guidelines. *Immunity* vol. 41 14–20 (2014).
61. Luque-Martin, R., Mander, P. K., Leenen, P. J. M. & Winther, M. P. J. Classic and new mediators for *in vitro* modelling of human macrophages. *J. Leukoc. Biol.* **109**, 549–560 (2021).
62. Wicks, I. P. & Roberts, A. W. Targeting GM-CSF in inflammatory diseases. *Nat. Rev. Rheumatol.* **12**, 37–48 (2016).
63. Hamilton, J. A. Colony-stimulating factors in inflammation and autoimmunity. *Nature Reviews Immunology* vol. 8 533–544 (2008).
64. Ushach, I. & Zlotnik, A. Biological role of granulocyte macrophage colony-stimulating factor (GM-CSF) and macrophage colony-stimulating factor (M-CSF) on cells of the myeloid lineage. *J. Leukoc. Biol.* **100**, 481–489 (2016).
65. Noster, R. *et al.* IL-17 and GM-CSF expression are antagonistically regulated by human T helper cells. *Sci. Transl. Med.* **6**, 241ra80-241ra80 (2014).
66. Perrella, O., Carrieri, P. B., De Mercato, R. & Buscaino, G. A. Markers of Activated T Lymphocytes and T Cell Receptor Gamma/ Delta+ in Patients with Multiple Sclerosis. *Eur. Neurol.* **33**, 152–155 (1993).
67. Codarri, L. *et al.* ROR γ t drives production of the cytokine GM-CSF in helper T cells, which is essential for the effector phase of autoimmune neuroinflammation. *Nat. Immunol.* **12**, 560–567 (2011).

68. McQualter, J. L. *et al.* Granulocyte macrophage colony-stimulating factor: A new putative therapeutic target in multiple sclerosis. *J. Exp. Med.* **194**, 873–881 (2001).
69. Boulakirba, S. *et al.* IL-34 and CSF-1 display an equivalent macrophage differentiation ability but a different polarization potential. *Sci. Rep.* **8**, 1–11 (2018).
70. Domschke, G. & Gleissner, C. A. CXCL4-induced macrophages in human atherosclerosis. *Cytokine* **122**, 154141 (2019).
71. Gleissner, C. A., Shaked, I., Little, K. M. & Ley, K. CXC Chemokine Ligand 4 Induces a Unique Transcriptome in Monocyte-Derived Macrophages. *J. Immunol.* **184**, 4810–4818 (2010).
72. Scheuerer, B. *et al.* The CXC-chemokine platelet factor 4 promotes monocyte survival and induces monocyte differentiation into macrophages. *Blood* **95**, 1158–1166 (2000).
73. Sierra-Filardi, E. *et al.* CCL2 Shapes Macrophage Polarization by GM-CSF and M-CSF: Identification of CCL2/CCR2-Dependent Gene Expression Profile. *J. Immunol.* **192**, 3858–3867 (2014).
74. Fu, X. L. *et al.* Interleukin 6 induces M2 macrophage differentiation by STAT3 activation that correlates with gastric cancer progression. *Cancer Immunol. Immunother.* **66**, 1597–1608 (2017).
75. Dominguez-Gutierrez, P. R., Kusmartsev, S., Canales, B. K. & Khan, S. R. Calcium Oxalate Differentiates Human Monocytes Into Inflammatory M1 Macrophages. *Front. Immunol.* **9**, 1863 (2018).
76. Lehtonen, A., Matikainen, S., Miettinen, M. & Julkunen, I. Granulocyte-macrophage colony-stimulating factor (GM-CSF)-induced STAT5 activation and target-gene expression during human monocyte/macrophage differentiation. *J. Leukoc. Biol.* **71**, 511–9 (2002).
77. Jaguin, M., Houlbert, N., Fardel, O. & Lecureur, V. Polarization profiles of human M-CSF-generated macrophages and comparison of M1-markers in classically

- activated macrophages from GM-CSF and M-CSF origin. *Cell. Immunol.* **281**, 51–61 (2013).
78. Xu, W., Zhao, X., Daha, M. R. & van Kooten, C. Reversible differentiation of pro- and anti-inflammatory macrophages. *Mol. Immunol.* **53**, 179–186 (2013).
 79. Lacey, D. C. *et al.* Defining GM-CSF– and Macrophage-CSF–Dependent Macrophage Responses by In Vitro Models. *J. Immunol.* **188**, 5752–5765 (2012).
 80. Xue, J. *et al.* Transcriptome-Based Network Analysis Reveals a Spectrum Model of Human Macrophage Activation. *Immunity* **40**, 274–288 (2014).
 81. Vogel, D. Y. S. *et al.* Human macrophage polarization in vitro: Maturation and activation methods compared. *Immunobiology* **219**, 695–703 (2014).
 82. Schneberger, D., Aharonson-Raz, K. & Singh, B. Monocyte and macrophage heterogeneity and Toll-like receptors in the lung. *Cell Tissue Res.* **343**, 97–106 (2011).
 83. Barletta, K. E. *et al.* Leukocyte compartments in the mouse lung: Distinguishing between marginated, interstitial, and alveolar cells in response to injury. *J. Immunol. Methods* **375**, 100–110 (2012).
 84. Cai, Y. *et al.* In vivo characterization of alveolar and interstitial lung macrophages in rhesus macaques: implications for understanding lung disease in humans. *J. Immunol.* **192**, 2821–9 (2014).
 85. Scott, C. L., Henri, S. & Guilleams, M. Mononuclear phagocytes of the intestine, the skin, and the lung. *Immunol. Rev.* **262**, 9–24 (2014).
 86. Snelgrove, R. J., Godlee, A. & Hussell, T. Airway immune homeostasis and implications for influenza-induced inflammation. *Trends Immunol.* **32**, 328–334 (2011).
 87. Ely, K. H., Cookenham, T., Roberts, A. D. & Woodland, D. L. Memory T cell populations in the lung airways are maintained by continual recruitment. *J. Immunol.* **176**, 537–43 (2006).
 88. Westphalen, K. *et al.* Sessile alveolar macrophages communicate with alveolar

- epithelium to modulate immunity. *Nature* **506**, 503–506 (2014).
89. Duan, M. *et al.* Distinct Macrophage Subpopulations Characterize Acute Infection and Chronic Inflammatory Lung Disease. *J. Immunol.* **189**, 946–955 (2012).
 90. Hussell, T. & Bell, T. J. Alveolar macrophages: plasticity in a tissue-specific context. *Nat. Rev. Immunol.* **14**, 81–93 (2014).
 91. Schneider, C. *et al.* Induction of the nuclear receptor PPAR- γ 3 by the cytokine GM-CSF is critical for the differentiation of fetal monocytes into alveolar macrophages. *Nat. Immunol.* **15**, 1026–1037 (2014).
 92. Joshi, N., Walter, J. M. & Misharin, A. V. Alveolar Macrophages. *Cell. Immunol.* **330**, 86–90 (2018).
 93. Trapnell, B. C. *et al.* Pulmonary alveolar proteinosis. *Nature Reviews Disease Primers* vol. 5 1–17 (2019).
 94. Mayer, A. K., Bartz, H., Fey, F., Schmidt, L. M. & Dalpke, A. H. Airway epithelial cells modify immune responses by inducing an anti-inflammatory microenvironment. *Eur. J. Immunol.* **38**, 1689–1699 (2008).
 95. Murray, P. J. & Wynn, T. A. Protective and pathogenic functions of macrophage subsets. (2011) doi:10.1038/nri3073.
 96. Atif, S. M., Gibbings, S. L. & Jakubzick, C. V. Isolation and identification of interstitial macrophages from the lungs using different digestion enzymes and staining strategies. in *Methods in Molecular Biology* vol. 1784 69–76 (Humana Press Inc., 2018).
 97. Schyns, J., Bureau, F. & Marichal, T. Lung interstitial macrophages: Past, present, and future. *Journal of Immunology Research* vol. 2018 (2018).
 98. Tan, S. Y. S. & Krasnow, M. A. Developmental origin of lung macrophage diversity. *Dev.* **143**, 1318–1327 (2016).
 99. Misharin, A. V., Morales-Nebreda, L., Mutlu, G. M., Budinger, G. R. S. & Perlman, H. Flow cytometric analysis of macrophages and dendritic cell subsets in the mouse lung. *Am. J. Respir. Cell Mol. Biol.* **49**, 503–510 (2013).

100. Bedoret, D. *et al.* Lung interstitial macrophages alter dendritic cell functions to prevent airway allergy in mice. *J. Clin. Invest.* **119**, 3723–3738 (2009).
101. Gibbings, S. L. *et al.* Three unique interstitial macrophages in the murine lung at steady state. *Am. J. Respir. Cell Mol. Biol.* **57**, 66–76 (2017).
102. Schyns, J. *et al.* Non-classical tissue monocytes and two functionally distinct populations of interstitial macrophages populate the mouse lung. *Nat. Commun.* **10**, 1–16 (2019).
103. Chakarov, S. *et al.* Two distinct interstitial macrophage populations coexist across tissues in specific subtissular niches. *Science (80-.).* **363**, (2019).
104. A-Gonzalez, N. *et al.* Phagocytosis imprints heterogeneity in tissue-resident macrophages. *J. Exp. Med.* **214**, 1281–1296 (2017).
105. Gong, J. L., McCarthy, K. M., Rogers, R. A. & Schneeberger, E. E. Interstitial lung macrophages interact with dendritic cells to present antigenic peptides derived from particulate antigens to T cells. *Immunology* **81**, 343–51 (1994).
106. Fathi, M. *et al.* Functional and morphological differences between human alveolar and interstitial macrophages. *Exp. Mol. Pathol.* **70**, 77–82 (2001).
107. Jakubzick, C. *et al.* Minimal differentiation of classical monocytes as they survey steady-state tissues and transport antigen to lymph nodes. *Immunity* **39**, 599–610 (2013).
108. Sabatel, C. *et al.* Exposure to Bacterial CpG DNA Protects from Airway Allergic Inflammation by Expanding Regulatory Lung Interstitial Macrophages. *Immunity* **46**, 457–473 (2017).
109. Edelson, J. D., MacFadden, D. K., Klein, M. & Rebeck, A. S. Autofluorescence of alveolar macrophages: problems and potential solutions. *Med. Hypotheses* **17**, 403–7 (1985).
110. Stübel, H. Die Fluoreszenz tierischer Gewebe in ultraviolettem Licht. *Pflüger's Arch. für die Gesamte Physiol. des Menschen und der Tiere* **142**, 1–14 (1911).
111. Haitinger, M. *Fluoreszenzmikroskopie. Ihre Anwendung in der Histologie und*

Chemie. Akademische Verlagsgesellschaft MBH. (1938).

112. Goodwin, R. H. Fluorescent Substances in Plants. *Annu. Rev. Plant Physiol.* **4**, 283–304 (1953).
113. O'Brien, T. P. (Terence P. . & McCully, M. E. (Margaret E. . *The study of plant structure : principles and selected methods.* (Termarcaphi, 1981).
114. Croce, A. C. & Bottiroli, G. Autofluorescence spectroscopy and imaging: A tool for biomedical research and diagnosis. *Eur. J. Histochem.* **58**, 320–337 (2014).
115. Billinton, N. & Knight, A. W. Seeing the wood through the trees: A review of techniques for distinguishing green fluorescent protein from endogenous autofluorescence. *Analytical Biochemistry* vol. 291 175–197 (2001).
116. Georgakoudi, I. & Quinn, K. P. Optical imaging using endogenous contrast to assess metabolic state. *Annual Review of Biomedical Engineering* vol. 14 351–367 (2012).
117. Monici, M. *et al.* Dependence of leukemic cell autofluorescence patterns on the degree of differentiation. *Photochem. Photobiol. Sci.* **2**, 981–987 (2003).
118. Alfano, R. R. *et al.* Laser Induced Fluorescence Spectroscopy from Native Cancerous and Normal Tissue. *IEEE J. Quantum Electron.* **20**, 1507–1511 (1984).
119. Masoudi-Nejad, A. & Asgari, Y. Metabolic Cancer Biology: Structural-based analysis of cancer as a metabolic disease, new sights and opportunities for disease treatment. *Seminars in Cancer Biology* vol. 30 21–29 (2015).
120. Buryakina, T. Y. Metabolism of HeLa cells revealed through autofluorescence lifetime upon infection with enterohemorrhagic *Escherichia coli*. *J. Biomed. Opt.* **17**, 101503 (2012).
121. Leblanc, L. & Dufour, Æ. Monitoring the identity of bacteria using their intrinsic fluorescence. *FEMS Microbiol. Lett.* **211**, 147–153 (2002).
122. Zimmermann, H. F., Trauthwein, H., Dingerdissen, U., Rieping, M. & Huthmacher, K. Monitoring aerobic *Escherichia coli* growth in shaken microplates by measurement of culture fluorescence. *Biotechniques* **36**, 580–584 (2004).

123. Bao, N., Jagadeesan, B., Bhunia, A. K., Yao, Y. & Lu, C. Quantification of bacterial cells based on autofluorescence on a microfluidic platform. *J. Chromatogr. A* **1181**, 153–158 (2008).
124. Mihalcescu, I., Van-Melle Gateau, M., Chelli, B., Pinel, C. & Ravanat, J. L. Green autofluorescence, a double edged monitoring tool for bacterial growth and activity in micro-plates. *Phys. Biol.* **12**, 066016 (2015).
125. Shilova, O. N., Shilov, E. S. & Deyev, S. M. The effect of trypan blue treatment on autofluorescence of fixed cells. *Cytom. Part A* **91**, 917–925 (2017).
126. Papazoglou, T. G. Malignancies and atherosclerotic plaque diagnosis-is laser induced fluorescence spectroscopy the ultimate solution? *Journal of Photochemistry and Photobiology, B: Biology* vol. 28 3–11 (1995).
127. Li, F. *et al.* Autofluorescence contributes to false-positive intracellular Foxp3 staining in macrophages: A lesson learned from flow cytometry. *J. Immunol. Methods* **386**, 101–107 (2012).
128. Eickhardt, S. *et al.* Autofluorescence in samples obtained from chronic biofilm infections – “all that glitters is not gold”. *Pathog. Dis.* **73**, (2015).
129. Pauly, J. L. *et al.* Fluorescent human lung macrophages analyzed by spectral confocal laser scanning microscopy and multispectral cytometry. *Microsc. Res. Tech.* **67**, 79–89 (2005).
130. Sköld, C. M., Eklund, A., Halldén, G. & Hed, J. Autofluorescence in human alveolar macrophages from smokers: Relation to cell surface markers and phagocytosis. *Exp. Lung Res.* **15**, 823–835 (1989).
131. Sköld, C. M., Lundahl, J., Halldén, G., Hallgren, M. & Eklund, A. Chronic smoke exposure alters the phenotype pattern and the metabolic response in human alveolar macrophages. *Clin. Exp. Immunol.* **106**, 108–113 (1996).
132. Streck, R. J. *et al.* A method for isolating human lung macrophages and observations of fluorescent phagocytes from the lungs of habitual cigarette smokers. *J. Immunol. Methods* **174**, 67–82 (1994).
133. Reiter, C. Fluorescence test to identify deep smokers. *Forensic Sci. Int.* **31**, 21–26

(1986).

134. Plowman, P. N. & Flemans, R. J. Human pulmonary macrophages: The relationship of smoking to the presence of sea blue granules and surfactant turnover. *J. Clin. Pathol.* **33**, 738–743 (1980).
135. Martin, R. R. Altered morphology and increased acid hydrolase content of pulmonary macrophages from cigarette smokers. *Am. Rev. Respir. Dis.* **107**, 596–601 (1973).
136. Lillemeier, B. F. *et al.* TCR and Lat are expressed on separate protein islands on T cell membranes and concatenate during activation. *Nat. Immunol.* **11**, 90–96 (2010).
137. Williamson, D. J. *et al.* Pre-existing clusters of the adaptor Lat do not participate in early T cell signaling events. *Nat. Immunol.* **12**, 655–662 (2011).
138. Sherman, E., Barr, V. & Samelson, L. E. Super-resolution characterization of TCR-dependent signaling clusters. *Immunol. Rev.* **251**, 21–35 (2013).
139. Mattila, P. K. *et al.* The Actin and Tetraspanin Networks Organize Receptor Nanoclusters to Regulate B Cell Receptor-Mediated Signaling. *Immunity* **38**, 461–474 (2013).
140. Maity, P. C. *et al.* B cell antigen receptors of the IgM and IgD classes are clustered in different protein islands that are altered during B cell activation. *Sci. Signal.* **8**, ra93–ra93 (2015).
141. Bierwagen, J. *et al.* Far-field autofluorescence nanoscopy. *Nano Lett.* **10**, 4249–4252 (2010).
142. The Nobel Prize in Chemistry 2014 - Press release. <https://www.nobelprize.org/prizes/chemistry/2014/press-release/>.
143. Dong, B. *et al.* Superresolution intrinsic fluorescence imaging of chromatin utilizing native, unmodified nucleic acids for contrast. *Proc. Natl. Acad. Sci. U. S. A.* **113**, 9716–9721 (2016).
144. Santhosh Kumar, B., Sandhyamani, S., Nazeer, S. S. & Jayasree, R. S. Rapid and

- simple method of photobleaching to reduce background autofluorescence in lung tissue sections. *Indian Journal of Biochemistry and Biophysics* vol. 52 107–110 (2015).
145. Sun, Y. & Chakrabartty, A. Cost-effective elimination of lipofuscin fluorescence from formalin-fixed brain tissue by white phosphor light emitting diode array. *Biochem. Cell Biol.* **94**, 545–550 (2016).
 146. Umino, T., Sköld, C. M., Pirruccello, S. J., Spurzem, J. R. & Rennard, S. I. Two-colour flow-cytometric analysis of pulmonary alveolar macrophages from smokers. *Eur. Respir. J.* **13**, 894–899 (1999).
 147. Halldén, G., Sköld, C. M., Eklund, A., Forslid, J. & Hed, J. Quenching of intracellular autofluorescence in alveolar macrophages permits analysis of fluorochrome labelled surface antigens by flow cytofluorometry. *J. Immunol. Methods* **142**, 207–214 (1991).
 148. Garn, H. Specific aspects of flow cytometric analysis of cells from the lung. *Exp. Toxicol. Pathol.* **57**, 21–24 (2006).
 149. Hodge, S. J., Hodge, G. L., Holmes, M. & Reynolds, P. N. Flow cytometric characterization of cell populations in bronchoalveolar lavage and bronchial brushings from patients with chronic obstructive pulmonary disease. *Cytometry* **61B**, 27–34 (2004).
 150. Arsić, A., Stajković, N., Spiegel, R. & Nikić-Spiegel, I. Effect of Vectashield-induced fluorescence quenching on conventional and super-resolution microscopy. *Sci. Rep.* **10**, 1–13 (2020).
 151. Van de Lest, C. H., Versteeg, E. M., Veerkamp, J. H. & Van Kuppevelt, T. H. Elimination of autofluorescence in immunofluorescence microscopy with digital image processing. *J. Histochem. Cytochem.* **43**, 727–730 (1995).
 152. Ovesný, M., Křížek, P., Borkovec, J., Švindrych, Z. & Hagen, G. M. ThunderSTORM: a comprehensive ImageJ plug-in for PALM and STORM data analysis and super-resolution imaging. *Bioinformatics* **30**, 2389–2390 (2014).
 153. Hoogendoorn, E. *et al.* The fidelity of stochastic single-molecule super-resolution

- reconstructions critically depends upon robust background estimation. *Sci. Rep.* **4**, 1–10 (2014).
154. Bromley, S. K. *et al.* The immunological synapse. *Annu. Rev. Immunol.* **19**, 375–396 (2001).
 155. Grakoui, A. *et al.* The immunological synapse: a molecular machine controlling T cell activation. *Science* **285**, 221–7 (1999).
 156. Monks, C. R. F., Freiberg, B. A., Kupfer, H., Sciaky, N. & Kupfer, A. Three-dimensional segregation of supramolecular activation clusters in T cells. *Nature* **395**, 82–86 (1998).
 157. Davis, D. M. *et al.* The human natural killer cell immune synapse. *Proc. Natl. Acad. Sci. U. S. A.* **96**, 15062–7 (1999).
 158. Treanor, B. *et al.* Microclusters of inhibitory killer immunoglobulin-like receptor signaling at natural killer cell immunological synapses. *J. Cell Biol.* **174**, 153–161 (2006).
 159. Campi, G., Varma, R. & Dustin, M. L. Actin and agonist MHC–peptide complex–dependent T cell receptor microclusters as scaffolds for signaling. *J. Exp. Med.* **202**, 1031–1036 (2005).
 160. Harwood, N. E. & Batista, F. D. The Cytoskeleton Coordinates the Early Events of B-cell Activation. *Cold Spring Harb. Perspect. Biol.* **3**, a002360–a002360 (2011).
 161. Bunnell, S. C. *et al.* T cell receptor ligation induces the formation of dynamically regulated signaling assemblies. *J. Cell Biol.* **158**, 1263–1275 (2002).
 162. Abeyweera, T. P., Merino, E. & Huse, M. Inhibitory signaling blocks activating receptor clustering and induces cytoskeletal retraction in natural killer cells. *J. Cell Biol.* **192**, 675–690 (2011).
 163. Liu, D. *et al.* Integrin-Dependent Organization and Bidirectional Vesicular Traffic at Cytotoxic Immune Synapses. *Immunity* **31**, 99–109 (2009).
 164. Chung, W., Abel, S. M. & Chakraborty, A. K. Protein Clusters on the T Cell Surface May Suppress Spurious Early Signaling Events. *PLoS One* **7**, e44444 (2012).

165. Schamel, W. W. A. & Alarcón, B. Organization of the resting TCR in nanoscale oligomers. *Immunol. Rev.* **251**, 13–20 (2013).
166. Rossboth, B. *et al.* TCRs are randomly distributed on the plasma membrane of resting antigen-experienced T cells. *Nat. Immunol.* **19**, 821–827 (2018).
167. Jaumouillé, V. & Grinstein, S. Receptor mobility, the cytoskeleton, and particle binding during phagocytosis. *Curr. Opin. Cell Biol.* **23**, 22–29 (2011).
168. Jutras, I. & Desjardins, M. PHAGOCYTOSIS: At the Crossroads of Innate and Adaptive Immunity. *Annu. Rev. Cell Dev. Biol.* **21**, 511–527 (2005).
169. Abbas Abul K., Lichtman, A. H. & Pillai, S. Cellular and Molecular Immunology. in *Elsevier* vol. 8^a ed. 76–77 (2015).
170. Barth, N. D., Marwick, J. A., Vendrell, M., Rossi, A. G. & Dransfield, I. The ‘Phagocytic synapse’ and clearance of apoptotic cells. *Frontiers in Immunology* vol. 8 1708 (2017).
171. Goodridge, H. S. *et al.* Activation of the innate immune receptor Dectin-1 upon formation of a \sim Phagocytic synapseTM. *Nature* **472**, 471–475 (2011).
172. Dustin, M. L. & Choudhuri, K. Signaling and Polarized Communication Across the T Cell Immunological Synapse. *Annu. Rev. Cell Dev. Biol.* **32**, 303–325 (2016).
173. Lin, J. *et al.* TIRF imaging of Fc gamma receptor microclusters dynamics and signaling on macrophages during frustrated phagocytosis. *BMC Immunol.* **17**, 5 (2016).
174. Freeman, S. A. *et al.* Integrins Form an Expanding Diffusional Barrier that Coordinates Phagocytosis. *Cell* **164**, 128–140 (2016).
175. Finetti, F., Cassioli, C. & Baldari, C. T. Transcellular communication at the immunological synapse: A vesicular traffic-mediated mutual exchange. *F1000Research* vol. 6 (2017).
176. Choudhuri, K. *et al.* Polarized release of T-cell-receptor-enriched microvesicles at the immunological synapse. *Nature* **507**, 118–123 (2014).
177. Margolis, L. & Sadovsky, Y. The biology of extracellular vesicles: The known

- unknowns. *PLOS Biol.* **17**, e3000363 (2019).
178. Johnstone, R. M., Adam, M., Hammond, J. R., Orr, L. & Turbide, C. Vesicle formation during reticulocyte maturation. Association of plasma membrane activities with released vesicles (exosomes). *J. Biol. Chem.* **262**, 9412–9420 (1987).
 179. Tetta, C., Ghigo, E., Silengo, L., Deregibus, M. C. & Camussi, G. Extracellular vesicles as an emerging mechanism of cell-to-cell communication. *Endocrine* **44**, 11–19 (2013).
 180. Veziroglu, E. M. & Mias, G. I. Characterizing Extracellular Vesicles and Their Diverse RNA Contents. *Frontiers in Genetics* vol. 11 700 (2020).
 181. Hessvik, N. P. & Llorente, A. Current knowledge on exosome biogenesis and release. *Cell. Mol. Life Sci.* **75**, 193–208 (2018).
 182. Kalluri, R. & LeBleu, V. S. The biology, function, and biomedical applications of exosomes. *Science* vol. 367 (2020).
 183. Gould, S. J. & Raposo, G. As we wait: coping with an imperfect nomenclature for extracellular vesicles. *J. Extracell. Vesicles* **2**, 20389 (2013).
 184. Rufino-Ramos, D. *et al.* Extracellular vesicles: Novel promising delivery systems for therapy of brain diseases. *Journal of Controlled Release* vol. 262 247–258 (2017).
 185. Zarovni, N. *et al.* Integrated isolation and quantitative analysis of exosome shuttled proteins and nucleic acids using immunocapture approaches. *Methods* **87**, 46–58 (2015).
 186. Davies, R. T. *et al.* Microfluidic filtration system to isolate extracellular vesicles from blood. *Lab Chip* **12**, 5202–5210 (2012).
 187. Ramirez, M. I. *et al.* Technical challenges of working with extracellular vesicles. *Nanoscale* vol. 10 881–906 (2018).
 188. Van Niel, G., D’Angelo, G. & Raposo, G. Shedding light on the cell biology of extracellular vesicles. *Nature Reviews Molecular Cell Biology* vol. 19 213–228

(2018).

189. Willms, E. *et al.* Cells release subpopulations of exosomes with distinct molecular and biological properties. *Sci. Rep.* **6**, 1–12 (2016).
190. Termini, C. M. & Gillette, J. M. Tetraspanins function as regulators of cellular signaling. *Frontiers in Cell and Developmental Biology* vol. 5 34 (2017).
191. Berditchevski, F. & Odintsova, E. Tetraspanins as Regulators of Protein Trafficking. *Traffic* **8**, 89–96 (2007).
192. Andreu, Z. & Yáñez-Mó, M. Tetraspanins in extracellular vesicle formation and function. *Front. Immunol.* **5**, 442 (2014).
193. Pluchino, S. & Smith, J. A. Explicating Exosomes: Reclassifying the Rising Stars of Intercellular Communication. *Cell* vol. 177 225–227 (2019).
194. Escola, J. M. *et al.* Selective enrichment of tetraspan proteins on the internal vesicles of multivesicular endosomes and on exosomes secreted by human B-lymphocytes. *J. Biol. Chem.* **273**, 20121–20127 (1998).
195. Bonifacino, J. S. & Traub, L. M. Signals for sorting of transmembrane proteins to endosomes and lysosomes. *Annual Review of Biochemistry* vol. 72 395–447 (2003).
196. Rous, B. A. *et al.* Role of adaptor complex AP-3 in targeting wild-type and mutated CD63 to lysosomes. *Mol. Biol. Cell* **13**, 1071–1082 (2002).
197. Baietti, M. F. *et al.* Syndecan-syntenin-ALIX regulates the biogenesis of exosomes. *Nat. Cell Biol.* **14**, 677–685 (2012).
198. Latysheva, N. *et al.* Syntenin-1 Is a New Component of Tetraspanin-Enriched Microdomains: Mechanisms and Consequences of the Interaction of Syntenin-1 with CD63. *Mol. Cell. Biol.* **26**, 7707–7718 (2006).
199. Quast, T. *et al.* CD81 is essential for the formation of membrane protrusions and regulates Rac1-activation in adhesion-dependent immune cell migration. *Blood* **118**, 1818–1827 (2011).
200. Tejera, E. *et al.* CD81 regulates cell migration through its association with Rac

- GTPase. *Mol. Biol. Cell* **24**, 261–273 (2013).
201. Sala-Valdés, M. *et al.* EWI-2 and EWI-F link the tetraspanin web to the actin cytoskeleton through their direct association with ezrin-radixin-moesin proteins. *J. Biol. Chem.* **281**, 19665–19675 (2006).
 202. Neisch, A. L. & Fehon, R. G. Ezrin, Radixin and Moesin: Key regulators of membrane-cortex interactions and signaling. *Current Opinion in Cell Biology* vol. 23 377–382 (2011).
 203. Schuh, M. An actin-dependent mechanism for long-range vesicle transport. *Nat. Cell Biol.* **13**, 1431–1436 (2011).
 204. Ross, J. L., Ali, M. Y. & Warshaw, D. M. Cargo transport: molecular motors navigate a complex cytoskeleton. *Current Opinion in Cell Biology* vol. 20 41–47 (2008).
 205. Müller, M. T. *et al.* Interaction of microtubules and actin during the post-fusion phase of exocytosis. *Sci. Rep.* **9**, 1–15 (2019).
 206. Porat-Shliom, N., Milberg, O., Masedunskas, A. & Weigert, R. Multiple roles for the actin cytoskeleton during regulated exocytosis. *Cellular and Molecular Life Sciences* vol. 70 2099–2121 (2013).
 207. Eitzen, G. Actin remodeling to facilitate membrane fusion. *Biochimica et Biophysica Acta - Molecular Cell Research* vol. 1641 175–181 (2003).
 208. Vietri, M., Radulovic, M. & Stenmark, H. The many functions of ESCRTs. *Nature Reviews Molecular Cell Biology* vol. 21 25–42 (2020).
 209. Stuffers, S., Sem Wegner, C., Stenmark, H. & Brech, A. Multivesicular Endosome Biogenesis in the Absence of ESCRTs. *Traffic* **10**, 925–937 (2009).
 210. Buschow, S. I. *et al.* MHC II In dendritic cells is targeted to lysosomes or t cell-induced exosomes via distinct multivesicular body pathways. *Traffic* **10**, 1528–1542 (2009).
 211. Petersen, S. H. *et al.* The role of tetraspanin CD63 in antigen presentation via MHC class II. *Eur. J. Immunol.* **41**, 2556–2561 (2011).

212. Piccin, A., Murphy, W. G. & Smith, O. P. Circulating microparticles: pathophysiology and clinical implications. *Blood Rev.* **21**, 157–171 (2007).
213. Al-Nedawi, K. *et al.* Intercellular transfer of the oncogenic receptor EGFRvIII by microvesicles derived from tumour cells. *Nat. Cell Biol.* **10**, 619–624 (2008).
214. Chevillet, J. R. *et al.* Quantitative and stoichiometric analysis of the microRNA content of exosomes. *Proc. Natl. Acad. Sci. U. S. A.* **111**, 14888–14893 (2014).
215. Valadi, H. *et al.* Exosome-mediated transfer of mRNAs and microRNAs is a novel mechanism of genetic exchange between cells. *Nat. Cell Biol.* **9**, 654–659 (2007).
216. Mathieu, M., Martin-Jaular, L., Lavieu, G. & Théry, C. Specificities of secretion and uptake of exosomes and other extracellular vesicles for cell-to-cell communication. *Nature Cell Biology* vol. 21 9–17 (2019).
217. Raposo, G. *et al.* B lymphocytes secrete antigen-presenting vesicles. *J. Exp. Med.* **183**, 1161–72 (1996).
218. Tkach, M. *et al.* Qualitative differences in T-cell activation by dendritic cell-derived extracellular vesicle subtypes. *EMBO J.* **36**, 3012–3028 (2017).
219. Luga, V. *et al.* Exosomes mediate stromal mobilization of autocrine Wnt-PCP signaling in breast cancer cell migration. *Cell* **151**, 1542–1556 (2012).
220. Tomasetti, M., Lee, W., Santarelli, L. & Neuzil, J. Exosome-derived microRNAs in cancer metabolism: Possible implications in cancer diagnostics and therapy. *Experimental and Molecular Medicine* vol. 49 e285 (2017).
221. Kosaka, N. *et al.* Neutral sphingomyelinase 2 (nSMase2)-dependent exosomal transfer of angiogenic micrornas regulate cancer cell metastasis. *J. Biol. Chem.* **288**, 10849–10859 (2013).
222. Chen, G. *et al.* Exosomal PD-L1 contributes to immunosuppression and is associated with anti-PD-1 response. *Nature* **560**, 382–386 (2018).
223. Murphy, D. E. *et al.* Extracellular vesicle-based therapeutics: natural versus engineered targeting and trafficking. *Experimental and Molecular Medicine* vol. 51 1–12 (2019).

224. de Jong, B., Barros, E. R., Hoenderop, J. G. J. & Rigalli, J. P. Recent advances in extracellular vesicles as drug delivery systems and their potential in precision medicine. *Pharmaceutics* vol. 12 1–37 (2020).
225. Wollman, A. J. M., Nudd, R., Hedlund, E. G. & Leake, M. C. From animaculum to single molecules: 300 years of the light microscope. *Open Biology* vol. 5 (2015).
226. Abbe, E. Beiträge zur Theorie des Mikroskops und der mikroskopischen Wahrnehmung. *Arch. für Mikroskopische Anat.* **9**, 413–418 (1873).
227. Mittelbrunn, M. *et al.* Unidirectional transfer of microRNA-loaded exosomes from T cells to antigen-presenting cells. *Nat. Commun.* **2**, 1–10 (2011).
228. Gabrielli, M. *et al.* Active endocannabinoids are secreted on extracellular membrane vesicles. *EMBO Rep.* **16**, 213–220 (2015).
229. Higginbotham, J. N. *et al.* Amphiregulin exosomes increase cancer cell invasion. *Curr. Biol.* **21**, 779–786 (2011).
230. Lai, C. P. *et al.* Visualization and tracking of tumour extracellular vesicle delivery and RNA translation using multiplexed reporters. *Nat. Commun.* **6**, 1–12 (2015).
231. Colombo, F. *et al.* Cytokines stimulate the release of microvesicles from myeloid cells independently from the P2X7 receptor/acid sphingomyelinase pathway. *Front. Immunol.* **9**, 204 (2018).
232. De Boer, P., Hoogenboom, J. P. & Giepmans, B. N. G. Correlated light and electron microscopy: Ultrastructure lights up! *Nature Methods* vol. 12 503–513 (2015).
233. Arasu, U. T., Härkönen, K., Koistinen, A. & Rilla, K. Correlative light and electron microscopy is a powerful tool to study interactions of extracellular vesicles with recipient cells. *Exp. Cell Res.* **376**, 149–158 (2019).
234. Chen, C. *et al.* Imaging and Intracellular Tracking of Cancer-Derived Exosomes Using Single-Molecule Localization-Based Super-Resolution Microscope. *ACS Appl. Mater. Interfaces* **8**, 25825–25833 (2016).
235. Nizamudeen, Z. *et al.* Rapid and accurate analysis of stem cell-derived extracellular vesicles with super resolution microscopy and live imaging. *Biochim.*

Biophys. Acta - Mol. Cell Res. **1865**, 1891–1900 (2018).

236. Perou, C. M. *et al.* Molecular portraits of human breast tumours. *Nature* **406**, 747–752 (2000).
237. Sørlie, T. *et al.* Gene expression patterns of breast carcinomas distinguish tumor subclasses with clinical implications. *Proc. Natl. Acad. Sci. U. S. A.* **98**, 10869–10874 (2001).
238. Chen, C. *et al.* Visualization and intracellular dynamic tracking of exosomes and exosomal miRNAs using single molecule localization microscopy. *Nanoscale* **10**, 5154–5162 (2018).
239. Lennon, K. M. *et al.* Single molecule characterization of individual extracellular vesicles from pancreatic cancer. *J. Extracell. Vesicles* **8**, 1685634 (2019).
240. Ettinger, A. & Wittmann, T. Fluorescence live cell imaging. in *Methods in cell biology* vol. 123 77–94 (2014).
241. Ishikawa-Ankerhold, H. C., Ankerhold, R. & Drummen, G. P. C. Advanced Fluorescence Microscopy Techniques—FRAP, FLIP, FLAP, FRET and FLIM. *Molecules* **17**, 4047–4132 (2012).
242. Axelrod, D. Total Internal Reflection Fluorescence Microscopy. in *Methods in cell biology* vol. 89 169–221 (2008).
243. Fooksman, D. R., Grönvall, G. K., Tang, Q. & Edidin, M. Clustering Class I MHC Modulates Sensitivity of T Cell Recognition. *J. Immunol.* **176**, 6673–6680 (2006).
244. Culley, F. J. *et al.* Natural Killer Cell Signal Integration Balances Synapse Symmetry and Migration. *PLoS Biol.* **7**, e1000159 (2009).
245. Crites, T. J. *et al.* Supported Lipid Bilayer Technology for the Study of Cellular Interfaces. *Curr. Protoc. Cell Biol.* **68**, 24.5.1-24.5.31 (2015).
246. Sezgin, E. Super-resolution optical microscopy for studying membrane structure and dynamics. *J. Phys. Condens. Matter* (2017) doi:10.1088/1361-648X/aa7185.
247. Izeddin, I. *et al.* Wavelet analysis for single molecule localization microscopy. *Opt. Express* **20**, 2081 (2012).

248. Stallinga, S. & Rieger, B. Accuracy of the Gaussian Point Spread Function model in 2D localization microscopy. *Opt. Express* **18**, 24461 (2010).
249. Thompson, R. E., Larson, D. R. & Webb, W. W. Precise nanometer localization analysis for individual fluorescent probes. *Biophys. J.* **82**, 2775–2783 (2002).
250. Smith, C. S., Joseph, N., Rieger, B. & Lidke, K. A. Fast, single-molecule localization that achieves theoretically minimum uncertainty. *Nat. Methods* **7**, 373–375 (2010).
251. Huang, F., Schwartz, S. L., Byars, J. M. & Lidke, K. A. Simultaneous multiple-emitter fitting for single molecule super-resolution imaging. *Biomed. Opt. Express* **2**, 1377 (2011).
252. Novák, T., Gajdos, T., Sinkó, J., Szabó, G. & Erdélyi, M. TestSTORM: Versatile simulator software for multimodal super-resolution localization fluorescence microscopy. *Sci. Rep.* **7**, 951 (2017).
253. Schindelin, J. *et al.* Fiji: An open-source platform for biological-image analysis. *Nature Methods* vol. 9 676–682 (2012).
254. Ambrose, A. R. *et al.* Corrected Super-Resolution Microscopy Enables Nanoscale Imaging of Autofluorescent Lung Macrophages. *Biophys. J.* **119**, 2403–2417 (2020).
255. Théry, C., Amigorena, S., Raposo, G. & Clayton, A. Isolation and Characterization of Exosomes from Cell Culture Supernatants and Biological Fluids. *Curr. Protoc. Cell Biol.* **30**, 3.22.1-3.22.29 (2006).
256. Coillard, A. & Segura, E. In vivo Differentiation of Human Monocytes. *Front. Immunol.* **10**, 1907 (2019).
257. Sköld, C. M., Eklund, A., Halldén, G. & Hed, J. Autofluorescence in human alveolar macrophages from smokers: Relation to cell surface markers and phagocytosis. *Exp. Lung Res.* **15**, 823–835 (1989).
258. Schnell, S. A., Staines, W. A. & Wessendorf, M. W. Reduction of lipofuscin-like autofluorescence in fluorescently labeled tissue. *J. Histochem. Cytochem.* **47**, 719–730 (1999).

259. Neumann, M. & Gabel, D. Simple method for reduction of autofluorescence in fluorescence microscopy. *J. Histochem. Cytochem.* **50**, 437–439 (2002).
260. McWhorter, F. Y., Wang, T., Nguyen, P., Chung, T. & Liu, W. F. Modulation of macrophage phenotype by cell shape. *Proc. Natl. Acad. Sci. U. S. A.* **110**, 17253–17258 (2013).
261. Heinrich, F. *et al.* Morphologic, phenotypic, and transcriptomic characterization of classically and alternatively activated canine blood-derived macrophages in vitro. *PLoS One* **12**, e0183572 (2017).
262. Vereyken, E. J. F. *et al.* Classically and alternatively activated bone marrow derived macrophages differ in cytoskeletal functions and migration towards specific CNS cell types. *J. Neuroinflammation* **8**, 58 (2011).
263. Rostam, H. M., Reynolds, P. M., Alexander, M. R., Gadegaard, N. & Ghaemmaghami, A. M. Image based Machine Learning for identification of macrophage subsets. *Sci. Rep.* **7**, 1–11 (2017).
264. Ettensohn, D. B., Jankowski, M. J., Duncan, P. G. & Lalor, P. A. Bronchoalveolar lavage in the normal volunteer subject: 1. Technical aspects and intersubject variability. *Chest* **94**, 275–280 (1988).
265. Davies, J. Q. & Gordon, S. Isolation and culture of human macrophages. *Methods Mol. Biol.* **290**, 105–116 (2005).
266. Chávez-Galán, L., Olleros, M. L., Vesin, D. & Garcia, I. Much more than M1 and M2 macrophages, there are also CD169+ and TCR+ macrophages. *Frontiers in Immunology* vol. 6 263 (2015).
267. Stern, A. C. & Jones, T. C. The side-effect profile of GM-CSF. *Infection* **20**, S124–S127 (1992).
268. Crawford, J. *et al.* Myeloid growth factors, version 2.2017. *JNCCN Journal of the National Comprehensive Cancer Network* vol. 15 1520–1541 (2017).
269. Parameswaran, N. & Patial, S. Tumor necrosis factor- α signaling in macrophages. *Crit. Rev. Eukaryot. Gene Expr.* **20**, 87–103 (2010).

270. Rey-Giraud, F., Hafner, M. & Ries, C. H. In Vitro Generation of Monocyte-Derived Macrophages under Serum-Free Conditions Improves Their Tumor Promoting Functions. *PLoS One* **7**, e42656 (2012).
271. Byrne, A. J., Mathie, S. A., Gregory, L. G. & Lloyd, C. M. Pulmonary macrophages: Key players in the innate defence of the airways. *Thorax* vol. 70 1189–1196 (2015).
272. Mularski, A., Marie-Anaïs, F., Mazzolini, J. & Niedergang, F. Observing frustrated phagocytosis and phagosome formation and closure using total internal reflection fluorescence microscopy (TIRFM). in *Methods in Molecular Biology* vol. 1784 165–175 (Humana Press Inc., 2018).
273. Saraiva, M. & O’Garra, A. The regulation of IL-10 production by immune cells. *Nature Reviews Immunology* vol. 10 170–181 (2010).
274. Steen, E. H. *et al.* The Role of the Anti-Inflammatory Cytokine Interleukin-10 in Tissue Fibrosis. *Advances in Wound Care* vol. 9 184–198 (2020).
275. Surre, J. *et al.* Strong increase in the autofluorescence of cells signals struggle for survival. *Sci. Rep.* **8**, 1–14 (2018).
276. Huang, B., Bates, M. & Zhuang, X. Super-resolution fluorescence microscopy. *Annu. Rev. Biochem.* **78**, 993–1016 (2009).
277. Garcia-Parajo, M. F., Cambi, A., Torreno-Pina, J. A., Thompson, N. & Jacobson, K. Nanoclustering as a dominant feature of plasma membrane organization. *J. Cell Sci.* **127**, 4995–5005 (2014).
278. Kläsener, K., Maity, P. C., Hobeika, E., Yang, J. & Reth, M. B cell activation involves nanoscale receptor reorganizations and inside-out signaling by Syk. *Elife* **2014**, (2014).
279. Paegeon, S. V. *et al.* Superresolution microscopy reveals nanometer-scale reorganization of inhibitory natural killer cell receptors upon activation of NKG2D. *Sci. Signal.* **6**, (2013).
280. Oszmiana, A. *et al.* The Size of Activating and Inhibitory Killer Ig-like Receptor Nanoclusters Is Controlled by the Transmembrane Sequence and Affects

Signaling. *Cell Rep.* **15**, 1957–1972 (2016).

281. Allard, B., Panariti, A. & Martin, J. G. Alveolar Macrophages in the Resolution of Inflammation, Tissue Repair, and Tolerance to Infection. *Frontiers in immunology* vol. 9 1777 (2018).
282. Byrne, A. J., Mathie, S. A., Gregory, L. G. & Lloyd, C. M. Pulmonary macrophages: Key players in the innate defence of the airways. *Thorax* vol. 70 1189–1196 (2015).
283. Aggarwal, N. R., King, L. S. & D'Alessio, F. R. Diverse macrophage populations mediate acute lung inflammation and resolution. *American Journal of Physiology - Lung Cellular and Molecular Physiology* vol. 306 (2014).
284. Kugathasan, K. *et al.* CD11c⁺ antigen presenting cells from the alveolar space, lung parenchyma and spleen differ in their phenotype and capabilities to activate naïve and antigen-primed T cells. *BMC Immunol.* **9**, 48 (2008).
285. York, I. A. & Rock, K. L. ANTIGEN PROCESSING AND PRESENTATION BY THE CLASS I MAJOR HISTOCOMPATIBILITY COMPLEX. *Annu. Rev. Immunol.* **14**, 369–396 (1996).
286. York, I. A., Goldberg, A. L., Mo, X. Y. & Rock, K. L. Proteolysis and class I major histocompatibility complex antigen presentation. *Immunol. Rev.* **172**, 49–66 (1999).
287. Miyazaki, T., Suzuki, G. & Yamamura, K. ichi. The role of macrophages in antigen presentation and T cell tolerance. *Int. Immunol.* **5**, 1023–1033 (1993).
288. Townsend, A. & Bodmer, H. Antigen recognition by class I-restricted T lymphocytes. *Annual Review of Immunology* vol. 7 601–624 (1989).
289. Chaplin, D. D. Overview of the immune response. *J. Allergy Clin. Immunol.* **125**, S3 (2010).
290. Murugesan, S. *et al.* Formin-generated actomyosin arcs propel t cell receptor microcluster movement at the immune synapse. *Journal of Cell Biology* vol. 215 383–399 (2016).

291. Veerman, R. E., Güçlüler Akpınar, G., Eldh, M. & Gabrielsson, S. Immune Cell-Derived Extracellular Vesicles – Functions and Therapeutic Applications. *Trends in Molecular Medicine* vol. 25 382–394 (2019).
292. Lanyu, Z. & Feilong, H. Emerging role of extracellular vesicles in lung injury and inflammation Lanyu, Z., & Feilong, H. (2019). Emerging role of extracellular vesicles in lung injury and inflammation. In *Biomedicine and Pharmacotherapy* (Vol. 113). Elsevier Masson SAS. <https://doi.org/10.1016/j.biopha.2019.113>. *Biomedicine and Pharmacotherapy* vol. 113 (2019).
293. Soni, S. *et al.* Alveolar macrophage-derived microvesicles mediate acute lung injury. *Thorax* **71**, 1020–1029 (2016).
294. Lee, H., Abston, E., Zhang, D., Rai, A. & Jin, Y. Extracellular vesicle: An emerging mediator of intercellular crosstalk in lung inflammation and injury. *Frontiers in Immunology* vol. 9 924 (2018).
295. O’Farrell, H. E. & Yang, I. A. Extracellular vesicles in chronic obstructive pulmonary disease (COPD). *Journal of Thoracic Disease* vol. 11 S2141–S2154 (2019).
296. Lee, H., Zhang, D., Zhu, Z., Dela Cruz, C. S. & Jin, Y. Epithelial cell-derived microvesicles activate macrophages and promote inflammation via microvesicle-containing microRNAs. *Sci. Rep.* **6**, (2016).
297. Li, X. *et al.* Challenges and opportunities in exosome research-Perspectives from biology, engineering, and cancer therapy. *APL Bioengineering* vol. 3 (2019).
298. Brennan, K. *et al.* A comparison of methods for the isolation and separation of extracellular vesicles from protein and lipid particles in human serum. *Sci. Rep.* **10**, 1–13 (2020).
299. Hsu, Y. P., Meng, X. & VanNieuwenhze, M. S. Methods for visualization of peptidoglycan biosynthesis. in *Methods in Microbiology* vol. 43 3–48 (Academic Press Inc., 2016).
300. Chazotte, B. Labeling membrane glycoproteins or glycolipids with fluorescent wheat germ agglutinin. *Cold Spring Harb. Protoc.* **6**, pdb.prot5623 (2011).

301. Villar, S. A., Torcida, S. & Acosta, G. G. Median Filtering: A New Insight. *J. Math. Imaging Vis.* **58**, 130–146 (2017).
302. Hubert, M. & Debruyne, M. Breakdown value. *Wiley Interdiscip. Rev. Comput. Stat.* **1**, 296–302 (2009).
303. Frieden, B. R. NEW RESTORING ALGORITHM FOR THE PREFERENTIAL ENHANCEMENT OF EDGE GRADIENTS. *J Opt Soc Am* **66**, 280–283 (1976).
304. Huang, T. S., Yang, G. J. & Tang, G. Y. A Fast Two-Dimensional Median Filtering Algorithm. *IEEE Trans. Acoust.* **27**, 13–18 (1979).
305. Fang, L. & Jinsong, F. Salt and pepper noise removal by adaptive median filter and minimal surface inpainting. in *Proceedings of the 2009 2nd International Congress on Image and Signal Processing, CISP'09* (2009). doi:10.1109/CISP.2009.5303579.
306. Zhu, Y. & Huang, C. An Improved Median Filtering Algorithm for Image Noise Reduction. *Phys. Procedia* **25**, 609–616 (2012).
307. Guo, Z. Y. & Le, Z. Improved adaptive median filter. in *Proceedings - 2014 10th International Conference on Computational Intelligence and Security, CIS 2014* 44–46 (Institute of Electrical and Electronics Engineers Inc., 2015). doi:10.1109/CIS.2014.118.
308. Baddeley, D., Jayasinghe, I. D., Cremer, C., Cannell, M. B. & Soeller, C. Light-induced dark states of organic fluochromes enable 30 nm resolution imaging in standard media. *Biophys. J.* **96**, L22–L24 (2009).
309. Cremer, C. *et al.* Superresolution imaging of biological nanostructures by spectral precision distance microscopy. *Biotechnol. J.* **6**, 1037–1051 (2011).
310. Christine Hsiao, C. H. *et al.* The effects of macrophage source on the mechanism of phagocytosis and intracellular survival of Leishmania. *Microbes Infect.* **13**, 1033–1044 (2011).
311. Junt, T. *et al.* Subcapsular sinus macrophages in lymph nodes clear lymph-borne viruses and present them to antiviral B cells. *Nature* **450**, 110–114 (2007).

312. Cobb, D. A. & Gendelman, H. E. Exosomes and Neuroregulation. in *Neuroimmune Pharmacology* 313–328 (Springer International Publishing, 2017). doi:10.1007/978-3-319-44022-4_20.
313. Wang, L. *et al.* Role of lung surfactant in phagocytic clearance of apoptotic cells by macrophages in rats. *Lab. Investig.* **86**, 458–466 (2006).
314. Hulsmans, M. *et al.* Macrophages Facilitate Electrical Conduction in the Heart. *Cell* **169**, 510–522.e20 (2017).
315. Murray, P. J. & Wynn, T. A. Protective and pathogenic functions of macrophage subsets. *Nature Reviews Immunology* vol. 11 723–737 (2011).
316. Guilliams, M. *et al.* Unsupervised High-Dimensional Analysis Aligns Dendritic Cells across Tissues and Species. *Immunity* **45**, 669–684 (2016).
317. Langlet, C. *et al.* CD64 Expression Distinguishes Monocyte-Derived and Conventional Dendritic Cells and Reveals Their Distinct Role during Intramuscular Immunization. *J. Immunol.* **188**, 1751–1760 (2012).
318. Tamoutounour, S. *et al.* CD64 distinguishes macrophages from dendritic cells in the gut and reveals the Th1-inducing role of mesenteric lymph node macrophages during colitis. *Eur. J. Immunol.* **42**, 3150–3166 (2012).
319. T’Jonck, W., Guilliams, M. & Bonnardel, J. Niche signals and transcription factors involved in tissue-resident macrophage development. *Cell. Immunol.* **330**, 43–53 (2018).
320. Dugast, A. S. *et al.* Decreased Fc receptor expression on innate immune cells is associated with impaired antibody-mediated cellular phagocytic activity in chronically HIV-1 infected individuals. *Virology* **415**, 160–167 (2011).
321. Harrison, P. T., Davis, W., Norman, J. C., Hockaday, A. R. & Allen, J. M. Binding of monomeric immunoglobulin G triggers FcγRI-mediated endocytosis. *J. Biol. Chem.* **269**, 24396–24402 (1994).
322. DeLeo, A. M. & Ikezu, T. Extracellular Vesicle Biology in Alzheimer’s Disease and Related Tauopathy. *J. Neuroimmune Pharmacol.* **13**, 292–308 (2018).

323. Zhang, Y., Liu, Y., Liu, H. & Tang, W. H. Exosomes: Biogenesis, biologic function and clinical potential. *Cell and Bioscience* vol. 9 1–18 (2019).
324. Cheng, L., Wang, Y. & Huang, L. Exosomes from M1-Polarized Macrophages Potentiate the Cancer Vaccine by Creating a Pro-inflammatory Microenvironment in the Lymph Node. *Mol. Ther.* **25**, 1665–1675 (2017).
325. Saunderson, S. C., Dunn, A. C., Crocker, P. R. & McLellan, A. D. CD169 mediates the capture of exosomes in spleen and lymph node. *Blood* **123**, 208–216 (2014).
326. Lee, H., Zhang, D., Laskin, D. L. & Jin, Y. Functional Evidence of Pulmonary Extracellular Vesicles in Infectious and Noninfectious Lung Inflammation. *J. Immunol.* **201**, 1500–1509 (2018).
327. Walker, N. D. *et al.* Exosomes from differentially activated macrophages influence dormancy or resurgence of breast cancer cells within bone marrow stroma. *Cell Death Dis.* **10**, 1–16 (2019).
328. Charrin, S., Jouannet, S., Boucheix, C. & Rubinstein, E. Tetraspanins at a glance. *J. Cell Sci.* **127**, 3641–3648 (2014).
329. Ambrose, A. R., Hazime, K. S., Worboys, J. D., Niembro-Vivanco, O. & Davis, D. M. Synaptic secretion from human natural killer cells is diverse and includes supramolecular attack particles. *Proc. Natl. Acad. Sci. U. S. A.* **117**, 23717–23720 (2020).
330. Fritzsche, M. *et al.* Self-organizing actin patterns shape membrane architecture but not cell mechanics. *Nat. Commun.* **8**, 1–14 (2017).
331. Stricker, J., Falzone, T. & Gardel, M. L. Mechanics of the F-actin cytoskeleton. *J. Biomech.* **43**, 9–14 (2010).
332. Monastyrska, I., Rieter, E., Klionsky, D. J. & Reggiori, F. Multiple roles of the cytoskeleton in autophagy. *Biological Reviews* vol. 84 431–448 (2009).
333. Lanzetti, L. Actin in membrane trafficking. *Current Opinion in Cell Biology* vol. 19 453–458 (2007).
334. Anitei, M. & Hoflack, B. Bridging membrane and cytoskeleton dynamics in the

- secretory and endocytic pathways. *Nature Cell Biology* vol. 14 11–19 (2012).
335. Malacombe, M., Bader, M. F. & Gasman, S. Exocytosis in neuroendocrine cells: New tasks for actin. *Biochimica et Biophysica Acta - Molecular Cell Research* vol. 1763 1175–1183 (2006).
 336. Fritzsche, M. *et al.* Cytoskeletal actin dynamics shape a ramifying actin network underpinning immunological synapse formation. *Sci. Adv.* **3**, (2017).
 337. Carisey, A. F., Mace, E. M., Saeed, M. B., Davis, D. M. & Orange, J. S. Nanoscale Dynamism of Actin Enables Secretory Function in Cytolytic Cells. *Curr. Biol.* **28**, 489-502.e9 (2018).
 338. Gidlöf, O. *et al.* Proteomic profiling of extracellular vesicles reveals additional diagnostic biomarkers for myocardial infarction compared to plasma alone. *Sci. Rep.* **9**, 1–13 (2019).
 339. Van Spriel, A. B. Tetraspanins in the humoral immune response. *Biochemical Society Transactions* vol. 39 512–517 (2011).
 340. Levy, S. & Shoham, T. The tetraspanin web modulates immune-signalling complexes. *Nature Reviews Immunology* vol. 5 136–148 (2005).
 341. Witherden, D. A., Boismenu, R. & Havran, W. L. CD81 and CD28 Costimulate T Cells Through Distinct Pathways. *J. Immunol.* **165**, 1902–1909 (2000).
 342. Mittelbrunn, M., Yáñez-Mó, M., Sancho, D., Ursa, Á. & Sánchez-Madrid, F. Cutting Edge: Dynamic Redistribution of Tetraspanin CD81 at the Central Zone of the Immune Synapse in Both T Lymphocytes and APC. *J. Immunol.* **169**, 6691–6695 (2002).
 343. Mondal, A., Ashiq, K. A., Phulpagar, P., Singh, D. K. & Shiras, A. Effective Visualization and Easy Tracking of Extracellular Vesicles in Glioma Cells. *Biol. Proced. Online* **21**, 4 (2019).
 344. Extracellular Vesicles Hub | ONI. <https://oni.bio/extracellular-vesicles/>.
 345. de Kruijff, B. & Cullis, P. R. The influence of poly(l-lysine) on phospholipid polymorphism Evidence that electrostatic polypeptide-phospholipid interactions

- can modulate bilayer/non-bilayer transitions. *BBA - Biomembr.* **601**, 235–240 (1980).
346. Pachmann, K. & Leibold, W. Insolubilization of protein antigens on polyacrylic plastic beads using poly-L-lysine. *J. Immunol. Methods* **12**, 81–89 (1976).
 347. Santos, A. M. *et al.* Capturing resting T cells: The perils of PLL correspondence. *Nature Immunology* vol. 19 203–205 (2018).
 348. Nimmerjahn, F. & Ravetch, J. V. Fcγ receptors as regulators of immune responses. *Nature Reviews Immunology* vol. 8 34–47 (2008).
 349. van Hezel, M. E., Nieuwland, R., van Bruggen, R. & Juffermans, N. P. The ability of extracellular vesicles to induce a pro-inflammatory host response. *International Journal of Molecular Sciences* vol. 18 (2017).
 350. Hussain, M. T., Iqbal, A. J. & Norling, L. V. The Role and Impact of Extracellular Vesicles in the Modulation and Delivery of Cytokines during Autoimmunity. *Int. J. Mol. Sci.* **21**, 7096 (2020).
 351. Davies, L. C., Jenkins, S. J., Allen, J. E. & Taylor, P. R. Tissue-resident macrophages. *Nat. Immunol.* **14**, 986–995 (2013).
 352. Svedberg, F. R. *et al.* The lung environment controls alveolar macrophage metabolism and responsiveness in type 2 inflammation. *Nat. Immunol.* **20**, 571–580 (2019).
 353. Chugh, P. & Paluch, E. K. The actin cortex at a glance. *J. Cell Sci.* **131**, (2018).
 354. Gil-Krzewska, A. *et al.* An actin cytoskeletal barrier inhibits lytic granule release from natural killer cells in patients with Chediak-Higashi syndrome. *J. Allergy Clin. Immunol.* **142**, 914-927.e6 (2018).
 355. Garzetti, L. *et al.* Activated macrophages release microvesicles containing polarized M1 or M2 mRNAs. *J. Leukoc. Biol.* **95**, 817–825 (2014).
 356. Théry, C. *et al.* Indirect activation of naïve CD4⁺ T cells by dendritic cell-derived exosomes. *Nat. Immunol.* **3**, 1156–1162 (2002).
 357. Giri, P. K. & Schorey, J. S. Exosomes Derived from M. Bovis BCG Infected

Macrophages Activate Antigen-Specific CD4⁺ and CD8⁺ T Cells In Vitro and In Vivo. *PLoS One* **3**, e2461 (2008).

358. Ramachandra, L. *et al.* Mycobacterium tuberculosis synergizes with ATP to induce release of microvesicles and exosomes containing major histocompatibility complex class II molecules capable of antigen presentation. *Infect. Immun.* **78**, 5116–5125 (2010).
359. Barkal, A. A. *et al.* Engagement of MHC class I by the inhibitory receptor LILRB1 suppresses macrophages and is a target of cancer immunotherapy article. *Nat. Immunol.* **19**, 76–84 (2017).
360. Takahashi, S. Molecular functions of SIRPα and its role in cancer (Review). *Biomedical Reports* vol. 9 3–7 (2018).
361. Wang, M. *et al.* Effect of exosome biomarkers for diagnosis and prognosis of breast cancer patients. *Clin. Transl. Oncol.* **20**, 906–911 (2018).
362. Belhadj, Z. *et al.* A combined “eat me/don’t eat me” strategy based on extracellular vesicles for anticancer nanomedicine. *J. Extracell. Vesicles* **9**, 1806444 (2020).
363. Kamekar, S. *et al.* Exosomes facilitate therapeutic targeting of oncogenic KRAS in pancreatic cancer. *Nature* **546**, 498–503 (2017).
364. Wang, Y. *et al.* Macrophage-derived extracellular vesicles: diverse mediators of pathology and therapeutics in multiple diseases. *Cell Death and Disease* vol. 11 1–18 (2020).
365. Li, N. L., Fu, L., Uchtenhagen, H., Achour, A. & Burshtyn, D. N. Cis association of leukocyte Ig-like receptor 1 with MHC class I modulates accessibility to antibodies and HCMV UL18. *Eur. J. Immunol.* **43**, 1042–1052 (2013).